University of Thessaly
School of Engineering
Department of Mechanical Engineering

PhD Thesis

NON-LINEAR HOMOGENIZATION THEORIES WITH APPLICATIONS TO TRIP STEELS

by

IOANNA PAPADIOTI
Diploma in Civil Engineering, University of Thessaly, 2012
M.Sc., Department of Mechanical Engineering, University of Thessaly, 2013

A Thesis
Submitted in Partial Fulfilment of the
Requirements for the Degree of
Doctor of Philosophy
2016

The approval of the PhD Thesis by the Department of Mechanical Engineering, School of Engineering, University of Thessaly does not imply acceptance of the author's views (N. 5343/32 $\alpha\rho$. 202 $\pi\alpha\rho$. 2).

Approved by the Following Members of the Thesis Committee:

First Member (Supervisor)

Professor Nikolaos Aravas
Department of Mechanical Engineering, University of Thessaly

Second Member

Professor Gregory Haidemenopoulos
Department of Mechanical Engineering, University of Thessaly

Third Member

Assistant Professor Alexis Kermanidis
Department of Mechanical Engineering, University of Thessaly

Fourth Member

Lecturer Michalis Agoras
Department of Mechanical Engineering, University of Thessaly

Fifth Member

Professor Antonios Giannakopoulos
School of Applied Mathematical and Physical Science, National Technical University

Sixth Member

Tenured Assistant Professor Kostas Danas
C.N.R.S., École Polytechnique, University of Paris-Saclay

Seventh Member

Professor Athanasios Papathanasiou
Department of Civil Engineering, University of Thessaly

Acknowledgements

The research reported in the thesis was carried out at the Laboratory of Mechanics & Strength of Materials under the doctoral program of the Department of Mechanical Engineering of the University of Thessaly (UTH). The thesis work was funded by fellowships from the Department of Mechanical Engineering via the Research Committee of University of Thessaly and the Institute for Research and Technology Thessaly (I.RE.TE.TH.).

First and foremost I would like to express my sincere gratitude to my thesis advisor, Professor Nikolaos Aravas who was abundantly helpful and offered invaluable assistance, support and guidance. I would like to thank him for the tremendous amount of knowledge that he transmitted to me all these years, as well as for his immense influence in my way of thinking.

I would also like to thank Assistant Professor Kostas Danas, member of my Thesis committee, who introduced me to three-dimensional (3-D) finite-element simulations. I am extremely grateful and indebted to him for his expert, sincere and valuable guidance.

I would like to express my gratitude to Professor Gregory Haidemenopoulos and Assistant Professor Alexis Kermanidis for their special interest in my work. I gratefully thank Professor Antonios Giannakopoulos for his insightful comments, as well as Professor Athanasios Papathanasiou and Lecturer Michalis Agoras for accepting to be members of my thesis committee. I feel extremely honored to have had a committee of such a high scientific caliber.

Last but not the least, I would like to thank my family: my parents and my sisters for their support throughout writing this thesis.

Ioanna Papadioti

October 2016, Volos.

Abstract

Non-Linear Homogenization Theories with Applications to TRIP Steels

Ioanna Papadioti

Supervisor: Professor Nikolaos Aravas

This work is concerned with the development of a general model for $N-$phase isotropic, incompressible, rate-independent elasto-plastic materials at finite strains. The model is based on the nonlinear homogenization variational (or modified secant) method which makes use of a linear comparison composite (LCC) material to estimate the effective flow stress of the nonlinear composite material. The homogenization approach leads to an optimization problem which needs to be solved numerically for the general case of a $N-$phase composite. In the special case of a two-phase composite an analytical result is obtained for the effective flow stress of the elasto-plastic composite material. Next, the model is validated by periodic three-dimensional unit cell calculations comprising a large number of spherical inclusions (of various sizes and of two different types) distributed randomly in a matrix phase. We find that the use of the lower Hashin-Shtrikman bound for the LCC gives the best predictions by comparison with the unit cell calculations for both the macroscopic stress-strain response as well as for the average strains in each of the phases. The formulation is subsequently extended to include hardening of the different phases.

Furthermore, a method for the numerical integration of the resulting constitutive equations in the context of a displacement driven finite element formulation is developed. The constitutive model is, then, implemented in a general-purpose finite element program. Interestingly, the model is found to be in excellent agreement even in the case where each of the phases follows a rather different hardening response.
The homogenization theory is also used to develop a constitutive model for the mechanical behavior of multiphase TRIP steels. The calibration of the model is based on uniaxial tension tests on TRIP steels. The problems of plastic flow localization and necking in tension are analyzed in detail. The constitutive model is used also for the calculation of "forming limit diagrams" for sheets made of TRIP steels; it is found that the TRIP effect increases the necking localization strains.

Keywords: Homogenization; Elasto-plasticity; Composite materials; Finite strains; TRIP steels

Contents

List of Figures

List of Tables

Chapter 1

Introduction

The main objective of homogenization is to predict the macroscopic behavior of composite materials in terms of the behavior of their constituents and prescribed statistical information about their microstructure. Homogenization methods are powerful tools for the simulation of the mechanical behavior composites, at a reasonable computational cost. Linking the mechanical response of composites to the underlying microstructure is relevant in a variety of technological applications. One example is the design and the optimization of the forming operations of multiphase metallic alloys.

The present thesis is concerned with the analytical and numerical estimation of the effective as well as the phase average response of $N-$phase incompressible isotropic elasto-plastic metallic composites. Special attention is given to particulate microstructures, i.e., composite materials which can be considered to comprise a distinct matrix phase and an isotropic distribution of spherical particles [76] (or in a more general setting an isotropic distribution of phases [75]). In the present work, the particles are considered to be stiffer than the matrix phase, which is the case in most metallic materials of interest, such as TRIP steels, dual phase steels, aluminum alloys and others. Such materials, usually contain second-phase particles (e.g., intermetallics, carbon particles) or just second and third phase variants (e.g., retained austenite, bainite, martensitic phases). In addition, these phases/particles tend to reinforce the yield strength of the composite while they usually have different strength and hardening behavior than the host matrix phase.

Historically, emphasis was originally placed on the determination of the elastic constants of a polycrystal from those of a single crystal with first theoretical considerations by Voigt and Reuss. Later, the focus was on the estimation of the effective or overall behavior of linear elastic composite materials. The homogenization methods which were developed include the variational principles of Hashin and Shtrikman [20], which are particularly well suited to estimate the effective behavior of composites with particulate random microstructures. There is also the self-consistent approximation, developed in several different physical contexts by various authors (e.g., Hershey [22], Kröner [33], Willis [75]), which is known to be fairly accurate for polycrystals and other materials with granular microstructures. For nonlinear (e.g., plastic, viscoplastic, etc.) composites, rigorous methods have not been available until fairly recently, even though efforts along these lines have been going on for some time,

particularly in the context of ductile polycrystals (e.g., Hill [25], Hutchinson [27]). Making use of a nonlinear extension of the Hashin-Shtrikman (HS) variational principles, due to Willis [77], the first bounds of the HS type for nonlinear composites were derived by Talbot and Willis [70].

Ponte Castañeda [48] proposed a more general variational approach making use of optimally chosen "linear comparison composites". This approach is not only capable of delivering bounds of the HS type for nonlinear composites, but, in addition, can be used to generate bounds and estimates of other types, such as self-consistent estimates and three-point bounds (Ponte Castañeda [49]). A different, but equivalent method for the special class of power-law materials has been proposed by Suquet [66]. Talbot and Willis [71] provided a simultaneous generalization of the variational principles of Talbot and Willis [70] and the linear comparison composite method of Ponte Castañeda [48], which has the potential to give improved estimates for certain special, non-standard situations.

More recently, Ponte Castañeda ([50],[53]) proposed a second approach that makes use of an "anisotropic composite linear comparison material". While this method does not yield bounds, it appears to give more accurate results.

In the literature of nonlinear homogenization there exists a large number of studies for two-phase composite materials. The reader is referred to Ponte Castañeda and Suquet [52], Ponte Castañeda [53], Idiart *et al.* [30], and Idiart [29] for a review of the nonlinear homogenization schemes such as the ones used in the present work and relevant estimates. Nonetheless, very few studies exist in the context of three- or $N-$phase rate independent elasto-plastic composites.

In view of this, the present work uses the nonlinear variational homogenization method (Ponte Castañeda [48]) or equivalently the modified secant method (Suquet [67]), which makes use of a linear comparison composite (LCC) material, to estimate the effective response of a $N-$phase nonlinear composite material. Even though, this method exists for several years most of the studies in the context of composite materials have been focused on two-phase composites where the optimization process required by the method can be done analytically (see for instance [13]). Nevertheless, as the number of phases increases to three or more the optimization can only be done numerically. Perhaps, that is the reason that in his original work, Ponte Castañeda [49] proposed general expressions (and bounds) for $N-$phase composites, but its numerical/analytical resolution remained untractable until today due to the complex optimization procedures required by the nonlinear homogenization method.

It should be pointed out at this point that these homogenization theories treat separately the elastic (which in the present case is trivial) and the plastic homogenization problem. That of course has certain impact if cyclic loading is considered which is beyond the scope of the present work and is not considered here. Nevertheless, recently, Lahellec and Suquet [34] proposed an incremental variational formulation for materials with a hereditary behavior described by two potentials: a free energy and a dissipation function. This method has been introduced mainly to deal with the coupled elasto-plastic response of composites in an attempt to resolve the cyclic response of these materials (see also recent work by Brassart

et al. [8]). Note that these more advanced methods use the aforementioned or variants of the LCC estimates. In this regard, the present study, albeit not using this coupled scheme, reveals the nature of equations required to deal with a general $N-$phase composite material and could be potentially useful in the future for such more complete incremental schemes, which are based upon those simpler LCC homogenization theories.

1.1 Scope of the present work

The scope of the present work is to provide a semi-analytical model for $N-$phase isotropic, incompressible rate-independent elasto-plastic materials. Simple analytical expressions are given for the effective yield stress of a two-phase composite (see also [13]) while a simple semi-analytical expression (requiring the solution of a constrained optimization problem for $N-1$ scalar quantities) is given for the $N-$phase composite. Additional analytical expressions are also provided for the phase concentration tensors and average strains in each phase in terms of the aforementioned optimized scalar quantities. In the context of two- and three-phase materials the model is assessed by appropriate three-dimensional multi-particle two- and three-phase periodic unit cell calculations considering both hardening and non-hardening phases. The agreement is found to be good not only for the effective yield stress but also for the phase average strains thus allowing for the extension of this model to include arbitrary isotropic hardening of the phases.

A methodology for the numerical integration of the resulting elastic-plastic equations is developed and the model is implemented into the ABAQUS general purpose finite element code [23]. This code provides a general interface so that a particular constitutive model can be introduced via a "user subroutine" named UMAT (User MATerial). The predictions of the model agree well with the results of detailed unit cell finite element calculations of a composite with hardening phases.

Then, the homogenization theory is used to develop a constitutive model for the mechanical behavior of TRIP (TRansformation Induced Plasticity) steels. TRIP steels are basically composite materials with evolving volume fractions of the constituent phases. Specifically, we consider four-phase TRIP steels that consist of a ferritic matrix with dispersed bainite and austenite, which transforms gradually into martensite as the material deforms plastically. We consider the total strain to be the sum of elastic, plastic and transformation parts. The elastic behavior of TRIP steels is described with standard isotropic linear hypoelasticity of homogeneous solids, since the elastic properties of all constituent phases are basically the same. The homogenization techniques for non-linear composites are used to determine the effective properties and overall behavior of TRIP steels. The transformation part is proportional to the rate of change of the volume fraction of martensite due to martensitic transformation, which is described by the modified Olson-Cohen transformation kinetics model proposed by Stringfellow *et al.* [64].

A method for the numerical integration of the resulting constitutive equations in the context of a displacement driven finite element formulation is developed and the model is implemented into the ABAQUS. The calibration of the model is based on uniaxial tension tests

on TRIP steels. We also develop a method for the numerical integration of the constitutive model under plane stress conditions. In these problems the out-of-plane component of the deformation gradient is not defined kinematically and the general method needs to be modified.
The problems of plastic flow localization and necking in tension are analyzed in detail. The constitutive model is used also for the calculation of "forming limit diagrams" for sheets made of TRIP steels. The predictions of the analysis are compared to experimental data from the same TRIP steel which was used for the calibration. Calculations are also conducted for a non-transforming steel for comparison purposes.
Standard notation is used throughout. Boldface symbols denote tensors the orders of which are indicated by the context. All tensor components are written with respect to a fixed Cartesian coordinate system with base vectors $\mathbf{e}_i$ $(i = 1, 2, 3)$, and the summation convention is used for repeated Latin indices, unless otherwise indicated. The prefice det indicates the determinant, a superscript T the transpose, a superposed dot the material time derivative, and the subscripts s and a the symmetric and anti-symmetric parts of a second order tensor. Let $\mathbf{a}$, $\mathbf{b}$ be vectors, $\mathbf{A}$, $\mathbf{B}$ second-order tensors, and $\mathbf{C}$ a fourth-order tensor; the following products are used in the text $(\mathbf{a}\,\mathbf{b})_{ij} = a_i\, b_j$, $\mathbf{A} : \mathbf{B} = A_{ij}\, B_{ij}$, $(\mathbf{A}\cdot\mathbf{B})_{ij} = A_{ik}\, B_{kj}$, $(\mathbf{A}\,\mathbf{B})_{ijkl} = A_{ij}\, B_{kl}$, $(\mathbf{C} : \mathbf{A})_{ij} = C_{ijkl}\, A_{kl}$, and $(\mathbf{C} : \mathbf{D})_{ijkl} = C_{ijpq}\, D_{pqkl}$. The inverse $\mathbf{C}^{-1}$ of a fourth-order tensor $\mathbf{C}$ that has the "minor" symmetries $C_{ijkl} = C_{jikl} = C_{ijlk}$ is defined so that $\mathbf{C} : \mathbf{C}^{-1} = \mathbf{C}^{-1} : \mathbf{C} = \mathbf{I}$, where $\mathbf{I}$ is the symmetric fourth-order identity tensor with Cartesian components $I_{ijkl} = (\delta_{ik}\,\delta_{jl} + \delta_{il}\,\delta_{jk})/2$, δ_{ij} being the Kronecker delta.

1.2 Thesis overview

The Thesis proceeds with Chapter 2, where we derive a semi-analytical model for $N-$phase isotropic, incompressible rate-independent elasto-plastic materials. Specifically, we use the methodology developed by Ponte Castañeda and co-workers ([48],[67]) which makes use of a linear comparison composite (LCC) material, to estimate the effective flow stress of the non-linear composite material. Additional semi-analytical expressions are also provided for the phase concentration tensors and average strains in each phase in terms of the aforementioned optimized scalar quantities. In the following, the homogenization techniques are applied to two- and three-phase elastoplastic composites, as well as, four-phase TRIP steels.
In Chapter 3, we examine the validity of the homogenization model using periodic three-dimensional unit cell calculations comprising a large number of spherical inclusions (of various sizes and of two different types) distributed randomly in a matrix phase. We find that in the context of two- and three-phase materials the use of the lower Hashin-Shtrikman bound for the LCC gives the best predictions by comparison with the unit cell calculations for both the macroscopic stress-strain response as well as for the average strains in each of the phases. In the special case of a two-phase composite an analytical result is obtained for the effective flow stress of the elasto-plastic composite material. Additional analytical expressions are also provided for the phase concentration tensors and average strains in each phase in terms of the aforementioned optimized scalar quantities. The agreement is found to be good not

only for the effective yield stress but also for the phase average strains thus allowing for the extension of this model to include arbitrary isotropic hardening of the phases.
In Chapter 4, we present an approximate method for the prediction of the incremental elastoplastic behavior of macroscopically isotropic composites made of N isotropic, rate-independent, elastic-plastic **hardening** phases. The elastic and plastic response of the homogenized composite are treated independently, and combined later to obtain the full elastic-plastic response. The elastic properties of all constituent phases are basically the same. Thus, in order to describe the elastic behavior of the composite material we use standard isotropic linear hypoelasticity of homogeneous solids. The plastic behavior of the composite material is determined by using the homogenization technique described in Chapter 2. The constitutive equations are developed for the case of finite geometry changes. The constitutive model is once again validated using periodic three-dimensional unit cell calculations.
In Chapter 5, we present a constitutive model for four-phase TRIP steels. The homogenization techniques for non-linear composites, described in Chapter 2, are used to determine the effective properties and overall behavior of TRIP steels. We develop a methodology for the numerical integration of the resulting elastoplastic constitutive equations and the model is implemented into the ABAQUS. Experimental data of uniaxial tension tests in TRIP steels are used for the calibration of the model. Then, we use the constitutive model to study in detail the problems of plastic flow localization and necking in tension. We also use the model to calculate "forming limit diagrams" for sheets made of TRIP steels. Calculations are also conducted for a non-transforming steel for comparison purposes.
Finally, Chapter 6 provides a brief summary of the contribution of this work together with some prospects for future work.

Chapter 2

Homogenization Theory

2.1 Introduction

The goal of this chapter is to derive a semi-analytical model for $N-$phase isotropic, incompressible rate-independent elasto-plastic materials. Specifically, we use the methodology developed by Ponte Castañeda and co-workers ([48],[67]) which makes use of a linear comparison composite (LCC) material, to estimate the effective flow stress of the nonlinear composite material. Additional semi-analytical expressions are also provided for the phase concentration tensors and average strains in each phase in terms of the aforementioned optimized scalar quantities.
Even though, this method exists for several years most of the studies in the context of composite materials have been focused on two-phase composites where the optimization process required by the method can be done analytically (see for instance [13]). Nevertheless, as the number of phases increases to three or more the optimization can only be done numerically.

2.2 Power-law creep and perfect plasticity

We consider an incompressible creeping solid characterized by a power-law stress potential U of the form

$$U(\sigma_e) = \frac{\sigma_0\,\dot{\varepsilon}_0}{n+1}\left(\frac{\sigma_e}{\sigma_0}\right)^{n+1}, \tag{2.1}$$

where σ_0 is a reference stress, $\dot{\varepsilon}_0$ a reference strain rate, n the creep exponent ($1 \leq n \leq \infty$), $\sigma_e = \sqrt{\frac{3}{2}\,\mathbf{s}:\mathbf{s}}$ the von Mises equivalent stress, $\boldsymbol{\sigma}$ the stress tensor, $p = \sigma_{kk}/3$ the hydrostatic stress, and $\mathbf{s} = \boldsymbol{\sigma} - p\,\boldsymbol{\delta}$ the stress deviator, $\boldsymbol{\delta}$ being the second-order identity tensor. The corresponding deformation rate $\mathbf{D}$ is defined as

$$\mathbf{D} = \frac{\partial U}{\partial \boldsymbol{\sigma}} = \dot{\bar{\varepsilon}}\,\mathbf{N}, \qquad \dot{\bar{\varepsilon}} = \dot{\varepsilon}_0\left(\frac{\sigma_e}{\sigma_0}\right)^n, \qquad \mathbf{N} = \frac{\partial \sigma_e}{\partial \boldsymbol{\sigma}} = \frac{3}{2\,\sigma_e}\mathbf{s}\,, \tag{2.2}$$

where $\mathbf{N}$ is a second order tensor of constant magnitude ($\mathbf{N}:\mathbf{N} = \frac{3}{2}$) that defines the direction of $\mathbf{D}$ and $\dot{\bar{\varepsilon}} = \sqrt{\frac{2}{3}\,\mathbf{D}:\mathbf{D}}$ is the equivalent plastic strain rate that defines the

magnitude of $\mathbf{D}$. Note that $D_{kk} = 0$.
The special case in which the exponent takes the value of unity ($n = 1$) corresponds to a linearly viscous solid:

$$U_L(\sigma_e) = \frac{\sigma_e^2}{6\,\mu}, \qquad \mathbf{D} = \frac{\partial U_L}{\partial \boldsymbol{\sigma}} = \frac{\mathbf{s}}{2\,\mu}, \tag{2.3}$$

where $\mu = \sigma_0/(3\,\dot{\varepsilon}_0)$ is the viscosity.
The other limiting case $n \to \infty$ corresponds to a perfectly plastic solid that obeys the von Mises yield condition with flow stress σ_0. In this case the stress function (2.1) becomes[1]

$$U_\infty(\sigma_e) = \begin{cases} 0 & \text{when} \quad \sigma_e \le \sigma_0\,, \\ \infty & \text{when} \quad \sigma_e > \sigma_0\,. \end{cases} \tag{2.4}$$

The threshold stress σ_0 in (2.4) is the flow stress of the material, and the flow rule is written in the form

$$\mathbf{D} = \dot{\bar{\varepsilon}}\,\mathbf{N}, \qquad \mathbf{N} = \frac{3}{2\,\sigma_e}\mathbf{s}\,, \qquad (\text{with} \quad \dot{\bar{\varepsilon}} = 0 \quad \text{if} \quad \sigma_e < \sigma_0), \tag{2.5}$$

where the equivalent plastic strain rate $\dot{\bar{\varepsilon}}$ is not defined locally by the constitutive equations and becomes one of the primary unknowns in the rate boundary value problem.

2.3 Homogenization method for non-linear viscous solids

We consider a composite material made of N isotropic, incompressible viscoplastic phases. The phases are distributed randomly and are characterized by viscoplastic stress potentials $U^{(r)}$ of the form (2.1) with constants $\left(\sigma_0^{(r)}, \dot{\varepsilon}_0, n^{(r)}\right)$ and $\mu^{(r)}$ in the linear case, i.e.,

$$U^{(r)}\left(\sigma_e^{(r)}\right) = \frac{\sigma_0^{(r)}\,\dot{\varepsilon}_0}{n^{(r)}+1}\left(\frac{\sigma_e^{(r)}}{\sigma_0^{(r)}}\right)^{n^{(r)}+1}, \qquad U_L^{(r)}(\sigma_e^{(r)}) = \frac{{\sigma_e^{(r)}}^2}{6\,\mu^{(r)}}, \tag{2.6}$$

where $\sigma_e^{(r)}$ is the von Mises equivalent stress in phase r. The volume fraction of each phase is $c^{(r)}$ $\left(\sum_{r=1}^{N} c^{(r)} = 1\right)$.
The constitutive equation of the isotropic nonlinear composite is written in terms of the effective viscoplastic stress potential $\tilde{U}(\boldsymbol{\sigma})$, so that

$$\mathbf{D} = \frac{\partial \tilde{U}}{\partial \boldsymbol{\sigma}}, \tag{2.7}$$

where $\boldsymbol{\sigma}$ and $\mathbf{D}$ are respectively the macroscopic stress and deformation rate in the composite. An estimate for $\tilde{U}$ is obtained by using the variational methodology of Ponte Castañeda and co-workers ([48], [51], [52]). This methodology has also been proposed independently for

[1] Here we take into account that $\lim_{n\to\infty} \frac{A^{n+1}}{n+1} = \begin{cases} 0 & \text{if } A \le 1, \\ \infty & \text{if } A > 1. \end{cases}$

power-law materials by [40] and interpreted as a secant homogenization method by [67]. The final form of the estimate reads

$$\tilde{U}(\sigma_e) = \sup_{\mu^{(r)} \geq 0} \left[U_L\left(\sigma_e, \tilde{\mu}(\mu^{(r)})\right) - \sum_{r=1}^{N} c^{(r)}\, v^{(r)}\left(\sigma_e^{(r)}, \mu^{(r)}\right) \right], \qquad U_L = \frac{\sigma_e^2}{6\,\tilde{\mu}(\mu^{(r)})}, \tag{2.8}$$

where σ_e is the macroscopic von Mises equivalent stress,

$$v^{(r)}\left(\sigma_e^{(r)}, \mu^{(r)}\right) = \sup_{\sigma_e^{(r)} \geq 0} \left[U_L^{(r)}\left(\sigma_e^{(r)}, \mu^{(r)}\right) - U^{(r)}\left(\sigma_e^{(r)}\right) \right], \tag{2.9}$$

$$U_L^{(r)} = \frac{{\sigma_e^{(r)}}^2}{6\,\mu^{(r)}}, \qquad U^{(r)} = \frac{\sigma_0^{(r)}\,\dot{\varepsilon}_0}{n^{(r)}+1} \left(\frac{\sigma_e^{(r)}}{\sigma_0^{(r)}} \right)^{n^{(r)}+1}. \tag{2.10}$$

The effective stress potential $\tilde{U}(\boldsymbol{\sigma})$ is defined in (2.8) in terms of the quadratic effective stress potential $\tilde{U}_L$ of a "linear comparison composite" (LCC) evaluated at the macroscopic stress σ_e and the "corrector functions" $v^{(r)}$, which are defined in (2.9) as the optimal difference between the quadratic potentials $U_L^{(r)}$ and the actual potentials of the non-linear materials $U^{(r)}$. The stress tensors $\sigma_e^{(r)}$ in (2.9) are obtained by the "sup" operation in that equation and hence $v^{(r)}$ are only functions of the individual viscosities of the linearized phases, $\mu^{(r)}$. It is worth noting at this point that the estimate (2.8) of $\tilde{U}$ may have the character of a rigorous bound provided that the corresponding estimate $\tilde{U}_L$ has also the same character of a bound as discussed in the following. Nonetheless the scope of the present work is to insist mainly on a good estimate by comparison with numerical unit cell calculations and not necessarily on rigorous bounds.

In this view, the quadratic potential $\tilde{U}_L$ of the LCC in (2.8b) uses the effective viscosity $\tilde{\mu}$ of the LCC that depends on the individual viscosities $\mu^{(r)}$ and the corresponding volume fractions $c^{(r)}$. One way to estimate $\tilde{\mu}$ is to use the well-known Hashin-Shtrikman relationship for particulate composites (e.g., see Willis [76])

$$\tilde{\mu}\left(\mu^{(r)}\right) = \left(\sum_{s=1}^{N} \frac{c^{(s)}\,\mu^{(s)}}{3\,\mu_0 + 2\,\mu^{(s)}} \right) \left(\sum_{r=1}^{N} \frac{c^{(r)}}{3\,\mu_0 + 2\,\mu^{(r)}} \right)^{-1}, \tag{2.11}$$

where μ_0 is a "reference viscosity" to be chosen appropriately. An upper bound for $\tilde{\mu}$ is produced by (2.11) when μ_0 is chosen to be the maximum of all $\mu^{(r)}$ and a lower bound is produced when μ_0 is the minimum of all $\mu^{(r)}$ (Willis [76]). The "reference viscosity" can be chosen in various ways:

i) Hashin-Shtrikman: $\mu_0 = \mu^{(r)}$

ii) Arithmetic average: $\mu_0 = \sum_{r=1}^{N} c^{(r)}\,\mu^{(r)}$

iii) Harmonic average: $\frac{1}{\mu_0} = \sum_{r=1}^{N} \frac{c^{(r)}}{\mu^{(r)}}$

iv) Self-consistent scheme: $\mu_0 = \dfrac{\sum_{s=1}^{N} \frac{c^{(s)}\,\mu^{(s)}}{3\,\mu_0+2\,\mu^{(s)}}}{\sum_{r=1}^{N} \frac{c^{(r)}}{3\,\mu_0+2\,\mu^{(r)}}}$

An important observation made by several authors is that the Hashin-Shtrikman **bounds** are accurate **estimates** for composites with particulate microstructures, at least for two-phase systems at moderate volume fraction (Bonnenfant *et al.* [7]); in particular, the upper bound is a good estimate when the stiffest material is the matrix phase and contains inclusions of the most compliant material, whereas the lower bound is a good estimate for the inverse situation in which the most compliant material is the matrix phase containing inclusions of the stiffest material.

When no phase plays clearly the role of a matrix, the effective properties of the composite may be estimated by the "self-consistent" method of Hill [25]. In this case, the relevant microstructure is granular in character, being composed of ellipsoidal particles of the different phases with varying size so as to fill space. Equation (2.11) provides Hills self-consistent estimate, if μ_0 is identified with the effective modulus $\tilde{\mu}$; in this case, (2.11) becomes a polynomial equation of order $2\,N$ for $\tilde{\mu}$ (Willis [76]).

2.3.1 Perfectly plastic phases

We consider the case of perfectly plastic phases ($n^{(r)} \to \infty$). The optimization in (2.8) and (2.9) as $n^{(r)} \to \infty$ is carried out in three steps. In the first step, we consider the optimization over $\sigma_e^{(r)}$ in (2.9). All creep exponents are set equal in the second step, i.e., we set $n^{(1)} = n^{(2)} = \cdots = n^{(N)} \equiv n$. In the final third step we consider the limit $n \to \infty$. Details of the calculations are given in the following.

Step 1: Calculation of $\sigma_e^{(r)}$ in (2.9)

The "inner" optimization in (2.9) is carried out by setting equal to zero the derivatives

$$\frac{\partial}{\partial \sigma_e^{(r)}} \left(U_L^{(r)} - U^{(r)} \right) = 0 \quad \Rightarrow \quad \left(\frac{\sigma_e^{(r)}}{3\,\mu^{(r)}} - \frac{\partial U^{(r)}}{\partial \sigma_e^{(r)}} \right) = 0$$

$$\Rightarrow \quad \left[\frac{\sigma_e^{(r)}}{3\,\mu^{(r)}} - \dot{\varepsilon}_0 \left(\frac{\sigma_e^{(r)}}{\sigma_0^{(r)}} \right)^{n^{(r)}} \right] = 0 \tag{2.12}$$

which defines the optimal values of $\sigma_e^{(r)}$ as

$$\sigma_e^{(r)} = \left[\frac{\left(\sigma_0^{(r)}\right)^{n^{(r)}}}{3\,\mu^{(r)}\,\dot{\varepsilon}_0} \right]^{\frac{1}{n^{(r)}-1}} \equiv \hat{\sigma}_e^{(r)}. \tag{2.13}$$

When the optimal values $\hat{\sigma}_e^{(r)}$ are substituted into (2.8), the expression for the estimate of the effective stress potential becomes

$$\tilde{U}(\sigma_e) = \sup_{\mu^{(r)}\geq 0} \left\{ \frac{\sigma_e^2}{6\,\tilde{\mu}(\mu^{(r)})} - \frac{1}{2}\sum_{r=1}^{N} \frac{n^{(r)}-1}{n^{(r)}+1} \left[\frac{\left(\sigma_0^{(r)}\right)^{n^{(r)}}}{\dot{\varepsilon}_0} \right]^{\frac{2}{n^{(r)}-1}} \frac{c^{(r)}}{\left(3\,\mu^{(r)}\right)^{\frac{n^{(r)}+1}{n^{(r)}-1}}} \right\}, \tag{2.14}$$

where $\tilde{\mu}(\mu^{(r)})$ is defined in (2.11). Substitution of the expression (2.11) for $\tilde{\mu}$ into (2.14) leads to

$$\tilde{U}(\sigma_e) = \sup_{\substack{y^{(r)}\geq 0 \\ y^{(1)}=1}} \sup_{\mu^{(1)}>0} \left[F\left(y^{(r)}\right) \frac{\sigma_e^2}{6\,\mu^{(1)}} - I\left(\mu^{(1)}, y^{(r)}\right) \right], \tag{2.15}$$

where

$$F\left(y^{(r)}\right) = \frac{\mu^{(1)}}{\tilde{\mu}} = \frac{\sum_{r=1}^{N} \frac{c^{(r)}\,y^{(r)}}{3\,\frac{y^{(r)}}{y_0}+2}}{\sum_{s=1}^{N} \frac{c^{(s)}}{3\,\frac{y^{(s)}}{y_0}+2}} \equiv \frac{T_1\left(y^{(i)}\right)}{T_2\left(y^{(i)}\right)}, \tag{2.16}$$

$$I\left(\mu^{(1)}, y^{(r)}\right) = \frac{1}{2}\sum_{r=1}^{N} c^{(r)} \frac{n^{(r)}-1}{n^{(r)}+1} \left[\frac{\left(\sigma_0^{(r)}\right)^{n^{(r)}}}{\dot{\varepsilon}_0} \right]^{\frac{2}{n^{(r)}-1}} \left(\frac{y^{(r)}}{3\,\mu^{(1)}} \right)^{\frac{n^{(r)}+1}{n^{(r)}-1}}, \tag{2.17}$$

$$y^{(r)} = \frac{\mu^{(1)}}{\mu^{(r)}} \quad (\text{with } \; y^{(1)}=1), \qquad \text{and} \qquad y_0 = \frac{\mu^{(1)}}{\mu_0}. \tag{2.18}$$

The value of the optimization parameter y_0 depends on the choice of the "reference viscosity":

i) Hashin-Shtrikman: $\mu_0 = \mu^{(1)}$

$$y_0 = 1 \quad \Rightarrow \quad \frac{\partial y_0}{\partial y^{(r)}} = 0, \tag{2.19}$$

ii) Arithmetic average: $\mu_0 = \sum_{r=1}^{N} c^{(r)}\,\mu^{(r)}$

$$\frac{1}{y_0} = \frac{\mu_0}{\mu^{(1)}} = \sum_{r=1}^{N} c^{(r)} \frac{\mu^{(r)}}{\mu^{(1)}} = \sum_{r=1}^{N} \frac{c^{(r)}}{y^{(r)}} \;\Rightarrow\; -\frac{1}{y_0^2}\frac{\partial y_0}{\partial y^{(i)}} = -\frac{c^{(i)}}{{y^{(i)}}^2} \;\Rightarrow\; \frac{\partial y_0}{\partial y^{(i)}} = c^{(i)} \left(\frac{y_0}{y^{(i)}} \right)^2, \tag{2.20}$$

iii) Harmonic average: $\frac{1}{\mu_0} = \sum_{r=1}^{N} \frac{c^{(r)}}{\mu^{(r)}}$

$$y_0 = \frac{\mu^{(1)}}{\mu_0} = \sum_{r=1}^{N} c^{(r)} \frac{\mu^{(1)}}{\mu^{(r)}} = \sum_{r=1}^{N} c^{(r)}\,y^{(r)} \quad \Rightarrow \quad \frac{\partial y_0}{\partial y^{(i)}} = y^{(i)}, \tag{2.21}$$

iv) Self-consistent scheme: $\mu_0 = \frac{\sum_{s=1}^{N} \frac{c^{(s)}\,\mu^{(s)}}{3\,\mu_0+2\,\mu^{(s)}}}{\sum_{r=1}^{N} \frac{c^{(r)}}{3\,\mu_0+2\,\mu^{(r)}}}$

$$\frac{1}{\mu_0} = \frac{\sum_{r=1}^{N} \frac{c^{(r)}}{3\,\mu_0+2\,\mu^{(r)}}}{\sum_{s=1}^{N} \frac{c^{(s)}\,\mu^{(s)}}{3\,\mu_0+2\,\mu^{(s)}}} \quad \Rightarrow \quad \frac{\mu^{(1)}}{\mu_0} = \frac{\sum_{r=1}^{N} \frac{c^{(r)}}{3\frac{\mu_0}{\mu^{(1)}}+2\frac{\mu^{(r)}}{\mu^{(1)}}}}{\sum_{s=1}^{N} \frac{c^{(s)}\frac{\mu^{(s)}}{\mu^{(1)}}}{3}\frac{\mu_0}{\mu^{(1)}}+2\frac{\mu^{(s)}}{\mu^{(1)}}} \quad \Rightarrow \quad y_0 = \frac{\sum_{r=1}^{N} \frac{\frac{c^{(r)}}{y^{(r)}}}{\frac{3}{y_0}+\frac{2}{y^{(r)}}}}{\sum_{s=1}^{N} \frac{\frac{c^{(s)}}{y^{(s)}}}{\frac{3}{y_0}+\frac{2}{y^{(s)}}}}. \tag{2.22}$$

In order to define the optimal values $\mu^{(1)} = \hat{\mu}^{(1)}\left(c^{(r)}, \sigma_0^{(r)}, n^{(r)}, \sigma_e\right)$ and $y^{(r)} = \hat{y}^{(r)}\left(c^{(r)}, \sigma_0^{(r)}, n^{(r)}, \sigma_e\right)$ we consider the optimization over $\mu^{(1)}$ and $y^{(r)}$ in (2.15).
The optimal value of $\mu^{(1)}$ in (2.15) is determined by calculating the partial derivative of $\tilde{U}(\sigma_e)$ with respect to $\mu^{(1)}$ and setting it equal to zero:

$$\frac{\partial \tilde{U}}{\partial \mu^{(1)}} = -\frac{1}{6}\left[F\left(\frac{\sigma_e}{\mu^{(1)}}\right)^2 + 6\frac{\partial I}{\partial \mu^{(1)}}\right] = 0, \tag{2.23}$$

where

$$\frac{\partial I}{\partial \mu^{(1)}} = -\frac{3}{2}\sum_{r=1}^{N} c^{(r)} \left(\frac{{\sigma_0^{(r)}}^{n^{(r)}}}{\dot{\varepsilon}_0}\right)^{\frac{2}{n^{(r)}-1}} \frac{{y^{(r)}}^{\frac{n^{(r)}+1}{n^{(r)}-1}}}{\left(3\,\mu^{(1)}\right)^{\frac{2\,n^{(r)}}{n^{(r)}-1}}}, \tag{2.24}$$

so that (2.23) becomes

$$F\left(y^{(r)}\right)\,\sigma_e^2 - \sum_{r=1}^{N} c^{(r)} \left(\frac{{\sigma_0^{(r)}}^{n^{(r)}}}{3\,\mu^{(1)}\,\dot{\varepsilon}_0}\right)^{\frac{2}{n^{(r)}-1}} {y^{(r)}}^{\frac{n^{(r)}+1}{n^{(r)}-1}} = 0,$$

which yields

$$\mu^{(1)} = \frac{1}{3}\left[\frac{1}{F\left(y^{(r)}\right)\sigma_e^2}\sum_{r=1}^{N} c^{(r)} \left(\frac{{\sigma_0^{(r)}}^{n^{(r)}}}{\dot{\varepsilon}_0}\right)^{\frac{2}{n^{(r)}-1}} {y^{(r)}}^{\frac{n^{(r)}+1}{n^{(r)}-1}}\right]^{\frac{n^{(r)}-1}{2}} \equiv \hat{\mu}^{(1)}\left(y^{(r)}\right) > 0. \tag{2.25}$$

For those $y^{(r)} > 0$, i.e., $y^{(r)} \neq 0$, optimization of (2.15) with respect to $y^{(r)}$ yields:

$$\frac{\partial \tilde{U}}{\partial y^{(r)}} = \frac{\partial F}{\partial y^{(r)}}\frac{\sigma_e^2}{6\,\mu^{(1)}} - \frac{\partial I}{\partial y^{(r)}} = 0, \qquad r = 2, 3, \cdots, N. \tag{2.26}$$

where

$$\frac{\partial I}{\partial y^{(i)}} = \frac{1}{2}\frac{c^{(i)}}{\left(3\,\mu^{(1)}\right)^{\frac{n^{(i)}+1}{n^{(i)}-1}}} \left(\frac{y^{(i)}\,{\sigma_0^{(i)}}^{n^{(i)}}}{\dot{\varepsilon}_0}\right)^{\frac{2}{n^{(i)}-1}},$$

so that the optimality condition (2.26) becomes

$$\frac{\partial F}{\partial y^{(i)}}\,\sigma_e^2\left(3\,\mu^{(1)}\right)^{\frac{2}{n^{(i)}-1}} - c^{(i)}\left(\frac{y^{(i)}\,{\sigma_0^{(i)}}^{n^{(i)}}}{\dot{\varepsilon}_0}\right)^{\frac{2}{n^{(i)}-1}} = 0, \quad i = 2, 3, \cdots, N. \tag{2.27}$$

Equations (2.25) and (2.27) define the optimal values $\mu^{(1)}$ and $y^{(r)}$.
The optimal values of $\mu^{(1)}$ and $y^{(r)}$ depend on the values of the volume fractions $c^{(r)}$, the material properties $(\sigma_0^{(r)}, n^{(r)}, \dot{\varepsilon}_0)$, and the macroscopic von Mises equivalent stress σ_e.

The composite dissipation function is defined from (2.15):

$$\tilde{U}\left(\sigma_e\right) = \frac{1}{6}\frac{F\left(\hat{y}^{(r)}\left(\sigma_e\right)\right)}{\hat{\mu}^{(1)}\left(\sigma_e\right)}\,\sigma_e^2 - I\left(\hat{\mu}^{(1)}\left(\sigma_e\right), \hat{y}^{(r)}\left(\sigma_e\right)\right), \tag{2.28}$$

and the flow rule is

$$\mathbf{D} = \frac{\partial \tilde{U}}{\partial \boldsymbol{\sigma}} = \frac{\partial \tilde{U}}{\partial \sigma_e}\frac{\partial \sigma_e}{\partial \boldsymbol{\sigma}} \equiv \dot{\tilde{\varepsilon}}\,\mathbf{N}, \qquad \dot{\tilde{\varepsilon}} = \frac{\partial \tilde{U}}{\partial \sigma_e}, \qquad \mathbf{N} = \frac{\partial \sigma_e}{\partial \boldsymbol{\sigma}} = \frac{3}{2\,\sigma_e}\,\mathbf{s}.$$

Using (2.28), we find that

$$\dot{\tilde{\varepsilon}} = \frac{\partial \tilde{U}}{\partial \sigma_e} = \underbrace{F}_{\frac{\hat{\mu}^{(1)}}{\tilde{\mu}}}\frac{\sigma_e}{3\,\hat{\mu}^{(1)}} + \underbrace{\frac{\partial \tilde{U}}{\partial \hat{\mu}^{(1)}}}_{0}\frac{\partial \hat{\mu}^{(1)}}{\partial \sigma_e} + \sum_{i=1}^{N}\underbrace{\frac{\partial \tilde{U}}{\partial \hat{y}^{(i)}}}_{0}\frac{\partial \hat{y}^{(i)}}{\partial \sigma_e} = \frac{\sigma_e}{3\,\tilde{\mu}},$$

where the partial derivatives $\frac{\partial \tilde{U}}{\partial \hat{\mu}^{(1)}}$ and $\frac{\partial \tilde{U}}{\partial \hat{y}^{(i)}}$ vanish due to the optimization conditions (2.23) and (2.26).
The flow rule now takes the form

$$\mathbf{D} = \dot{\tilde{\varepsilon}}\,\mathbf{N} = \frac{\sigma_e}{3\,\tilde{\mu}}\,\mathbf{N} = \frac{\mathbf{s}}{2\,\tilde{\mu}}, \qquad \tilde{\mu} = \tilde{\mu}\left(\hat{\mu}^{(r)}\right), \quad \text{and} \quad \hat{\mu}^{(r)} = \frac{\hat{\mu}^{(1)}\left(\sigma_e, c^{(s)}, \sigma_0^{(s)}\right)}{\hat{y}^{(r)}\left(\sigma_e, c^{(s)}, \sigma_0^{(s)}\right)}. \tag{2.29}$$

Step 2: Equal creep exponents $\left(n^{(1)} = n^{(2)} = \cdots = n^{(N)} \equiv n\right)$

When all "creep exponents" are set equal, i.e., $n^{(1)} = n^{(2)} = \cdots = n^{(N)} \equiv n$, equation (2.15) becomes

$$\tilde{U} = \sup_{\substack{y^{(r)}\geq 0 \\ y^{(1)}=1}}\ \sup_{\mu^{(1)}>0}\left[\frac{\sigma_e^2}{6\,\mu^{(1)}}F\left(y^{(r)}\right) - \frac{n-1}{2(n+1)}\frac{H\left(y^{(r)}\right)}{\left(3\,\mu^{(1)}\right)^{\frac{n+1}{n-1}}}\right], \tag{2.30}$$

where now

$$F\left(y^{(r)}\right) = \frac{\mu^{(1)}}{\tilde{\mu}} = \frac{\sum_{r=1}^{N}\frac{c^{(r)}\,y^{(r)}}{3\frac{y^{(r)}}{y_0}+2}}{\sum_{s=1}^{N}\frac{c^{(s)}}{3\frac{y^{(s)}}{y_0}+2}} \equiv \frac{T_1}{T_2} \quad \text{and} \quad H\left(y^{(r)}\right) = \sum_{r=1}^{N} c^{(r)}\left[\frac{\left(\sigma_0^{(r)}\right)^n}{\dot{\varepsilon}_0}\right]^{\frac{2}{n-1}}\left(y^{(r)}\right)^{\frac{n+1}{n-1}}.$$

The optimality conditions (2.25) and (2.27) of the previous step take now the form

$$\mu^{(1)} = \frac{1}{3}\left[\frac{H\left(y^{(r)}\right)}{F\left(y^{(r)}\right)}\frac{1}{\sigma_e^2}\right]^{\frac{n-1}{2}} \equiv \hat{\mu}^{(1)}\left(y^{(r)}\right) > 0, \tag{2.31}$$

$$\frac{\partial F}{\partial y^{(i)}}\,\sigma_e^2\,\left(3\,\mu^{(1)}\right)^{\frac{2}{n^{(i)}-1}} - c^{(i)}\left(\frac{y^{(i)}{\sigma_0^{(i)}}^{n^{(i)}}}{\dot{\varepsilon}_0}\right)^{\frac{2}{n^{(i)}-1}} = 0, \qquad i = 2,3,\cdots,N. \tag{2.32}$$

Substituting the optimal value of $\mu^{(1)}$ from (2.31) in (2.32) we get

$$\frac{\partial F}{\partial y^{(i)}}\frac{H}{F} - c^{(i)}\left(\frac{y^{(i)}{\sigma_0^{(i)}}^{n}}{\dot{\varepsilon}_0}\right)^{\frac{2}{n-1}} = 0, \qquad i = 2,3,\cdots,N. \tag{2.33}$$

and (2.30) becomes

$$\tilde{U}(\sigma_e) = \frac{\sigma_e^{n+1}}{n+1}\sqrt{\sup_{\substack{y^{(r)}\geq 0\\ y^{(1)}=1}}\frac{[F(y^{(r)})]^{n+1}}{[H(y^{(r)})]^{n-1}}} = \frac{\sigma_e^{n+1}}{n+1}\left[\sup_{\substack{y^{(r)}\geq 0\\ y^{(1)}=1}}\frac{F\left(y^{(r)}\right)}{H\left(y^{(r)}\right)^{\frac{n-1}{n+1}}}\right]^{\frac{n+1}{2}}. \tag{2.34}$$

It is interesting to note that the expression for the effective stress potential given in (2.34) is of the power-law type defined in (2.1), i.e., when all phases have the same creep exponent n, the effective behavior of the composite is also of the power-law type with creep exponent n implying that $\tilde{U}$ is a homogeneous function of degree $n+1$ in $\boldsymbol{\sigma}$. Also, the optimal values of $y^{(r)}$ in (2.34) are now **independent** of the macroscopic von Mises equivalent stress σ_e.

Step 3: Perfectly plastic phases ($n \to \infty$)

Using (2.34) and taking into account that

$$\lim_{n\to\infty}\frac{[a(n)]^{n+1}}{n+1} = \begin{cases} 0 & \text{when } \; a(\infty) \leq 1\,, \\ \infty & \text{when } \; a(\infty) > 1\,, \end{cases} \tag{2.35}$$

we find

$$\lim_{n\to\infty}\tilde{U}(\sigma_e) = \begin{cases} 0 \quad \text{when} \quad \sigma_e\sqrt{\sup\limits_{\substack{y^{(r)}\geq 0\\ y^{(1)}=1}}\frac{F\left(y^{(r)}\right)}{H_\infty\left(y^{(r)}\right)}} \leq 1\,, \\ \infty \;\; \text{when} \quad \sigma_e\sqrt{\sup\limits_{\substack{y^{(r)}\geq 0\\ y^{(1)}=1}}\frac{F\left(y^{(r)}\right)}{H_\infty\left(y^{(r)}\right)}} > 1\,, \end{cases} \tag{2.36}$$

where

$$F\left(y^{(r)}\right) = \frac{\mu^{(1)}}{\tilde{\mu}} = \frac{\sum\limits_{r=1}^{N}\frac{c^{(r)}\,y^{(r)}}{3\frac{y^{(r)}}{y_0}+2}}{\sum\limits_{s=1}^{N}\frac{c^{(s)}}{3\frac{y^{(s)}}{y_0}+2}} \equiv \frac{T_1}{T_2}, \qquad H_\infty\left(y^{(r)}\right) \equiv \lim_{n\to\infty}H\left(y^{(r)}\right) = \sum_{r=1}^{N}c^{(r)}\left(\sigma_0^{(r)}\right)^2 y^{(r)}. \tag{2.37}$$

The threshold of the function in (2.36) corresponds to the definition of the effective yield function, i.e.,

$$\sigma_e^2\sup_{\substack{y^{(r)}\geq 0\\ y^{(1)}=1}}\left[\frac{F\left(y^{(r)}\right)}{H_\infty\left(y^{(r)}\right)}\right] = 1 \qquad \Rightarrow$$

$$\sigma_e^2 = \frac{1}{\sup\limits_{\substack{y^{(r)}\geq 0\\ y^{(1)}=1}} \left[\frac{F\left(y^{(r)}\right)}{H_\infty\left(y^{(r)}\right)}\right]} = \inf_{\substack{y^{(r)}\geq 0\\ y^{(1)}=1}} \left[\frac{H_\infty\left(y^{(r)}\right)}{F\left(y^{(r)}\right)}\right] = -\sup_{\substack{y^{(r)}\geq 0\\ y^{(1)}=1}} \left[-\frac{H_\infty\left(y^{(r)}\right)}{F\left(y^{(r)}\right)}\right] \equiv \tilde{\sigma}_0^2.$$

Equation (2.36) can be written also as

$$\lim_{n\to\infty} \tilde{U}(\sigma_e) = \begin{cases} 0 & \text{when} \quad \sigma_e \leq \tilde{\sigma}_0\,, \\ \infty & \text{when} \quad \sigma_e > \tilde{\sigma}_0\,, \end{cases} \tag{2.38}$$

with

$$\boxed{\tilde{\sigma}_0 = \sqrt{\inf_{\substack{y^{(r)}\geq 0\\ y^{(1)}=1}} \frac{H_\infty\left(y^{(r)}\right)}{F\left(y^{(r)}\right)}}}\,,\ r=2,...,N \tag{2.39}$$

where $H_\infty\left(y^{(r)}\right)$ and $F\left(y^{(r)}\right)$ are defined in (2.37), i.e.,

$$\boxed{\tilde{\sigma}_0(c^{(r)},\sigma_0^{(r)}) = \sqrt{\inf_{\substack{y^{(i)}\geq 0\\ y^{(1)}=1\\ i=2,...,N}} \left(\sum_{r=1}^{N} c^{(r)}{\sigma_0^{(r)}}^2\, y^{(r)}\right)\left(\sum_{p=1}^{N} \frac{c^{(p)}}{3\,y^{(p)}+2\,y_0}\right)\left(\sum_{s=1}^{N} \frac{c^{(s)}\,y^{(s)}}{3\,y^{(s)}+2\,y_0}\right)^{-1}}}\,. \tag{2.40}$$

Comparing the above equation (2.38) with (2.4), we conclude that, when all phases are perfectly plastic ($n=\infty$), the form of the estimated effective stress potential $\tilde{U}(\sigma_e)$ corresponds to a perfectly plastic material that obeys the von Mises yield condition with a flow stress $\tilde{\sigma}_0$ defined in (2.40). This effective flow stress, in turn, is a function of the phase volume fractions $c^{(r)}$ as well as of the phase flow stresses $\sigma_0^{(r)}$.

Calculation of the estimated effective yield stress $\tilde{\sigma}_0$ requires the solution of the constrained optimization problem in (2.40) for the values of $y^{(r)}$, which define in turn the appropriate values of the viscosities $\mu^{(r)}$ (see (2.18)). In the special case of a two-phase composite the solution of the optimization problem in (2.40) can be found analytically as described in section 3.2. The solution of more general cases presented in the following are obtained by using the methodology of Kaufman *et al.* [32] and the CONMAX software (http://www.netlib.org/opt/conmax.f) for the solution of the optimization problem in (2.40). Instructions for CONMAX are given in Appendix I.

The optimal values $y^{(r)}$ in (2.40) depend on the values of the volume fractions $c^{(r)}$ and the flow stresses $\sigma_0^{(r)}$ of the phases but are **independent** of the macroscopic stress state. Also, depending on the parameters of the problem, the optimal values $\hat{y}^{(r)} = \hat{\mu}^{(1)}/\hat{\mu}^{(r)}$ may be one of the extreme values 0 or ∞. The value $\hat{y}^{(r)}=0$ corresponds to a rigid comparison material for phase r, whereas $\hat{y}^{(r)}=\infty$ corresponds to an incompressible comparison material with zero stiffness (i.e., to an "incompressible void" comparison material). It should be noted that it is possible to have $\hat{y}^{(r)} = \hat{\mu}^{(1)}/\hat{\mu}^{(r)} = 0$ (rigid comparison material) even for finite $\sigma_0^{(r)}$ (e.g., see deBotton and Ponte Castañeda [13] and section 3.2 below).

In CONMAX we need some derivatives. The calculations are discussed in Appendix IV.

2.4 Strain-rate concentration in the phases

An approximation for the strain field in the non-linear composite may be obtained from the strain field in the LCC evaluated at the optimal comparison moduli $\hat{\mu}^{(r)}$ defined by the optimization problem in (2.8). In particular, the *average* deformation rate field in the phases $\mathbf{D}^{(r)}$ may be written in terms of the macroscopic deformation rate $\mathbf{D}$ in the form (Ponte Castañeda and co-workers [51], [56], [31],[54]):

$$\mathbf{D}^{(r)} = \mathbf{A}^{(r)}\left(\hat{\mu}^{(i)}(\sigma_e)\right) : \mathbf{D}, \qquad r = 1, 2, \cdots, N, \tag{2.41}$$

where $\mathbf{A}^{(r)}$ are the fourth-order strain concentration tensors of the LCC, evaluated at the *optimal* values[2], $\hat{\mu}^{(r)}$ of the comparison moduli, defined by the solution of the optimization problem in (2.8). It is emphasized that the optimal values $\hat{\mu}^{(r)}$ depend in a nonlinear manner upon the macroscopic von Mises equivalent σ_e, and consequently the strain concentration tensors $\mathbf{A}^{(r)}$ are in general nonlinear functions of the macroscopic stress tensor $\boldsymbol{\sigma}$.
For isotropic composite materials with random microstructures having "ellipsoidal symmetry", $\mathbf{A}^{(r)}$ is of the form (Ponte Castañeda [51])

$$\mathbf{A}^{(r)} = \mathbf{E}^{(r)} : \left(\sum_{s=1}^{N} c^{(s)}\,\mathbf{E}^{(s)}\right)^{-1}, \qquad \mathbf{E}^{(r)} = \left[\boldsymbol{\mathcal{I}} + \mathbf{S}_0 : \boldsymbol{\mathcal{L}}_0^{-1} : \left(\boldsymbol{\mathcal{L}}^{(r)} - \boldsymbol{\mathcal{L}}_0\right)\right]^{-1}, \tag{2.42}$$

where $\boldsymbol{\mathcal{I}}$ is the symmetric fourth order identity tensor with Cartesian components $\mathcal{I}_{ijkl} = (\delta_{ik}\,\delta_{jl} + \delta_{il}\,\delta_{jk})/2$, $\mathbf{S}_0$ is the well known tensor of Eshelby [14] for the linear "reference material" with elasticity tensor $\boldsymbol{\mathcal{L}}_0$ introduced in (2.11), and

$$\boldsymbol{\mathcal{L}}_0 = 2\,\mu_0\,\boldsymbol{\mathcal{K}} + 3\,\kappa_0\,\boldsymbol{\mathcal{J}}, \quad \boldsymbol{\mathcal{L}}^{(r)} = 2\,\hat{\mu}^{(r)}\,\boldsymbol{\mathcal{K}} + 3\,\kappa^{(r)}\,\boldsymbol{\mathcal{J}}, \quad \boldsymbol{\mathcal{J}} = \frac{1}{3}\boldsymbol{\delta}\,\boldsymbol{\delta}, \quad \boldsymbol{\mathcal{K}} = \boldsymbol{\mathcal{I}} - \boldsymbol{\mathcal{J}}. \tag{2.43}$$

The quantities (μ_0, κ_0) and $(\hat{\mu}^{(r)}, \kappa^{(r)})$ in (2.43) are the shear and bulk viscosities of the LCC; the bulk viscosities κ_0 and $\kappa^{(r)}$ are set to ∞ after the final expression for $\mathbf{D}^{(r)}$ in (2.41) is derived, in order to take into account the incompressible nature of the phases and the composite.
For composites consisting of an isotropic matrix and a uniform distribution of *spherical* inclusions, the Eshelby tensor has the form

$$\mathbf{S}_0 = \frac{6\,(\kappa_0 + 2\,\mu_0)}{5\,(3\,\kappa_0 + 4\,\mu_0)}\boldsymbol{\mathcal{K}} + \frac{3\,\kappa_0}{3\,\kappa_0 + 4\,\mu_0}\boldsymbol{\mathcal{J}}. \tag{2.44}$$

Using (2.43) and (2.44) in (2.42b) and taking into account that $\boldsymbol{\mathcal{J}} : \boldsymbol{\mathcal{J}} = \boldsymbol{\mathcal{J}}$, $\boldsymbol{\mathcal{K}} : \boldsymbol{\mathcal{K}} = \boldsymbol{\mathcal{K}}$, and $\boldsymbol{\mathcal{J}} : \boldsymbol{\mathcal{K}} = \mathbf{0}$, we conclude that

$$\mathbf{E}^{(r)} = \frac{5\,\mu_0\,(3\,\kappa_0 + 4\,\mu_0)}{\mu_0\,(9\,\kappa_0 + 8\,\mu_0) + 6\,(\kappa_0 + 2\,\mu_0)\,\hat{\mu}^{(r)}}\boldsymbol{\mathcal{K}} + \frac{3\,\kappa_0 + 4\,\mu_0}{3\,\kappa^{(r)} + 4\,\mu_0}\boldsymbol{\mathcal{J}}. \tag{2.45}$$

[2]Henceforth the superscript $\hat{(\cdot)}$ serves to denote the optimal value of the relevant quantity obtained by the corresponding optimization described in the previous section.

We have that

$$\sum_{s=1}^{N} c^{(s)}\,\mathbf{E}^{(s)} = \sum_{s=1}^{N} c^{(s)} \left[\frac{5\,\mu_0\,(3\,\kappa_0+4\,\mu_0)}{\mu_0\,(9\,\kappa_0+8\,\mu_0)+6\,(\kappa_0+2\,\mu_0)\,\mu^{(s)}}\boldsymbol{\mathcal{K}} + \frac{3\,\kappa_0+4\,\mu_0}{3\,\kappa^{(s)}+4\,\mu_0}\boldsymbol{\mathcal{J}}\right]$$
$$= \left(\sum_{s=1}^{N} c^{(s)}\frac{3\,\kappa_0+4\,\mu_0}{3\,\kappa^{(s)}}+4\,\mu_0\right)\boldsymbol{\mathcal{J}} + \left[\sum_{s=1}^{N}\frac{5\,c^{(s)}\,\mu_0\,(3\,\kappa_0+4\,\mu_0)}{\mu_0\,(9\,\kappa_0+8\,\mu_0)+6\,(\kappa_0+2\,\mu_0)\,\mu^{(s)}}\right]\boldsymbol{\mathcal{K}}. \tag{2.46}$$

Then

$$\left(\sum_{s=1}^{N} c^{(s)}\,\mathbf{E}^{(s)}\right)^{-1} = \left(\sum_{s=1}^{N} c^{(s)}\frac{3\,\kappa_0+4\,\mu_0}{3\,\kappa^{(s)}+4\,\mu_0}\right)^{-1}\boldsymbol{\mathcal{J}} + \left[\sum_{s=1}^{N}\frac{5\,c^{(s)}\,\mu_0\,(3\,\kappa_0+4\,\mu_0)}{\mu_0\,(9\,\kappa_0+8\,\mu_0)+6\,(\kappa_0+2\,\mu_0)\,\mu^{(s)}}\right]^{-1}\boldsymbol{\mathcal{K}} \tag{2.47}$$

Next, using (2.42), after some lengthy but otherwise straightforward calculations we reach the following expression for the strain concentration tensors:

$$\mathbf{A}^{(r)} = \frac{1}{3\,\kappa^{(r)}+4\,\mu_0}\left(\sum_{s=1}^{N}\frac{c^{(s)}}{3\,\kappa^{(s)}+4\,\mu_0}\right)^{-1}\boldsymbol{\mathcal{J}} +$$
$$+\frac{1}{\mu_0\,(9\,\kappa_0+8\,\mu_0)+6\,(\kappa_0+2\,\mu_0)\,\hat{\mu}^{(r)}}\left[\sum_{s=1}^{N}\frac{c^{(s)}}{\mu_0\,(9\,\kappa_0+8\,\mu_0)+6\,(\kappa_0+2\,\mu_0)\,\hat{\mu}^{(s)}}\right]^{-1}\boldsymbol{\mathcal{K}}. \tag{2.48}$$

Finally, using (2.41), taking into account the incompressibility condition $D_{kk}=0$ (or $\boldsymbol{\mathcal{J}}:\mathbf{D}=\mathbf{0}$), and considering the limit $\kappa_0\to\infty$, we find

$$\mathbf{D}^{(r)} = \lim_{\kappa_0\to\infty}\left(\mathbf{A}^{(r)}:\mathbf{D}\right) = \alpha^{(r)}\,\mathbf{D}, \qquad \boxed{\alpha^{(r)} = \frac{1}{3\,\mu_0+2\,\hat{\mu}^{(r)}}\left(\sum_{s=1}^{N}\frac{c^{(s)}}{3\,\mu_0+2\,\hat{\mu}^{(s)}}\right)^{-1}}. \tag{2.49}$$

Equation (2.49) implies that

$$\dot{\bar{\varepsilon}}^{(r)} = \sqrt{\frac{2}{3}\,\mathbf{D}^{(r)}:\mathbf{D}^{(r)}} = \alpha^{(r)}\sqrt{\frac{2}{3}\,\mathbf{D}:\mathbf{D}} = \alpha^{(r)}\,\dot{\bar{\varepsilon}} \qquad \text{or} \qquad \boxed{\frac{d\bar{\varepsilon}^{(r)}}{d\bar{\varepsilon}} = \alpha^{(r)}}, \tag{2.50}$$

where $\dot{\bar{\varepsilon}}^{(r)}$ and $\dot{\bar{\varepsilon}}$ are the average equivalent strain rates in the phases and the average macroscopic equivalent strain rate respectively.
Taking into account Equation (2.18), the strain concentration values $\alpha^{(r)}$ defined in (2.49) can be written in the form

$$\boxed{\alpha^{(r)} = \frac{\hat{y}^{(r)}}{3\,\hat{y}^{(r)}+2\,y_0}\left(\sum_{s=1}^{N}\frac{c^{(s)}\,\hat{y}^{(s)}}{3\,\hat{y}^{(s)}+2\,y_0}\right)^{-1}}, \tag{2.51}$$

where $\hat{y}^{(r)}$ are the optimal values of $y^{(r)}$ resulting from the optimization in (2.40).
The variation of $\alpha^{(i)}$ with respect to $c^{(r)}$ and $\sigma_0^{(r)}$ is discussed in Appendix IV.

2.5 A summary of the constitutive equations used for $\mathbf{D}^p$

The results of the previous sections are used for the description of the plastic deformation rate $\mathbf{D}^p$ of elastoplastic composites as follows.
Each of the phases is viscoplastic and obeys a constitutive equation of the form

$$\mathbf{D}^{p(r)} = \dot{\bar{\varepsilon}}^{(r)}\,\mathbf{N}, \qquad \mathbf{N} = \frac{3}{2\,\sigma_e}\,\mathbf{s}, \qquad r = 1, 2, ..., n \tag{2.52}$$

where

$$\dot{\bar{\varepsilon}}^{(r)} = \frac{\sigma_e}{3\,\mu^{(r)}\left(\sigma_e\right)}, \qquad \mu^{(r)}\left(\sigma_e\right) = \frac{1}{3}\frac{\sigma_0^{(r)}}{\dot{\varepsilon}_0}\left(\frac{\sigma_0^{(r)}}{\sigma_e}\right)^{n^{(r)}-1}. \tag{2.53}$$

When the constituent phases are perfectly plastic the corresponding flow stress of the composite material $\tilde{\sigma}_0$ is determined from the solution of a constrained optimization problem:

$$\tilde{\sigma}_0 = \sqrt{\inf_{\substack{y^{(i)}\geq 0 \\ y^{(1)}=1 \\ i=2,...,N}} \left(\sum_{r=1}^{N} c^{(r)}{\sigma_0^{(r)}}^2\, y^{(r)}\right)\left(\sum_{p=1}^{N}\frac{c^{(p)}}{3\,y^{(p)}+2\,y_0}\right)\left(\sum_{s=1}^{N}\frac{c^{(s)}\,y^{(s)}}{3\,y^{(s)}+2\,y_0}\right)^{-1}}. \tag{2.54}$$

where N is the number of phases, $(c^{(i)}, \sigma_0^{(i)})$ are the volume fraction and flow stress of phase i, and $y^{(i)}$ are positive optimization parameters.

Chapter 3

Perfect Plasticity

3.1 Introduction

The scope of the present chapter is to validate the homogenization model which was previously presented, using periodic three-dimensional unit cell calculations comprising a large number of spherical inclusions (of various sizes and of two different types) distributed randomly in a matrix phase. We find that in the context of two- and three-phase materials the use of the lower Hashin-Shtrikman bound for the LCC gives the best predictions by comparison with the unit cell calculations for both the macroscopic stress-strain response as well as for the average strains in each of the phases.
In the special case of a two-phase composite an analytical result is obtained for the effective flow stress of the elasto-plastic composite material. Additional analytical expressions are also provided for the phase concentration tensors and average strains in each phase in terms of the aforementioned optimized scalar quantities.The agreement is found to be good not only for the effective yield stress but also for the phase average strains thus allowing for the extension of this model to include arbitrary isotropic hardening of the phases.

3.2 The two-phase perfectly plastic composite — An analytic estimate for the effective flow stress and the strain concentration factors

We consider an isotropic two-phase composite ($N = 2$, $c^{(1)} + c^{(2)} = 1$). In that case it is possible to obtain analytical expressions for the optimal value of $\hat{y}^{(2)}$ and then determine $\tilde{\sigma}_0$. The estimate for $\tilde{\sigma}_0$ depends on the chosen value of the reference viscosity μ_0 in (2.11). Results for various choices of μ_0 will be discussed briefly later in this section. First of all, we present in some detail the formulation based on a Hashin-Strikman lower bound with $\mu_0 = \mu^{(1)}$ ($y_0 = 1$); as it will be discussed in the following section 3.3, this particular choice of μ_0 shows the best agreement with detailed unit cell finite element calculations. For $\mu_0 = \mu^{(1)}$,

the ratio H_∞/F in (2.39) takes the value

$$\frac{H_\infty\left(y^{(2)}\right)}{F\left(y^{(2)}\right)} = {\sigma_0^{(1)}}^2\left(c^{(1)} + c^{(2)}\, r^2\, y^{(2)}\right)\frac{2 + 3\,c^{(2)} + 3\,c^{(1)}\,y^{(2)}}{2\,c^{(1)} + \left(3 + 2\,c^{(2)}\right)y^{(2)}}, \qquad r = \frac{\sigma_0^{(2)}}{\sigma_0^{(1)}} > 1. \tag{3.1}$$

The optimum value of $y^{(2)}$ to be used in (2.39) is calculated by using the condition

$$\frac{\partial}{\partial y^{(2)}}\left(\frac{H_\infty}{F}\right) = 0 \tag{3.2}$$

together with the constraint $y^{(2)} \geq 0$. After some lengthy, but straightforward, calculations we find the resulting optimal value $\hat{y}^{(2)}$ to be

$$\hat{y}^{(2)} = \begin{cases} \dfrac{-2\,c^{(1)} + \frac{5}{\sqrt{3}}\sqrt{\left(3+2\,c^{(2)}\right)\frac{1}{r^2} - 2\,c^{(2)}}}{3+2\,c^{(2)}} & \text{if} \quad 1 \leq r \leq r_{\rm cr} \quad \left(c^{(2)} \leq c_{\rm cr}^{(2)}\right), \\ 0 & \text{if} \quad r \geq r_{\rm cr} \quad \left(c^{(2)} \geq c_{\rm cr}^{(2)}\right), \end{cases} \tag{3.3}$$

where

$$r_{\rm cr} = \frac{5}{\sqrt{4 + 6\,c^{(2)}}} \qquad \text{and} \qquad c_{\rm cr}^{(2)} = \frac{1}{6}\left[\left(\frac{5}{r}\right)^2 - 4\right]. \tag{3.4}$$

According to (3.3), for a given particle concentration $c^{(2)}$, when the contrast ratio $r = \sigma_0^{(2)}/\sigma_0^{(1)}$ is larger than a value $r_{\rm cr}$, the comparison material for phase 2 (particles) is rigid ($\hat{y}^{(2)} = 0$).

The corresponding estimate for the effective flow stress resulting from (2.39) is

$$\boxed{\frac{\tilde{\sigma}_0}{\sigma_0^{(1)}} = \begin{cases} \dfrac{5\,c^{(2)}\,r + c^{(1)}\sqrt{9 + 6\,c^{(2)} - 6\,c^{(2)}\,r^2}}{3+2\,c^{(2)}} & \text{if} \quad 1 \leq r \leq r_{\rm cr} \quad \left(c^{(2)} \leq c_{\rm cr}^{(2)}\right), \\ \frac{1}{2}\sqrt{4 + 6\,c^{(2)}} & \text{if} \quad r_{\rm cr} \leq r \quad \left(c_{\rm cr}^{(2)} \leq c^{(2)}\right). \end{cases}} \tag{3.5}$$

The result stated in (3.5) was first presented by Ponte Castañeda and deBotton [55], who used a "dissipation function" formulation (as opposed to the "stress potential" approach used here). For all volume fractions $c^{(2)}$, there is a value $r_{\rm cr}$ of the contrast ratio $r = \sigma_0^{(2)}/\sigma_0^{(1)}$ beyond which the predicted effective flow stress $\tilde{\sigma}_0$ does not vary with r. For values of r larger than $r_{\rm cr}$, the optimal value of $y^{(2)} = \mu^{(1)}/\mu^{(2)}$ vanishes or $\mu^{(2)} = \infty$, i.e., for $r \geq r_{\rm cr}$ the comparison material 2 (particles) does not deform; therefore, further increase of $\sigma_0^{(2)}$ does not change the effective flow stress $\tilde{\sigma}_0$.

The estimate for the effective flow stress $\tilde{\sigma}_0$ depends on the choice of the reference viscosity μ_0. Here we present results for various additional choices of μ_0:

i) Hashin-Shtrikman (upper bound): $\mu_0 = \mu^{(2)}$

The optimal value $\hat{y}^{(2)}$ is found to be

$$\hat{y}^{(2)} = \frac{6\,c^{(2)} + 5\,\sqrt{3\,r^2\left(5 - 2\,c^{(2)}\right) - 6\,c^{(1)}}}{25\,r^2 - 2\left(5 - 3\,c^{(2)}\right)} \tag{3.6}$$

and the corresponding estimate for the effective flow stress is

$$\boxed{\frac{\tilde{\sigma}_0}{\sigma_0^{(1)}} = \frac{5\,c^{(1)} + c^{(2)}\sqrt{3\,r^2\left(5 - 2\,c^{(2)}\right) - 6\,c^{(1)}}}{5 - 2\,c^{(2)}}} \tag{3.7}$$

ii) Harmonic average: $\frac{1}{\mu_0}=\sum_{r=1}^{N}\frac{c^{(r)}}{\mu^{(r)}}$

The optimal value $\hat{y}^{(2)}$ is found to be

$$\hat{y}^{(2)}=\begin{cases}\frac{2\,c^{(2)}\left(2+c^{(2)}\right)-2\left(3-c^{(2)}\right)c^{(1)}\,r^2+5\sqrt{9\,r^2-6\,c^{(1)}\,c^{(2)}\left(r^2-1\right)^2}}{-2\left(3-c^{(2)}\right)c^{(2)}+\left[9+2\left(9-c^{(2)}\right)c^{(2)}\right]r^2} & \text{if} \quad 1\le r\le r_{\rm cr},\\ 0 & \text{if} \quad r\ge r_{\rm cr},\end{cases} \tag{3.8}$$

where

$$r_{\rm cr}=\frac{1}{2}\sqrt{\frac{50-4\,c^{(2)}\left(7+c^{(2)}\right)}{c^{(1)}\left(2+c^{(2)}\right)}} \tag{3.9}$$

and the corresponding estimate for the effective flow stress is

$$\boxed{\frac{\tilde{\sigma}_0}{\sigma_0^{(1)}}=\begin{cases}\sqrt{\frac{3-c^{(2)}\left(\left(11-8\,c^{(2)}\right)c^{(2)}+\left(2-c^{(2)}\left(13-8\,c^{(2)}\right)\right)r^2-\frac{10}{3}\,c^{(1)}\sqrt{9\,r^2-6\,c^{(1)}c^{(2)}\left(r^2-1\right)^2}\right)}{3+8\,c^{(1)}c^{(2)}}} & \text{if} \quad 1\le r\le r_{\rm cr},\\ \sqrt{\frac{1+0.5\,c^{(2)}}{1-c^{(2)}}} & \text{if} \quad r_{\rm cr}\le r.\end{cases}} \tag{3.10}$$

iii) Self-consistent scheme: $\mu_0=\frac{\sum_{s=1}^{N}\frac{c^{(s)}\,\mu^{(s)}}{3\,\mu_0+2\,\mu^{(s)}}}{\sum_{r=1}^{N}\frac{c^{(r)}}{3\,\mu_0+2\,\mu^{(r)}}}$

- if $\quad 0\le c^{(2)}\le 0.4$

  The optimal value $\hat{y}^{(2)}$ is found to be

$$\hat{y}^{(2)}=\begin{cases}\frac{5\left(c^{(1)}+r\,c^{(2)}\right)-2\,r}{\left[3+5(r-1)c^{(2)}\right]r} & \text{if} \quad 1\le r\le r_{\rm cr} \quad \left(c_{\rm cr}^{(2)}\le c^{(2)}\le 0.4\right),\\ \sqrt{\frac{c^{(1)}}{1-2.5\,c^{(2)}}} & \text{if} \quad r\ge r_{\rm cr} \quad \left(0\le c^{(2)}\le c_{\rm cr}^{(2)}\right),\end{cases} \tag{3.11}$$

  where

$$r_{\rm cr}=\frac{c^{(1)}}{0.4-c^{(2)}} \qquad \text{and} \qquad c_{\rm cr}^{(2)}=\frac{0.4\,r-1}{r-1}. \tag{3.12}$$

  and the corresponding estimate for the effective flow stress is

$$\boxed{\frac{\tilde{\sigma}_0}{\sigma_0^{(1)}}=\begin{cases}\sqrt{1+\frac{r-1}{3}\left[8+5\,c^{(2)}\,(r-1)-2\,r\right]c^{(2)}} & \text{if} \quad 1\le r\le r_{\rm cr} \quad \left(c_{\rm cr}^{(2)}\le c^{(2)}\le 0.4\right),\\ \sqrt{\frac{c^{(1)}}{1-2.5\,c^{(2)}}} & \text{if} \quad r_{\rm cr}\le r \quad \left(0\le c^{(2)}\le c_{\rm cr}^{(2)}\right).\end{cases}} \tag{3.13}$$

- if $\quad 0.4\le c^{(2)}\le 1$

  The optimal value $\hat{y}^{(2)}$ is found to be

$$\hat{y}^{(2)}=\frac{5\left(c^{(1)}+r\,c^{(2)}\right)-2\,r}{\left[3+5\,(r-1)\,c^{(2)}\right]r}. \tag{3.14}$$

  and the corresponding estimate for the effective flow stress is

$$\boxed{\frac{\tilde{\sigma}_0}{\sigma_0^{(1)}}=\sqrt{1+\frac{r-1}{3}\left[8+5\,c^{(2)}\,(r-1)-2\,r\right]c^{(2)}}.} \tag{3.15}$$

iv) Bishop - Hill bounds:

- upper bound

$$\boxed{\frac{\tilde{\sigma}_0}{\sigma_0^{(1)}} = c^{(1)} + c^{(2)}\, r} \tag{3.16}$$

- lower bound

$$\boxed{\frac{\tilde{\sigma}_0}{\sigma_0^{(1)}} = 1} \tag{3.17}$$

Figure 3.1 shows the predicted $\tilde{\sigma}_0$ for various choices of μ_0 for a volume fraction $c^{(2)} = 0.30$. The curves marked H-S$^-$ and H-S$^+$ correspond to $\mu_0 = \mu^{(1)}$ and $\mu_0 = \mu^{(2)}$ respectively and "self consistent" corresponds to $\mu_0 = \tilde{\mu}$. Note that the Hashin-Shtrikman lower bound H-S$^-$ ($\mu_0 = \mu^{(1)}$) gives the lowest value for $\tilde{\sigma}_0$, the Hashin-Shtrikman upper bound H-S$^-$ ($\mu_0 = \mu^{(2)}$) gives the highest value for $\tilde{\sigma}_0$ and the self-consistent estimate falls within the Hashin-Shtrikman bounds. We emphasize that the Hashin-Shtrikman lower bound H-S$^-$ ($\mu_0 = \mu^{(1)}$) shows the best agreement with detailed unit cell finite element calculations presented in the following section. That is the reason why we choose to use the Hashin-Shtrikman lower bound H-S$^-$ in our calculations.
The strain concentration values $\alpha^{(r)}$ given in (2.51) can be written in the form

$$\boxed{\alpha^{(1)} = \frac{d\bar{\varepsilon}^{(1)}}{d\bar{\varepsilon}} = \frac{1}{(2\,y_0 + 3)\,\mathcal{D}}}, \qquad \boxed{\alpha^{(2)} = \frac{d\bar{\varepsilon}^{(2)}}{d\bar{\varepsilon}} = \frac{\hat{y}^{(2)}}{(2\,y_0 + 3\,\hat{y}^{(2)})\,\mathcal{D}}}, \tag{3.18}$$

where

$$\boxed{\mathcal{D} = \frac{c^{(1)}}{2\,y_0 + 3} + \frac{c^{(2)}\,\hat{y}^{(2)}}{2\,y_0 + 3\,\hat{y}^{(2)}}} \tag{3.19}$$

and $\hat{y}^{(2)}$ is defined in (3.3),(3.6),(3.8),(3.11) or (3.14) according to the choice of the reference viscosity μ_0.

3.3 Unit cell finite element calculations

In this section we present the results of unit cell finite element calculations for a composite material made up of a statistically isotropic random distribution of isotropic, linearly-elastic perfectly-plastic spherical inclusions embedded in a continuous, isotropic, linearly-elastic perfectly-plastic matrix. The Mises plasticity model is used in the finite element calculations. The elastic Young modulus for all phases is three orders of magnitude higher than the highest yield stress involved; this minimizes the effects of elasticity and the results are very close to those of rigid-perfectly-plastic materials.
We study numerically two- and three-phase composites. The matrix is labelled as phase 1 and the reinforcing particles are spherical and have higher flow stresses ($\sigma_0^{(i)} > \sigma_0^{(1)}, i > 1$). The periodic unit cell is a cube with edge size L and is constructed using the method presented by Segurado and Llorca [63] (see also [15]) and extended to polydisperse inclusion

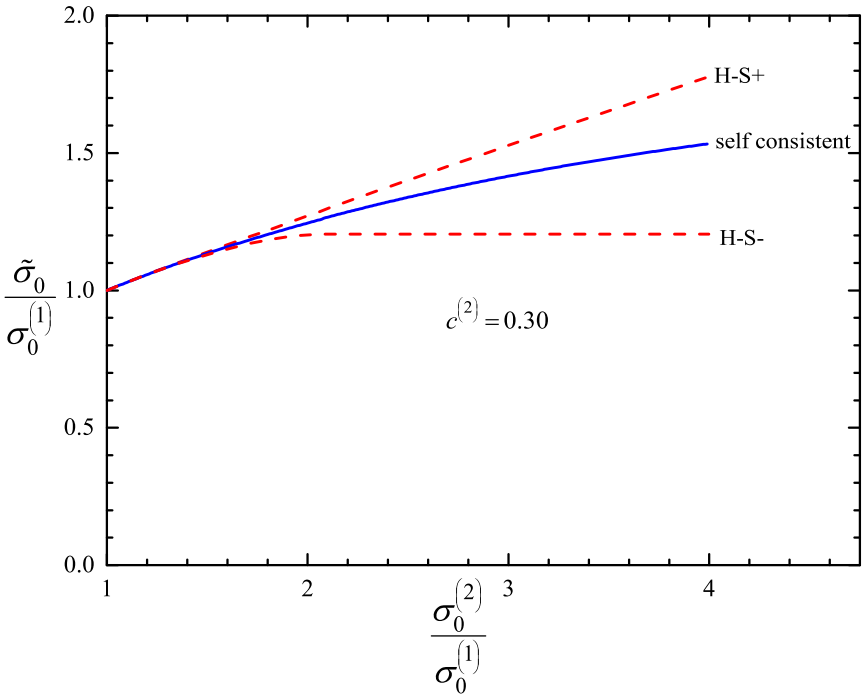

Figure 3.1: Variation of effective normalized flow stress $\tilde{\sigma}_0/\sigma_0^{(1)}$ with contrast ratio $r = \sigma_0^{(2)}/\sigma_0^{(1)}$ as predicted by various models for a volume fraction $c^{(2)} = 0.30$.

distributions by Lopez-Pamies et al. [35]. The virtual microstructure contains a dispersion of a sufficiently large number of non-overlapping spheres of uniform (monodisperse) or different (polydisperse) size. The inclusions are randomly located within the cell and are generated using the Random Sequential Adsorption Algorithm (RSA) [60]. In addition, the unit cell is periodic, i.e., it can be repeated in all three directions to represent a 3-D periodic structure. For the two-phase composite and for $c^{(2)} \leq 0.20$ monodisperse spheres are used; for higher volume fractions polydisperse (variable size) distributions are used. In the present study, the two-phase polydisperse approach of Lopez-Pamies et al. [35] is readily extended to obtain virtual microstructures with three-phases or more. For instance, denoting the matrix phase with 1 and the two inclusion phases with 2 and 3, the extension is straightforward and requires the continuous alternation of spheres of phase 2 and spheres of phase 3 during the RSA process. Of course this simple extension can be repeated as often as necessary to obtain an $N-$phase virtual microstructure provided that the concentration of each of the phases is known.

Monodisperse microstructures

The monodisperse microstructure is a periodic cubic unit cell of volume $L^3 = 1$ containing a random dispersion of 30 non-overlapping identical spheres. Evidently, the accuracy of the solution and the computer time to solve the problem increases with the number of particles in the unit cell ([35],[11]). The final particle arrangement has to be statistically isotropic (all directions in the unit cell are equivalent) and, in addition, it should be suitable for finite

element discretization. Both conditions can be fulfilled using the Random Sequential Adsorption (RSA) algorithm to generate the coordinates of the particle centers (Rintoul and Torquato, [60]).
According to this method, the particle center positions are generated randomly and sequentially. The sequential addition of particles is constrained so that the distance between the particles with other particles and with the boundaries of the cubic unit cell take a minimum value that guaranties adequate spatial discretization(see, e.g., Segurado and Llorca, [63]; Fritzen *et al.*, [15]). In particular:

- The center-to-center distance between a new particle i in the sequential algorithm and any previously accepted particle $j = 1, 2, ..., i-1$ has to be greater than the minimum value $s_1 = 2\,R_m(1 + d_1)$, where the offset distance d_1 is fixed here at $d_1 = 0.02$. This condition can be written in the compact form

$$\left\|\mathbf{X}^i - \mathbf{X}^j - \mathbf{h}\right\| \geq s_1. \tag{3.20}$$

  where $\mathbf{X}^i$, $\mathbf{X}^j$ denote the location of the center of particles i, j and $\mathbf{h}$ is a vector with entries 0, L or $-L$ for each of its three Cartesian components with respect to the principal axes of the cubic unit cell.

- The particles should be considerably distant from the boundaries of the unit cell as imposed by the following inequalities

$$\left\|X_k^i - R_m\right\| \geq s_2 \qquad \text{and} \qquad \left\|X_k^i + R_m - L\right\| \geq s_2 \qquad (k = 1, 2, 3)\,, \tag{3.21}$$

  where $s_2 = d_2\,R_m$ with d_2 being fixed here at $d_2 = 0.05$.

In the above expressions

$$R_m = L\left(\frac{3\,c}{4\,\pi\,N}\right)^{1/3} \tag{3.22}$$

represents the radius of the particles, where N is the number of particles in the unit cell. Figure 3.2 illustrates representative unit cells generated by the above algorithm for $N = 30$ with two different particle concentrations:(a) $c^{(2)} = 0.10$, (b) $c^{(2)} = 0.20$.
The RSA algorithm, in combination with Equations (3.20) and (3.21), was used to generate the particle center coordinates up to a sphere volume fraction $c^{(2)} = 0.20$. Above this volume fraction, it was not possible to accommodate 30 particles in the unit cell fulfilling all the conditions imposed by Equations (3.20) and (3.21). Unit cells with $c^{(2)}$ above the "jamming limit" (the final state of the process whereby no particles can be added) can be generated using particles with different sizes (polydisperse).

Polydisperse microstructures

The polydisperse microstructures are constructed using a similar constrained adsorption algorithm. We concentrate on polydisperse microstructures with three different families of particle sizes. Although there is not a specific rule for the creation of this kind of microstructures and there are many alternatives, in the present thesis we follow this procedure [35]:

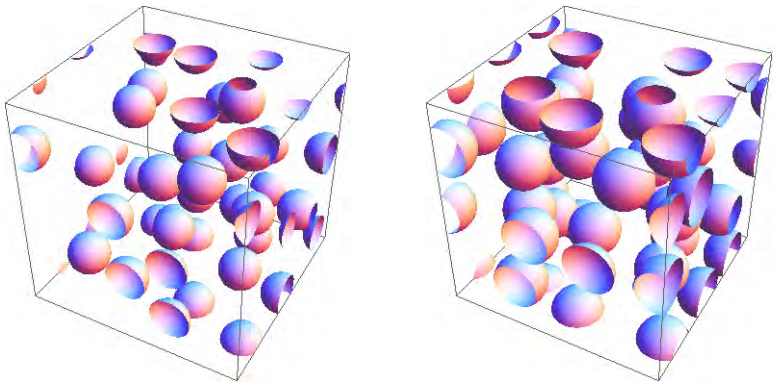

(a) (b)

Figure 3.2: Representative unit cells of unit volume $L^3 = 1$ containing $N = 30$ randomly distributed spherical particles of monodisperse sizes with two different concentrations: (a) $c^{(2)} = 0.10$ and (b) $c^{(2)} = 0.20$.

- Three different families of particles with radii $R_p^{(I)}$ and concentrations $c^{(I)}$ with $(I = 1, 2, 3)$ are utilized, such that:

$$\left\{R_p^{(1)}, R_p^{(2)}, R_p^{(3)}\right\} = \left\{R_p, \frac{7}{9}R_p, \frac{4}{9}R_p\right\} \quad \text{with} \quad R_p = L\left(\frac{3c^{(1)}}{4\pi N_p}\right)^{1/3}, \tag{3.23}$$

and

$$\left\{c^{(1)}, c^{(2)}, c^{(3)}\right\} = \{0.5c, 0.25c, 0.25c\} \quad \text{with} \quad c^{(1)} + c^{(2)} + c^{(3)} = c. \tag{3.24}$$

where N_p represents the number of particles with the largest radius $R_p^{(1)} = R_p$ in the unit cell and c the total volume fraction.

- The microstructures are generated sequentially by first adding the particles with the largest radius $R_p^{(1)}$ until the concentration reaches the value $c^{(1)} = 0.5c$, next adding the particles with radius $R_p^{(2)}$ until $c^{(1)} + c^{(2)} \simeq 0.75c$, and finally adding the particles with the smallest radius $R_p^{(3)}$ until $c^{(1)} + c^{(2)} + c^{(3)} \simeq c$.

At this point, it should be noted that through this construction process, the target concentration c can only be achieved approximately (up to a small error that depends on the various choices of the parameters). In addition, the centers of the particles should follow similar constraints to conditions (3.20) - (3.21) in order to guarantee adequate spatial discretization. In particular:

- The center-to-center distance between a new particle i in the sequential algorithm and any previously accepted particle $j = 1, 2, ..., i-1$ has to be greater than the minimum value s_1. This condition can be written in a compact form as follows:

$$\left\|\mathbf{X}^i - \mathbf{X}^j - \mathbf{h}\right\| \geq s_1, \qquad s_1 = \left(R_p^{(m_i)} + R_p^{(m_j)}\right)(1 + d_1), \tag{3.25}$$

- The particles should be substantially distant from the boundaries of the unit cell as imposed by the inequalities:

$$\left|X_k^i - R_p^{(m_i)}\right| \geq s_2, \qquad \left|X_k^i + R_p^{(m_i)} - 1\right| \geq s_2, \qquad s_2 = d_2 R_p^{(m_i)}, \quad (k = 1, 2, 3), \tag{3.26}$$

for $i, j = 1, 2, ..., N$ where N stands for the total number of particles in the unit cell. The offset parameters are set at $d_1 = 0.02$ and $d_2 = 0.05$ as in the monodisperse case, and the superscript $m_i = 1, 2, 3$ represents the size of the sphere that should be added at step i in the sequential construction process. Specifically, $m_i = 1$ if $c^{(m_i)} \leq c^{(1)}$, $m_i = 2$ if $c^{(1)} < c^{(m_i)} \leq c^{(1)} + c^{(2)}$ and $m_i = 3$ if $c^{(1)} + c^{(2)} < c^{(m_i)}$.

Figure 3.3 shows sample unit cells generated by the above algorithm for $N = 36$ with two different particle concentrations: (a) $c^{(2)} = 0.30$, and (b) $c^{(2)} = 0.40$.

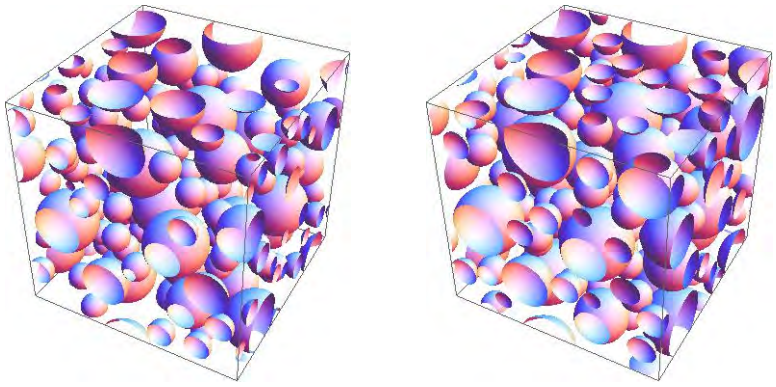

(a) (b)

Figure 3.3: Representative unit cells of unit volume $L^3 = 1$ containing $N = 36$ randomly distributed spherical particles of three different sizes with two different concentrations: (a) $c^{(2)} = 0.30$ and (b) $c^{(2)} = 0.40$.

In a similar way, we can create a **three-phase** cubic unit cell, consisted of a cubic matrix, containing spherical inclusions of two different phases. In particular, we use a Random Sequential Algorithm similar to the one previously described to create two different three-phase unit cells, called from now on $V1$ and $V2$.
In details, we use a group of spheres with different radii , for each one of the inclusion phases. Let $c^{(1)}$ stand for the volume fraction of the matrix phase, and $c^{(2)}$, $c^{(3)}$ the volume fractions of the inclusion phases. Then we have a total $c^{tot} = c^{(2)} + c^{(3)}$ of inclusion phases, with $c^{(1)} + c^{tot} = 1$. The whole procedure can be summarized in the following steps:

- We make use of three different families of particles with radii $R_p^{(I)}$ and concentrations $c^{(I)}$ with $(I = 1, 2, 3)$ for each one of the inclusion phases. For our case, we can utilize:

$$\left\{R_{px}^{(1)}, R_{px}^{(2)}, R_{px}^{(3)}\right\} = \{1, 0.5, 0.1\} \tag{3.27}$$

and

$$\left\{{c_x}^{(1)}, {c_x}^{(2)}, {c_x}^{(3)}\right\} = \{0.6c_x, 0.2c_x, 0.2c_x\} \tag{3.28}$$

with $x = 2, 3$ denoting each of the two different inclusion phases.

- We add: $(c_2/c_{tot}) \times c_2^{(1)} \times c_{tot}$ of particles with radius $R_{p2}^{(1)}$ of phase 2, and particles with radius $R_{p3}^{(1)}$ of phase 3 until the rest of $c_2^{(1)} \times c_{tot}$ is filled.
  Then we do the same for the second group of spheres. We add $(c_2/c_{tot}) \times c_2^{(2)} \times c_{tot}$ of particles with radius $R_{p2}^{(2)}$ of phase 2 and particles with radius $R_{p3}^{(2)}$ of phase 3, until the rest of $c_2^{(2)} \times c_{tot}$ is filled. The same goes for sphere group 3.

The only difference between $V1$ and $V2$, is that for the $V2$ unit cell, we use more groups of spheres, of the same radii, to construct the microstructure. That makes the $V2$ microstructure a more complex, but also more random and realistic model of a three-phase steel.
In order to guarantee adequate spatial discretization, again the randomly generated coordinates of the centers of the particles, are enforced to satisfy constraints similar to (3.25) and (3.26). Figure 3.4 shows representative $V1$ and $V2$ unit cells, for volume fractions $c^{(1)} = 0.60$, $c^{(2)} = 0.25$ and $c^{(3)} = 0.15$.

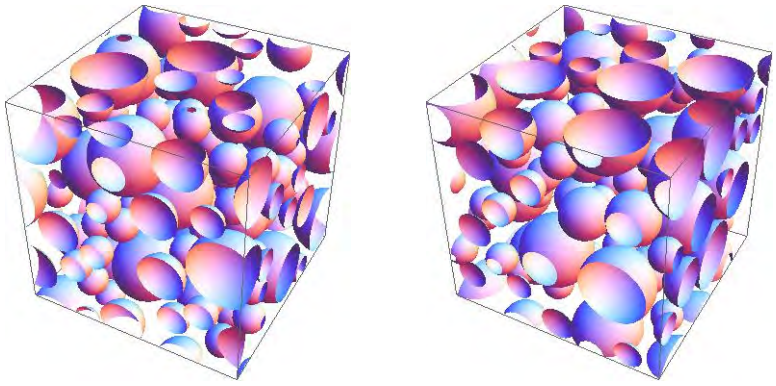

(a) (b)

Figure 3.4: Three-Phase unit cells containing $c^{(1)} = 0.60$, $c^{(2)} = 0.25$ and $c^{(3)} = 0.15$, where (a) is for $V1$ and (b) is for $V2$.

At this point it should be noted, that the various parameters of the RSA can be modified in order to produce various combinations of particle positions, resulting to a different geometry each time. However, due to the randomness of the dispersion, the unit cells remain isotropic [17].

Meshing

Finite element discretizations of the cubic unit cell were created from the particle center distributions using the mesh generator code NETGEN [62], which has the capability to create periodic meshes as required. All calculations were carried out using the ABAQUS general

purpose finite element code (Hibbitt [23]). Three dimensional 10-node quadratic tetrahedral elements with a constant pressure interpolation were used (C3D10H in ABAQUS); all analyses were carried out incrementally and accounted for geometry changes due to deformation (finite strain solutions).
Figure 3.5 shows three finite element meshes of increasing refinement for a distribution of monodisperse particles with concentration $c^{(2)} = 0.20$. Mesh sensitivity studies reveal that meshes with approximately 200,000 degrees of freedom (Fig. 3.5(b)) produce accurate results [17]. Figure 3.6 shows the finite element meshes used for a two-phase composite with volume fractions $c^{(2)}$ =0.10, 0.20, 0.30, and 0.40. The distributions are monodisperse for $c^{(2)}$ =0.10 and 0.20, and polydisperse for $c^{(2)}$ =0.30 and 0.40. Figure 3.7 shows a typical finite element mesh of a unit cell for a three-phase composite for a matrix with volume fraction $c^{(1)} = 0.60$ and two families of inclusions with $c^{(2)} = 0.25$ and $c^{(3)} = 0.15$.

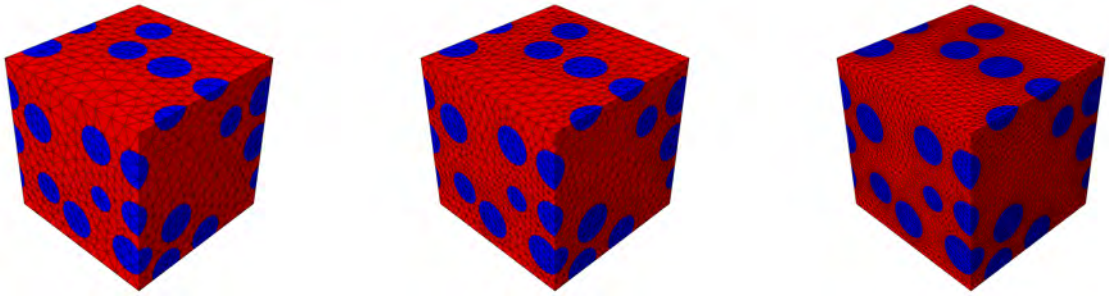

(a) (b) (c)

Figure 3.5: Three representative meshes in the undeformed configuration for a distribution of monodisperse particles with concentration $c^{(2)} = 0.20$: (a) moderate mesh, (b) fine mesh, and (c) very fine mesh. The finite element meshes have (39,417; 112,281; 699,481) nodes and (15,703; 45,679; 293,054) elements respectively. The corresponding total numbers of degrees of freedom, including pressures, are (86,845; 245,485; 1,512,335).

3.3.1 The effective yield stress

We determine numerically the effective yield stress by solving the problem of a unit cell loaded in uniaxial tension. Periodicity conditions are imposed on the boundary of the unit cell. A detailed discussion of the periodic boundary conditions on a unit cell can be found in Suquet [65] or Michel *et al.* [41]. Here, the periodic boundary conditions on the unit cell are imposed as follows (see Mbiakop *et al.* [38] and Appendix II for more details). Referring to Fig. 3.8, if we fix vertex 1 in order to eliminate rigid body translations, then, in view of the periodicity of the displacement field, we can write the displacements $\mathbf{u}$ at vertices 2, 4, and 5 of the unit cell in the form

$$u_i^{(2)} = (F_{i1} - \delta_{i1})\, L, \qquad u_i^{(4)} = (F_{i2} - \delta_{i2})\, L, \qquad u_i^{(5)} = (F_{i3} - \delta_{i3})\, L, \tag{3.29}$$

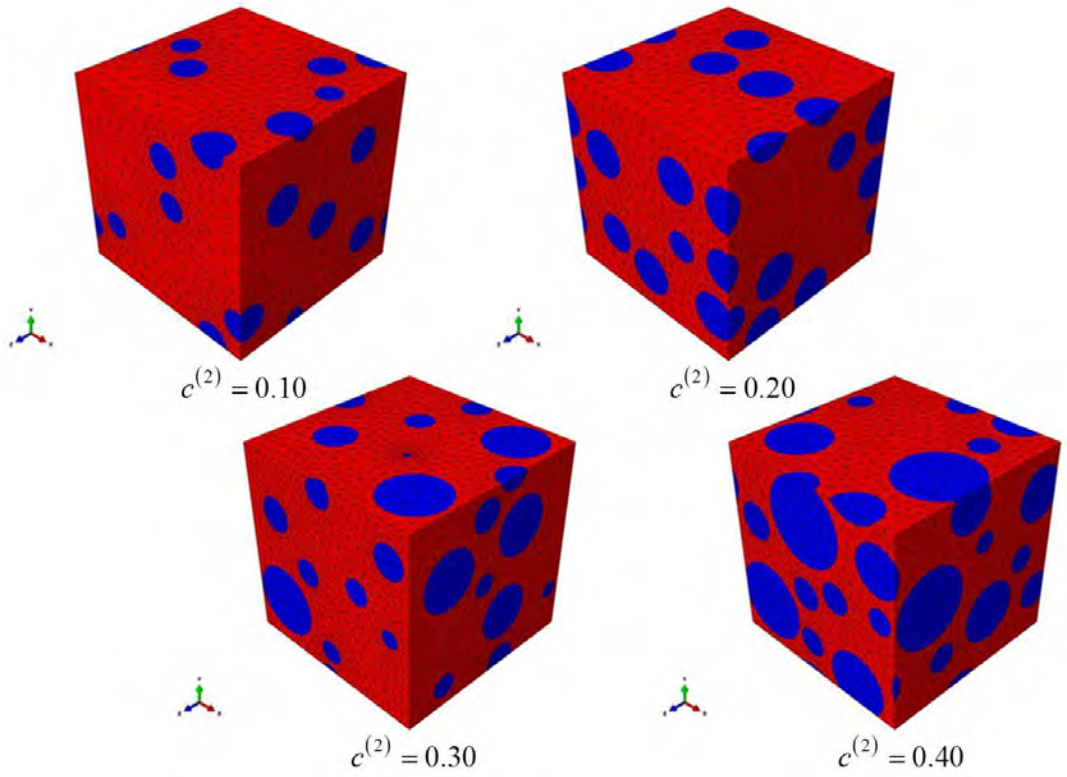

Figure 3.6: Finite element discretization of cubic unit cells for two-phase composites containing a random distribution of 30 spherical particles for volume fractions of 10, 20, 30 and 40%. The finite element meshes have (200,869; 112,281; 165,371; 159,303) nodes and (83,270; 45,679; 67,790; 65,543) elements respectively. The corresponding total numbers of degrees of freedom, including pressures, are (436,067; 245,485; 360,533; 346,823).

where F_{ij} are the components of the macroscopic deformation gradient $\mathbf{F}$. The periodicity of the problem requires also that the displacements of material points at the same position on opposite faces of the cell should satisfy the conditions

$$\mathbf{u}^{\text{RIGHT}} - \mathbf{u}^{\text{LEFT}} = \mathbf{u}^{(2)}, \qquad \mathbf{u}^{\text{TOP}} - \mathbf{u}^{\text{BOTTOM}} = \mathbf{u}^{(4)}, \qquad \mathbf{u}^{\text{FRONT}} - \mathbf{u}^{\text{BACK}} = \mathbf{u}^{(5)}, \quad (3.30)$$

where the superscripts (LEFT, RIGHT), (BOTTOM, TOP), and (BACK, FRONT) denote collectively all materials points located respectively on the faces of the cell at $(X_1 = 0, X_1 = L)$, $(X_2 = 0, X_2 = L)$, and $(X_3 = 0, X_3 = L)$. Equations (3.30) show that the periodic constraints between all corresponding opposite boundary points can be written in terms of the displacements of the three vertex points $(\mathbf{u}^{(2)}, \mathbf{u}^{(4)}, \mathbf{u}^{(5)})$, which are defined, in turn, in (3.29) by the macroscopic deformation gradient $\mathbf{F}$. In ABAQUS, for given $\mathbf{F}$, we impose boundary conditions on $(\mathbf{u}^{(2)}, \mathbf{u}^{(4)}, \mathbf{u}^{(5)})$ according to (3.29), and the periodicity constraints (3.30) are enforced through a "user MPC" subroutine (or the "EQUATION" option).

For the problem of uniaxial tension in direction 1, the deformation gradient is of the form

$$\mathbf{F} = \lambda\, \mathbf{e}_1\, \mathbf{e}_1 + \lambda_t(\mathbf{e}_2\, \mathbf{e}_2 + \mathbf{e}_3\, \mathbf{e}_3), \quad (3.31)$$

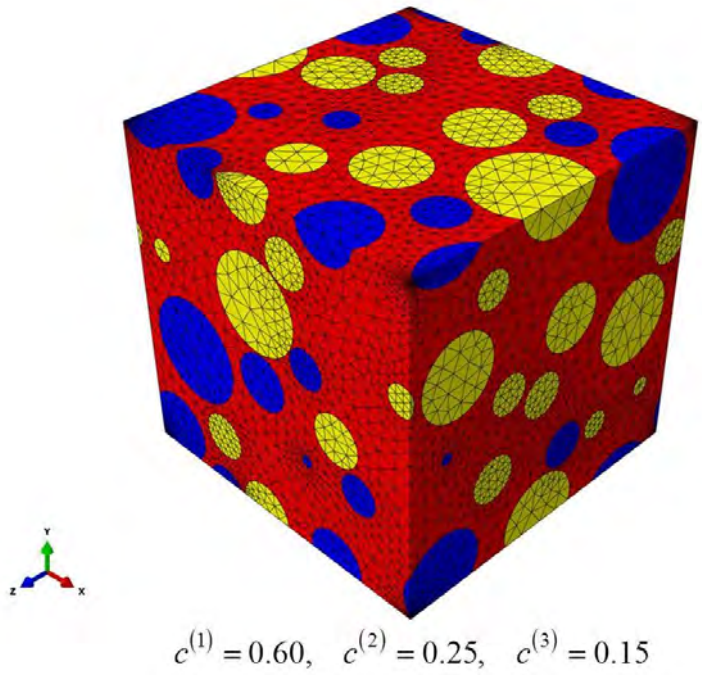

Figure 3.7: Finite element discretization of a cubic unit cell for a three-phase composite containing a random distribution of 30 polydisperse spherical particles with volume fractions $c^{(2)} = 0.25$ (yellow) and $c^{(3)} = 0.15$ (blue). The finite element mesh has 303,953 nodes, 124,225 elements, and the total number of degrees of freedom, including pressures, is 663,409.

where (λ, λ_t) are the axial and transverse stretch ratios and $\mathbf{e}_i$ the base vectors along the coordinate axes shown in Fig. 3.8; the boundary conditions (3.29) become

$$u_1^{(2)} = (\lambda - 1)\, L, \qquad u_2^{(4)} = u_3^{(5)} = (\lambda_t - 1)\, L, \tag{3.32}$$

$$u_2^{(2)} = u_3^{(2)} = \quad u_1^{(4)} = u_3^{(4)} = \quad u_1^{(5)} = u_2^{(5)} = 0. \tag{3.33}$$

In ABAQUS, we prescribe $u_1^{(2)}$ (i.e., λ) and set $R_2^{(4)} = R_3^{(5)} = 0$, where $R_i^{(N)}$ denotes the i-th component of the force at node N. The quantities $R_1^{(2)}$ and $(u_2^{(4)}, u_3^{(5)})$, i.e., λ_t, are determined by the finite element solution. The corresponding macroscopic stresses σ_{ij} are determined from the numerical calculation of the average stresses $< \sigma_{ij} >$ in the finite element solution:[1]

$$< \sigma_{ij} >= \frac{1}{V_{\text{cell}}} \int_{\text{cell}} \sigma_{ij}(\mathbf{x})\, dV, \tag{3.34}$$

where V_{cell} is the total volume of the deformed finite element mesh.
The conditions $u_2^{(4)} = u_3^{(5)}$ and $< \sigma_{22} >=< \sigma_{33} >=< \sigma_{12} >=< \sigma_{13} >=< \sigma_{23} >= 0$ are used to verify the correctness of the finite element solution.
The nodal displacement $u_1^{(2)}$ was increased gradually, the solution was developed incrementally, and the average stress $< \sigma_{11} >$ was determined by (3.34) at the end of every increment.

[1] The alternative calculation $< \sigma_{11} >= R_1^{(2)}/A_{\text{cell}}$ appears to be less convenient as it requires evaluation of cross sectional area of the deformed cell A_{cell}.

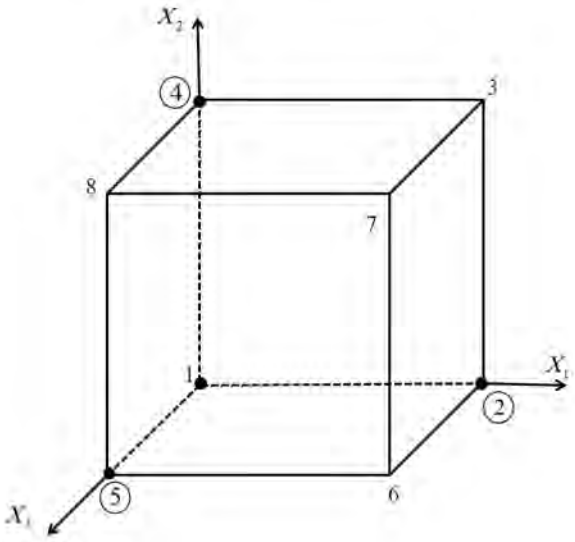

Figure 3.8: Periodic unit cell.

As $u_1^{(2)}$ increases, the calculated average stress $< \sigma_{11} >$ reaches a constant value, which defines the effective flow stress of the composite $\tilde{\sigma}_0$.

Figure 3.9 shows the variation of the calculated effective flow stress from the unit cell finite element calculations with the contrast ratio $r = \sigma_0^{(2)}/\sigma_0^{(1)}$ for various volume fractions, together with the predictions (3.5) of the homogenization model, based on the Hashin-Shtrikman lower bound H-S$^-$ ($\mu_0 = \mu^{(1)}$).[2] For that data shown in Fig. 3.9, the maximum difference between the predictions (2.40) and the results of the unit cell finite element calculations is $\pm 3\%$ (note that the vertical axis in Fig. 3.1 starts at the value of 1). It is also interesting to mention that an increase of the flow stress $\sigma_0^{(2)}$ in the inclusions beyond (approximately) two times the flow stress of the matrix ($2\,\sigma_0^{(1)}$) does not change the effective flow stress of the composite for all volume fractions considered here. The finite element calculations confirm the fact that, for $\sigma_0^{(2)} \gtrsim 2\,\sigma_0^{(1)}$, the inclusions do not deform plastically in the deforming unit cell and are in agreement with earlier numerical results of Suquet [68] for $c^{(2)} = 30\%$ and by Ponte Castañeda and Suquet [58] and Idiart *et al.* [30] for $c^{(2)} = 15\%$. As we will see in the following, this result is due to the fact that the particles behave as being rigid beyond further increase of $\sigma_0^{(2)}$.

Figure 3.10 shows the variation of $\tilde{\sigma}_0/\sigma_0^{(1)}$ of a three-phase composite for different values of the volume fraction $c^{(3)}$ as determined from the unit cell finite element calculations and the predictions (2.40) of the homogenization model. The material data are typical for a TRIP[3] steel with a ferritic matrix (phase 1) containing retained austenite (phase 2), which transforms gradually to martensite (phase 3) as the TRIP steel deforms plastically (e.g., see Papatriantafillou *et al.* [47]).

In order to check the isotropy of the unit cell, we carried out calculations for uniaxial

[2] Of all possible choices for μ_0 shown in Fig. 3.1, the Hashin-Shtrikman lower bound H-S$^-$ ($\mu_0 = \mu^{(1)}$) gives the closest estimate to the predictions of the unit cell results.

[3] TRIP is the acronym for **TR**ansformation **I**nduced **P**lasticity.

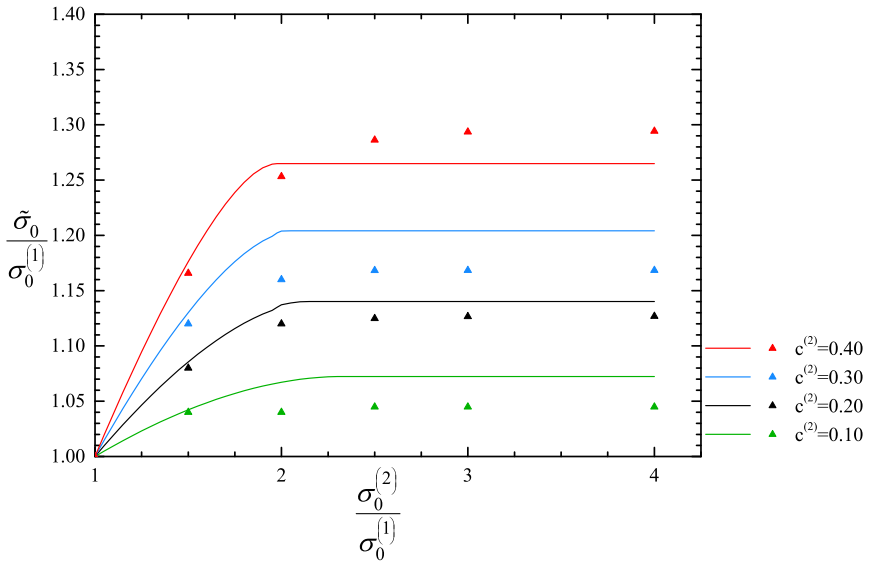

Figure 3.9: Variation of normalized effective flow stress $\tilde{\sigma}_0/\sigma_0^{(1)}$ with contrast ratio $r = \sigma_0^{(2)}/\sigma_0^{(1)}$ for different values of the volume fraction $c^{(2)}$. The full triangles are the results of the unit cell finite element calculations and the solid lines are the predictions (3.5) of the model based on the H-S$^-$ estimate ($\mu_0 = \mu^{(1)}$). The maximum difference between the numerical results and the analytical estimates is 3%.

tension in directions 2 and 3. In all cases, the results were identical to those shown in Figs. 3.9 and 3.10.

3.3.2 The strain concentration tensors

The unit cell finite element calculations discussed above were used also to determine the strain concentration factors defined in (2.49) as follows. At the end of every increment in the finite element solution the average value of the Eulerian logarithmic strain tensor $\boldsymbol{\varepsilon}^{(r)}$ was determined in every phase of the composite, where the superscript (r) denotes "phase r". The macroscopic axial logarithmic strain was also determined as $\bar{\varepsilon} = \ln \lambda$, where λ is the axial stretch ratio used in (3.32) to drive the finite element calculations. Interestingly, the components of $< \boldsymbol{\varepsilon}^{(r)} >$ are found to be proportional to $\bar{\varepsilon}$ in the context of the present study; in particular, it is found that

$$< \varepsilon_{ij}^{(r)} >= C_{ij}\, \bar{\varepsilon}, \tag{3.35}$$

which leads to the following estimate for the strain concentration $\alpha^{(r)}$:

$$\alpha^{(r)} = \frac{d\bar{\varepsilon}^{(r)}}{d\bar{\varepsilon}} = \sqrt{\frac{2}{3}\, C_{ij}\, C_{ij}}. \tag{3.36}$$

Figure 3.11 shows the variation of the strain concentration factors $\alpha^{(r)}$ in a two-phase composite with the contrast ratio $r = \sigma_0^{(2)}/\sigma_0^{(1)}$ for various volume fractions as determined from

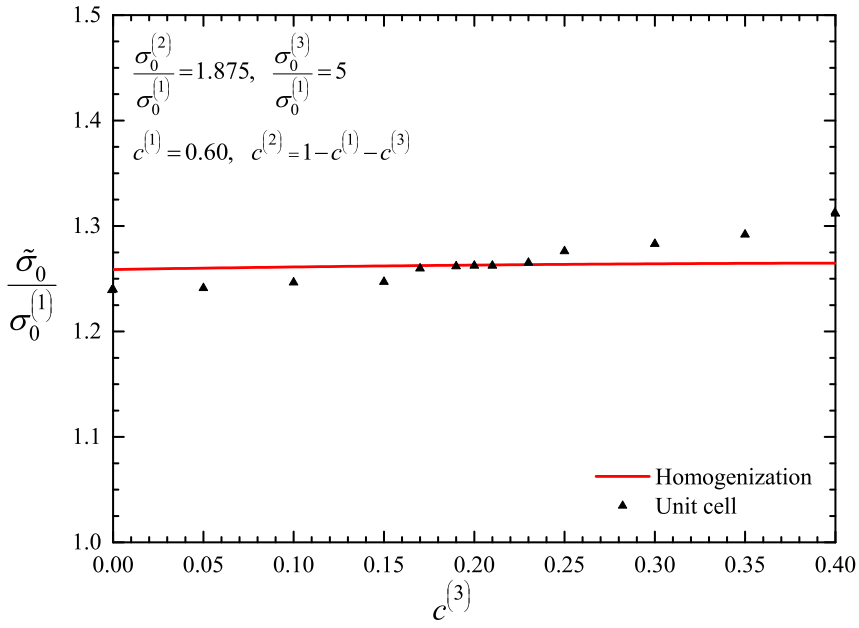

Figure 3.10: Variation of effective normalized flow stress $\tilde{\sigma}_0/\sigma_0^{(1)}$ of a three-phase composite with a matrix volume fraction $c^{(1)} = 0.60$ for different values of the volume fraction $c^{(3)}$. The homogenization estimates are based on H-S$^-$ and the contrast ratios are $\sigma_0^{(2)}/\sigma_0^{(1)} = 1.875$ and $\sigma_0^{(3)}/\sigma_0^{(1)} = 5$.

the unit cell finite element calculations (equation (3.35)) and the homogenization theory (equations (3.18)—(3.19)).

An important observation in the context of this figure is that at a contrast ratio of $r \simeq 2$, a sharp transition is observed where the particles start behaving as being rigid, i.e., the average strain in the particle is almost zero. This is validated by both the model and the numerical results. In terms of the homogenization procedure, this implies that the case of infinite contrast, i.e., rigid particles, and finite contrast is very similar beyond a value of $r \simeq 2$. A weak dependence of this sharp transition upon the volume fraction c is observed in these figures.

Similar plots for a three-phase composite are shown in Fig. 3.12. The predictions of the homogenization theory agree well with the results of the unit cell finite element calculations. Figure 3.12 shows, in turn, the strain concentration factors in a three-phase material. The comparison between the model and the finite element simulations is qualitatively good, whereas the model tends to underestimate the straining of the middle phase, i.e., the one with yield stress $\sigma_0^{(2)}/\sigma_0^{(1)} = 1.875$. Again, in the case of the third phase, when $\sigma_0^{(3)}/\sigma_0^{(1)} = 5$, the particle behaves as rigid which is consistent with the observations of the previous figure.

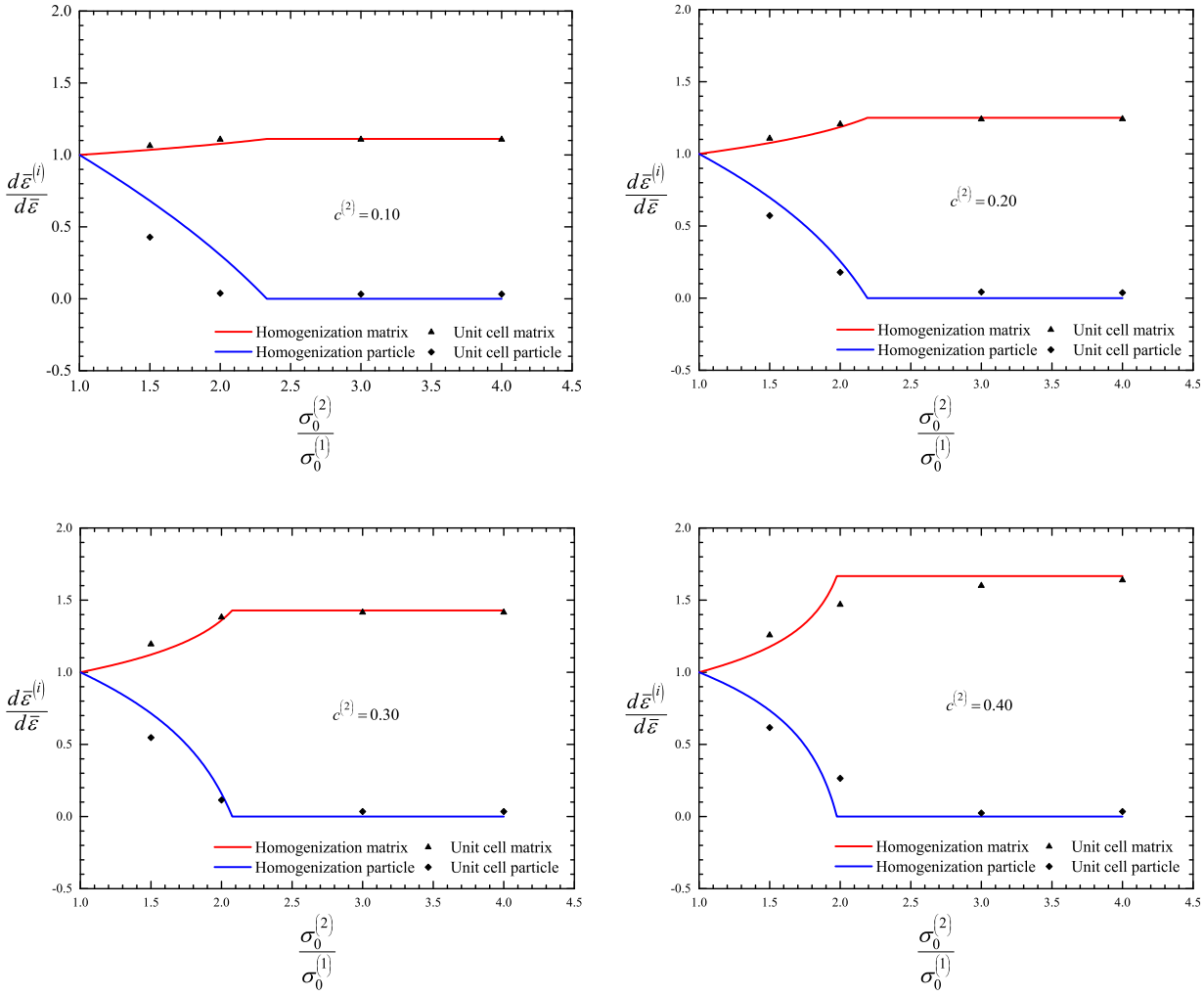

Figure 3.11: Strain concentration factors $\alpha^{(i)} = d\bar{\varepsilon}^{(i)}/d\bar{\varepsilon}$ as determined from unit cell finite element calculations and homogenization theory (equations (3.18) and (3.19)) for a two-phase composite.

3.3.3 Dependence of the effective flow stress on J_3

Suquet and Ponte Castañeda ([69],[57]) studied the effective mechanical behavior of weakly inhomogeneous composites and showed that, for the case of incompressible "power-law" phases, the effective potential of the composite may depend, to second order, on the third invariant of the applied strain.

We carry out detailed unit cell finite element calculations in order to check for a possible dependence of the effective yield stress $\tilde{\sigma}_0$ on the third invariant J_3 of the stress deviator $\mathbf{s}$ ($J_3 = \det\mathbf{s}$, where 'det' denotes the determinant). We identify the coordinate axes shown in Fig. 3.8 with the principal directions of the stress tensor and write the principal stresses in

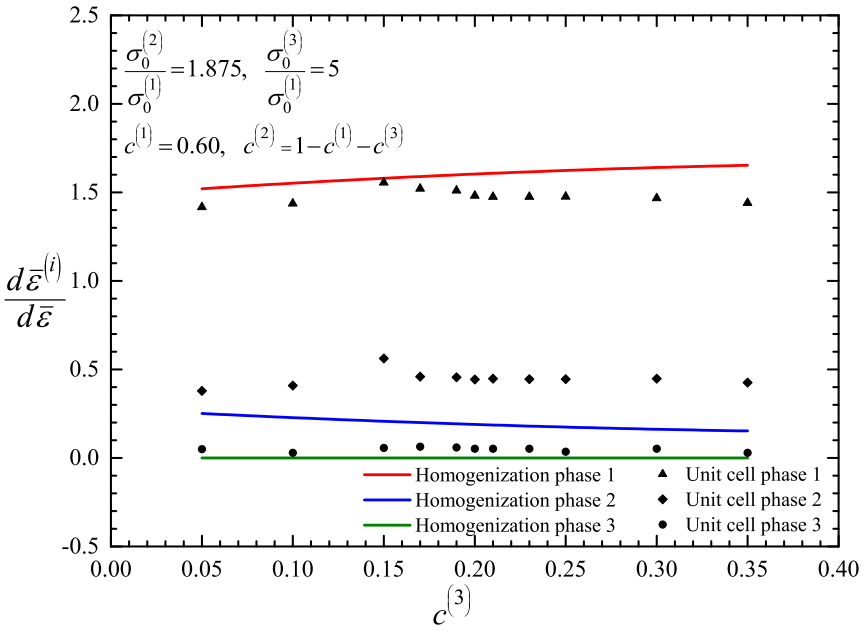

Figure 3.12: Strain concentration factors $\alpha^{(i)} = d\bar{\varepsilon}^{(i)}/d\bar{\varepsilon}$ as determined from unit cell finite element calculations and homogenization theory (equation (2.51)) for a three-phase composite.

the form

$$\left\{ \begin{array}{c} \sigma_1 \\ \sigma_2 \\ \sigma_3 \end{array} \right\} = \sigma_e \left(X_\Sigma \left\{ \begin{array}{c} 1 \\ 1 \\ 1 \end{array} \right\} + \frac{2}{3} \left\{ \begin{array}{c} \cos\left(\theta + \frac{\pi}{6}\right) \\ \sin\theta \\ -\cos\left(\theta - \frac{\pi}{6}\right) \end{array} \right\} \right), \tag{3.37}$$

where $X_\Sigma = p/\sigma_e$ is the stress triaxiality and θ is the "Lode angle", so that

$$J_3 = \det\mathbf{s} = -\frac{2}{27}\,\sigma_e^3\,\sin 3\theta. \tag{3.38}$$

Angle θ takes values in the range $-30^\circ \leq \theta \leq 30^\circ$, where, to within a hydrostatic stress, $\theta = -30^\circ$ corresponds to uniaxial tension, $\theta = 0$ to pure shear, and $\theta = 30^\circ$ to uniaxial compression.

It is stressed at this point that the composite materials considered in this work are plastically incompressible and thus the applied stress triaxiality affects only the elastic part which is of no interest here. Thus the only relevant invariant studied in this section, apart from the J_2 invariant, is the third deviatoric invariant J_3 defined above. The study of the effect of J_3, in turn, allows for a complete analysis of general triaxial loading states.

As a consequence of the applied periodic boundary conditions and the symmetry of the problem, the macroscopic (average) deformation of the unit cell is entirely described by the displacements of the "reference vertices" (2,4,5), as shown in Fig. 3.8, which can be written in the form

$$\mathbf{u}^{(2)} = U_1\,\mathbf{e}_1, \qquad \mathbf{u}^{(4)} = U_2\,\mathbf{e}_2, \qquad \mathbf{u}^{(5)} = U_3\,\mathbf{e}_3. \tag{3.39}$$

In ABAQUS, the displacements (U_1, U_2, U_3) are tied, through "user multipoint constraints", to the degrees of freedom of a fictitious node, which is properly displaced so that the desired triaxiality X_Σ and Lode angle θ are achieved. Details of the numerical formulation can be found in Mbiakop *et al.* [39] (see also Barsoum and Faleskog [3] and Appendix III).

We carry out finite element calculations in which the unit cell is loaded with $X_\Sigma = 1/3$ and Lode angles in the range $-30° \leq \theta \leq 30°$. The finite element analysis is carried out incrementally; at the end of each increment the average stress $< \boldsymbol{\sigma} >$ and the corresponding von Mises equivalent stress $\bar{\sigma}_e = \sqrt{\frac{3}{2} < \mathbf{s} > : < \mathbf{s} >}$ are calculated. As the applied displacement of the fictitious node increases, $\bar{\sigma}_e$ takes a constant value, which defines the effective flow stress $\tilde{\sigma}_0$ of the periodic composite.

In order to verify that the desired values have been indeed achieved, the triaxiality and Lode angle corresponding to the average stress $< \boldsymbol{\sigma} >$ are determined at the end of every increment. Also, since the coordinate axes in the finite element solution are assumed to coincide with the principal stress directions, the conditions $< \sigma_{12} > = < \sigma_{13} > = < \sigma_{23} > = 0$ are checked at the end of every increment to verify the accuracy of the finite element solution.

Figure 3.13 shows the variation of the effective flow stress $\tilde{\sigma}_0$, as determined from unit cell finite element calculations, with Lode angle θ for particle volume fractions $c^{(2)}$ =0.10, 0.20 and 0.40. Figure 3.13 shows that the effective flow stress of the composite is essentially independent of the third stress invariant J_3, which is in agreement with earlier results by Ponte Castañeda and Suquet [58] and Idiart [29] in the case of rigid particles.

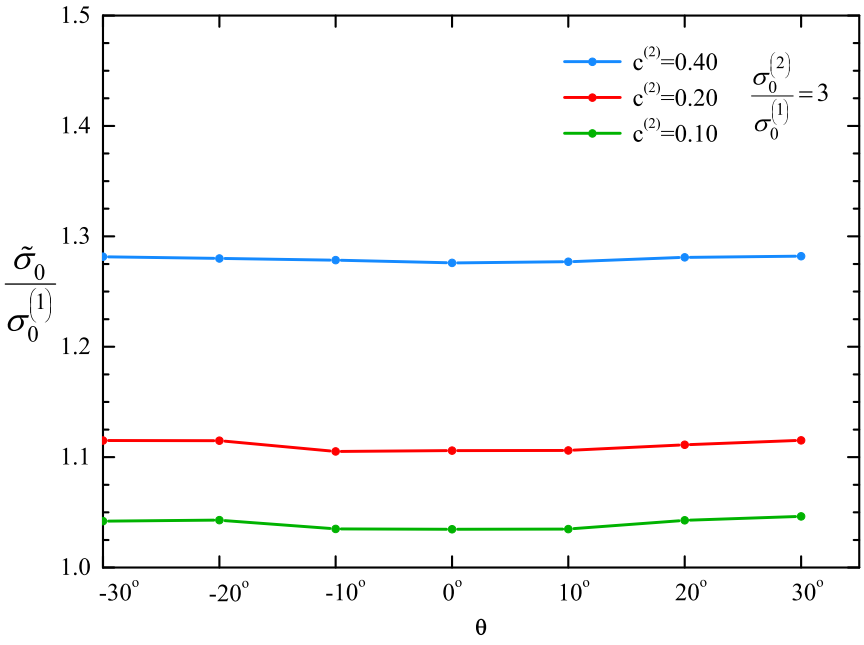

Figure 3.13: Variation of effective normalized flow stress $\tilde{\sigma}_0/\sigma_0^{(1)}$ with Lode angle θ for $X_\Sigma = 1/3$ and particle volume fractions of 10, 20 and 40%.

Chapter 4

Hardening Phases

4.1 Introduction

In this chapter we present an approximate method for the prediction of the incremental elastoplastic behavior of macroscopically isotropic composites made of N isotropic, rate-independent, elastic-plastic **hardening** phases. Let the flow stresses $\sigma_y^{(i)}$ of each phase be known functions of the corresponding equivalent plastic strains $\bar{\varepsilon}^{(i)}$ $(i = 1, 2, \ldots, N)$. At every point of the homogenized composite the "internal variables" that characterize the local state of the homogenized continuum are the local values of the equivalent plastic strains in the phases $\mathbf{q} = \left(\bar{\varepsilon}^{(1)}, \bar{\varepsilon}^{(2)}, \cdots, \bar{\varepsilon}^{(N)}\right)$.
The elastic and plastic response of the homogenized composite are treated independently, and combined later to obtain the full elastic-plastic response. The total deformation rate is written as the sum of elastic and plastic parts:

$$\mathbf{D} = \mathbf{D}^e + \mathbf{D}^p \tag{4.1}$$

The elastic properties of all constituent phases are basically the same. Thus, in order to describe the elastic behavior of the composite material we use standard isotropic linear hypoelasticity of homogeneous solids. The plastic behavior of the composite material is determined by using the homogenization technique described in Chapter 2. The constitutive equations are developed for the case of finite geometry changes.

4.2 Constitutive formulation

As we previously mentioned, the total deformation rate is written as the sum of elastic and plastic parts:

$$\mathbf{D} = \mathbf{D}^e + \mathbf{D}^p \tag{4.2}$$

In the following, the constitutive equations for the constituent parts of $\mathbf{D}$ are presented.

4.2.1 The elastic part of the deformation rate $\mathbf{D}^e$

The elastic properties of the phases are basically the same and the composite material can be viewed as homogeneous in the elastic region. Isotropic linear hypoelasticity is assumed :

$$\mathbf{D}^e = \boldsymbol{\mathcal{M}}^e : \overset{\triangledown}{\boldsymbol{\sigma}} \qquad \text{or} \qquad \overset{\triangledown}{\boldsymbol{\sigma}} = \boldsymbol{\mathcal{L}}^e : \mathbf{D}^e, \tag{4.3}$$

where $\overset{\triangledown}{\boldsymbol{\sigma}}$ is the Jaumann derivative of the stress tensor $\boldsymbol{\sigma}$, $\boldsymbol{\mathcal{M}}^e$ is the elastic compliance tensor defined as

$$\boldsymbol{\mathcal{M}}^e = \frac{1}{2\,\mu}\,\boldsymbol{\mathcal{K}} + \frac{1}{3\,\kappa}\,\boldsymbol{\mathcal{J}}, \qquad \boldsymbol{\mathcal{L}}^e = \boldsymbol{\mathcal{M}}^{e\,-1} = 2\,\mu\,\boldsymbol{\mathcal{K}} + 3\,\kappa\,\boldsymbol{\mathcal{J}}, \qquad \boldsymbol{\mathcal{J}} = \frac{1}{3}\,\boldsymbol{\delta}\,\boldsymbol{\delta}, \qquad \boldsymbol{\mathcal{K}} = \boldsymbol{\mathcal{I}} - \boldsymbol{\mathcal{J}}, \tag{4.4}$$

μ and κ denote the elastic shear and bulk moduli, $\boldsymbol{\delta}$ and $\boldsymbol{\mathcal{I}}$ the second- and symmetric fourth-order identity tensors, with Cartesian components δ_{ij} (the Kronecker delta) and $\mathcal{I}_{ijkl} = (\delta_{ik}\,\delta_{jl} + \delta_{il}\,\delta_{jk})/2$.

4.2.2 The plastic part of the deformation rate $\mathbf{D}^p$

The plastic part of the deformation rate $\mathbf{D}^p$ is determined in terms of the plastic properties of the constituent phases by using the homogenization theory described in Chapter 2. The corresponding constitutive equation can be written as

$$\mathbf{D}^p = \dot{\bar{\varepsilon}}\,\mathbf{N} = \frac{\mathbf{s}}{2\,\tilde{\mu}}, \qquad \mathbf{N} = \frac{3}{2\,\sigma_e}\,\mathbf{s}, \qquad \sigma_e = \sqrt{\frac{3}{2}\,\mathbf{s} : \mathbf{s}}, \qquad \dot{\bar{\varepsilon}} = \sqrt{\frac{2}{3}\mathbf{D}^p : \mathbf{D}^p} = \frac{\sigma_e}{3\,\tilde{\mu}}, \tag{4.5}$$

where $\tilde{\mu}$ is determined from the homogenization theory.
The phases are viscoplastic and the flow rule for each one is written in the form

$$\mathbf{D}^{p(r)} = \dot{\bar{\varepsilon}}^{(r)}\,\mathbf{N}, \qquad \mathbf{N} = \frac{3}{2\,\sigma_e}\mathbf{s}, \qquad r = 1, 2, \cdots, N \tag{4.6}$$

where

$$\dot{\bar{\varepsilon}}^{(r)} = \frac{\sigma_e}{3\,\mu^{(r)}\,(\sigma_e)}, \qquad \mu^{(r)}\,(\sigma_e) = \frac{1}{3}\frac{\sigma_0^{(r)}}{\dot{\varepsilon}_0}\left(\frac{\sigma_0^{(r)}}{\sigma_e}\right)^{n^{(r)}-1}. \tag{4.7}$$

4.3 Numerical integration of constitutive equations

In this section, we present a method for the numerical integration of the resulting constitutive equations in the context of a displacement driven finite element formulation. Let t be a loading (time-like) parameter and consider an infinitesimal change from t_n to $t_{n+1} = t_n + \Delta t$, where Δt is "small". We use the notation A_n and A_{n+1} to denote the values of A at the start t_n and the end t_{n+1} of the increment and set $\Delta A = A_{n+1} - A_n$. We assume that the effective flow stress is, to a first approximation, constant over the period (t_n, t_{n+1}) and can be determined by the optimization problem in (2.40), in which the flow stresses of the phases take values

$$\sigma_0^{(i)} = (1-\beta)\;\sigma_0^{(i)}\Big|_n + \beta\;\sigma_0^{(i)}\Big|_{n+1}, \qquad 0 \le \beta \le 1. \tag{4.8}$$

where

$$\sigma_0^{(i)}\Big|_n = \sigma_y^{(i)}\left(\bar{\varepsilon}_n^{(i)}\right) \qquad \text{and} \qquad \sigma_0^{(i)}\Big|_{n+1} = \sigma_y^{(i)}\left(\bar{\varepsilon}_{n+1}^{(i)}\right) = \sigma_y^{(i)}\left(\bar{\varepsilon}_n^{(i)} + \Delta\bar{\varepsilon}^{(i)}\right). \tag{4.9}$$

Put in other words, the composite is assumed to behave as "incrementally perfectly plastic" with a flow stress $\tilde{\sigma}_0(\mathbf{q}_{n+1})$, which is updated at every increment. The value of $\tilde{\sigma}_0(\mathbf{q}_{n+1})$ is calculated by the solution of the corresponding optimization problem (2.40) using the $\sigma_0^{(i)}$ values defined in (4.8). The solution of the optimization problem (2.40) defines also the optimal values $\hat{y}^{(r)}(\mathbf{q}_{n+1})$, which determine the corresponding strain concentration factors $\alpha^{(i)}$ in (2.51) for the increment. The actual calculation is implicit in general, except when $\beta = 0$ is used in (4.8).

The Mises plasticity model is used, so over any time increment (t_n, t_{n+1}) the effective yield condition of the composite is written in the form

$$\Phi\left(\boldsymbol{\sigma}, \mathbf{q}_{n+1}\right) = \sigma_e - \tilde{\sigma}_0\left(\mathbf{q}_{n+1}\right) = 0, \tag{4.10}$$

where $\tilde{\sigma}_0\left(\mathbf{q}_{n+1}\right)$ is determined from the solution of the optimization problem (2.40) with $\sigma_0^{(i)}$ defined in (4.8).

The evolution of the equivalent plastic strains in the phases are written in terms of the strain concentration factors $\alpha^{(i)}$ defined in (2.51) in terms of the optimal values $\hat{y}^{(r)}\left(\mathbf{q}_{n+1}\right)$, i.e.,

$$\dot{q}_i = \dot{\bar{\varepsilon}}\,\alpha^{(i)}(\mathbf{q}_{n+1}), \qquad\qquad i = 1, 2, \cdots, N. \tag{4.11}$$

In a finite element environment, the solution is developed incrementally and the constitutive equations are integrated numerically at the element Gauss integration points. In a displacement based finite element formulation the solution is deformation driven. Let $\mathbf{F}$ denote the deformation gradient tensor. At a given Gauss point, the solution $(\mathbf{F}_n, \boldsymbol{\sigma}_n, \mathbf{q}_n)$ at time t_n as well as the deformation gradient $\mathbf{F}_{n+1}$ at time $t_{n+1} = t_n + \Delta t$ are known and the problem is to determine $(\boldsymbol{\sigma}_{n+1}, \mathbf{q}_{n+1})$.

The time variation of the deformation gradient $\mathbf{F}$ during the time increment $[t_n, t_{n+1}]$ can be written as:

$$\mathbf{F}(t) = \Delta\mathbf{F}(t) \cdot \mathbf{F}_n = \mathbf{R}(t) \cdot \mathbf{U}(t) \cdot \mathbf{F}_n, \qquad t_n \le t \le t_{n+1}, \tag{4.12}$$

where $\mathbf{R}(t)$ and $\mathbf{U}(t)$ are the rotation and right stretch tensors associated with $\Delta\mathbf{F}(t)$. The corresponding deformation rate tensor $\mathbf{D}(t)$ and spin $\mathbf{W}(t)$ can be written as:

$$\mathbf{D}(t) \equiv \left[\dot{\mathbf{F}}(t) \cdot \mathbf{F}^{-1}(t)\right]_s = \left[\Delta\dot{\mathbf{F}}(t) \cdot \Delta\mathbf{F}^{-1}(t)\right]_s, \tag{4.13}$$

and

$$\mathbf{W}(t) \equiv \left[\dot{\mathbf{F}}(t) \cdot \mathbf{F}^{-1}(t)\right]_a = \left[\Delta\dot{\mathbf{F}}(t) \cdot \Delta\mathbf{F}^{-1}(t)\right]_a, \tag{4.14}$$

where the subscripts s and a denote the symmetric and anti-symmetric parts, respectively. If it is assumed that the Lagrangian triad associated with $\Delta\mathbf{F}(t)$ (i.e., the eigenvectors of $\mathbf{U}(t)$) remains fixed over the time interval (t_n, t_{n+1}), it can be shown readily that

$$\mathbf{D}(t) = \mathbf{R}(t) \cdot \dot{\mathbf{E}}(t) \cdot \mathbf{R}^T(t), \quad \mathbf{W}(t) = \dot{\mathbf{R}}(t) \cdot \mathbf{R}^T(t), \tag{4.15}$$

and

$$\overset{\triangledown}{\boldsymbol{\sigma}}(t) = \mathbf{R}(t) \cdot \dot{\hat{\boldsymbol{\sigma}}}(t) \cdot \mathbf{R}^T(t) \tag{4.16}$$

where a superscript T indicates the transpose of a second-order tensor, $\mathbf{E}(t) = \ln \mathbf{U}(t)$ is the logarithmic strain relative to the configuration at the start of the increment, and

$$\hat{\boldsymbol{\sigma}}(t) = \mathbf{R}^T(t) \cdot \boldsymbol{\sigma}(t) \cdot \mathbf{R}(t). \tag{4.17}$$

It is noted that at the start of the increment ($t = t_n$)

$$\Delta\mathbf{F}_n = \mathbf{R}_n = \mathbf{U}_n = \boldsymbol{\delta}, \qquad \hat{\boldsymbol{\sigma}}_n = \boldsymbol{\sigma}_n, \quad \text{and} \qquad \mathbf{E}_n = \mathbf{0}, \tag{4.18}$$

whereas at the end of the increment ($t = t_{n+1}$)

$$\Delta\mathbf{F}_{n+1} = \mathbf{F}_{n+1} \cdot \mathbf{F}_n^{-1} = \mathbf{R}_{n+1} \cdot \mathbf{U}_{n+1} = \text{known}, \quad \text{and} \quad \mathbf{E}_{n+1} = \ln \mathbf{U}_{n+1} = \text{known}. \tag{4.19}$$

Then, the constitutive equations of the model can be written in the following form

$$\mathbf{D} = \mathbf{D}^e + \mathbf{D}^p \quad \Rightarrow \quad \dot{\mathbf{E}} = \dot{\mathbf{E}}^e + \dot{\mathbf{E}}^p, \tag{4.20}$$

$$\overset{\triangledown}{\boldsymbol{\sigma}} = \boldsymbol{\mathcal{L}}^e : \mathbf{D}^e \quad \Rightarrow \quad \dot{\hat{\boldsymbol{\sigma}}} = \boldsymbol{\mathcal{L}}^e : \dot{\mathbf{E}}^e, \tag{4.21}$$

$$\mathbf{D}^p = \dot{\bar{\varepsilon}}\, \hat{\mathbf{N}}, \quad \Rightarrow \quad \dot{\mathbf{E}}^p = \dot{\bar{\varepsilon}}\, \hat{\mathbf{N}}, \tag{4.22}$$

$$\mathbf{D}^{p(i)} = \alpha^{(i)}\, \mathbf{D}^p \quad \Rightarrow \quad \dot{q}_i = \dot{\bar{\varepsilon}}\, \alpha^{(i)}(\mathbf{q}), \qquad i = 1, 2, \cdots, N, \tag{4.23}$$

$$\text{with} \qquad \boldsymbol{\mathcal{L}}^e = 2\,G\,\boldsymbol{\mathcal{K}} + 3\,\kappa\,\boldsymbol{\mathcal{J}}, \qquad \hat{\mathbf{N}} = \frac{3}{2\,\sigma_e}\hat{\mathbf{s}}, \qquad \sigma_e = \sqrt{\frac{3}{2}\,\hat{\mathbf{s}} : \hat{\mathbf{s}}}. \tag{4.24}$$

It should be emphasized that equation (4.22) that defines the plastic deformation rate $\dot{\mathbf{E}}^p$ and equation (4.23) require numerical integration, whereas the rest of the equations can be integrated exactly:

$$\Delta\mathbf{E} = \Delta\mathbf{E}^e + \Delta\mathbf{E}^p, \tag{4.25}$$

$$\hat{\boldsymbol{\sigma}}_{n+1} = \boldsymbol{\sigma}_n + \boldsymbol{\mathcal{L}}^e : \Delta\mathbf{E}^e = \boldsymbol{\sigma}_n + \boldsymbol{\mathcal{L}}^e : (\Delta\mathbf{E} - \Delta\mathbf{E}^p) = \hat{\boldsymbol{\sigma}}^e - \boldsymbol{\mathcal{L}}^e : \Delta\mathbf{E}^p, \tag{4.26}$$

where $\hat{\boldsymbol{\sigma}}^e = \boldsymbol{\sigma}_n + \boldsymbol{\mathcal{L}}^e : \Delta\mathbf{E}$ is the (known) "elastic predictor".
We use two different methodologies for the integration of the aforementioned constitutive equations. In the first, we use the backward Euler method for the numerical integration of (4.22), and the forward Euler method for (4.23); in the second, we use the backward Euler method for the integration of both (4.22) and (4.23). In both cases, we use the *backward* Euler method for the integration of the "plastic flow" equation since previous experience (Aravas and Ponte Castañeda [2]) showed that it is imperative in order to be able to use increments of reasonable size.

4.3.1 Integration using a combination of the backward and the forward Euler schemes

A *backward* Euler integration scheme is used for the numerical integration of the flow rule (4.22):

$$\Delta \mathbf{E}^p = \Delta\bar{\varepsilon}\,\hat{\mathbf{N}}_{n+1}. \tag{4.27}$$

The elasticity equation (4.26) becomes

$$\hat{\boldsymbol{\sigma}}_{n+1} = \hat{\boldsymbol{\sigma}}^e - 2\,G\,\Delta\bar{\varepsilon}\,\hat{\mathbf{N}}_{n+1}. \tag{4.28}$$

Considering the deviatoric part of last equation and using the definition (4.24) of $\hat{\mathbf{N}}_{n+1}$ we conclude that the stress deviator $\hat{\mathbf{s}}_{n+1}$ is co-linear with the deviatoric part of the elastic predictor $\hat{\mathbf{s}}^e$

$$\hat{\mathbf{s}}_{n+1} = \hat{\mathbf{s}}^e - \frac{3\,G\,\Delta\bar{\varepsilon}}{\sigma_e^e}\,\hat{\mathbf{s}}_{n+1} \qquad \text{or} \qquad \hat{\mathbf{s}}_{n+1} = \left(1 + \frac{3\,G\,\Delta\bar{\varepsilon}}{\sigma_e^e}\right)^{-1} \hat{\mathbf{s}}^e, \tag{4.29}$$

Therefore, we can determine the direction $\hat{\mathbf{N}}_{n+1}$ of the plastic strain rate at t_{n+1} by using the known elastic predictor as

$$\hat{\mathbf{N}}_{n+1} = \frac{3}{2\,\sigma_e|_{n+1}}\,\hat{\mathbf{s}}_{n+1} = \frac{3}{2\,\sigma_e^e}\,\hat{\mathbf{s}}^e \equiv \hat{\mathbf{N}}^e = \text{known}. \tag{4.30}$$

where $\sigma_e^e = \sqrt{\frac{3}{2}\,\hat{\mathbf{s}}^e : \hat{\mathbf{s}}^e}$ is the von Mises equivalent stress of the elastic predictor. Projecting (4.28) in the direction of the plastic strain rate $\hat{\mathbf{N}}_{n+1}$

$$\hat{\boldsymbol{\sigma}}_{n+1} : \hat{\mathbf{N}}_{n+1} = \hat{\boldsymbol{\sigma}}^e : \hat{\mathbf{N}}^e - 2\,G\,\Delta\bar{\varepsilon}\,\hat{\mathbf{N}}_{n+1} : \hat{\mathbf{N}}_{n+1} \tag{4.31}$$

and taking into account that $\hat{\boldsymbol{\sigma}} : \hat{\mathbf{N}} = \sigma_e$ and $\hat{\mathbf{N}} : \hat{\mathbf{N}} = \frac{3}{2}$, we derive

$$\sigma_e|_{n+1} = \sigma_e^e - 3\,G\,\Delta\bar{\varepsilon}. \tag{4.32}$$

Thus, the yield condition (4.10) can be written at the end of the increment in the form

$$\Phi\left(\Delta\bar{\varepsilon}\right) \equiv \sigma_e^e - 3\,G\,\Delta\bar{\varepsilon} - \tilde{\sigma}_0\left(\mathbf{q}_n + \Delta\mathbf{q}\right) = 0. \tag{4.33}$$

The evolution of the equivalent plastic strains in the phases (4.23) using the *forward* Euler scheme are written also as

$$\Delta q_i = \Delta\bar{\varepsilon}\,\alpha^{(i)}(\mathbf{q}_n), \qquad\qquad i = 1, 2, \cdots, N. \tag{4.34}$$

The problem of integrating the elastoplastic equations for the homogenized composite reduces to the solution of the set of $N+1$ non-linear equations (4.33) and (4.34) for $\Delta\bar{\varepsilon}$ and $\Delta\mathbf{q} = \left(\Delta\bar{\varepsilon}^{(1)}, \Delta\bar{\varepsilon}^{(2)}, \cdots, \Delta\bar{\varepsilon}^{(N)}\right)$. These equations are solved by using Newton's method. In every Newton iteration the values of $\Delta\mathbf{q}$ are used to calculate the corresponding $\sigma_0^{(i)}$ from (4.8) and then the optimization problem (2.40) is solved by using the CONMAX software [32] to determine the optimal values $\hat{y}^{(i)}$; the values of the effective flow stress $\tilde{\sigma}_0$ and the strain

concentration factors $\alpha^{(i)}$ are then determined and the iterations are continued until the set tolerances are met. Details on the calculation of the Jacobian of the Newton loop are given in Appendix IV.
It is emphasized that the calculations are much simpler for a two-phase composite; in that case, one does not need to invoke CONMAX, since $\tilde{\sigma}_0$ is defined analytically by (3.5).
Once $\Delta\bar{\varepsilon}$ and $\Delta\mathbf{q}$ are calculated, equations (4.28) and (4.34) are used to determine the stress $\hat{\boldsymbol{\sigma}}_{n+1}$ and the state variables $\mathbf{q}_{n+1}$ and the true stresses are calculated as

$$\boldsymbol{\sigma}_{n+1} = \mathbf{R}_{n+1} \cdot \hat{\boldsymbol{\sigma}}_{n+1} \cdot \mathbf{R}_{n+1}^{T}. \tag{4.35}$$

Remark 1. In the special case where the value $\beta = 0$ is used in (4.8), the effective flow stress of the composite $\tilde{\sigma}_0$ and the strain concentration factors $\alpha^{(i)}$ are determined using the values of the flow stresses of the phases $\sigma_0^{(i)}\Big|_n$ at the start of the increment, and equations (4.33) and (4.34) can be solved analytically:

$$\Delta\bar{\varepsilon} = \frac{\sigma_e^e - \tilde{\sigma}_0\left(\mathbf{q}_n\right)}{3\,G} \qquad \text{and} \qquad \Delta q_i = \Delta\bar{\varepsilon}\,\alpha^{(i)}(\mathbf{q}_n). \tag{4.36}$$

4.3.2 Integration using the backward Euler method on all variables

We recall equation (4.32):

$$\sigma_e|_{n+1} = \sigma_e^e - 3\,G\,\Delta\bar{\varepsilon},$$

and use a *backward* Euler scheme for the numerical integration of (4.23):

$$\Delta q_i = \Delta\bar{\varepsilon}\,\alpha^{(i)}(\mathbf{q}_n + \Delta\mathbf{q}) \tag{4.37}$$

The yield condition now becomes

$$\Phi\left(\Delta\bar{\varepsilon}\right) \equiv \sigma_e^e - 3\,G\,\Delta\bar{\varepsilon} - \bar{\sigma}_0\left(\mathbf{q}_n + \Delta\mathbf{q}\right) = 0. \tag{4.38}$$

Equations (4.38) and (4.37) is now a system of non-linear equations that needs to be solved for $\Delta\bar{\varepsilon}$ and $\Delta\mathbf{q}$. We chose $\Delta\bar{\varepsilon}$ as the primary unknown and treat (4.38) as the basic equation, in which $\Delta\mathbf{q}$ are defined by (4.37). Within each iteration for $\Delta\bar{\varepsilon}$, the system of equations (4.37) is solved for $\Delta\mathbf{q}$ by using another Newton loop. Details on the calculation of the Jacobian of the Newton loop are given in Appendix IV.
The integration scheme described above is implemented into the ABAQUS general purpose finite element program [23]. The finite element formulation is based on the weak form of the momentum balance, the solution is carried out incrementally, and the discretized nonlinear equations are solved using Newton's method. In the calculations, the Jacobian of the global Newton scheme is approximated by the tangent stiffness matrix. Such an approximation

of the Jacobian is first-order accurate as the size of the increment $\Delta t \to 0$; it should be emphasized, however, that the aforementioned approximation influences only the rate of convergence of the Newton loop and not the accuracy of the results.
At this point we should also note that both computational models, the one with the integration using the *backward* Euler method and the one with the integration using a combination of the *backward* and the *forward* Euler method are equally accurate since their results are identical. Thus, in the following we choose to use the computational model of the latter case which is simpler.

4.4 The linearization moduli

When the finite element method is used for the solution to the problem, the "linearization moduli" C_{ijkl} are required :

$$C_{ijkl} \simeq R_{im}|_{n+1}\, R_{jn}|_{n+1}\, R_{kp}|_{n+1}\, R_{lq}|_{n+1}\, \hat{C}_{mnpq}, \qquad \text{where} \qquad \hat{\mathbf{C}} = \frac{\partial \hat{\boldsymbol{\sigma}}_{n+1}}{\partial \mathbf{E}_{n+1}}. \tag{4.39}$$

Generally, $\mathbf{C}$ depends not only on the constitutive model but also on the algorithm used for the numerical integration of the constitutive equations. The equation that defines $\hat{\boldsymbol{\sigma}}_{n+1}$ is

$$\hat{\boldsymbol{\sigma}}_{n+1} = \boldsymbol{\sigma}_n + \boldsymbol{\mathcal{L}}^e : \Delta\mathbf{E} - 2\,G\,\Delta\bar{\varepsilon}\,\hat{\mathbf{N}}^e \tag{4.40}$$

so that

$$d\hat{\boldsymbol{\sigma}}_{n+1} = \boldsymbol{\mathcal{L}}^e : d\mathbf{E}_{n+1} - 2\,G\,\left(d\bar{\varepsilon}\,\hat{\mathbf{N}}^e + \Delta\bar{\varepsilon}^p\, d\hat{\mathbf{N}}^e\right), \tag{4.41}$$

where

$$d\hat{\mathbf{N}}^e = \frac{2\,G}{\sigma_e^e}\left(\frac{3}{2}\,\boldsymbol{\mathcal{K}} - \hat{\mathbf{N}}^e\,\hat{\mathbf{N}}^e\right) : d\mathbf{E}_{n+1}.$$

The yield condition

$$\sigma_e|_{n+1} - \bar{\sigma}_0|_{n+1} = 0 \tag{4.42}$$

is used for the determination of $\hat{\mathbf{C}}$ as follows

$$\begin{aligned}
0 &= \underbrace{\frac{\partial \sigma_e|_{n+1}}{\partial \hat{\boldsymbol{\sigma}}_{n+1}}}_{\hat{\mathbf{N}}_{n+1}=\hat{\mathbf{N}}^e} : d\boldsymbol{\sigma}_{n+1} - \sum_{k=1}^{N} \left.\frac{\partial \bar{\sigma}_0}{\partial \bar{\varepsilon}^{(k)}}\right|_{n+1} d\bar{\varepsilon}^{(k)} \\
&= \hat{\mathbf{N}}^e : \left[\boldsymbol{\mathcal{L}}^e : d\mathbf{E}_{n+1} - 2\,G\,\left(d\bar{\varepsilon}\,\hat{\mathbf{N}}^e + \Delta\bar{\varepsilon}\,d\hat{\mathbf{N}}^e\right)\right] - \sum_{k=1}^{N} \left.\frac{\partial \bar{\sigma}_0}{\partial \sigma_0^{(k)}}\right|_{n+1} h_{n+1}^{(k)}\,\alpha_n^{(i)}\,d\bar{\varepsilon} \\
&= \underbrace{\hat{\mathbf{N}}^e : \boldsymbol{\mathcal{L}}^e}_{2\,G\,\hat{\mathbf{N}}^e} : d\mathbf{E}_{n+1} - 2\,G\,\left(d\bar{\varepsilon}\,\underbrace{\hat{\mathbf{N}}^e : \hat{\mathbf{N}}^e}_{3/2} + \Delta\bar{\varepsilon}\,\underbrace{\hat{\mathbf{N}}^e : d\hat{\mathbf{N}}^e}_{0}\right) - \underbrace{\sum_{k=1}^{N}\left(\left.\frac{\partial \bar{\sigma}_0}{\partial \sigma_0^{(k)}}\right|_{n+1} h_{n+1}^{(k)}\,\alpha_n^{(i)}\right)}_{H_{n+1}}\,d\bar{\varepsilon} \\
&= 2\,G\,\hat{\mathbf{N}}^e : d\mathbf{E}_{n+1} - (3\,G + H_{n+1})\,d\bar{\varepsilon},
\end{aligned} \tag{4.43}$$

Therefore $d\bar{\varepsilon}$ can be written as

$$d\bar{\varepsilon} = \frac{2\,G}{3\,G + H_{n+1}}\,\hat{\mathbf{N}}^e : d\mathbf{E}_{n+1}. \tag{4.44}$$

Finally, we substitute $d\bar{\varepsilon}$ from (4.44) into (4.41) to derive

$$\begin{aligned} d\hat{\boldsymbol{\sigma}}_{n+1} &= \boldsymbol{\mathcal{L}}^e : d\mathbf{E}_{n+1} - 2\,G\left[\frac{2\,G}{3\,G + H_{n+1}}\left(\hat{\mathbf{N}}^e : d\mathbf{E}_{n+1}\right)\hat{\mathbf{N}}^e + \Delta\bar{\varepsilon}\,\frac{2\,G}{\sigma_e^e}\left(\frac{3}{2}\,\boldsymbol{\mathcal{K}} - \hat{\mathbf{N}}^e\,\hat{\mathbf{N}}^e\right) : d\mathbf{E}_{n+1}\right] \\ &= \left\{\boldsymbol{\mathcal{L}}^e - 4\,G\left[\frac{1}{3 + \frac{H_{n+1}}{G}}\hat{\mathbf{N}}^e\,\hat{\mathbf{N}}^e + \Delta\bar{\varepsilon}\frac{G}{\sigma_e^e}\left(\frac{3}{2}\,\boldsymbol{\mathcal{K}} - \hat{\mathbf{N}}^e\,\hat{\mathbf{N}}^e\right)\right]\right\} : d\mathbf{E}_{n+1} \\ &= \left\{\boldsymbol{\mathcal{L}}^e - 4\,G\left(\frac{1}{3 + \frac{H_{n+1}}{G}} - \Delta\bar{\varepsilon}\frac{G}{\sigma_e^e}\right)\hat{\mathbf{N}}^e\,\hat{\mathbf{N}}^e - 6\,G\,\Delta\bar{\varepsilon}\frac{G}{\sigma_e^e}\,\boldsymbol{\mathcal{K}}\right\} : d\mathbf{E}_{n+1}. \end{aligned} \tag{4.45}$$

Therefore the linearization moduli are determined from

$$\hat{\mathbf{C}} = \boldsymbol{\mathcal{L}}^e - 4\,G\left(\frac{1}{3 + \frac{H_{n+1}}{G}} - \Delta\bar{\varepsilon}\frac{G}{\sigma_e^e}\right)\hat{\mathbf{N}}_{n+1}\,\hat{\mathbf{N}}_{n+1} - 6\,G\,\Delta\bar{\varepsilon}\frac{G}{\sigma_e^e}\,\boldsymbol{\mathcal{K}}. \tag{4.46}$$

Finally, (4.39) yields

$$\mathbf{C} \simeq \boldsymbol{\mathcal{L}}^e - 4\,G\left(\frac{1}{3 + \frac{H_{n+1}}{G}} - \Delta\bar{\varepsilon}\frac{G}{\sigma_e^e}\right)\mathbf{N}_{n+1}\,\mathbf{N}_{n+1} - 6\,G\,\Delta\bar{\varepsilon}\frac{G}{\sigma_e^e}\,\boldsymbol{\mathcal{K}}. \tag{4.47}$$

4.5 The role of UMAT(User MATerial subroutine)

The constitutive model described above is implemented into the ABAQUS general purpose finite element code [23]. This code provides a general interface so that a particular constitutive model can be introduced via a "user subroutine" named UMAT (User MATerial).
UMAT subroutines can be used with any ABAQUS procedure that includes mechanical behavior and are called by ABAQUS at every integration point of all elements for which the material definition includes a user-defined material behavior. The subroutine UMAT passes in all the information at the start of the increment, i.e., $\mathbf{F}_n$, $\boldsymbol{\sigma}_n$, $\bar{\varepsilon}_n^{(r)}$, as well as $\mathbf{F}_{n+1}$ and the user has to calculate the values of the corresponding quantities at the end of the increment, i.e., $\boldsymbol{\sigma}_{n+1}$, and $\bar{\varepsilon}_{n+1}^{(r)}$. A UMAT subroutine must also provide the material Jacobian matrix $\partial\left(\Delta\boldsymbol{\sigma}\right)/\partial\left(\Delta\boldsymbol{\varepsilon}\right)$ corresponding to the mechanical constitutive model under consideration.
When developing a UMAT subroutine the user is also free to define solution-dependent state variables (STATEV) and ABAQUS will store their values at the end of every increment, making them available for future calculations on subsequent increments. Solution dependent variables need to be updated to their values at the end of every increment.
The basic variables predefined in a general UMAT subroutine are summarized in Table 4.1. In the context of the UMAT developed to model the composite material, new variables were also introduced. The following table (Table 4.2) presents the state variables (STATEV) defined for the specific model.

Variable	Definition
NDI	Number of direct stress components
NSHR	Number of shear stress components
NTENS	Number of total stress components
NPROPS	Number of material constants
NSTATEV	Number of extra state variables to be used
NOEL	Number of Element being processed
NPT	Number of Integration point being processed
LAYER	Layer number (for composite shells and solids)
KSPT	Section point number within the current layer
KINC	Increment number
KSTEP	Step number
PROPS(NPROPS)	Array containing the user specified material constants
STRESS(NTENS)	Array containing the stress components
STATEV(NSTATEV)	Array containing the user defined state variables
STRAN(NTENS)	Array containing the total strains
DSTRAN(NTENS)	Array containing the strain increments
DDSDDE(NTENS,NTENS)	Material Jacobian $\partial(\Delta\boldsymbol{\sigma})/\partial(\Delta\boldsymbol{\varepsilon})$ to be defined
TIME(1)	Step time at the beginning of the current increment
TIME(2)	Total time at the beginning of the current increment
DTIME	Time increment
PNEWDT	Ratio $DTIME_{new}/DTIME_{current}$
DROT(3,3)	Rotation increment matrix
DFGRD0(3,3)	Deformation gradient at increment start
DFGRD1(3,3)	Deformation gradient at the end of the increment
CMNAME	User-Defined material name

Table 4.1: Interpretation of the predefined variables in a UMAT subroutine.

4.6 Unit cell finite element calculations

In this section we present the results of unit cell finite element calculations for a composite material made up of a statistically isotropic random distribution of isotropic, linearly-elastic hardening-plastic spherical inclusions embedded in a continuous, isotropic, linearly-elastic hardening-plastic matrix. The Mises plasticity model is used in the calculations. All analyses were carried out incrementally and accounted for geometry changes due to deformation (finite strain solutions).

In all cases analyzed, the matrix material is identified as "phase 1" and the flow stress $\sigma_y^{(i)}$

STATEV #	Definition
1	Equivalent plastic strain of the composite material $\bar{\varepsilon}$
2	Plasticity flag (0 $\rightarrow$ Elasticity, 1 $\rightarrow$ Plasticity)
3 - 6	Volume fractions of the constituent phases $c^{(i)}$
7 - 10	Equivalent plastic strain of the constituent phases $\bar{\varepsilon}^{(i)}$
11 - 14	Optimization parameters $y^{(i)}$

Table 4.2: The State variables defined in UMAT for the model for composite materials

of "phase i" is a function of the corresponding equivalent plastic strain $\bar{\varepsilon}$:

$$\sigma_y^{(i)}\left(\bar{\varepsilon}^{(i)}\right) = \sigma_0^{(i)}\left(1+\frac{\bar{\varepsilon}^{(i)}}{\varepsilon_0}\right)^{\frac{1}{\eta^{(i)}}}, \qquad \varepsilon_0 = 0.005, \tag{4.48}$$

where $\sigma_0^{(i)} = \sigma_y^{(i)}(0)$ is the yield stress of phase i, E is the elastic Young's modulus, and the hardening exponents $\eta^{(i)}$ take values in the region $1 \leq \eta^{(i)} \leq \infty$, with the limiting case $\eta^{(i)} = \infty$ corresponding to perfect plasticity. Note that this hardening exponents are completely uncorrelated to the creep exponent $n^{(i)}$ used in the definitions of the stress potentials in the previous sections. Figure 4.1 illustrates stress-strain curves for different values of the hardening exponents $\eta^{(i)}$.

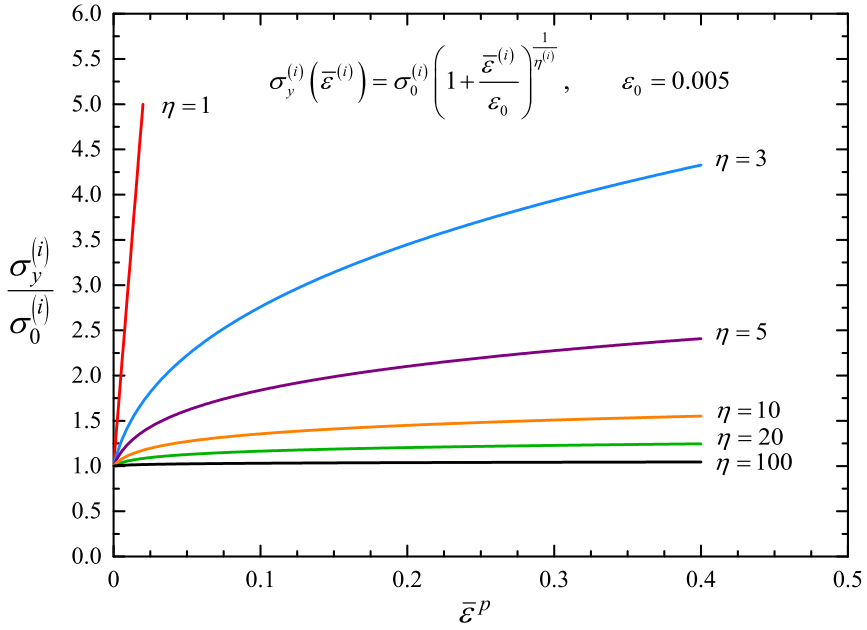

Figure 4.1: Stress-strain curves for different values of the hardening exponents $\eta^{(i)}$.

The following values are used for Young's modulus E and Poisson ratio ν:

$$E = 220\text{GPa}, \qquad \nu = 0.3. \tag{4.49}$$

In addition, one-element finite element calculations were carried out, in which the element is subjected to the same deformation gradient as the unit cell and the corresponding uniform

stress state in the element is calculated by using the algorithm described in section 4.3 for the homogenized material.

4.6.1 Two-phase composites

We analyze first a two-phase composite with

$$\frac{\sigma_0^{(2)}}{\sigma_0^{(1)}} = 1.5, \qquad \eta^{(1)} = 5, \qquad \eta^{(2)} = 3. \tag{4.50}$$

The corresponding stress-strain curves of the phases in uniaxial tension are shown in Fig. 4.2.

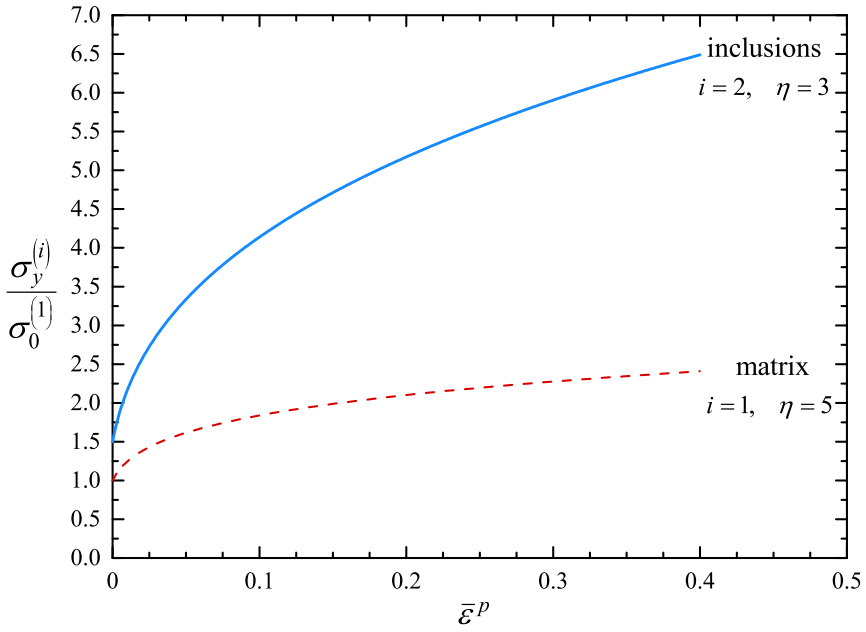

Figure 4.2: Uniaxial stress-strain curves of phases.

Figure 4.3 shows the deformed unit cell at $\lambda = 1.15$ for various inclusion volume fractions $c^{(2)}$.

Figure 4.4 shows the results of the unit cell finite element calculations together with the predictions of the homogenization model for the case of uniaxial tension in direction 1 and for inclusion volume fractions $c^{(2)}$ =0.10, 0.20, 0.30, and 0.40. The quantity $\tilde{\sigma}$ in Fig. 4.4 is the average stress $< \sigma_{11} >$ in the unit cell calculations and the uniform σ_{11} stress component in the corresponding one-element homogenization calculation. The predictions of the homogenization model agree well with the numerical results. It is also evident from these figures that as we increase the volume fraction of the stiffer particle phase which also has a higher hardening exponent, this leads to a reinforcement of the composite both at the level of the yield strength as well as in its hardening response. It is also interesting to note that even though we have added the hardening behavior of the phases heuristically to the

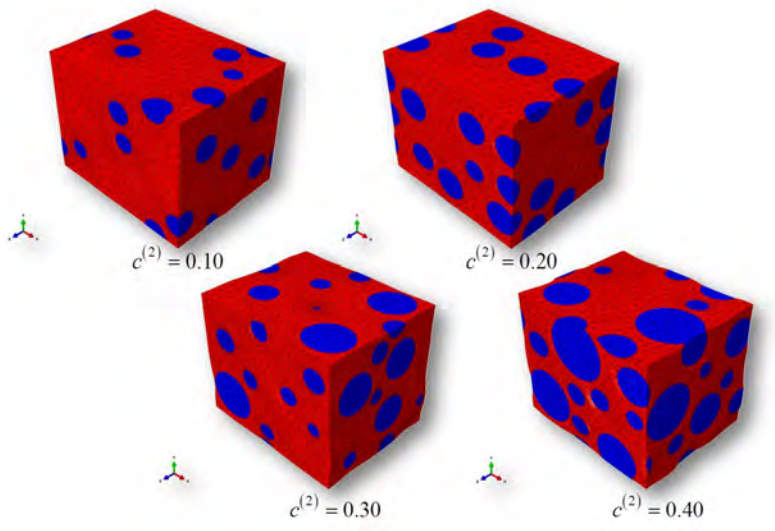

Figure 4.3: Deformed configurations of unit cells in uniaxial tension ($\lambda = 1.15$) for various values of the volume fraction $c^{(2)}$.

homogenization model for perfectly plastic phases (see equation (3.5)), the corresponding analytical estimates are in excellent agreement with those obtained by the finite element calculations (see also relevant discussion in [68]). This, in turn, suggests that such a simplified approach is sufficient for this class of materials.

The unit cell finite element calculations discussed above were used also to determine the strain concentration factors. Figure 4.5 shows the variation of the strain concentration factors $\alpha^{(r)}$ as determined from the unit cell finite element calculations (equation (3.35)) and the homogenization theory (equation (2.51)) in a two-phase composite for the case of uniaxial tension in direction 1 and for inclusion volume fractions $c^{(2)}$ =0.10, 0.20, 0.30, and 0.40.

Calculations are also carried out for finite shear deformation. In this case, the deformation gradient used in (3.29) is of the form

$$\mathbf{F} = \boldsymbol{\delta} + \gamma\, \mathbf{e}_1\, \mathbf{e}_2, \tag{4.51}$$

where γ is the amount of shearing on the 1-2 plane. Figure 4.6 shows the deformed unit cell at $\gamma = 0.15$ for various inclusion volume fractions $c^{(2)}$.

Figure 4.7 shows the results of the unit cell finite element calculations together with the predictions of the homogenization model for the case of finite shear on the 1-2 plane and for inclusion volume fractions $c^{(2)}$ =0.10, 0.20, 0.30, and 0.40. The quantity $\tilde{\tau}$ in Fig. 4.7 is

$$\tilde{\tau} = \sqrt{\frac{1}{2}\, s_{ij}\, s_{ij}}\,, \tag{4.52}$$

where s_{ij} is identified with the average deviatoric stresses $< s_{ij} >$ in the unit cell calculations and with the uniform deviatoric stresses s_{ij} in the one-element homogenization calculations. Again, the predictions of the homogenization model agree well with the numerical results.

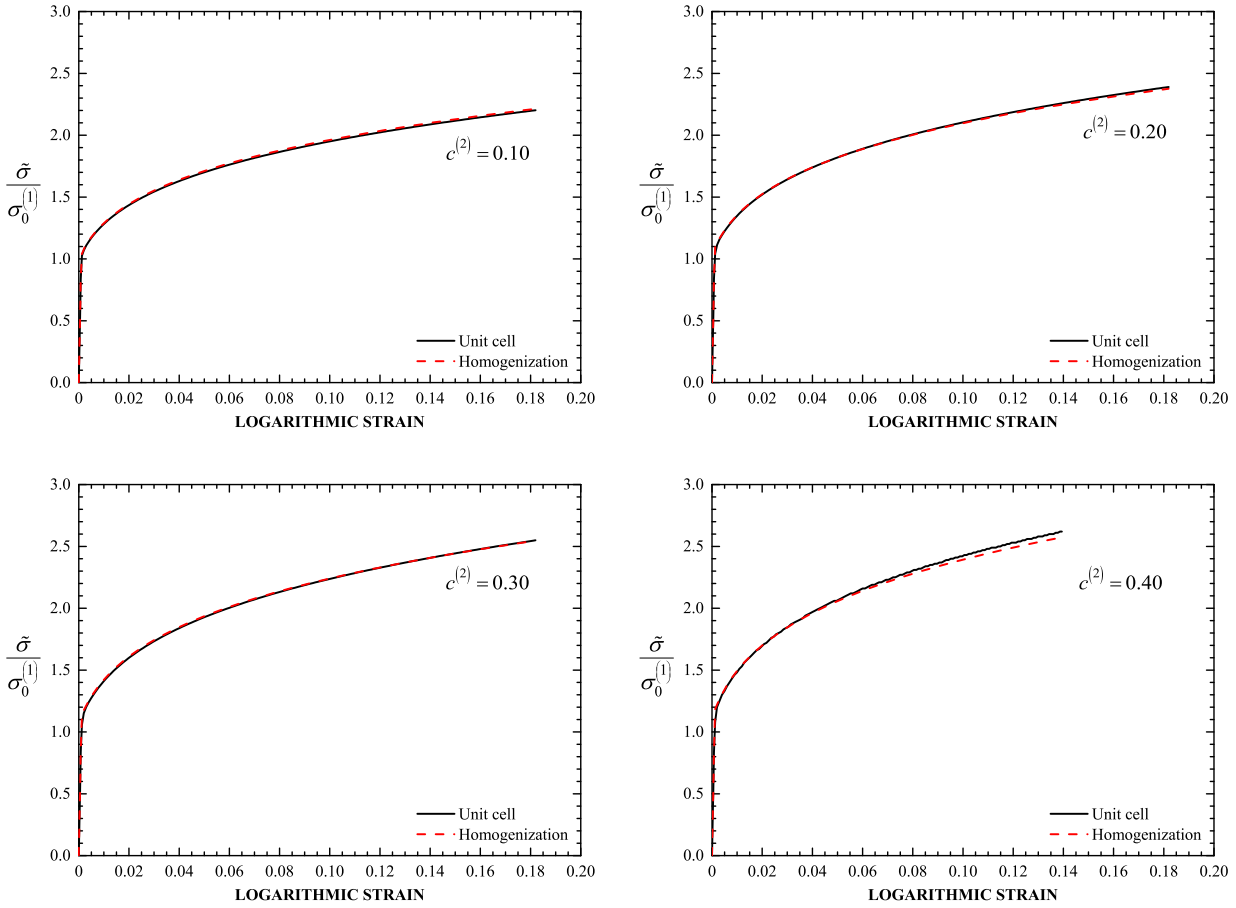

Figure 4.4: Stress-strain curves of the two-phase composite in uniaxial tension for different values of the volume fraction $c^{(2)}$. The solid lines are the results of the unit cell finite element calculations and the dash lines are the predictions (2.40) of the model based on the H-S$^-$ estimate ($\mu_0 = \mu^{(1)}$).

Similar observations to those made in the context of Figure 4.4 could also be made in Figure 4.7 regarding the effect of volume fraction and the hardening exponent of the phases upon the effective response under shear loadings. Figure 4.8 shows the variation of the strain concentration factors $\alpha^{(r)}$ as determined from the unit cell finite element calculations (equation (3.35)) and the homogenization theory (equation (2.51)) in a two-phase composite for the case of simple shear and for inclusion volume fractions $c^{(2)}$ =0.10, 0.20, 0.30, and 0.40.

Finally calculations are also carried out for the case of compression. Figure 4.9 shows the deformed unit cell at $\lambda = 0.85$ for various inclusion volume fractions $c^{(2)}$.

Figure 4.10 shows the results of the unit cell finite element calculations together with the predictions of the homogenization model for the case of compression in direction 1 and for inclusion volume fractions $c^{(2)}$ =0.10, 0.20, 0.30, and 0.40. The quantity $\tilde{\sigma}$ in Fig. 4.10 is the average stress $| < \sigma_{11} > |$ in the unit cell calculations and the uniform $|\sigma_{11}|$ stress component in the corresponding one-element homogenization calculation. Figure 4.11 shows

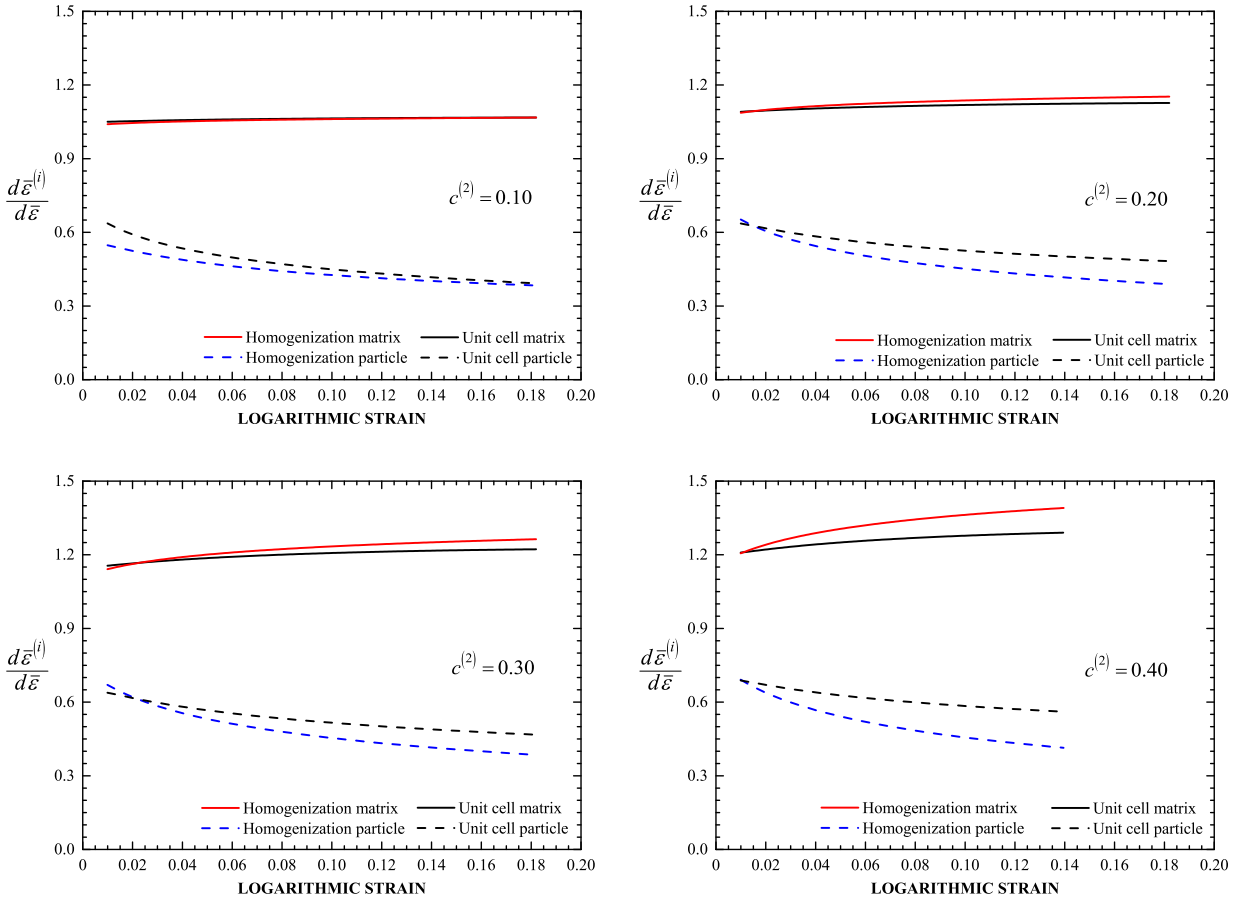

Figure 4.5: Strain concentration factors $\alpha^{(i)} = d\bar{\varepsilon}^{(i)}/d\bar{\varepsilon}$ as determined from unit cell finite element calculations and homogenization theory (equation (2.51)) for a two-phase composite.

the variation of the strain concentration factors $\alpha^{(r)}$ as determined from the unit cell finite element calculations (equation (3.35)) and the homogenization theory (equation (2.51)) in a two-phase composite for the case of compression and for inclusion volume fractions $c^{(2)}$ =0.10, 0.20, 0.30, and 0.40. The predictions of the homogenization model agree well with the numerical results.

4.6.2 Three-phase composites

We consider next a three-phase composite with

$$\frac{\sigma_0^{(2)}}{\sigma_0^{(1)}} = 1.875, \quad \frac{\sigma_0^{(3)}}{\sigma_0^{(1)}} = 5, \qquad \eta^{(1)} = 5, \quad \eta^{(2)} = 3, \quad \eta^{(3)} = 2.5. \tag{4.53}$$

and composition $c^{(1)} = 0.60$, $c^{(2)} = 0.25$, and $c^{(3)} = 0.15$. The problems of uniaxial tension, finite shear deformation and compression are solved.
Figures 4.12 – 4.14 show the deformed unit cells for uniaxial tension at $\lambda = 1.20$, finite shear $\gamma = 0.20$ and compression at $\lambda = 0.80$ and the corresponding stress-strain curves. The

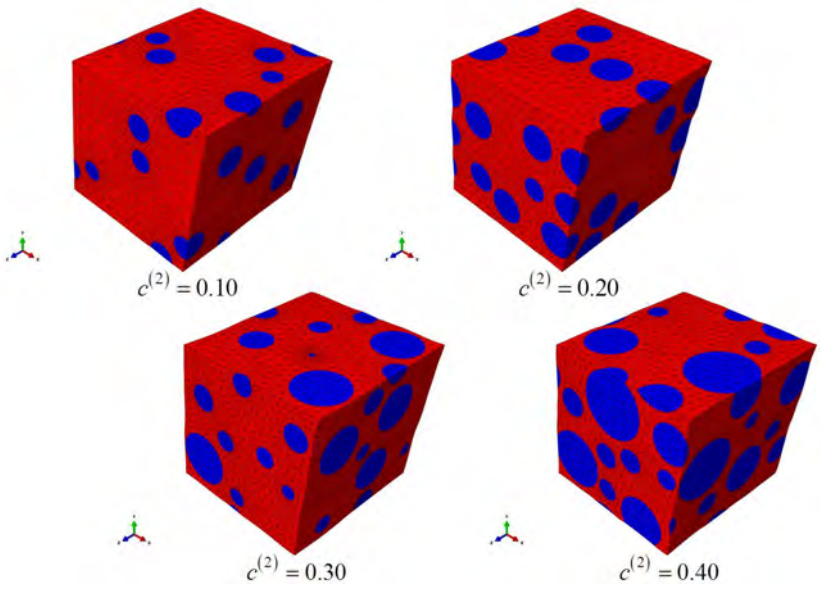

Figure 4.6: Deformed configurations of unit cells in simple shear ($\gamma = 0.15$) for various values of the volume fraction $c^{(2)}$.

predictions of the homogenization model agree well with the results of the unit cell finite element calculations.
In order to check the isotropy of the unit cell, we carried out calculations for uniaxial tension in directions 2 and 3, for simple shear in plane 13 and 23 and for compression in directions 2 and 3. In all cases, the results were identical to those shown in Figs. 4.12, 4.13 and 4.14.
Figures 4.15 – 4.17 show the variation of the strain concentration factors $\alpha^{(r)}$ as determined from the unit cell finite element calculations (equation (3.35)) and the homogenization theory (equation (2.51)) in a three-phase composite for the case of uniaxial tension, simple shear and compression. The predictions of the homogenization model agree well with the results of the unit cell finite element calculations. The model is capable of predicting sufficiently well both the initial yield strength of the three-phase composite as well the hardening evolution as a function of the applied strains in uniaxial tension, uniaxial compression and shear loadings.

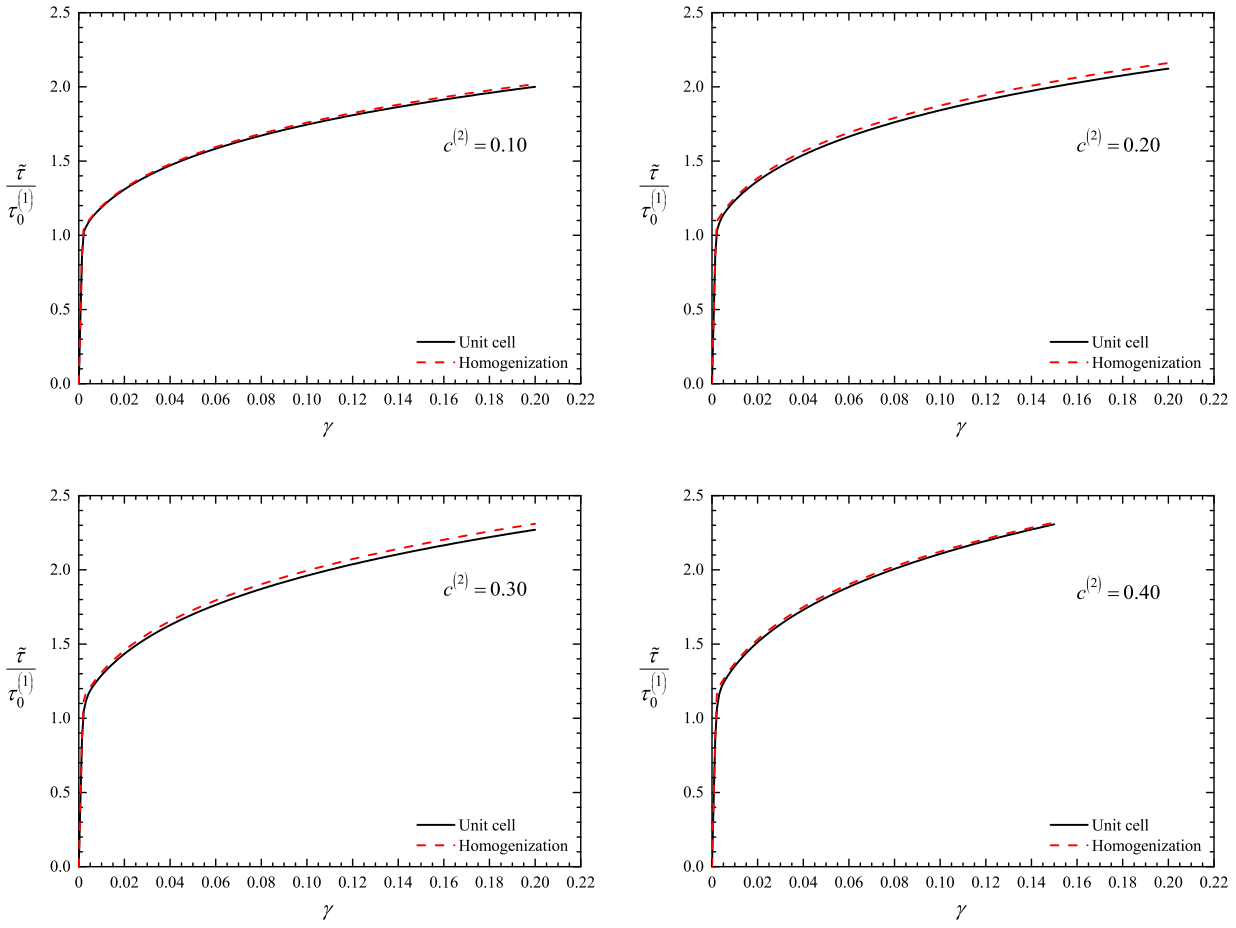

Figure 4.7: Shear stress-shear strain curves of the two-phase composite in simple shear for different values of the volume fraction $c^{(2)}$. The solid lines are the results of the unit cell finite element calculations and the dash lines are the predictions (2.40) of the model based on the H-S$^-$ estimate ($\mu_0 = \mu^{(1)}$).

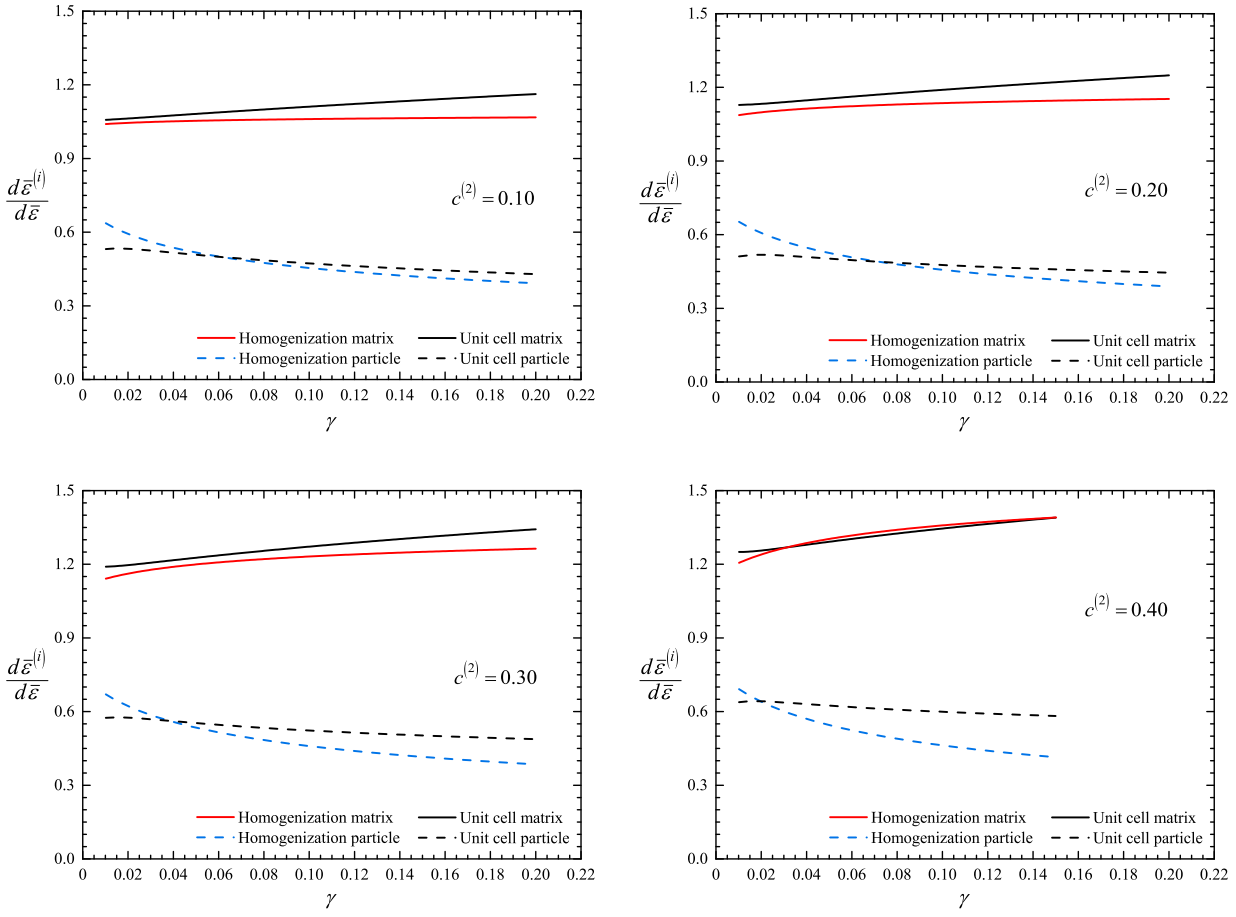

Figure 4.8: Strain concentration factors $\alpha^{(i)} = d\bar{\varepsilon}^{(i)}/d\bar{\varepsilon}$ as determined from unit cell finite element calculations and homogenization theory (equation (2.51)) for a two-phase composite.

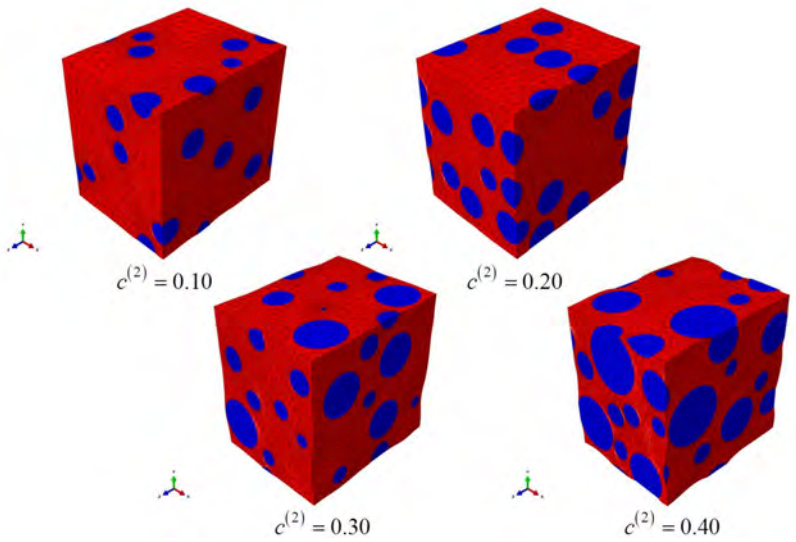

Figure 4.9: Deformed configurations of unit cells in compression ($\lambda = 0.85$) for various values of the volume fraction $c^{(2)}$.

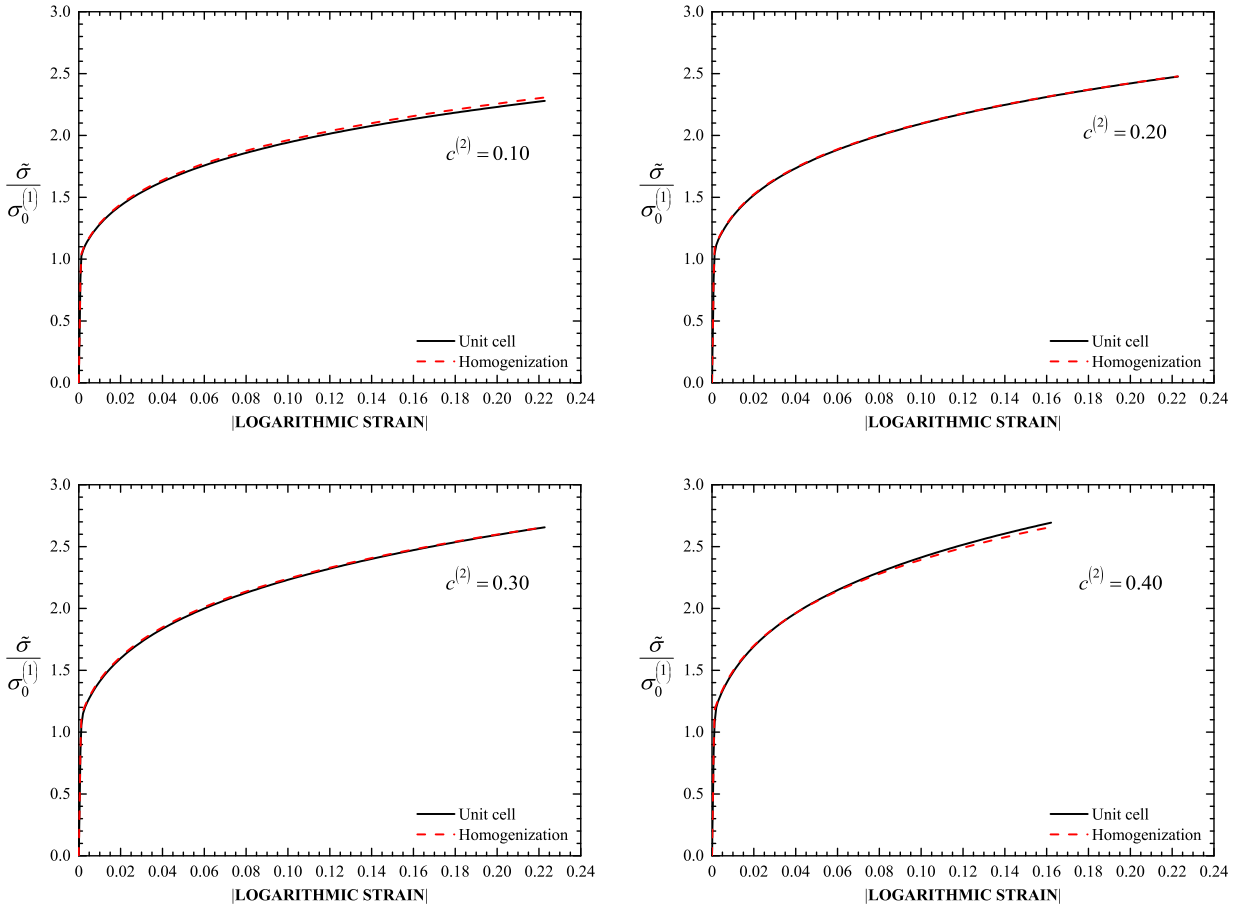

Figure 4.10: Stress-strain curves of the two-phase composite in compression for different values of the volume fraction $c^{(2)}$. The solid lines are the results of the unit cell finite element calculations and the dash lines are the predictions (2.40) of the model based on the H-S$^-$ estimate ($\mu_0 = \mu^{(1)}$).

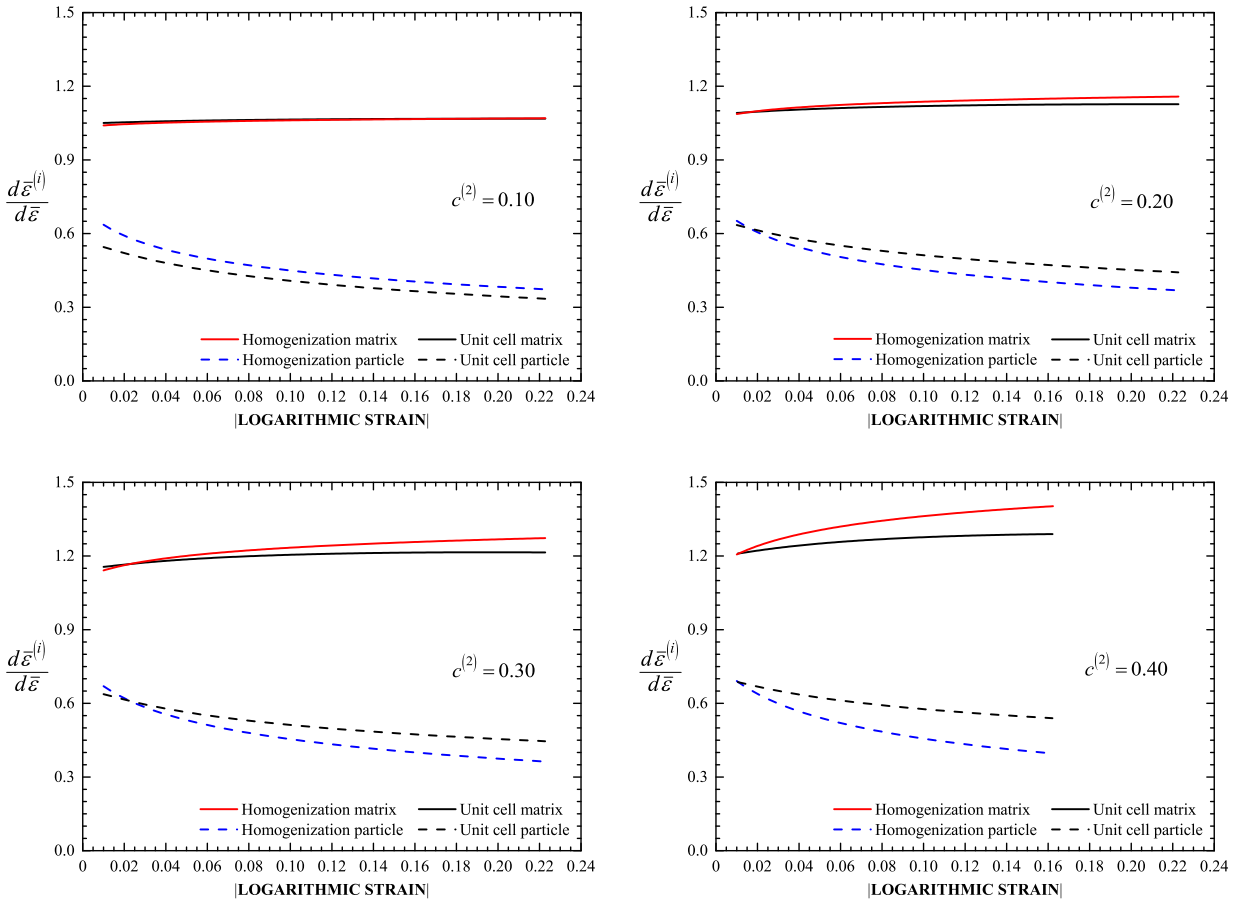

Figure 4.11: Strain concentration factors $\alpha^{(i)} = d\bar{\varepsilon}^{(i)}/d\bar{\varepsilon}$ as determined from unit cell finite element calculations and homogenization theory (equation (2.51)) for a two-phase composite.

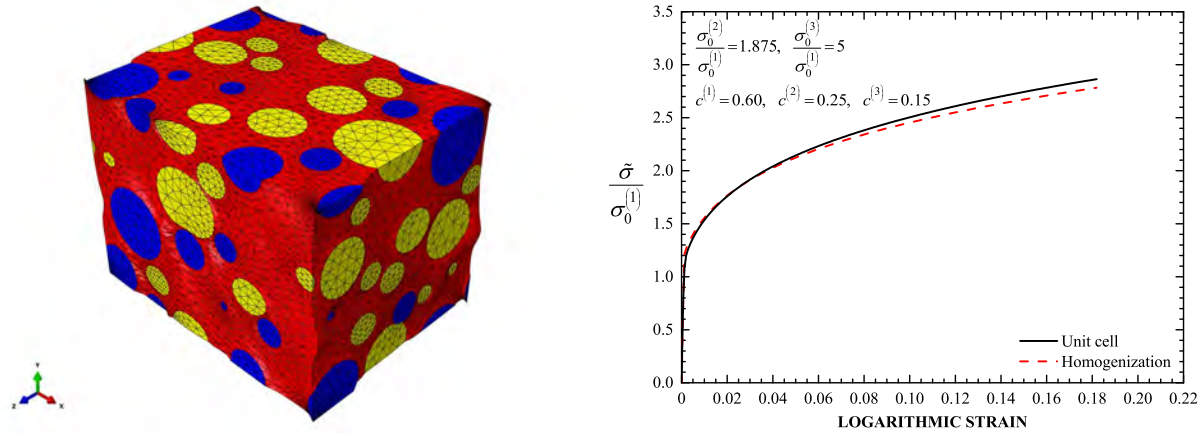

Figure 4.12: Deformed configuration of unit cell of the three-phase composite in uniaxial tension ($\lambda = 1.20$) and stress-strain curves of the three-phase composite. The solid lines are the results of the unit cell finite element calculations and the dash lines are the predictions (2.40) of the model based on the H-S$^-$ estimate ($\mu_0 = \mu^{(1)}$).

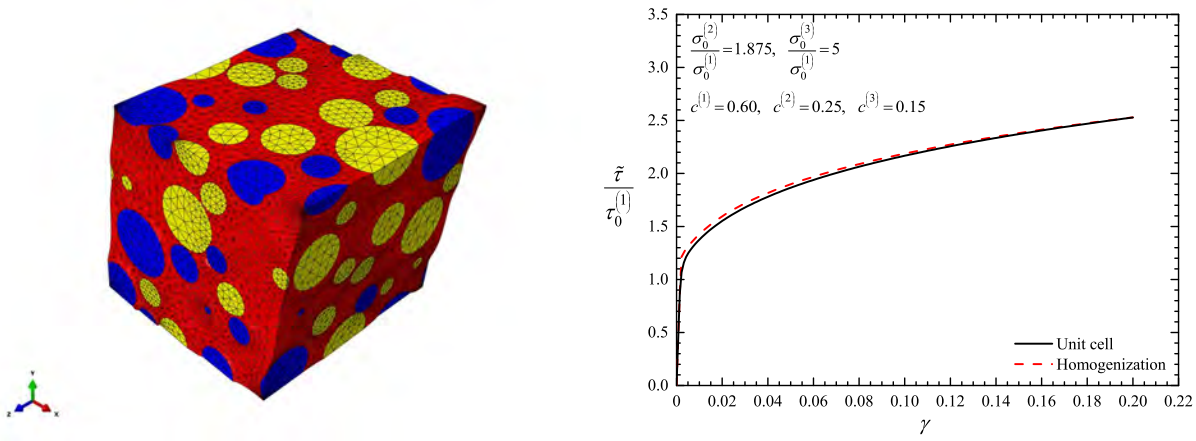

Figure 4.13: Deformed configuration of unit cell of the three-phase composite in simple shear ($\gamma = 0.20$) and shear stress - shear strain curves of the three-phase composite. The solid lines are the results of the unit cell finite element calculations and the dash lines are the predictions (2.40) of the model based on the H-S$^-$ estimate ($\mu_0 = \mu^{(1)}$).

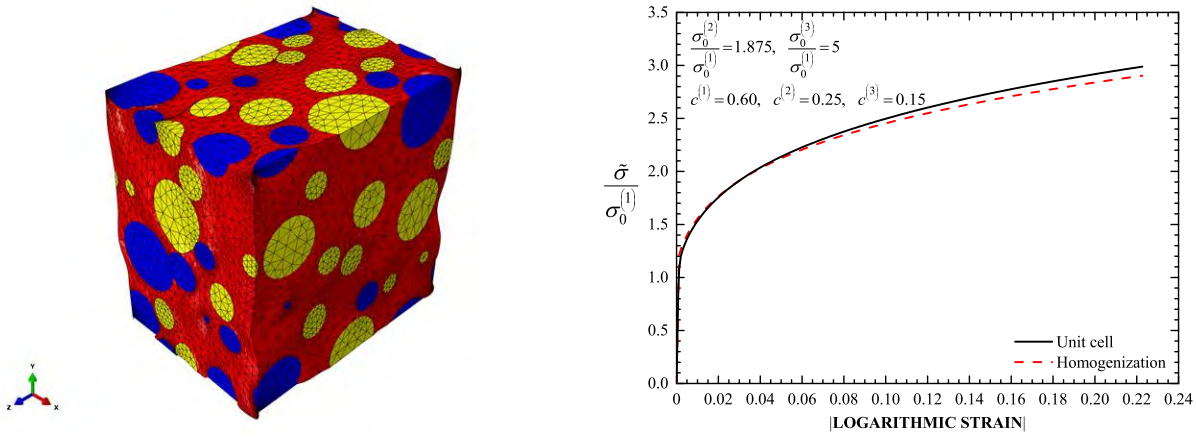

Figure 4.14: Deformed configuration of unit cell of the three-phase composite in compression ($\lambda = 0.80$) and stress-strain curves of the three-phase composite. The solid lines are the results of the unit cell finite element calculations and the dash lines are the predictions (2.40) of the model based on the H-S$^-$ estimate ($\mu_0 = \mu^{(1)}$).

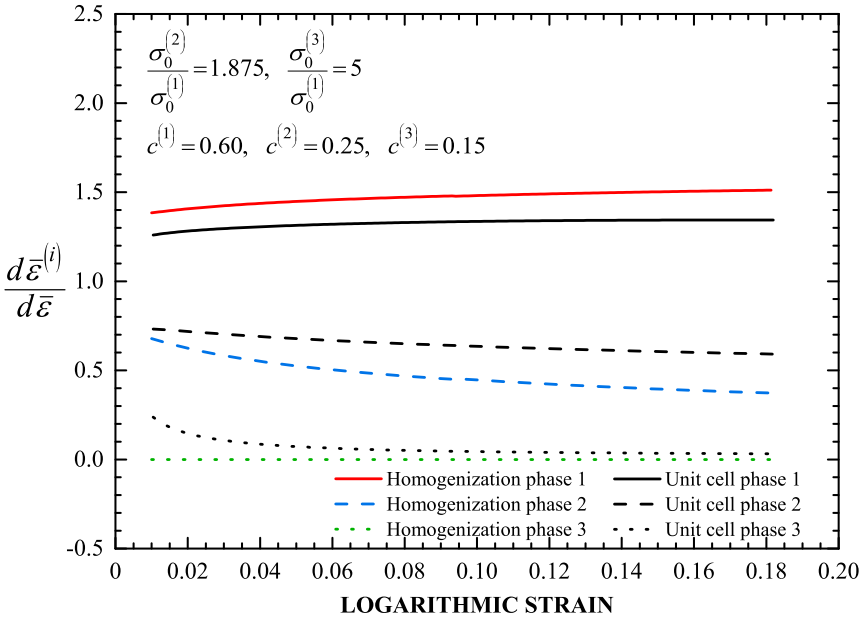

Figure 4.15: Strain concentration factors $\alpha^{(i)} = d\bar{\varepsilon}^{(i)}/d\bar{\varepsilon}$ as determined from unit cell finite element calculations and homogenization theory (equation (2.51)) for a three-phase composite for the case of uniaxial tension.

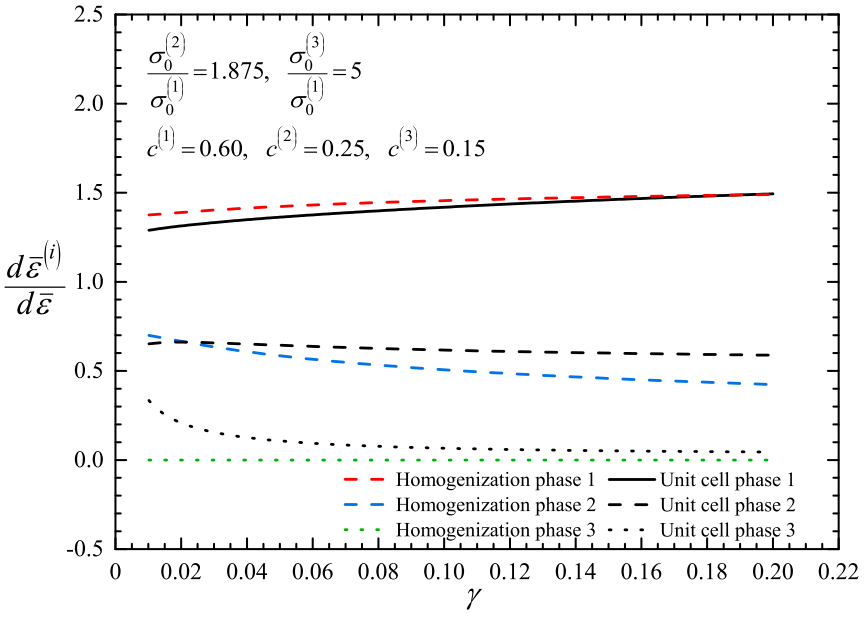

Figure 4.16: Strain concentration factors $\alpha^{(i)} = d\bar{\varepsilon}^{(i)}/d\bar{\varepsilon}$ as determined from unit cell finite element calculations and homogenization theory (equation (2.51)) for a three-phase composite for the case of simple shear.

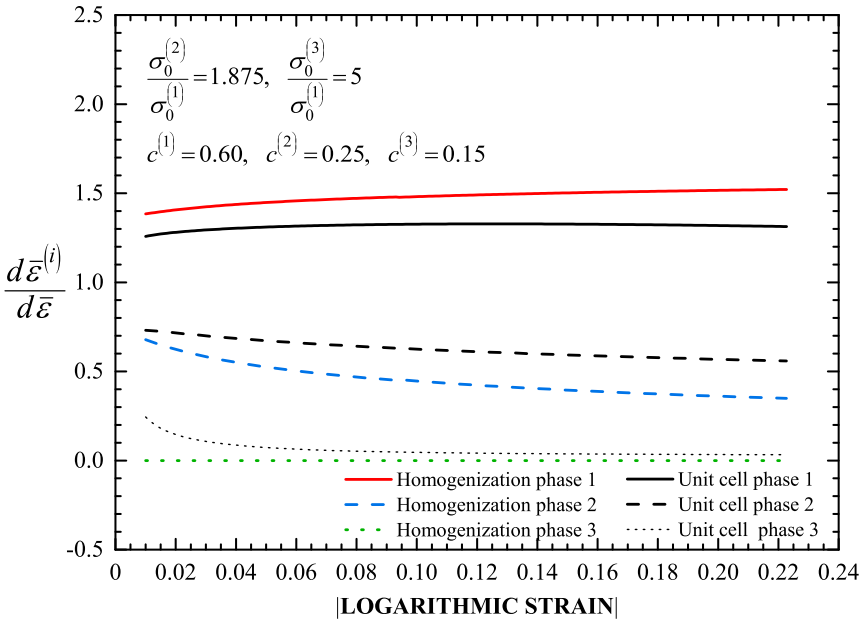

Figure 4.17: Strain concentration factors $\alpha^{(i)} = d\bar{\varepsilon}^{(i)}/d\bar{\varepsilon}$ as determined from unit cell finite element calculations and homogenization theory (equation (2.51)) for a three-phase composite for the case of compression.

Chapter 5

Applications - TRIP Steels

5.1 Introduction

In this chapter, we develop a constitutive model for TRIP steels that consist of four individual constituents: ferrite, bainite, retained austenite and martensite. The homogenization techniques for non-linear composites, described in Chapter 2, are used to determine the effective properties and overall behavior of TRIP steels. We develop a method for the numerical integration of the resulting constitutive equations in the context of a displacement driven finite element formulation and the model is implemented into the ABAQUS. The calibration of the model is based on uniaxial tension tests on TRIP steels. Then, we use the constitutive model to study in detail the problems of plastic flow localization and necking in tension. We also use the model to calculate "forming limit diagrams" for sheets made of TRIP steels. Calculations are also conducted for a non-transforming steel for comparison purposes.

5.2 Constitutive modeling of TRIP steels

In this section, a constitutive model for TRIP steels is developed. As it was previously mentioned, we consider four-phase TRIP steels that consist of a ferritic matrix with dispersed bainite and austenite, which transforms gradually into martensite as the material deforms plastically. The following labels are used for the constituent phases: (1) for ferrite, (2) for bainite, (3) or (a) for austenite and (4) or (m) for martensite. The constitutive equations are developed for the case of finite geometry changes.
An important aspect of the martensitic transformation is the strain softening which occurs due to the strain associated with the transformation process. This strain softening is accounted for by introducing in the constitutive model an additional deformation rate that is proportional to the rate of increase of the volume fraction of martensite. The total deformation rate can be split into elastic, plastic and transformation parts:

$$\mathbf{D} = \mathbf{D}^e + \mathbf{D}^p + \mathbf{D}^{TRIP} \tag{5.1}$$

Standard isotropic linear hypoelasticity of homogeneous solids is used in order to describe the elastic behavior of the TRIP steels since the elastic properties of all phases are fundamentally the same. The constitutive equation of the plastic part $\mathbf{D}^p$ is determined by using the homogenization theory described in Chapter 2. The transformation part $\mathbf{D}^{TRIP}$ has both deviatoric and volumetric parts and is proportional to the rate of change of the volume fraction of martensite due to martensitic transformation, which is described by the modified Olson-Cohen transformation kinetics model proposed by Stringfellow *et al.* [64].

5.2.1 Constitutive formulation

The constitutive equation for $\mathbf{D}^e$ as mentioned in section 4.2.1 is written as

$$\mathbf{D}^e = \boldsymbol{\mathcal{M}}^e : \overset{\nabla}{\boldsymbol{\sigma}} \qquad \text{or} \qquad \overset{\nabla}{\boldsymbol{\sigma}} = \boldsymbol{\mathcal{L}}^e : \mathbf{D}^e, \tag{5.2}$$

where $\overset{\nabla}{\boldsymbol{\sigma}}$ is the Jaumann derivative of the stress tensor $\boldsymbol{\sigma}$, $\boldsymbol{\mathcal{M}}^e$ is the elastic compliance tensor and $\boldsymbol{\mathcal{L}}^e$ is the elastic tensor.
The plastic part of the deformation rate $\mathbf{D}^p$ is determined in terms of the plastic properties of the constituent phases by using the homogenization theory described in Chapter 2. The corresponding constitutive equation, as mentioned in section 4.2.2 is of the form

$$\mathbf{D}^p = \dot{\bar{\varepsilon}}\,\mathbf{N} = \frac{\mathbf{s}}{2\,\tilde{\mu}}, \qquad \mathbf{N} = \frac{3}{2\,\sigma_e}\,\mathbf{s}, \qquad \sigma_e = \sqrt{\frac{3}{2}\,\mathbf{s} : \mathbf{s}}, \qquad \dot{\bar{\varepsilon}} = \sqrt{\frac{2}{3}\mathbf{D}^p : \mathbf{D}^p} = \frac{\sigma_e}{3\,\tilde{\mu}}, \tag{5.3}$$

where $\tilde{\mu}$ is determined from the homogenization theory.
Finally, regarding the transformation part $\mathbf{D}^{TRIP}$ Stringfellow *et al.* [64] proposed the following form:

$$\mathbf{D}^{TRIP} = A\dot{f}\,\mathbf{N} + \frac{1}{3}\,\dot{\varepsilon}_v^p\,\boldsymbol{\delta} \qquad \text{with} \qquad \mathbf{N} = \frac{3}{2\,\sigma_e}\mathbf{s}, \qquad \sigma_e = \sqrt{\frac{3}{2}\,\mathbf{s} : \mathbf{s}}, \tag{5.4}$$

where σ_e is the von Mises equivalent stress, $\mathbf{s}$ is the deviatoric stress tensor, $\boldsymbol{\delta}$ is the second-order identity tensor, $A(\sigma_e) = A_0 + A_1 \frac{\sigma_e}{s_a^*}$ is a dimensionless function and $\dot{\varepsilon}_v^p = \Delta_v \dot{f}$ is the transformation dilatation rate. Details of the formulation are given in Papatriantafillou [46]. Therefore, we conclude that the constitutive equation for $\mathbf{D}^{TRIP}$ can be written as:

$$\mathbf{D}^{TRIP} = \left[A(\sigma_e)\,\mathbf{N} + \frac{1}{3}\,\Delta_v\,\boldsymbol{\delta}\right]\dot{f} \tag{5.5}$$

5.2.1.1 Evolution of the volume fraction of the phases

Stringfellow *et al.* [64] extended the one-dimensional model of Olson and Cohen [45] for the kinetics of martensitic transformation and developed a general model that considers in addition to temperature and plastic strain the effects of stress triaxiality as well. The model of Olson and Cohen [45] is based on the observation that strain-induced nucleation occurs primarily at shear-band intersections. The evolution equation for the volume fraction of martensite f derived by Stringfellow *et al.* [64] is of the form

$$\dot{f} = c^{(a)}\left(A_f\,\dot{\bar{\varepsilon}}^{(a)} + B_f\,\dot{X}_\Sigma\right), \tag{5.6}$$

where $c^{(a)}$ is the volume fraction of austenite, $\bar{\varepsilon}^{(a)}$ is the representative equivalent plastic strain in the austenite, X_Σ is the stress triaxiality defined as the ratio of the hydrostatic stress $p = \sigma_{kk}/3$ to the von Mises equivalent stress σ_e, i.e., $X_\Sigma = p/\sigma_e$ and parameters A_f and B_f are defined as ([64])

$$A_f = \alpha\,\beta_0\,r\,(1-f_{sb})\,(f_{sb})^{r-1}\,P, \tag{5.7}$$

$$B_f = \frac{g_2}{\sqrt{2\pi}\,s_g}\,\beta_0\,(f_{sb})^r \exp\left[-\frac{1}{2}\left(\frac{g-\bar{g}}{s_g}\right)^2\right] H(\dot{X}_\Sigma), \tag{5.8}$$

where H is the Heaviside unit step function and f_{sb} is the volume fraction of shear bands in the austenite defined by ([45])

$$f_{sb} = 1 - \exp\left[-\alpha\,\bar{\varepsilon}^{(a)}\right]. \tag{5.9}$$

In the previous expressions α is a constant that represents the rate of shear band formation $df_{sb}/d\bar{\varepsilon}^{(a)}$ in the austenite at low strains, $P(g)$ is the probability that a shear band will serve as a nucleation site for martensite

$$P(g) = \frac{1}{\sqrt{2\pi}\,s_g}\int_{-\infty}^{g} \exp\left[-\frac{1}{2}\left(\frac{g'-\bar{g}}{s_g}\right)^2\right] dg', \tag{5.10}$$

where g is a normalized thermodynamic driving force defined as

$$g(\Theta, X_\Sigma) = g_0 - g_1\,\Theta + g_2\,X_\Sigma, \tag{5.11}$$

with (g_0, g_1, g_2) positive dimensionless constants, Θ a normalized temperature related to temperature T according to the equation

$$\Theta(T) = \frac{T - M^\sigma_{s,ut}}{M_{d,ut} - M^\sigma_{s,ut}}, \qquad M^\sigma_{s,ut} \le T \le M_{d,ut}, \tag{5.12}$$

and $(M^\sigma_{s,ut}, M_{d,ut})$ are the absolute (M^σ_s, M_d) temperatures for uniaxial tension.
In the following the evolution equations for $c^{(1)}$, $c^{(2)}$ and $c^{(a)}$ are presented. Starting with the definition $c^{(1)} = V^{(1)}/V$, we derive $\dot{c}^{(1)} = -c^{(1)}\,\dot{V}/V$. Finally, using that $\dot{V}/V = \dot{\varepsilon}^p_v \simeq \Delta_v\,\dot{f}$, we find that

$$\dot{c}^{(1)} = -c^{(1)}\,\Delta_v\,\dot{f}. \tag{5.13}$$

Likewise, we conclude that

$$\dot{c}^{(2)} = -c^{(2)}\,\Delta_v\,\dot{f}, \tag{5.14}$$

and, since $c^{(1)} + c^{(2)} + c^{(a)} + f = 1$, we find $\dot{c}^{(a)} = -(\dot{f} + \dot{c}^{(1)} + \dot{c}^{(2)})$ or

$$\dot{c}^{(a)} = -\left[1 - \left(c^{(1)} + c^{(2)}\right)\,\Delta_v\right]\,\dot{f}. \tag{5.15}$$

5.2.1.2 Summary of constitutive equations

The constitutive model developed in the previous sections consists of the following equations:

$$\text{Constitutive Formulation:} \qquad \mathbf{D} = \mathbf{D}^e + \mathbf{D}^p + \mathbf{D}^{TRIP} \tag{5.16}$$

$$\text{Elastic behavior:} \qquad \overset{\triangledown}{\boldsymbol{\sigma}} = \boldsymbol{\mathcal{L}}^e : \mathbf{D}^e \tag{5.17}$$

$$\text{Plastic Strain of the composite:} \qquad \mathbf{D}^p = \dot{\bar{\varepsilon}}\,\mathbf{N}, \qquad \dot{\bar{\varepsilon}} = \frac{\sigma_e}{3\,\tilde{\mu}} \tag{5.18}$$

$$\text{Transformation Deformation Rate:} \qquad \mathbf{D}^{TRIP} = \left[A\,\mathbf{N} + \frac{1}{3}\,\Delta_v\,\boldsymbol{\delta} \right] \dot{f} \tag{5.19}$$

where

$$\mathbf{N} = \frac{3}{2\,\sigma_e}\,\mathbf{s}, \qquad \sigma_e = \sqrt{\frac{3}{2}\,\mathbf{s} : \mathbf{s}} \tag{5.20}$$

and the evolution equations of the volume fractions are given by

$$\text{Ferrite:} \qquad \dot{c}^{(1)} = -c^{(1)}\,\Delta_v\,\dot{f} \tag{5.21}$$

$$\text{Bainite:} \qquad \dot{c}^{(2)} = -c^{(2)}\,\Delta_v\,\dot{f} \tag{5.22}$$

$$\text{Retained Austenite:} \qquad \dot{c}^{(a)} = -\left(\dot{c}^{(1)} + \dot{c}^{(2)} + \dot{c}^{(m)} \right) \tag{5.23}$$

$$\text{Martensite:} \qquad \dot{f} = c^{(a)} \left(A_f\,\dot{\bar{\varepsilon}}^{(a)} + B_f\,\dot{X}_\Sigma \right) \tag{5.24}$$

In the equations stated above, the quantities $\tilde{\mu}$, A, A_f and B_f have the following functional dependencies:

$$\tilde{\mu} = \tilde{\mu}\left(\sigma_e, c^{(r)}\right), \quad A = A(\sigma_e), \quad A_f = A_f\left(\dot{\bar{\varepsilon}}^{(a)}, X_\Sigma\right), \quad B_f = B_f\left(\dot{\bar{\varepsilon}}^{(a)}, X_\Sigma, \dot{X}_\Sigma\right) \tag{5.25}$$

5.2.2 Numerical integration of constitutive equations

In this section, we present a method for the numerical integration of the resulting constitutive equations of TRIP steels in the context of a displacement driven finite element formulation. At a Gauss point in the finite element mesh, the solution $\left(\mathbf{F}_n, \boldsymbol{\sigma}_n, c_n^{(r)}\right)$ at time t_n as well as the deformation gradient $\mathbf{F}_{n+1}$ at time $t_{n+1} = t_n + \Delta t$ are known and the problem is to determine $\boldsymbol{\sigma}_{n+1}$, $c_{n+1}^{(r)}$.

The constitutive equations summarized in section 5.2.1.2 can be written in the following form:

$$\mathbf{D} = \mathbf{D}^e + \mathbf{D}^{in} \quad \Rightarrow \quad \dot{\mathbf{E}} = \dot{\mathbf{E}}^e + \dot{\mathbf{E}}^{in}, \tag{5.26}$$

$$\overset{\triangledown}{\boldsymbol{\sigma}} = \boldsymbol{\mathcal{L}}^e : \mathbf{D}^e \quad \Rightarrow \quad \dot{\hat{\boldsymbol{\sigma}}} = \boldsymbol{\mathcal{L}}^e : \dot{\mathbf{E}}^e, \tag{5.27}$$

$$\mathbf{D}^{in} = \dot{\bar{\varepsilon}}\,\mathbf{N} + \left(A\,\mathbf{N} + \frac{1}{3}\Delta_v\boldsymbol{\delta} \right) \dot{f} \quad \Rightarrow \quad \dot{\mathbf{E}}^{in} = \left(\dot{\bar{\varepsilon}} + \frac{A}{\Delta_v}\,\dot{\varepsilon}_v^p \right) \mathbf{N} + \frac{1}{3}\,\dot{\varepsilon}_v^p \boldsymbol{\delta}, \tag{5.28}$$

$$\mathbf{D}^{p(i)} = \alpha^{(i)}\,\mathbf{D}^p \quad \Rightarrow \quad \dot{\bar{\varepsilon}}^{(i)} = \alpha^{(i)}\,\dot{\bar{\varepsilon}} \tag{5.29}$$

$$\text{with} \qquad \hat{\mathbf{N}} = \frac{3}{2\,\sigma_e}\hat{\mathbf{s}}, \qquad \dot{\varepsilon}_v^p = \Delta_v \dot{f}, \qquad \dot{\bar{\varepsilon}} = \frac{\sigma_e}{3\mu\,(\sigma_e)}, \qquad \alpha^{(i)} = \alpha^{(i)}\left(\bar{\varepsilon}^{(k)}\right) \tag{5.30}$$

The evolution equations of the volume fractions of the constituent phases are defined by the following equations:

$$\dot{f} = c^{(a)}\left(A_f\,\dot{\bar{\varepsilon}}^{(a)} + B_f\,\dot{X}_\Sigma\right) \tag{5.31}$$

$$\dot{c}^{(a)} = -\left(\dot{c}^{(1)} + \dot{c}^{(2)} + \dot{c}^{(m)}\right) \tag{5.32}$$

$$\dot{c}^{(1)} = -c^{(1)}\,\Delta_v \dot{f} \tag{5.33}$$

$$\dot{c}^{(2)} = -c^{(2)}\,\Delta_v \dot{f} \tag{5.34}$$

As mentioned previously in section 5.2.1.1, A_f and B_f depend on $\left(\bar{\varepsilon}^{(a)},\, X_\Sigma,\, \Theta\right)$.
At this point it should be noted that equation (5.28) that determines the inelastic deformation rate $\dot{\mathbf{E}}^{in}$ and equation (5.31) that defines the evolution of the volume fraction of martensite f, as well as equation (5.29) require numerical integration. The rest of the equations are integrated exactly:

$$\Delta\mathbf{E} = \Delta\mathbf{E}^e + \Delta\mathbf{E}^{in} \qquad \Rightarrow \qquad \Delta\mathbf{E}^e = \Delta\mathbf{E} - \Delta\mathbf{E}^{in}, \tag{5.35}$$

$$\hat{\boldsymbol{\sigma}}_{n+1} = \boldsymbol{\sigma}_n + \boldsymbol{\mathcal{L}}^e : \Delta\mathbf{E}^e = \boldsymbol{\sigma}_n + \boldsymbol{\mathcal{L}}^e : \left(\Delta\mathbf{E} - \Delta\mathbf{E}^{in}\right) = \hat{\boldsymbol{\sigma}}^e - \boldsymbol{\mathcal{L}}^e : \Delta\mathbf{E}^{in}, \tag{5.36}$$

$$c_{n+1}^{(1)} = c_n^{(1)} e^{-\Delta_v f}, \tag{5.37}$$

$$c_{n+1}^{(2)} = c_n^{(2)} e^{-\Delta_v f}, \tag{5.38}$$

$$c_{n+1}^{(a)} = 1 - \left(f_{n+1} + c_{n+1}^{(1)} + c_{n+1}^{(2)}\right) \tag{5.39}$$

where $\hat{\boldsymbol{\sigma}}^e = \boldsymbol{\sigma}_n + \boldsymbol{\mathcal{L}}^e : \Delta\mathbf{E}$ is the (known)"elastic predictor".
The remaining equations are

$$\dot{\mathbf{E}}^{in} = \left(\dot{\bar{\varepsilon}} + \frac{A}{\Delta_v}\,\dot{\varepsilon}_v^p\right)\hat{\mathbf{N}} + \frac{1}{3}\,\dot{\varepsilon}_v^p\boldsymbol{\delta}, \qquad \hat{\mathbf{N}} = \frac{3}{2\,\sigma_e}\,\hat{\mathbf{s}}, \qquad \dot{\varepsilon}_v^p = \Delta_v \dot{f}, \qquad \dot{\bar{\varepsilon}} = \frac{\sigma_e}{3\mu} \tag{5.40}$$

$$\dot{\bar{\varepsilon}}^{(i)} = \alpha^{(i)}\,\dot{\bar{\varepsilon}} \tag{5.41}$$

and

$$\dot{f} = c^{(a)}\left(A_f\,\dot{\bar{\varepsilon}}^{(a)} + B_f\,\dot{X}_\Sigma\right) \tag{5.42}$$

We use two different methodologies for the integration of the aforementioned constitutive equations. In the first, we use the *backward* Euler method for the numerical integration of the "plastic flow" equation (5.40), and the *forward* Euler method for (5.41) and (5.42); in the second, we use the *backward* Euler method for the integration of (5.40), (5.41) and (5.42). In both cases, we use the *backward* Euler method for the integration of the "plastic flow" equation since previous experience (Aravas and Ponte Castañeda [2]) showed that it is imperative in order to be able to use increments of reasonable size.

5.2.2.1 Integration using a combination of the backward and the forward Euler schemes

A *backward* Euler integration scheme is used for the numerical integration of the plastic flow rule (5.40):

$$\Delta\mathbf{E}^{in} = \left(\Delta\bar{\varepsilon} + \frac{A_{n+1}}{\Delta_v}\Delta\varepsilon_v^p\right)\hat{\mathbf{N}}_{n+1} + \frac{1}{3}\,\Delta\varepsilon_v^p\,\boldsymbol{\delta} \tag{5.43}$$

The elasticity equation (5.36) using equation (5.43) and setting $\boldsymbol{\mathcal{L}}^e = 2\,\mu\,\boldsymbol{\mathcal{K}} + 3\,\kappa\,\boldsymbol{\mathcal{J}}$ becomes

$$\hat{\boldsymbol{\sigma}}_{n+1} = \hat{\boldsymbol{\sigma}}^e - 2\,G\left(\Delta\bar{\varepsilon} + \frac{A_{n+1}}{\Delta_v}\Delta\varepsilon_v^p\right)\hat{\mathbf{N}}_{n+1} - \boldsymbol{\mathcal{K}}\,\Delta\varepsilon_v^p\,\boldsymbol{\delta} \tag{5.44}$$

Considering the deviatoric part of last equation and using the definition of $\hat{\mathbf{N}}_{n+1}$ we conclude that the stress deviator $\hat{\mathbf{s}}_{n+1}$ is co-linear with the deviatoric part of the elastic predictor $\hat{\mathbf{s}}^e$

$$\hat{\mathbf{s}}_{n+1} = \hat{\mathbf{s}}^e - \frac{3\,G}{\sigma_e|_{n+1}}\left(\Delta\bar{\varepsilon} + \frac{A_{n+1}}{\Delta_v}\Delta\varepsilon_v^p\right)\hat{\mathbf{s}}_{n+1} \quad \text{or} \quad \hat{\mathbf{s}}_{n+1} = \frac{\hat{\mathbf{s}}^e}{1 + \frac{3\,G}{\sigma_e|_{n+1}}\left(\Delta\bar{\varepsilon} + \frac{A_{n+1}}{\Delta_v}\Delta\varepsilon_v^p\right)} \tag{5.45}$$

Therefore, we can determine the direction $\hat{\mathbf{N}}_{n+1}$ of the plastic strain rate at t_{n+1} by using the known elastic predictor as follows

$$\hat{\mathbf{N}}_{n+1} = \frac{3}{2\,\sigma_e|_{n+1}}\,\hat{\mathbf{s}}_{n+1} = \frac{3}{2}\frac{1}{\sqrt{\frac{3}{2}\,\hat{\mathbf{s}}_{n+1} : \hat{\mathbf{s}}_{n+1}}}\,\hat{\mathbf{s}}_{n+1} = \frac{3}{2}\frac{1}{\sqrt{\frac{3}{2}\,\hat{\mathbf{s}}^e : \hat{\mathbf{s}}^e}}\,\hat{\mathbf{s}}^e \equiv \hat{\mathbf{N}}^e = \text{known} \tag{5.46}$$

Projecting (5.45) in the direction of the plastic strain rate $\hat{\mathbf{N}}_{n+1}$

$$\hat{\mathbf{s}}_{n+1} : \hat{\mathbf{N}}_{n+1} = \hat{\mathbf{s}}^e : \hat{\mathbf{N}}_{n+1} - \frac{3\,G}{\sigma_e|_{n+1}}\left(\Delta\bar{\varepsilon} + \frac{A_{n+1}}{\Delta_v}\Delta\varepsilon_v^p\right)\hat{\mathbf{s}}_{n+1} : \hat{\mathbf{N}}_{n+1} \tag{5.47}$$

and taking into account that $\hat{\boldsymbol{\sigma}} : \hat{\mathbf{N}} = \sigma_e$, we derive

$$\sigma_e|_{n+1} = \frac{\sigma_e^e - 3\,G\,\left(\Delta\bar{\varepsilon} + \frac{A_0}{\Delta_v}\,\Delta\varepsilon_v^p\right)}{1 + \frac{3\,G}{s_a^*}\frac{A_1}{\Delta_v}\,\Delta\varepsilon_v^p} \tag{5.48}$$

Therefore, the yield condition can be written at the end of the increment in the form

$$\sigma_e|_{n+1} - \tilde{\sigma}_0(c_{n+1}^{(i)}, \bar{\varepsilon}_{n+1}^{(i)}) = 0 \qquad \Rightarrow \qquad \frac{\sigma_e^e - 3\,G\,(\Delta\bar{\varepsilon} + \frac{A_0}{\Delta_v}\,\Delta\varepsilon_v^p)}{1 + \frac{3\,G}{s_a^*}\frac{A_1}{\Delta_v}\,\Delta\varepsilon_v^p} - \tilde{\sigma}_0(c_{n+1}^{(i)}, \bar{\varepsilon}_{n+1}^{(i)}) = 0$$

$$\Rightarrow \qquad \sigma_e^e - 3\,G\,(\Delta\bar{\varepsilon} + \frac{A_0}{\Delta_v}\,\Delta\varepsilon_v^p) - (1 + \frac{3\,G}{s_a^*}\frac{A_1}{\Delta_v}\,\Delta\varepsilon_v^p)\,\tilde{\sigma}_0(c_{n+1}^{(i)}, \bar{\varepsilon}_{n+1}^{(i)}) = 0 \tag{5.49}$$

The evolution of the equivalent plastic strain in the phases (5.41) and of the volume fraction of the martensite (5.42) using the *forward* Euler scheme are written also as

$$\Delta\bar{\varepsilon}^{(i)} = \Delta\bar{\varepsilon}\,\alpha_n^{(i)} \tag{5.50}$$

$$\Delta f = c_n^{(a)}\left(A_f|_n\,\alpha_n^{(a)}\,\Delta\bar{\varepsilon} + B_f|_n\,\Delta X_\Sigma\right) \tag{5.51}$$

with $$A_{n+1} = A_0 + A_1 \frac{\sigma_e|_{n+1}}{s_a^*} \tag{5.52}$$

$$\Delta\varepsilon_v^p = \Delta_v \, \Delta f \tag{5.53}$$

$$\Delta X_\Sigma = X_\Sigma|_{n+1} - X_\Sigma|_n = \left(\frac{p}{\sigma_e}\right)_{n+1} - \left(\frac{p}{\sigma_e}\right)_n \tag{5.54}$$

So we have the following 2 equations:

$$F_1 \equiv \sigma_e^e - 3\,G\,\left(\Delta\bar{\varepsilon} + \frac{A_0}{\Delta_v}\,\Delta\varepsilon_v^p\right) - \left(1 + \frac{3\,G}{s_a^*}\frac{A_1}{\Delta_v}\,\Delta\varepsilon_v^p\right)\tilde{\sigma}_0\left(c_{n+1}^{(i)}, \bar{\varepsilon}_{n+1}^{(i)}\right) = 0 \tag{5.55}$$

$$F_2 \equiv \Delta\varepsilon_v^p - \Delta_v\, c_n^{(3)}\left(A_f|_n\,\Delta\bar{\varepsilon}^{(3)} + B_f|_n\,\Delta X_\Sigma\right) = 0 \tag{5.56}$$

Equations (5.55) and (5.56) is now a system of non-linear equations that needs to be solved for $\Delta\bar{\varepsilon}$ and $\Delta\varepsilon_v^p$. Newton's method is used for the solution of the system. Details on the calculation of the Jacobian of the Newton loop are given in Appendix IV.

5.2.2.2 Integration using the backward Euler method on all variables

We recall equation (5.43):

$$\Delta\mathbf{E}^{in} = \left(\Delta\bar{\varepsilon} + \frac{A_{n+1}}{\Delta_v}\Delta\varepsilon_v^p\right)\hat{\mathbf{N}}_{n+1} + \frac{1}{3}\,\Delta\varepsilon_v^p\,\boldsymbol{\delta}$$

and use a *backward* Euler scheme for the numerical integration of (5.41) and (5.42):

$$\Delta\bar{\varepsilon}^{(i)} = \Delta\bar{\varepsilon}\,\alpha_{n+1}^{(i)} \tag{5.57}$$

$$\Delta f = c_{n+1}^{(\alpha)}\left(A_f|_{n+1}\,\Delta\bar{\varepsilon}^{(a)} + B_f|_{n+1}\,\Delta X_\Sigma\right) \tag{5.58}$$

So now we have the following 2 equations:

$$F_1 \equiv \sigma_e^e - 3\,G\,\left(\Delta\bar{\varepsilon} + \frac{A_0}{\Delta_v}\Delta\varepsilon_v^p\right) - \left(1 + \frac{3\,G}{s_a^*}\frac{A_1}{\Delta_v}\Delta\varepsilon_v^p\right)\tilde{\sigma}_0\left(c_{n+1}^{(i)}, \bar{\varepsilon}_{n+1}^{(i)}\right) = 0 \tag{5.59}$$

$$F_2 \equiv \Delta\varepsilon_v^p - \Delta_v\, c_{n+1}^{(3)}\left(A_f|_{n+1}\,\Delta\bar{\varepsilon}^{(3)} + B_f|_{n+1}\,\Delta X_\Sigma\right) = 0 \tag{5.60}$$

Equations (5.59) and (5.60) is now a system of non-linear equations that needs to be solved for $\Delta\bar{\varepsilon}$ and $\Delta\varepsilon_v^p$. Newton's method is used for the solution of the system. Details on the calculation of the Jacobian of the Newton loop are given in Appendix IV.

At this point we should emphasize that both computational models, the one with the integration using the *backward* Euler method and the one with the integration using a combination of the *backward* and the *forward* Euler method are equally accurate since their results are identical. Thus, in the following we choose to use the computational model of the latter case which is simpler.

5.2.3 The linearization moduli

As we mentioned in section 4.4, when the finite element method is used for the solution to the problem, the "linearization moduli" C_{ijkl} are required

$$C_{ijkl} \simeq R_{im}|_{n+1}\, R_{jn}|_{n+1}\, R_{kp}|_{n+1}\, R_{lq}|_{n+1}\, \hat{C}_{mnpq}, \qquad \text{where} \qquad \hat{\mathbf{C}} = \frac{\partial \hat{\boldsymbol{\sigma}}_{n+1}}{\partial \mathbf{E}_{n+1}}. \tag{5.61}$$

Generally, $\mathbf{C}$ depends not only on the constitutive model but also on the algorithm used for the numerical integration of the constitutive equations. The equation that defines $\hat{\boldsymbol{\sigma}}_{n+1}$ is

$$\hat{\boldsymbol{\sigma}}_{n+1} = \boldsymbol{\sigma}_n + \boldsymbol{\mathcal{L}}^e \colon \Delta\mathbf{E}^e = \boldsymbol{\sigma}_n + \boldsymbol{\mathcal{L}}^e : \left(\Delta\mathbf{E} - \Delta\mathbf{E}^{in}\right) \tag{5.62}$$

so that

$$d\hat{\boldsymbol{\sigma}} = \boldsymbol{\mathcal{L}}^e : d\mathbf{E}^e = \boldsymbol{\mathcal{L}}^e : d\mathbf{E} - \boldsymbol{\mathcal{L}}^e : d\mathbf{E}^{in} \tag{5.63}$$

$$= 2\,G\,d\mathbf{e} + \kappa\, d\mathrm{E}_{kk}\,\boldsymbol{\delta} - 2\,G\left(d\bar{\varepsilon} + \frac{A}{\Delta_v}\,d\varepsilon_v^p\right)\hat{\mathbf{N}} - \kappa\, d\varepsilon_v^p\,\boldsymbol{\delta} \;\Rightarrow$$

$$\Rightarrow \qquad d\hat{\boldsymbol{\sigma}} = 2\,G\left[d\mathbf{e} - \left(d\bar{\varepsilon} + \frac{A}{\Delta_v}\,d\varepsilon_v^p\right)\hat{\mathbf{N}}\right] + \kappa\left(d\mathrm{E}_{kk} - d\varepsilon_v^p\right)\boldsymbol{\delta} \tag{5.64}$$

and

$$d\hat{\mathbf{s}} = 2\,G\left[d\mathbf{e} - \left(d\bar{\varepsilon} + \frac{A}{\Delta_v}\,d\varepsilon_v^p\right)\hat{\mathbf{N}}\right], \qquad dp = \kappa\left(dE_{kk} - d\varepsilon_v^p\right) \tag{5.65}$$

where for simplicity we drop the subscripts $n+1$. In order to determine $d\hat{\boldsymbol{\sigma}}$ we need to define $d\bar{\varepsilon}$ and $d\varepsilon_v^p$.
We begin with the calculation of $d\boldsymbol{\sigma}_e$, dp and dX_Σ in terms of $d\mathbf{E}$, $d\bar{\varepsilon}$ and $d\varepsilon_v^p$.

$$\sigma_e^2 = \frac{3}{2}\,\hat{\mathbf{s}} : \hat{\mathbf{s}} \quad \Rightarrow \quad 2\,\sigma_e\,d\sigma_e = 3\,\hat{\mathbf{s}} : d\hat{\mathbf{s}} \quad \Rightarrow \quad d\sigma_e = \underbrace{\frac{3}{2\,\sigma_e}\hat{\mathbf{s}}}_{\hat{\mathbf{N}}} : d\hat{\mathbf{s}} = \hat{\mathbf{N}} : d\hat{\mathbf{s}} \quad \Rightarrow$$

$$d\sigma_e = 2\,G\,\hat{\mathbf{N}} : \left[d\mathbf{e} - \left(d\bar{\varepsilon} + \frac{A}{\Delta_v}\,d\varepsilon_v^p\right)\hat{\mathbf{N}}\right] = 2\,G\,\hat{\mathbf{N}} : d\mathbf{E} - 3\,G\left(d\bar{\varepsilon} + \frac{A}{\Delta_v}\,d\varepsilon_v^p\right) \tag{5.66}$$

Also,

$$dp = \kappa\,\boldsymbol{\delta} : d\mathbf{E} - \kappa\, d\varepsilon_v^p \tag{5.67}$$

Finally, using the definition $X_\Sigma = p/\sigma_e$ we derive

$$dX_\Sigma = \frac{dp}{\sigma_e} - \frac{p}{\sigma_e^2}\,d\sigma_e = \frac{dp - X_\Sigma\,d\sigma_e}{\sigma_e} \;\Rightarrow$$

$$dX_\Sigma = \frac{1}{\sigma_e}\left\{\kappa\,\boldsymbol{\delta} : d\mathbf{E} - \kappa\,d\varepsilon_v^p - X_\Sigma\left[2\,G\,\hat{\mathbf{N}} : d\mathbf{E} - 3\,G\left(d\bar{\varepsilon} + \frac{A}{\Delta_v}\,d\varepsilon_v^p\right)\right]\right\} \;\Rightarrow$$

$$\sigma_e\,dX_\Sigma = \kappa\,\boldsymbol{\delta} : d\mathbf{E} - \kappa\,d\varepsilon_v^p - 2\,G\,X_\Sigma\,\hat{\mathbf{N}} : d\mathbf{E} + 3\,G\,X_\Sigma\,d\bar{\varepsilon} + 3\,G\,X_\Sigma\frac{A}{\Delta_v}\,d\varepsilon_v^p \quad \Rightarrow$$

$$\Rightarrow \quad 3\,G\,X_\Sigma\,d\bar{\varepsilon} + \left(3\,G\,X_\Sigma\frac{A}{\Delta_v} - \kappa\right)d\varepsilon_v^p - \sigma_e\,dX_\Sigma = \left(2\,G\,X_\Sigma\,\hat{\mathbf{N}} - \kappa\,\boldsymbol{\delta}\right) : d\mathbf{E} \tag{5.68}$$

We continue with the calculation of $d\varepsilon_v^p$ in terms of $d\bar{\varepsilon}$ and dX_Σ

$$d\varepsilon_v^p = \Delta_v\, df = \Delta_v\, dc^{(4)} = \Delta_v\, c^{(3)} \left(A_f\, d\bar{\varepsilon}^{(3)} + B_f\, dX_\Sigma\right) = \Delta_v\, c^{(3)} \left(A_f\, \alpha^{(3)}\, d\bar{\varepsilon} + B_f\, dX_\Sigma\right) \Rightarrow$$
$$d\varepsilon_v^p = m\, d\bar{\varepsilon} + q\, dX_\Sigma\, H\left(dX_\Sigma\right) \qquad \Rightarrow \qquad m\, d\bar{\varepsilon} - d\varepsilon_v^p + q\, dX_\Sigma\, H\left(dX_\Sigma\right) = 0 \tag{5.69}$$

where

$$m = \Delta_v\, c^{(3)}\, \alpha^{(3)}\, A_f = m\left(c^{(3)}, \bar{\varepsilon}^{(3)}, \alpha^{(3)}, X_\Sigma\right) \tag{5.70}$$
$$q = \Delta_v\, c^{(3)}\, B_f = q\left(c^{(3)}, \bar{\varepsilon}^{p(3)}, X_\Sigma\right) \tag{5.71}$$

The yield condition

$$\Phi\left(\mathbf{s}, \bar{\varepsilon}^{(i)}, c^{(i)}\right) = \sigma_e\left(\mathbf{s}\right) - \tilde{\sigma}_0\left(\sigma_0^{(i)}\left(\bar{\varepsilon}^{(i)}\right), c^{(i)}\right) = 0 \tag{5.72}$$

is used for the determination of $\hat{\mathbf{C}}$ as follows

$$d\Phi = \hat{\mathbf{N}} : d\mathbf{s} - \sum_{i=1}^{4}\left(\frac{\partial\tilde{\sigma}_0}{\partial\bar{\varepsilon}^{(i)}}\, d\bar{\varepsilon}^{(i)} + \frac{\partial\tilde{\sigma}_0}{\partial c^{(i)}}\, dc^{(i)}\right) =$$
$$= 2\, G\, \hat{\mathbf{N}} : \left[d\mathbf{e} - \left(d\bar{\varepsilon} + \frac{A}{\Delta_v}\, d\varepsilon_v^p\right)\hat{\mathbf{N}}\right] - \sum_{i=1}^{4}\left(\frac{\partial\tilde{\sigma}_0}{\partial\sigma_0^{(i)}}\, h^{(i)} d\bar{\varepsilon}\, \alpha^{(i)} + \frac{\partial\tilde{\sigma}_0}{\partial c^{(i)}}\, d\varepsilon_v^p\, g^{(i)}\right) \qquad \Rightarrow$$
$$d\Phi = 2\, G\, \hat{\mathbf{N}} : d\mathbf{E} - 3\, G\left(d\bar{\varepsilon} + \frac{A}{\Delta_v}\, d\varepsilon_v^p\right) - d\bar{\varepsilon}\underbrace{\sum_{i=1}^{4}\left(\frac{\partial\tilde{\sigma}_0}{\partial\sigma_0^{(i)}} h^{(i)}\, \alpha^{(i)}\right)}_{H} - d\varepsilon_v^p\underbrace{\sum_{i=1}^{4}\left(\frac{\partial\tilde{\sigma}_0}{\partial c^{(i)}}\, g^{(i)}\right)}_{H_v} = 0 \Rightarrow$$
$$\Rightarrow \quad \left(3\, G + H\right) d\bar{\varepsilon} + \left(3\, G\frac{A}{\Delta_v} + H_v\right) d\varepsilon_v^p = 2\, G\, \hat{\mathbf{N}} : d\mathbf{E} \tag{5.73}$$

So equations (5.68), (5.69) and (5.73) can be written as follows

$$\begin{bmatrix} 3\, G\, X_\Sigma & 3\, G\, X_\Sigma \frac{A}{\Delta_v} - \kappa & -\sigma_e \\ m & -1 & q\, H\left(dX_\Sigma\right) \\ 3\, G + H & 3\, G\frac{A}{\Delta_v} + H_v & 0 \end{bmatrix} \begin{Bmatrix} d\bar{\varepsilon} \\ d\varepsilon_v^p \\ dX_\Sigma \end{Bmatrix} = \begin{Bmatrix} \left(2\, G\, X_\Sigma\, \hat{\mathbf{N}} - \kappa\, \boldsymbol{\delta}\right) : d\mathbf{E} \\ 0 \\ 2\, G\, \hat{\mathbf{N}} : d\mathbf{E} \end{Bmatrix}$$

$$\Rightarrow \begin{Bmatrix} d\bar{\varepsilon} \\ d\varepsilon_v^p \\ dX_\Sigma \end{Bmatrix} = \begin{Bmatrix} \left(a_1\, \hat{\mathbf{N}} + a_2\, \boldsymbol{\delta}\right) : d\mathbf{E} \\ \left(b_1\, \hat{\mathbf{N}} + b_2\, \boldsymbol{\delta}\right) : d\mathbf{E} \\ \left(c_1\, \hat{\mathbf{N}} + c_2\, \boldsymbol{\delta}\right) : d\mathbf{E} \end{Bmatrix} \tag{5.74}$$

$$d\bar{\varepsilon} = \left(a_1\, \hat{\mathbf{N}} + a_2\, \boldsymbol{\delta}\right) : d\mathbf{E}, \qquad d\varepsilon_v^p = \left(b_1\, \hat{\mathbf{N}} + b_2\, \boldsymbol{\delta}\right) : d\mathbf{E}, \qquad dX_\Sigma = \left(c_1\, \hat{\mathbf{N}} + c_2\, \boldsymbol{\delta}\right) : d\mathbf{E} \tag{5.75}$$

with

$$a_1 = \frac{2}{3\,D}\left[1 + q\frac{\kappa + X_\Sigma\, H_v}{\sigma_e}\, H\left(dX_\Sigma\right)\right], \qquad a_2 = -\frac{q}{D}\frac{\kappa}{\sigma_e}\left(\frac{A}{\Delta_v} + \frac{H_v}{3\,G}\right) H\left(dX_\Sigma\right),$$

$$b_1 = \frac{2}{3\,D}\left[m - q\, X_\Sigma \frac{H}{\sigma_e}\, H\left(dX_\Sigma\right)\right], \qquad b_2 = \frac{q}{D}\frac{\kappa}{\sigma_e}\left(1 + \frac{H}{3\,G}\right) H\left(dX_\Sigma\right),$$

$$c_1 = -\frac{2}{3\,D}\frac{1}{\sigma_e}\left[X_\Sigma\, H + m\left(\kappa + X_\Sigma\, H_v\right)\right], \qquad c_2 = \frac{1}{D}\frac{\kappa}{\sigma_e}\left[1 + \frac{H}{3\,G} + m\left(\frac{A}{\Delta_v} + \frac{H_v}{3\,G}\right)\right]$$

$$H = \sum_{i=1}^{4}\left(\frac{\partial\tilde{\sigma}_0}{\partial\sigma_0^{(i)}}\, h^{(i)}\, \alpha^{(i)}\right), \qquad H_v = \sum_{i=1}^{4}\left(\frac{\partial\tilde{\sigma}_0}{\partial c^{(i)}}\, g^{(i)}\right),$$

$$D = 1 + \frac{H}{3\,G} + m\left(\frac{A}{\Delta_v} + \frac{H_v}{3\,G}\right) + \frac{q}{\sigma_e}\left[\kappa\left(1 + \frac{H}{3\,G}\right) + X_\Sigma\left(H_v - \frac{A}{\Delta_v}H\right)\right] H\left(dX_\Sigma\right)$$

where

$$m = \Delta_v\, c^{(3)}\, \alpha^{(3)}\, A_f, \qquad q = \Delta_v\, c^{(3)}\, B_f$$

Therefore $d\mathbf{E}^{in}$ can be written in the following form

$$d\mathbf{E}^{in} = \left(d\bar{\varepsilon} + \frac{A}{\Delta_v}\, d\varepsilon_v^p\right)\hat{\mathbf{N}} + \frac{1}{3}\, d\varepsilon_v^p\, \boldsymbol{\delta} = \hat{\mathbf{N}}\left(d_1\,\hat{\mathbf{N}} + d_2\,\boldsymbol{\delta}\right) : d\mathbf{E} + \frac{1}{3}\boldsymbol{\delta}\left(b_1\,\hat{\mathbf{N}} + b_2\,\boldsymbol{\delta}\right) : d\mathbf{E} \;\Rightarrow$$

$$d\mathbf{E}^{in} = \left(d_1\,\hat{\mathbf{N}}\,\hat{\mathbf{N}} + d_2\,\hat{\mathbf{N}}\,\boldsymbol{\delta} + e_1\,\boldsymbol{\delta}\,\hat{\mathbf{N}} + e_2\,\boldsymbol{\delta}\,\boldsymbol{\delta}\right) : d\mathbf{E} \tag{5.76}$$

where

$$d_1 = a_1 + \frac{A}{\Delta_v}\, b_1, \qquad d_2 = a_2 + \frac{A}{\Delta_v}\, b_2, \qquad e_1 = \frac{1}{3}\, b_1, \qquad e_2 = \frac{1}{3}\, b_2$$

Finally, we substitute $d\mathbf{E}^{in}$ from (5.76) into (5.64) to derive

$$d\hat{\boldsymbol{\sigma}} = \boldsymbol{\mathcal{L}}^e : d\mathbf{E}^e = \boldsymbol{\mathcal{L}}^e : d\mathbf{E} - \boldsymbol{\mathcal{L}}^e : d\mathbf{E}^{in} = \boldsymbol{\mathcal{L}}^e : d\mathbf{E} - \left(2\,G\,\boldsymbol{\mathcal{K}} + 3\,\kappa\,\boldsymbol{\mathcal{J}}\right) : \left[\left(d\bar{\varepsilon} + \frac{A}{\Delta_v}\, d\varepsilon_v^p\right)\hat{\mathbf{N}} + \frac{1}{3}\, d\varepsilon_v^p\,\boldsymbol{\delta}\right]$$

$$= \boldsymbol{\mathcal{L}}^e : d\mathbf{E} - 2\,G\left(d\bar{\varepsilon} + \frac{A}{\Delta_v}\, d\varepsilon_v^p\right)\hat{\mathbf{N}} - \kappa\, d\varepsilon_v^p\,\boldsymbol{\delta}$$

$$= \boldsymbol{\mathcal{L}}^e : d\mathbf{E} - 2\,G\,\hat{\mathbf{N}}\left[\left(a_1\,\hat{\mathbf{N}} + a_2\,\boldsymbol{\delta}\right) : d\mathbf{E} + \frac{A}{\Delta_v}\left(b_1\,\hat{\mathbf{N}} + b_2\,\boldsymbol{\delta}\right) : d\mathbf{E}\right] - \kappa\,\boldsymbol{\delta}\left(b_1\,\hat{\mathbf{N}} + b_2\,\boldsymbol{\delta}\right) : d\mathbf{E}$$

$$\Rightarrow \qquad d\hat{\boldsymbol{\sigma}} = \left(2\,G\,\boldsymbol{\mathcal{K}} + 3\,\kappa\,\boldsymbol{\mathcal{J}} - f_1\hat{\mathbf{N}}\,\hat{\mathbf{N}} - f_2\,\hat{\mathbf{N}}\,\boldsymbol{\delta} - g_1\,\boldsymbol{\delta}\,\hat{\mathbf{N}} - g_2\,\boldsymbol{\delta}\,\boldsymbol{\delta}\right) : d\mathbf{E} \tag{5.77}$$

where

$$f_1 = 2\,G\left(a_1 + \frac{A}{\Delta_v}\, b_1\right), \qquad f_2 = 2\,G\left(a_2 + \frac{A}{\Delta_v}\, b_2\right), \qquad g_1 = \kappa\, b_1, \qquad g_2 = \kappa\, b_2$$

Therefore the linearization moduli are determined from

$$\hat{\mathbf{C}} = \left(2\,G\,\boldsymbol{\mathcal{K}} + 3\,\kappa\,\boldsymbol{\mathcal{J}} - f_1\hat{\mathbf{N}}\,\hat{\mathbf{N}} - f_2\,\hat{\mathbf{N}}\,\boldsymbol{\delta} - g_1\,\boldsymbol{\delta}\,\hat{\mathbf{N}} - g_2\,\boldsymbol{\delta}\,\boldsymbol{\delta}\right) \tag{5.78}$$

Finally, (5.61) yields

$$\mathbf{C} \simeq \left(2\,G\,\boldsymbol{\mathcal{K}} + 3\,\kappa\,\boldsymbol{\mathcal{J}} - f_1\mathbf{N}\,\mathbf{N} - f_2\,\mathbf{N}\,\boldsymbol{\delta} - g_1\,\boldsymbol{\delta}\,\mathbf{N} - g_2\,\boldsymbol{\delta}\,\boldsymbol{\delta}\right) \tag{5.79}$$

with

$$f_1 = 2\,G\left(a_1 + \frac{A}{\Delta_v}\, b_1\right), \qquad f_2 = 2\,G\left(a_2 + \frac{A}{\Delta_v}\, b_2\right), \qquad g_1 = \kappa\, b_1, \qquad g_2 = \kappa\, b_2$$

5.2.4 The role of UMAT(User MATerial subroutine)

As mentioned in the previous chapter, UMAT subroutines can be used with any ABAQUS procedure that includes mechanical behavior and are called by ABAQUS at every integration point of all elements for which the material definition includes a user-defined material behavior. The subroutine UMAT passes in all the information at the start of the increment, i.e., $\mathbf{F}_n$, $\boldsymbol{\sigma}_n$, $c_n^{(r)}$, $\bar{\varepsilon}_n^{(r)}$, as well as $\mathbf{F}_{n+1}$ and the user has to calculate the values of the corresponding quantities at the end of the increment, i.e., $\boldsymbol{\sigma}_{n+1}$, $c_{n+1}^{(r)}$ and $\bar{\varepsilon}_{n+1}^{(r)}$. The "linearization moduli" are also calculated in UMAT.

5.3 Computational model for plane stress

In this section the behavior of TRIP steels under plane stress conditions is analyzed. In this kind of problems, the out-of-plane strain components are not defined kinematically and the method described in the previous sections needs to be modified. Lets consider a thin plane disc of uniform thickness loaded in its plane. We consider that the $X_3 = 0$ plane coincides with the mean plane of the disc and the in-plane displacement field are of the form

$$u_1 = u_1\left(X_1, X_2\right) \qquad \text{and} \qquad u_2 = u_2\left(X_1, X_2\right). \tag{5.80}$$

In isotropic materials, the corresponding form of the deformation gradient and the stress tensor are

$$[F] = \begin{bmatrix} F_{11} & F_{12} & 0 \\ F_{21} & F_{22} & 0 \\ 0 & 0 & F_{33} \end{bmatrix} \qquad \text{and} \qquad [\sigma] = \begin{bmatrix} \sigma_{11} & \sigma_{12} & 0 \\ \sigma_{21} & \sigma_{22} & 0 \\ 0 & 0 & 0 \end{bmatrix}, \tag{5.81}$$

or in a more compact form

$$\mathbf{F} = F_{\alpha\beta}\,\mathbf{e}_\alpha\,\mathbf{e}_\beta + F_{33}\,\mathbf{e}_3\,\mathbf{e}_3 \qquad \text{and} \qquad \boldsymbol{\sigma} = \sigma_{\alpha\beta}\,\mathbf{e}_\alpha\,\mathbf{e}_\beta, \tag{5.82}$$

where Greek indices take values in the range $(1, 2)$.

The expression for the deformation gradient $[F]$ and equations (5.80) are consistent given that u_3 is a function only of X_3, i.e. $u_3 = u_3\left(X_3\right)$. Nonetheless, the out-of-plane displacement and the corresponding thickness variation, in finite strain problems, are functions of (X_1, X_2), when the in-plane displacement field is inhomogeneous. Thus, as the material deforms the plane stress conditions may not apply. Hutchinson et al. [28], Tvergaard [73] and Needleman and Tvergaard [44] studied under which conditions the plane stress assumption is valid. In this section we consider that, as the disk deforms, the thickness variation is negligible, so that the plane stress conditions apply and equations (5.80) and (5.81) hold to a good approximation.

In plane stress problems, the method described in section 5.2.2 needs to be modified since the out-of-plane component of the deformation gradient F_{33} is not defined kinematically. Therefore we decide to write the deformation gradient associated with the current increment

as follows

$$[\Delta F_{n+1}] = \begin{bmatrix} \Delta\bar{F}_{11} & \Delta\bar{F}_{12} & 0 \\ \Delta\bar{F}_{21} & \Delta\bar{F}_{22} & 0 \\ 0 & 0 & \Delta F_3 \end{bmatrix} \tag{5.83}$$

where $\Delta\bar{F}_{\alpha\beta}$ $\alpha, \beta = (1, 2)$ are the known in-plane components, and $\Delta F_3 = \lambda_3$ is the unknown out-of-plane component. Likewise, the right stretch tensor $[U_{n+1}]$ and the orthogonal tensor $[R_{n+1}]$ from the **Polar Decomposition** of $\mathbf{F}$ can be expressed as

$$[U_{n+1}] = \begin{bmatrix} \bar{U}_{11} & \bar{U}_{12} & 0 \\ \bar{U}_{21} & \bar{U}_{22} & 0 \\ 0 & 0 & \lambda_3 \end{bmatrix} \quad \text{and} \quad [R_{n+1}] = \begin{bmatrix} \cos\bar{\theta} & -\sin\bar{\theta} & 0 \\ \sin\bar{\theta} & \cos\bar{\theta} & 0 \\ 0 & 0 & 1 \end{bmatrix}, \tag{5.84}$$

and the logarithmic strain tensor $[\Delta E]$ can be written as

$$[\Delta E] = \begin{bmatrix} \Delta\bar{E}_{11} & \Delta\bar{E}_{12} & 0 \\ \Delta\bar{E}_{21} & \Delta\bar{E}_{22} & 0 \\ 0 & 0 & \Delta E_3 \end{bmatrix} \tag{5.85}$$

where bared quantities are known and $\Delta E_3 = \ln\lambda_3$ is the unknown out-of-plane component of $[\Delta E]$. As mentioned earlier, we note that the only difference with the method described in section 5.2.2 is that the values of ΔF_3 and therefore of ΔE_3 are unknown when the process of the numerical integration starts. The value of ΔE_3 is determined from the condition

$$\sigma_{33}|_{n+1} = \hat{\sigma}_{33}|_{n+1} = \mathbf{e}_3 \cdot \hat{\boldsymbol{\sigma}}_{n+1} \cdot \mathbf{e}_3 = 0 \tag{5.86}$$

where $\hat{\boldsymbol{\sigma}}_{n+1} = \mathbf{R}^T_{n+1} \cdot \boldsymbol{\sigma}_{n+1} \cdot \mathbf{R}_{n+1}$.
The logarithmic strain tensor can also be written as

$$\Delta\mathbf{E} = \Delta\bar{\mathbf{E}} + \Delta E_3\,\mathbf{a}, \quad \text{with} \quad \mathbf{a} = \mathbf{e}_3\,\mathbf{e}_3 = \mathbf{a}' + \frac{1}{3}\,\boldsymbol{\delta} \tag{5.87}$$

where $\Delta\bar{\mathbf{E}}$ is the known in-plane part of $\Delta\mathbf{E}$, and $\mathbf{a}'$ is the deviatoric part of $\mathbf{a}$:

$$\mathbf{a}' = \mathbf{a} - \frac{1}{3}\,a_{kk}\,\boldsymbol{\delta} = -\frac{1}{3}\,(\mathbf{e}_1\,\mathbf{e}_1 + \mathbf{e}_2\,\mathbf{e}_2 - 2\,\mathbf{e}_3\,\mathbf{e}_3) \tag{5.88}$$

5.3.1 Numerical integration of constitutive equations under plane stress conditions

Equations (5.35) - (5.42) are now written in the following form

$$\Delta\mathbf{E} = \Delta\mathbf{E}^e + \Delta\mathbf{E}^{in} \qquad \Rightarrow \qquad \Delta\mathbf{E}^e = \Delta\mathbf{E} - \Delta\mathbf{E}^{in}, \tag{5.89}$$

$$\begin{aligned} \hat{\boldsymbol{\sigma}}_{n+1} &= \boldsymbol{\sigma}_n + \boldsymbol{\mathcal{L}}^e : \left(\Delta\mathbf{E} - \Delta\mathbf{E}^{in}\right) = \boldsymbol{\sigma}_n + \boldsymbol{\mathcal{L}}^e : \left(\Delta\bar{\mathbf{E}} + \Delta E_3\,\mathbf{a} - \Delta\mathbf{E}^{in}\right) = \\ &= \bar{\boldsymbol{\sigma}}^e - \boldsymbol{\mathcal{L}}^e : \left(\Delta\mathbf{E}^{in} - \Delta E_3\,\mathbf{a}\right) \end{aligned} \tag{5.90}$$

$$\Delta\mathbf{E}^{in} = (\Delta\bar{\varepsilon} + A_{n+1}\,\Delta f)\,\hat{\mathbf{N}}_{n+1} + \frac{1}{3}\Delta\varepsilon^p_v\,\boldsymbol{\delta}, \tag{5.91}$$

with

$$\hat{\mathbf{N}}_{n+1} = \frac{3}{2\,\sigma_e|_{n+1}}\hat{\boldsymbol{\sigma}}_{n+1}, \qquad A_{n+1} = A_0 + A_1\frac{\sigma_e|_{n+1}}{s_a^*}, \qquad \Delta\varepsilon_v^p = \Delta_v\,\Delta f$$

$$\Delta\bar{\varepsilon}^{(i)} = \alpha_n^{(i)}\,\Delta\bar{\varepsilon} \tag{5.92}$$

$$\Delta f \;\; = c_n^{(3)}\left(A_f|_n\,\alpha_n^{(3)}\,\Delta\bar{\varepsilon} + B_f|_n\,\Delta X_\Sigma\right) \tag{5.93}$$

$$c_{n+1}^{(1)} = c_n^{(1)}\,\exp\left(-\Delta\varepsilon_v^p\right), \tag{5.94}$$

$$c_{n+1}^{(2)} = c_n^{(2)}\,\exp\left(-\Delta\varepsilon_v^p\right), \tag{5.95}$$

$$c_{n+1}^{(4)} = c_n^{(4)} + \frac{\Delta\varepsilon_v^p}{\Delta_v}, \tag{5.96}$$

$$c_{n+1}^{(3)} = 1 - \left(c_{n+1}^{(1)} + c_{n+1}^{(2)} + c_{n+1}^{(4)}\right) \tag{5.97}$$

where bared quantities are known and $\bar{\boldsymbol{\sigma}}^e = \boldsymbol{\sigma}_n + \boldsymbol{\mathcal{L}}^e : \Delta\bar{\mathbf{E}}$ is the"elastic predictor" that corresponds to the known part of $\Delta\mathbf{E}$. At this point, it should be noted the the elastic moduli $\boldsymbol{\mathcal{L}}^e$ used in the definition of $\bar{\boldsymbol{\sigma}}^e$ is the "full" elasticity tensor and not the plane stress moduli used in traditional small strain finite element analysis.
First, we calculate the deviatoric and spherical parts of $\hat{\boldsymbol{\sigma}}_{n+1}$:

$$\hat{\mathbf{s}}_{n+1} = \bar{\mathbf{s}}^e - 2\,G\left[\left(\Delta\mathbf{E}^{in}\right)' - \Delta E_3\,\mathbf{a}'\right] \tag{5.98}$$

$$p_{n+1} = \frac{1}{3}\,\hat{\boldsymbol{\sigma}}_{n+1} : \boldsymbol{\delta} = \bar{p}^e - \kappa\left(\Delta E_{kk}^{in} - \Delta E_3\right) \tag{5.99}$$

Combining equations (5.91), (5.98) and (5.99) we derive

$$\hat{\mathbf{s}}_{n+1} = \bar{\boldsymbol{\sigma}}^e - 2\,G\left[\left(\Delta\bar{\varepsilon} + A_{n+1}\,\Delta f\right)\mathbf{N}_{n+1} - \Delta E_3\,\mathbf{a}'\right] \tag{5.100}$$

$$p_{n+1} = \bar{p}^e - \kappa\left(\Delta\varepsilon_v^p - \Delta E_3\right) \tag{5.101}$$

Next, substituting $\hat{\mathbf{N}}_{n+1} = \frac{3}{2\,\sigma_e|_{n+1}}\,\hat{\boldsymbol{\sigma}}_{n+1}$ into (5.100) and solving for $\hat{\mathbf{s}}_{n+1}$ we find that $\hat{\mathbf{s}}_{n+1}$ and $\bar{\mathbf{s}}^e$ are not co - linear:

$$\hat{\mathbf{s}}_{n+1} = \frac{\bar{\mathbf{s}}^e + 2\,G\,\Delta E_3\,\mathbf{a}'}{1 + \frac{3\,G}{\sigma_e|_{n+1}}\left[\Delta\bar{\varepsilon} + \left(A_0 + A_1\frac{\sigma_e|_{n+1}}{s_a^*}\right)\frac{\Delta\varepsilon_v^p}{\Delta_v}\right]} \tag{5.102}$$

Finally, we calculate $\sigma_e|_{n+1}$ from equation (5.102):

$$\left(\sigma_e|_{n+1}\right)^2 = \frac{3}{2}\,\hat{\mathbf{s}}_{n+1} : \hat{\mathbf{s}}_{n+1} = \frac{3}{2}\frac{\left(\bar{\mathbf{s}}^e + 2\,G\,\Delta E_3\,\mathbf{a}'\right) : \left(\bar{\mathbf{s}}^e + 2\,G\,\Delta E_3\,\mathbf{a}'\right)}{\left[1 + \frac{3\,G}{\sigma_e|_{n+1}}\left(\Delta\bar{\varepsilon} + A_{n+1}\,\Delta f\right)\right]^2} \tag{5.103}$$

Thus, substituting $\bar{\mathbf{s}}^e : \bar{\mathbf{s}}^e = \frac{2}{3}\,\sigma_e^e$, $\bar{\mathbf{s}}^e : \mathbf{a}' = \bar{\mathbf{s}}^e : \mathbf{a} = \bar{s}_{33}^e$ and $\mathbf{a}' : \mathbf{a}' = \frac{2}{3}$ into the last equation we derive

$$\left(\sigma_e|_{n+1}\right)^2 = \frac{1}{\left[1 + \frac{3\,G}{\sigma_e|_{n+1}}\left(\Delta\bar{\varepsilon} + A_{n+1}\,\Delta f\right)\right]^2}\left(\bar{\sigma}_e^{e2} + 6\,G\,\Delta E_3\,\bar{s}_{33}^e + 4\,G^2\,\Delta E_3^2\right) \tag{5.104}$$

which can be solved for $\sigma_e|_{n+1}$:

$$\sigma_e|_{n+1} = \frac{G}{1 + \frac{3\,G}{s_a^*}\frac{A_1}{\Delta_v}\Delta\varepsilon_v^p}\left[F\left(\Delta E_3\right) - 3\left(\Delta\bar{\varepsilon} + \frac{A_0}{\Delta_v}\Delta\varepsilon_v^p\right)\right] \tag{5.105}$$

where

$$F\left(\Delta E_3\right) = \sqrt{\left(\frac{\bar{\sigma}_e^e}{G}\right)^2 + 6\frac{\bar{s}_{33}^e}{G}\Delta E_3 + 4\,\Delta E_3^2}$$

In order to determine the value of ΔE_3 we use the plane stress condition $\sigma_{33}|_{n+1} = s_{33}|_{n+1} + p_{n+1} = 0$ which, taking into account equations (5.102) and (5.101), yields

$$\frac{\bar{s}_{33}^e + \frac{4}{3}G\,\Delta E_3}{1 + \frac{3\,G}{\sigma_e|_{n+1}}\left[\Delta\bar{\varepsilon} + \left(A_0 + A_1\frac{\sigma_e|_{n+1}}{s_a^*}\right)\frac{\Delta\varepsilon_v^p}{\Delta_v}\right]} + p_{n+1} = 0 \tag{5.106}$$

To recapitulate, now we choose $\Delta\bar{\varepsilon}$, $\Delta\varepsilon_v^p$ and ΔE_3 as the basic unknowns and we have the following 3 equations (in contradiction with section 5.2.2 where we have 2 unknowns and 2 equations):

$$F_1 = \sigma_e|_{n+1} - \tilde{\sigma}_0\left(c_{n+1}^{(i)}, \bar{\varepsilon}_{n+1}^{(i)}\right) = 0 \tag{5.107}$$

$$F_2 = \Delta\varepsilon_v^p - \Delta_v\, c_n^{(3)}\left(A_f|_n\,\alpha_n^{(3)}\,\Delta\bar{\varepsilon} + B_f|_n\,\Delta X_\Sigma\right) = 0 \tag{5.108}$$

$$F_3 = \bar{s}_{33}^e + \frac{4}{3}G\,\Delta E_3 + \left\{1 + 3\,G\left[\frac{\Delta\bar{\varepsilon}}{\sigma_e|_{n+1}} + \left(\frac{A_0}{\sigma_e|_{n+1}} + \frac{A_1}{s_a^*}\right)\frac{\Delta\varepsilon_v^p}{\Delta_v}\right]\right\}p_{n+1} = 0 \tag{5.109}$$

Newton's method is used for the solution of the system. Details on the calculation of the Jacobian of the Newton loop are given in Appendix IV.
As soon as, the values of $\Delta\bar{\varepsilon}$, $\Delta\varepsilon_v^p$ and ΔE_3 are determined, we use equations (5.105), (5.101), (5.94), (5.95), (5.96) and (5.97) to define $\sigma_e|_{n+1}$, p_{n+1}, $c_{n+1}^{(1)}$, $c_{n+1}^{(2)}$, $c_{n+1}^{(a)}$ and $c_{n+1}^{(m)}$. Finally, the integration process is completed with the calculation of $\boldsymbol{\sigma}_{n+1}$

$$\boldsymbol{\sigma}_{n+1} = \mathbf{R}_{n+1}\cdot\hat{\boldsymbol{\sigma}}_{n+1}\cdot\mathbf{R}_{n+1}^T. \tag{5.110}$$

5.3.2 The linearization moduli under plane stress conditions

The linearization moduli which are required in the finite element method, were determined in section 5.2.3 as

$$\mathbf{C} = \left(2\,G\,\boldsymbol{\mathcal{K}} + 3\,\kappa\,\boldsymbol{\mathcal{J}} - f_1\mathbf{N}\,\mathbf{N} - f_2\,\mathbf{N}\,\boldsymbol{\delta} - g_1\,\boldsymbol{\delta}\,\mathbf{N} - g_2\,\boldsymbol{\delta}\,\boldsymbol{\delta}\right) \tag{5.111}$$

with

$$f_1 = 2\,G\left(a_1 + \frac{A}{\Delta_v}\,b_1\right), \qquad f_2 = 2\,G\left(a_2 + \frac{A}{\Delta_v}\,b_2\right), \qquad g_1 = \kappa\,b_1, \qquad g_2 = \kappa\,b_2$$

In plane strain problems, we can write the equation $d\boldsymbol{\sigma} = \mathbf{C} : d\mathbf{E}$ in matrix form

$$\left\{ \begin{array}{c} d\sigma_{11} \\ d\sigma_{22} \\ d\sigma_{33} \\ d\sigma_{12} \end{array} \right\} = \left[\begin{array}{cccc} C_{11} & C_{12} & C_{13} & C_{14} \\ C_{21} & C_{22} & C_{23} & C_{24} \\ C_{31} & C_{32} & C_{33} & C_{34} \\ C_{41} & C_{42} & C_{43} & C_{44} \end{array} \right] \left\{ \begin{array}{c} dE_{11} \\ dE_{22} \\ dE_{33} \\ 2\,dE_{12} \end{array} \right\} \tag{5.112}$$

but in plane stress problems, the linearization moduli $\bar{\mathbf{C}}$ used in ABAQUS needs to be of the form

$$\left\{ \begin{array}{c} d\sigma_{11} \\ d\sigma_{22} \\ d\sigma_{12} \end{array} \right\} = \left[\begin{array}{ccc} \bar{C}_{11} & \bar{C}_{12} & \bar{C}_{13} \\ \bar{C}_{21} & \bar{C}_{22} & \bar{C}_{23} \\ \bar{C}_{31} & \bar{C}_{32} & \bar{C}_{33} \end{array} \right] \left\{ \begin{array}{c} dE_{11} \\ dE_{22} \\ 2\,dE_{12} \end{array} \right\} \tag{5.113}$$

This form can be derived from equation (5.112) using the plane stress condition $\sigma_{33} = 0$. The plane stress condition also suggests that $d\sigma_{33} = 0$ or

$$C_{31}\,dE_{11} + C_{32}\,dE_{22} + C_{33}\,dE_{33} + 2\,C_{34}\,dE_{12} = 0 \tag{5.114}$$

which can be solved for dE_{33}:

$$dE_{33} = -\frac{1}{C_{33}}\left(C_{31}\,dE_{11} + C_{32}\,dE_{22} + 2\,C_{34}\,dE_{12}\right) \tag{5.115}$$

Thus, combining the last equation and equation (5.112) after some calculations we derive

$$\bar{C}_{11} = C_{11} - \frac{C_{13}}{C_{33}}\,C_{31}, \qquad \bar{C}_{12} = C_{12} - \frac{C_{13}}{C_{33}}\,C_{32}, \qquad \bar{C}_{13} = C_{14} - \frac{C_{13}}{C_{33}}\,C_{34} \tag{5.116}$$

$$\bar{C}_{21} = C_{21} - \frac{C_{23}}{C_{33}}\,C_{31}, \qquad \bar{C}_{22} = C_{22} - \frac{C_{23}}{C_{33}}\,C_{32}, \qquad \bar{C}_{23} = C_{24} - \frac{C_{23}}{C_{33}}\,C_{34} \tag{5.117}$$

$$\bar{C}_{31} = C_{41} - \frac{C_{43}}{C_{33}}\,C_{31}, \qquad \bar{C}_{32} = C_{42} - \frac{C_{43}}{C_{33}}\,C_{32}, \qquad \bar{C}_{33} = C_{44} - \frac{C_{43}}{C_{33}}\,C_{34} \tag{5.118}$$

For instance,

$$\begin{aligned} d\sigma_{11} &= C_{11}\,dE_{11} + C_{12}\,dE_{22} + C_{13}\,dE_{33} + 2\,C_{14}\,dE_{12} \\ &= C_{11}\,dE_{11} + C_{12}\,dE_{22} - \frac{C_{13}}{C_{33}}\left(C_{31}\,dE_{11} + C_{32}\,dE_{22} + 2\,C_{34}\,dE_{12}\right) + 2\,C_{14}\,dE_{12} \\ &= \left(C_{11} - \frac{C_{13}}{C_{33}}\,C_{31}\right) dE_{11} + \left(C_{12} - \frac{C_{13}}{C_{33}}\,C_{32}\right) dE_{22} + \left(C_{14} - \frac{C_{13}}{C_{33}}\,C_{34}\right) 2\,dE_{12} \end{aligned} \tag{5.119}$$

which indicates (5.116).

5.4 Calibration of the model

The constitutive model for the TRIP steel, which was presented in the previous sections, is now implemented into the ABAQUS through the subroutine UMAT in order to be calibrated.

However, before proceeding with the calibration of the model we need to determine the hardening behavior of the constituent phases. It should be emphasized that in addition to the mechanical behavior of TRIP steels, the $f-\varepsilon$ behavior is also highly influenced by the hardening of the constituent phases. In order to model the hardening behavior we use expressions of the following form

$$\sigma_y^{(r)} = H^{(r)}\left(\bar{\varepsilon}^{(r)}\right) \tag{5.120}$$

where r denotes the number of the phase, $\sigma_y^{(r)}$ the yield stress, $\bar{\varepsilon}^{(r)}$ the equivalent plastic strain and $H^{(r)}$ is the hardening expression. As mentioned earlier the labels used for the constituent phases are (1) for ferrite, (2) for bainite, (3) or (a) for retained austenite and (4) or (m) for martensite.

The hardening behavior of the phases is determined through a detailed bibliographic research. To elaborate, the hardening behavior of the ferrite, the bainite and the martensite were acquired from experimental data presented in Technical steel research [72]. In particular, for the ferritic phase we used the data of the annealed ferritic steel DOCOL 600, for the martensitic phase we used the data of the partly martensitic steel DOCOL 1400 (volume fraction of martensite 95%) and for the bainitic phase, the data from tensile tests performed in a 0.5% C steel subjected to thermal treatment in the range of bainite formation (coiling temperature of 950^{o}C). The chemical composition of ferritic steel DOCOL 600 and martensitic steel DOCOL 1400 are presented in Table 5.1.

The final step, following the intercritical annealing, in the production of TRIP steels, is isothermal holding in the bainite transformation range. During the formation of bainitic ferrite, carbon is rejected to the retained austenite. The carbon content of the retained austenite is raised to values above 1wt% [6], which, apart from chemical stabilization, raises its yield strength considerably. Values in the range of 500-550 MPa have been reported ([61],[78]). Thus the stress-strain curve of retained austenite lies above that of ferrite, which because of its very low carbon content, exhibits a lower yield strength.

Therefore, the hardening behavior for each phase at 23^{o}C is given by the following expressions (where $\sigma_y^{(r)}$ in MPa):

$$\sigma_y^{(1)} = 260\left(1+\frac{\bar{\varepsilon}}{0.0042}\right)^{\frac{1}{4.25}} \tag{5.121}$$

$$\sigma_y^{(2)} = 825\left(1+\frac{\bar{\varepsilon}}{0.0104}\right)^{\frac{1}{10.36}} \tag{5.122}$$

$$\sigma_y^{(a)} = 550\left(1+\frac{\bar{\varepsilon}}{0.1}\right)^{\frac{1}{4.2}} \tag{5.123}$$

$$\sigma_y^{(m)} = 1132\left(1+\frac{\bar{\varepsilon}}{0.0004}\right)^{\frac{1}{16.65}} \tag{5.124}$$

The hardening curves of the individual phases of the TRIP steel are acquired for the temperature of 23^{o}C due to the fact that the experimental data which will be used for the comparison with the FEM model are obtained in this temperature. Figure 5.1 illustrates the corresponding hardening curves.

Having determined the hardening behavior of the individual phases of the TRIP steel, we now proceed with the calibration of the model. For the calibration are used experimental data from interrupted tensile tests in a specific TRIP steel, the chemical composition of which is given in Table 5.2. Details on the experiments are given in Papatriantafillou [46].

The experimental steel, consists of 50% ferrite, 38% bainite and 12% retained austenite and

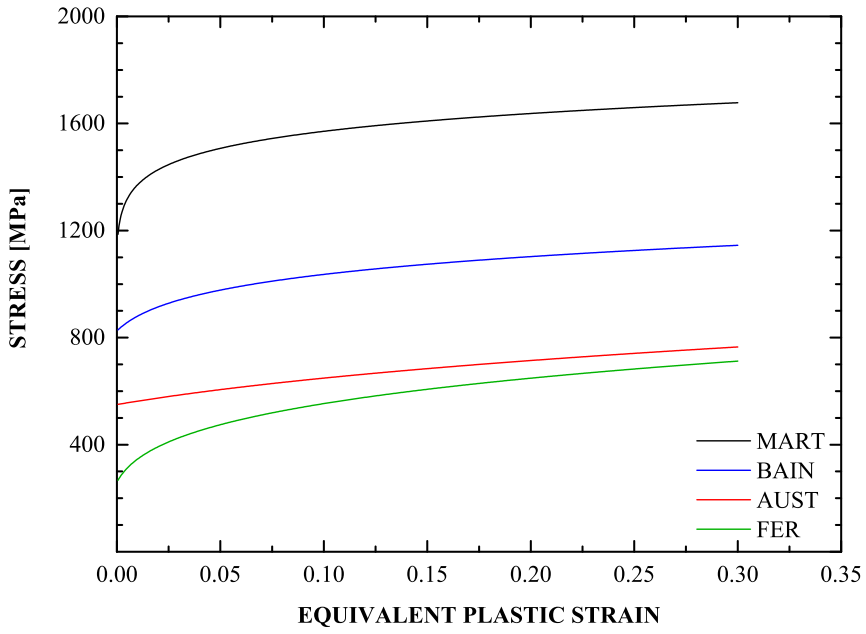

Figure 5.1: Hardening behavior of individual phases for the four-phase TRIP steel

STEEL	C	Mn	Si	Al	P	S	N	Cu	V
DOCOL 600	0.148	0.746	0.196	0.045	0.052	0.003	-	-	-
DOCOL 1400	0.170	1.590	0.500	0.046	0.010	0.001	0.006	0.010	0.010

Table 5.1: Chemical compositions of steels DOCOL 1400 and DOCOL 600 (wt%).

C	Mn	Si	Al	P
0.20	1.40	0.50	0.75	0.04

Table 5.2: Chemical composition of experimental TRIP steel (wt%).

the austenite gradually transforms into martensite as the material deforms plastically. At this point it should be noted that the tensile tests were interrupted at different stages of the deformation in order to measure the amount of martensite. The constitutive model developed in the present thesis, takes into account only the plastic *strain-induced* transformation mechanism, therefore at zero plastic strain the amount of martensite should be equal with the initial volume fraction (which is zero in the present case). However, due to the *stress-assisted* transformation mechanism the experimental data show an amount of martensite when the plastic strain is zero. Thus, in our calculations we consider that the initial volume fraction of the martensite does not equal zero. In particular, based on the experimental data, we use the following initial volume fractions for the individual phases: $c_0^{(1)} = 0.50$, $c_0^{(2)} = 0.38$, $c_0^{(m)} = 0.017$ and $c_0^{(a)} = 0.12 - c_0^{(m)} = 0.103$.

In order to calibrate the model, one-element finite element calculations for the problem of uniaxial tension were carried out. The corresponding uniform stress state in the element

is calculated by using the algorithm presented in section 5.2.2. The uniaxial tension problem is solved in ABAQUS by using one four-node isoparametric axisymmetric finite element (CAX4H in ABAQUS). The problem is solved incrementally and the end displacement is increased gradually until a final elongation of 30% is reached.
In the calculations we use the values $E = 220$ GPa and $\nu = 0.3$ for the elastic Young's modulus and Poisson's ratio, the values $M_{d,ut} = 80°\text{C}$ and $M^{\sigma}_{s,ut} = 15°\text{C}$, $T = 23°\text{C}$ and the relative volume change associated with the martensitic transformation is taken to be $\Delta_v = 0.02$.
The values of the parameters that enter the transformation kinetics model are chosen so that the predictions of the model agree with the $f - \varepsilon$ curves determined experimentally, where ε is the axial nominal strain. These values are shown in Table 5.3.

r	g_0	g_1	g_2	$\bar{g}$	s_g	A_0	A_1	s^*_a (MPa)	α	β_0
2	3400	4.7	493	3230	292	0.012	0.057	496	11.0	1.7

Table 5.3: Costants of the kinetic model used to fit the experimental data.

Figures 5.2, 5.3 and 5.4 display the predicted $f - \varepsilon$, $c^{(a)} - \varepsilon$ and $\sigma - \varepsilon$ curves together with the experimental data, where σ is the nominal stress. The model predictions fit the data reasonably well.

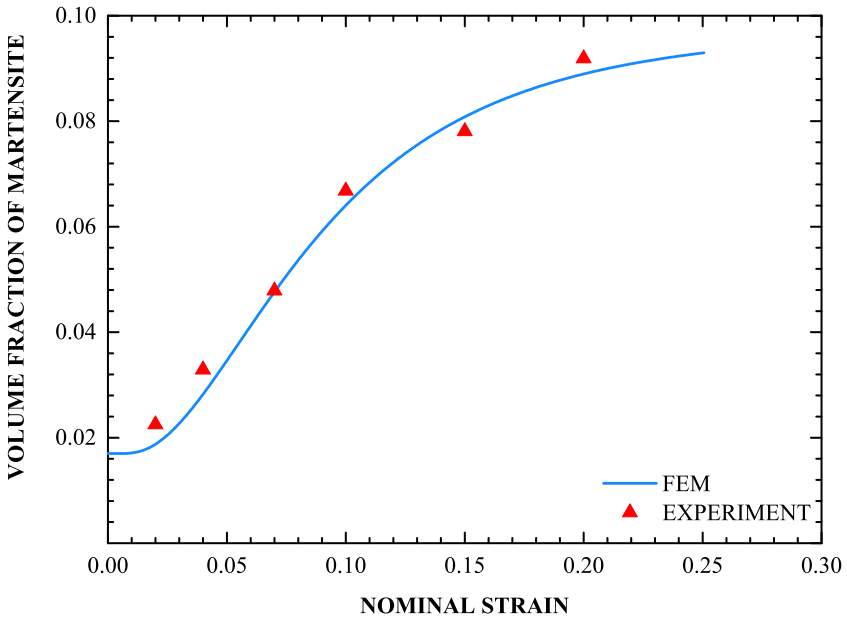

Figure 5.2: Predicted $f - \varepsilon$ curve together with the experimental data (red triangles).

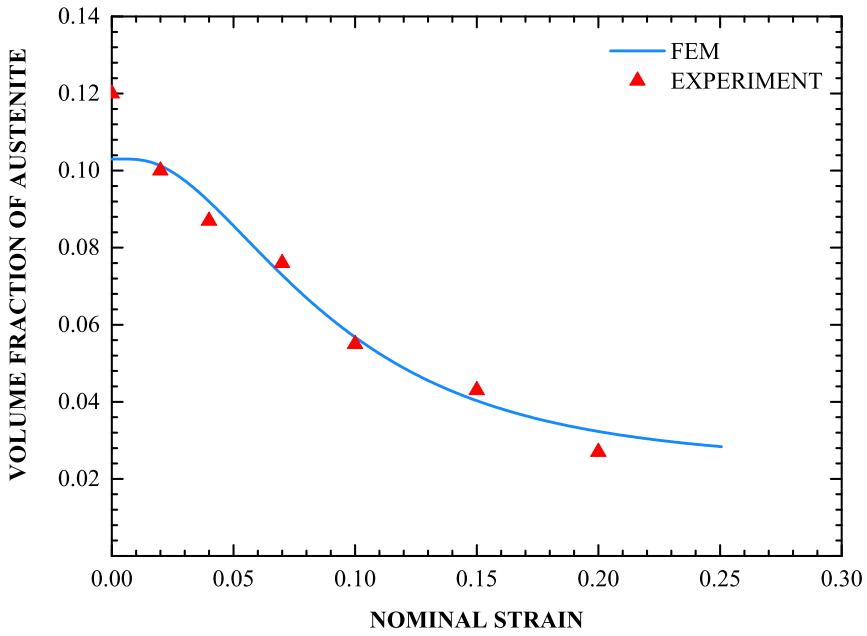

Figure 5.3: Predicted $c^{(a)} - \varepsilon$ curve together with the experimental data (red triangles).

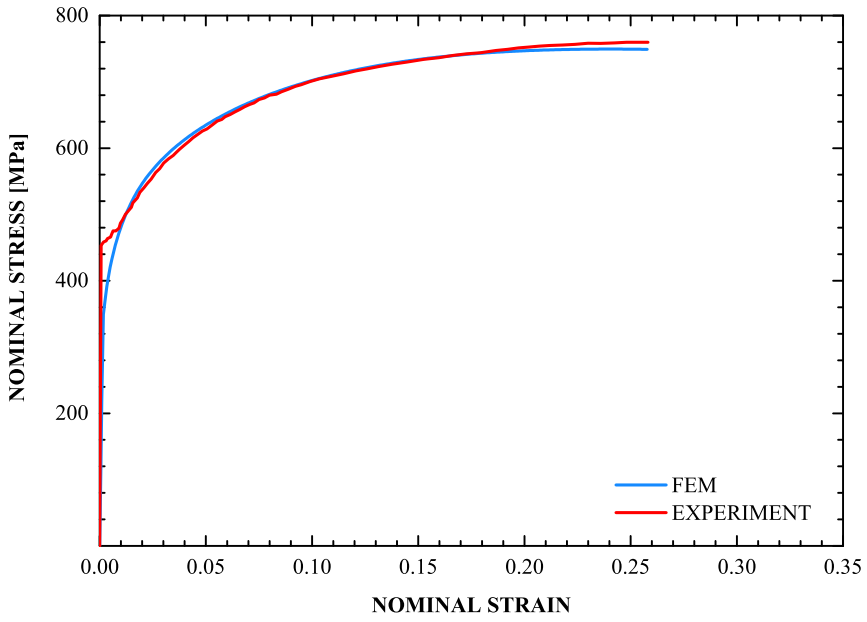

Figure 5.4: Predicted $\sigma - \varepsilon$ curve (blue line) together with the experimental data (red line).

5.5 Necking bifurcation

In this section, we use the constitutive model developed for the four-phase TRIP steel to study the development of a neck in a tension specimen in which a geometric imperfection is introduced. The calculations are carried out for both uniaxial and plane strain tension. In a separate set of calculations the same problem is studied for a non-transforming TRIP steel with the same initial values of the volume fractions of the four phases.

5.5.1 Necking in uniaxial tension

First, we examine the problem in uniaxial tension. Lets consider a cylindrical specimen with aspect ratio $L_0/R_0 = 3$, where $2\,L_0$ is its initial length and R_0 its initial radius (see Figure 5.5). The cylindrical system depicted in Figure 5.6 is introduced and each material particle in the specimen is identified by its position vector $\mathbf{X} = (r, z)$ in the undeformed configuration. We are interested in symmetric solutions and consider, only one quarter of the full cylinder, as shown in Figure 5.6. The analyses are carried out by using the finite element method. Figure 5.6 illustrates the finite element mesh used in the calculations ; it consists of 1350 four-node isoparametric axisymmetric elements (CAX4H in ABAQUS) in a 15×90 grid. As mentioned earlier, in order to encourage necking, we introduce a geometric imperfection in the undeformed configuration. In particular the initial radius of the specimen is assumed to vary in the z direction according to the formula (see Figure 5.7):

$$R\,(z) = R_0 - \xi R_0 \cos \frac{\pi z}{2\,L_0} \tag{5.125}$$

where we use the value $\xi = 0.005$. In this case the neck develops gradually.

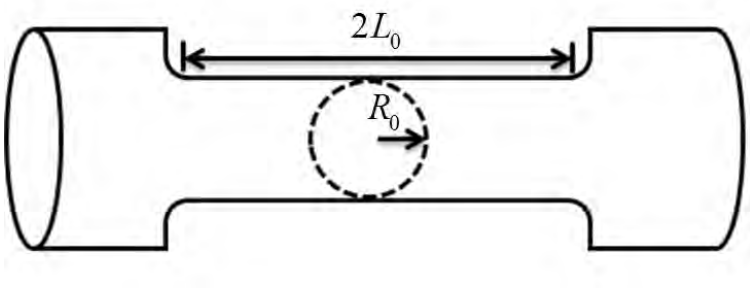

Figure 5.5: The cylindrical specimen analyzed.

We constrain all nodes along the midplane $z = 0$ to move only in the radial direction, and all nodes along the pole ($z-$axis) to have zero radial displacement. Figure 5.6 displays a schematic representation of the boundary conditions.
The deformation is driven by the uniform prescribed end displacement in the z-direction on the shear free end $z = L_0$; the lateral surface on $r = R_0$ is kept traction free. The initial values of the volume fractions of the constituent phases are: $c^{(1)} = 0.50$, $c^{(2)} = 0.38$, $c^{(a)} = 0.103$ and $c^{(m)} = 0.017$. The curves $\sigma_y^{(r)}, r = 1, 4$ that define the variation of the flow stress of the phases and the material data used in the calculations are those presented in section 5.4.
First, a 'perfect' specimen is analyzed in order to obtain the uniform solution. The analysis is conducted with one four-node isoparametric axisymmetric element (one-element test). Figure 5.8 illustrates the calculated $\sigma - \varepsilon$ curve for the transforming TRIP steel for the necking problem together with the corresponding uniform solution.
Calculations are also conducted for a non-transforming TRIP steel with the same initial values of the volume fractions of the four phases.

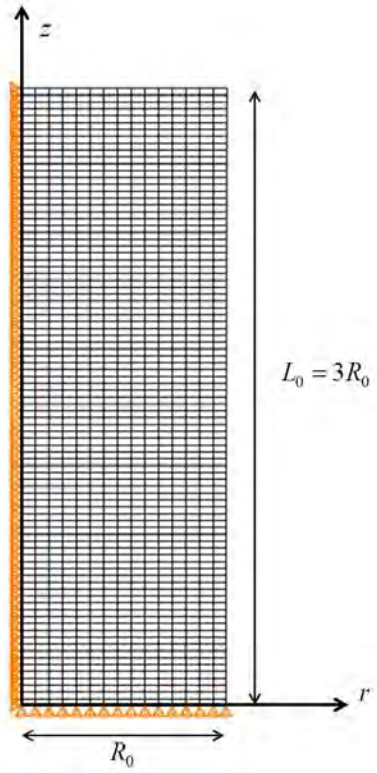

Figure 5.6: The finite element model used for the analysis and a schematic representation of the boundary conditions imposed.

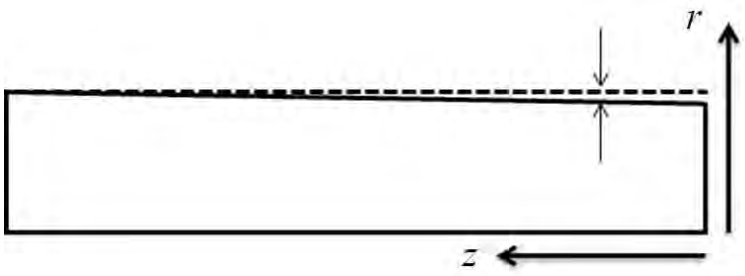

Figure 5.7: Schematic representation of the geometric imperfection.

Figure 5.9 illustrates the $\sigma - \varepsilon$ curves for both a transforming and a non-transforming steel. The arrows on the curves hint the point of maximum load, which co-occurs with the end of uniform elongation of the specimen. For the transforming (TRIP) steel we notice the end of uniform elongation at a nominal strain of 22.7% and 746 MPa stress, while for the non-transforming steel at 19.9% and 714 MPa. Figure 5.9 proves that the TRIP phenomenon in addition to hardening the material, increases considerably the range of uniform elongation as well.

Figure 5.10 depicts the evolution of the radius at the minimum cross section of the specimen for the transforming and non-transforming materials and Figure 5.11 shows the deformed

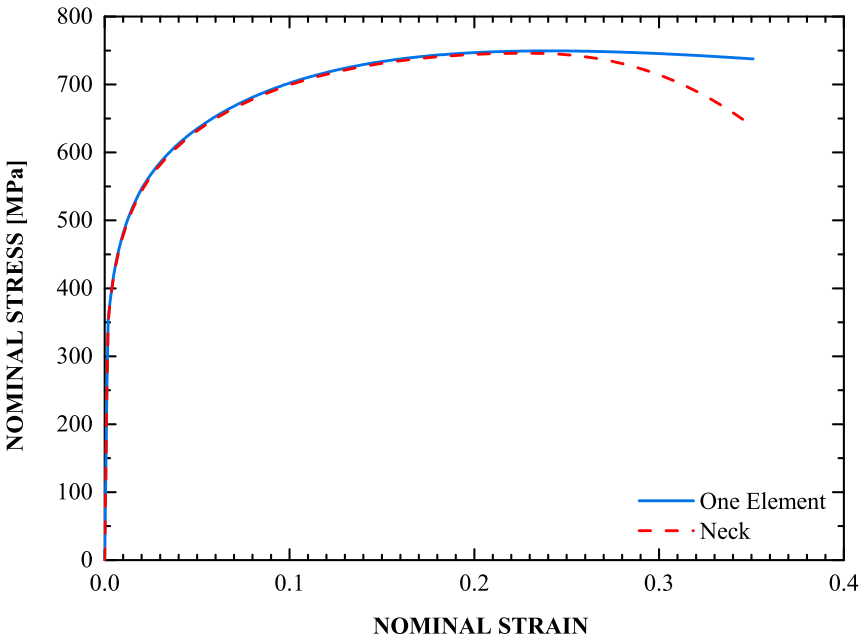

Figure 5.8: Stress-strain curves for the transforming TRIP steel predicted by a necking analysis and the corresponding uniform solution.

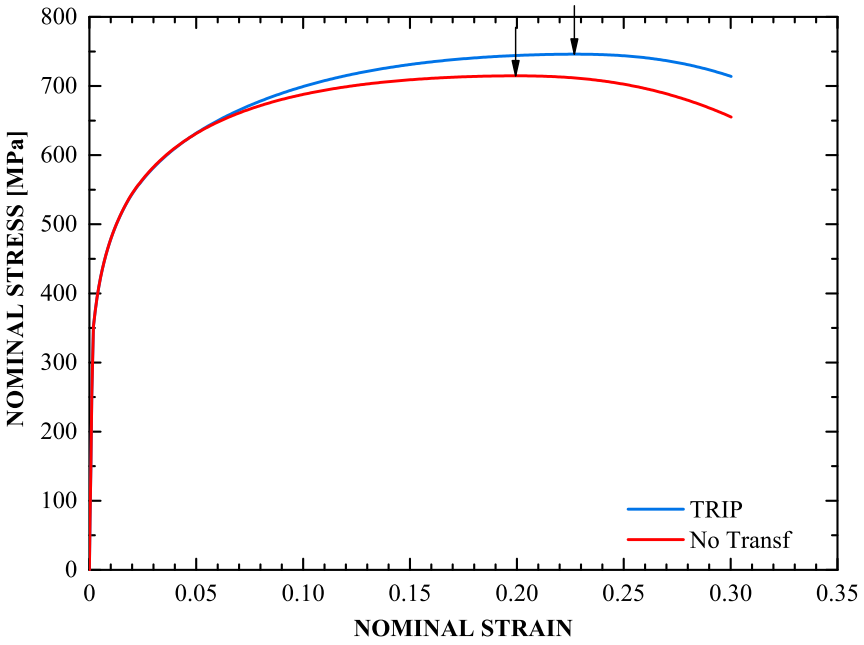

Figure 5.9: Stress-strain curves for a TRIP steel and a non-transforming steel. The arrows indicate the position of the maximum load.

configurations. We should note that at a nominal strain of 40%, the minimum cross section of the non-transforming material contracts 49.2%; whereas of the TRIP steel contracts 42.4%. Therefore, we conclude that the formation of martensite stabilizes the neck and leads to its propagation down the length of the specimen. This result was also presented by

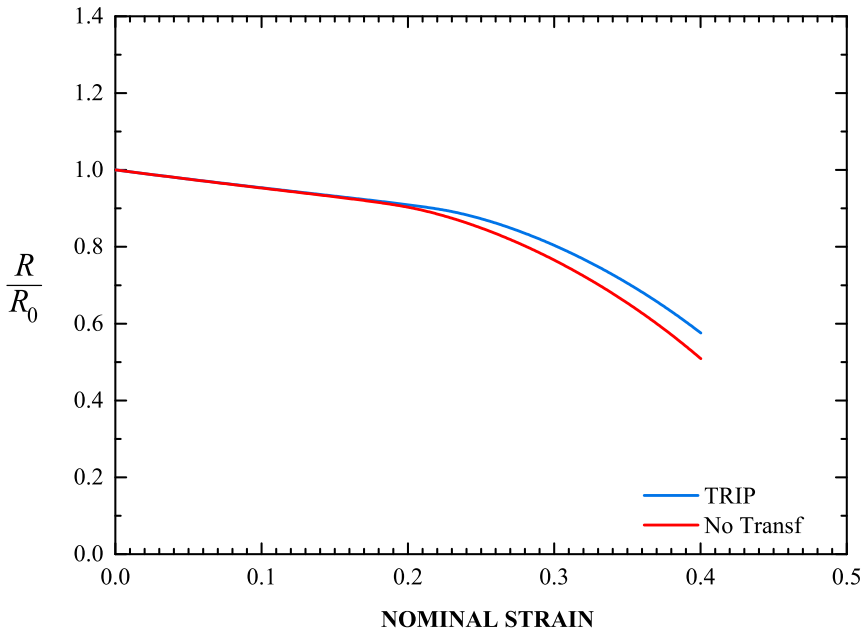

Figure 5.10: Evolution of the radius at the minimum cross section of the specimen for a TRIP steel and a non-transforming steel.

Papatriantafillou *et al.* [47], who used a rate dependent constitutive model for TRIP steels (as opposed to the rate independent model used here).

Figures 5.12 and 5.13 illustrate contours of the hydrostatic stress $p = \sigma_{kk}/3$ and of the

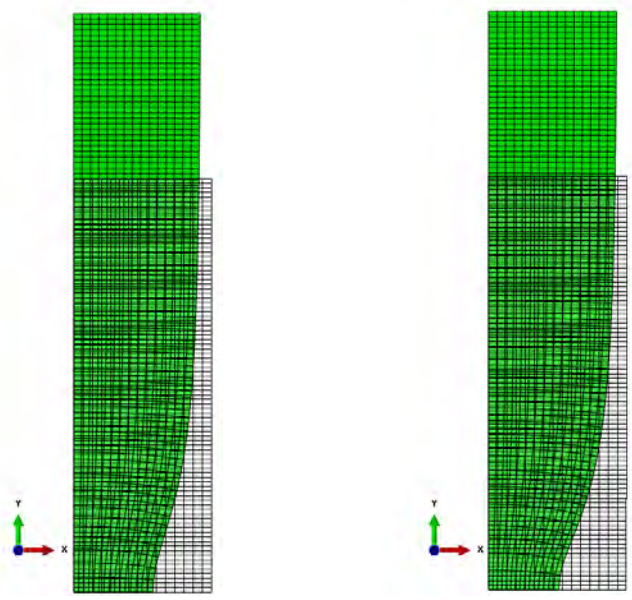

(a) (b)

Figure 5.11: Deformed configurations for a nominal strain of 40%: (a) transforming , (b) non-transforming steel.

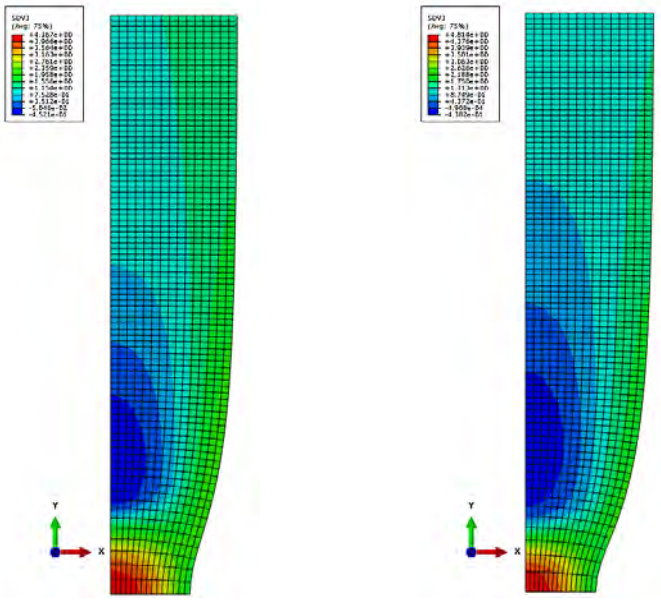

(a) (b)

Figure 5.12: Contours of hydrostatic stress $p = \sigma_{kk}/3$ for a nominal strain of 40%: (a) transforming , (b) non-transforming steel.

triaxiality ratio $X_\Sigma = p/\sigma_e$ for the transforming and non-transforming materials at a nominal strain of 40%. These two figures are similar to each other; both the hydrostatic stress and the triaxiality ratio take higher values in the non-transforming steel. In particular, $X_{\Sigma\,\max} \cong 0.818$ for the transforming and $X_{\Sigma\,\max} \cong 0.913$ for the non-transforming steel at a nominal strain of 40%; the maximum X_Σ value occurs at the center of the neck. On the other hand, in the case of uniform elongation, the triaxility ratio remains constant everywhere: $X_\Sigma = 1/3 = 0.333$.

As mentioned above, the hydrostatic stress p at the center of the neck is higher in the non-transforming specimen. This can be explained if we take into account that the reduction of the minimum cross section is higher in the non-transforming steel resulting in a higher level of hydrostatic stress (Bridgman [9]). The lower value of the triaxiality ratio $X_\Sigma = p/\sigma_e$ at the center of the TRIP specimen can also be explained. This is due to the fact that p is lower at the center of the TRIP specimen and simultaneously the transformation of austenite to martensite leads to a higher σ_e.

Last but not least, Figures 5.16 and 5.15 display contours of the volume fraction of the individual phases $c^{(r)}$ and the corresponding equivalent plastic strains $\bar{\varepsilon}^{(r)}$ for the transforming steel, at a nominal strain of 40%.

The formation of the neck, as we can see in Figure 5.15, is accompanied by a concentration of strain and a raise in triaxiality (Figure 5.13) at the center of the neck. Thus, the increased triaxiality at the neck leads to an enhanced driving force for transformation, which, in turn, causes higher levels of volume fraction of martensite in that region (Figure 5.16).

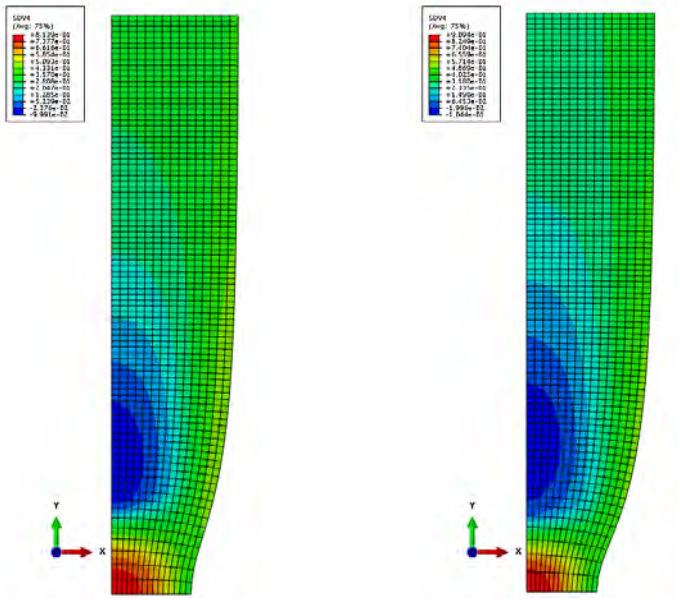

(a) (b)

Figure 5.13: Contours of triaxiality ratio $X_\Sigma = p/\sigma_e$ for a nominal strain of 40%: (a) transforming , (b) non-transforming steel.

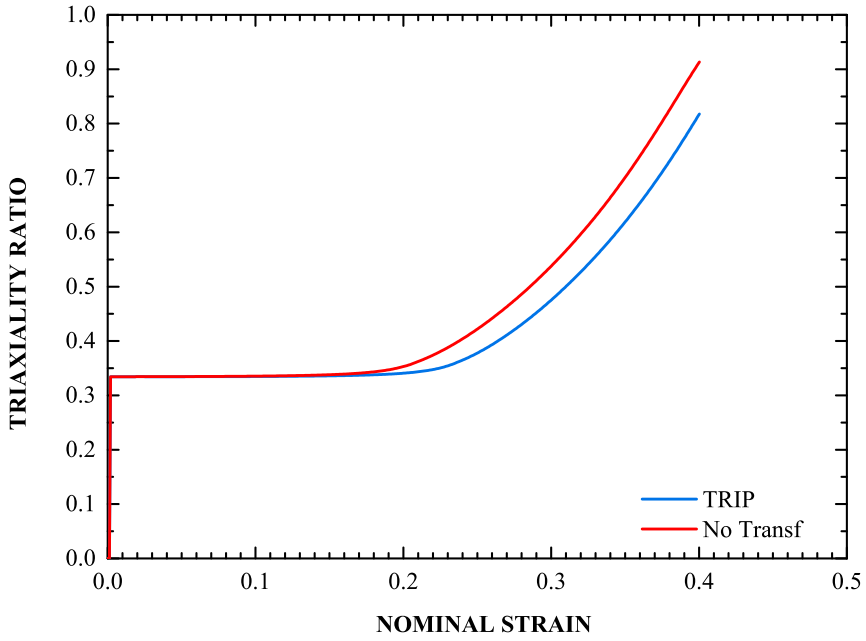

Figure 5.14: Evolution of the triaxiality ratio at the center of the specimen for a TRIP steel and a non-transforming steel.

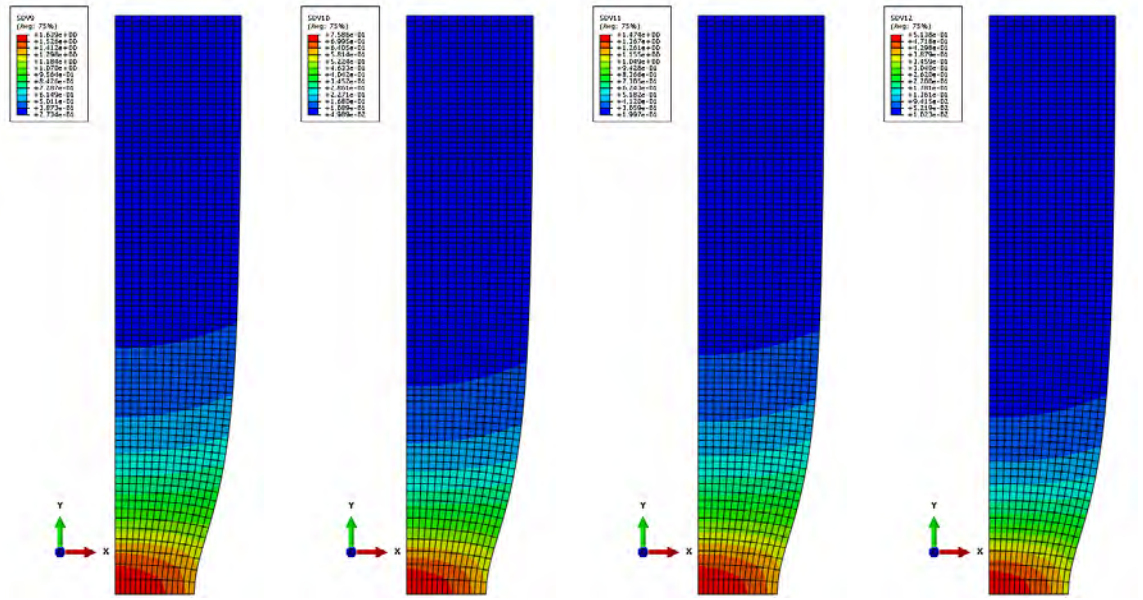

(a) (b) (c) (d)

Figure 5.15: Contours of equivalent plastic strain of the phases $\bar{\varepsilon}^{(r)}$ for the transforming steel at a nominal strain of 40%:(a) ferrite , (b) bainite , (c) austenite , (d) martensite.

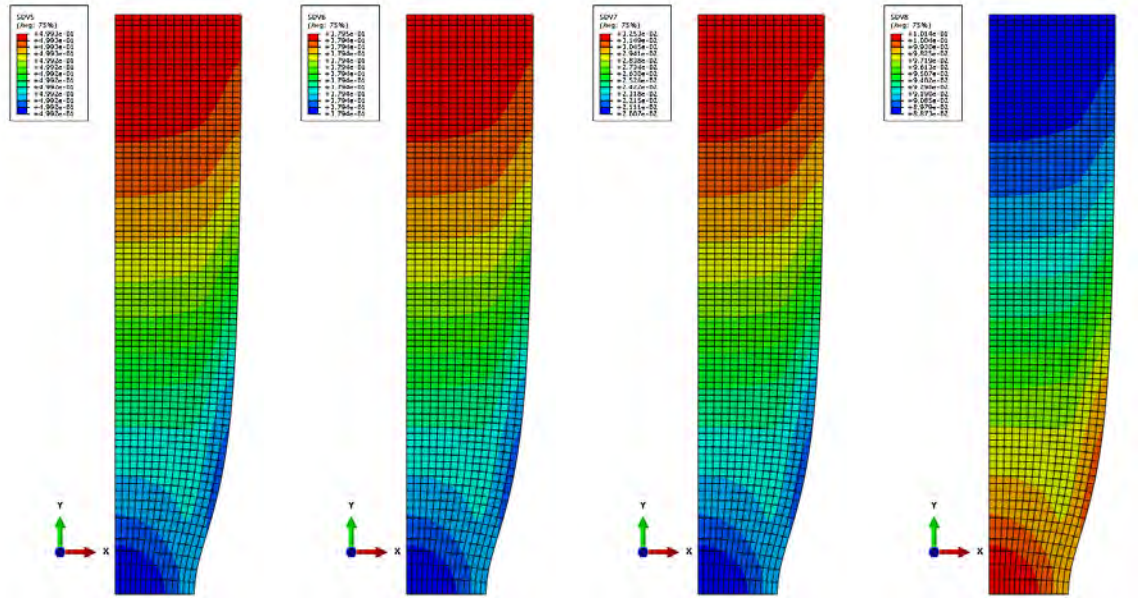

(a) (b) (c) (d)

Figure 5.16: Contours of volume fraction of phases for the transforming steel at a nominal strain of 40%: (a) ferrite , (b) bainite , (c) austenite , (d) martensite.

5.5.2 Necking in plane-strain tension

Next, we proceed with the necking of a bar under plane strain conditions. Lets consider a rectangular block with aspect ratio $L_0/B_0 = 3$, where $2\,L_0$ is the length of the specimen and

$2\,B_0$ its width (see Figure 5.17). We use the same finite element mesh, initial imperfection and material properties as in the axisymmetric problem presented in the previous section. The analysis is conducted by using four-node isoparametric plane strain elements (CPE4H in ABAQUS). Once again, a separate set of calculations is conducted for a non-transforming TRIP steel with same initial values of the volume fractions of the phases.

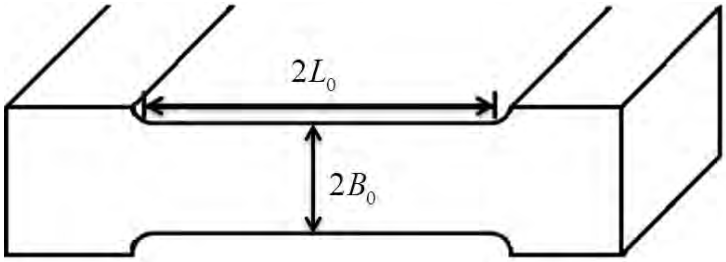

Figure 5.17: The rectangular specimen analyzed.

Figure 5.18 illustrates the $\sigma - \varepsilon$ curves for a transforming and a non-transforming steel under plane strain conditions. The two arrows on the curves, once again hint the point of maximum load, which co-occurs with the end of uniform elongation of the specimen. For the transforming (TRIP) steel we notice the end of uniform elongation at a nominal strain of 23.4% and 894 MPa stress, while for the non-transforming steel at 21.0% and 852 MPa. Thus, we reach the same conclusion as for the case of uniaxial tension: the TRIP phenomenon in addition to hardening the material, increases considerably the range of uniform elongation as well.

Figure 5.19 depicts the undeformed and deformed configurations at a nominal strain of 40% for the cases of uniaxial and plane strain tension. The neck in uniaxial tension is much less developed.

Figure 5.20 shows triaxiality contours after the neck develops in uniaxial and plane strain tension. The contours of the triaxiality ratio $X_\Sigma = p/\sigma_e$ take higher values in the plane strain case (Figure 5.20). At this point, it should be noted that in the case of uniaxial tension $X_{\Sigma\,\max} \cong 0.818$ and $X_{\Sigma\,\max} \cong 0.957$ in the plane strain case at a nominal strain of 40%; the maximum X_Σ value occurs at the center of the neck. The larger triaxiality value in plane strain has as a result an enhanced driving force for transformation and thus a higher volume fraction of martensite (Figure 5.21).

Figures 5.22 - 5.23 show contour plots of the hydrostatic stress p and the equivalent plastic strain $\bar{\varepsilon} = \int \sqrt{\frac{2}{3}\,\mathbf{D}^p : \mathbf{D}^p}\,dt$ for uniaxial and plane strain tension tests at a nominal strain of 40%. We observe a higher value of hydrostatic pressure in plane strain tension compared to uniaxial tension. This is due to the fact that the deformation in the-out-of plane direction is constrained, as opposed to the uniaxial tension case where there is no constraint.

To recapitulate, comparing the transforming and non-transforming steels we conclude that the TRIP phenomenon leads to stabilization of necking, causes propagation of the neck down

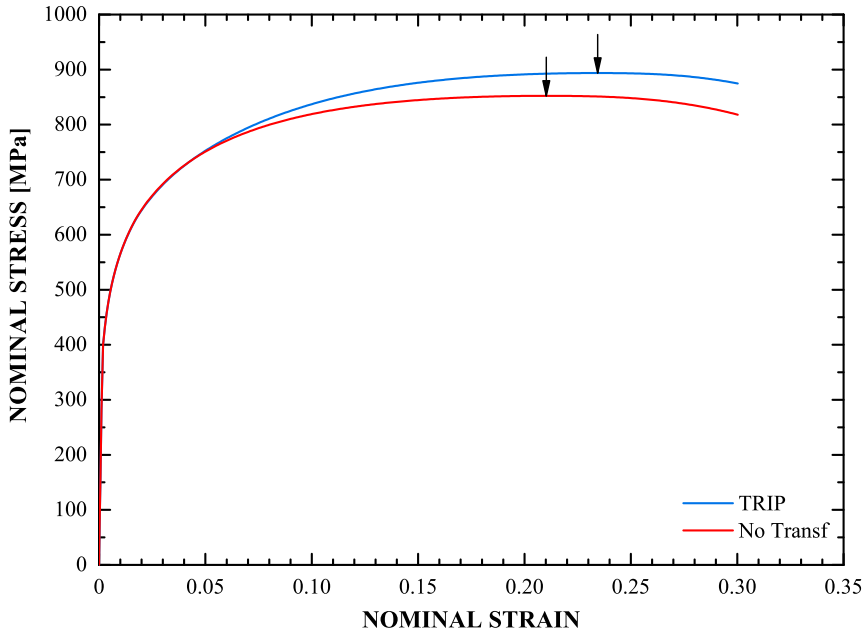

Figure 5.18: Stress-strain curves for a TRIP steel and a non-transforming steel in plane strain tension.

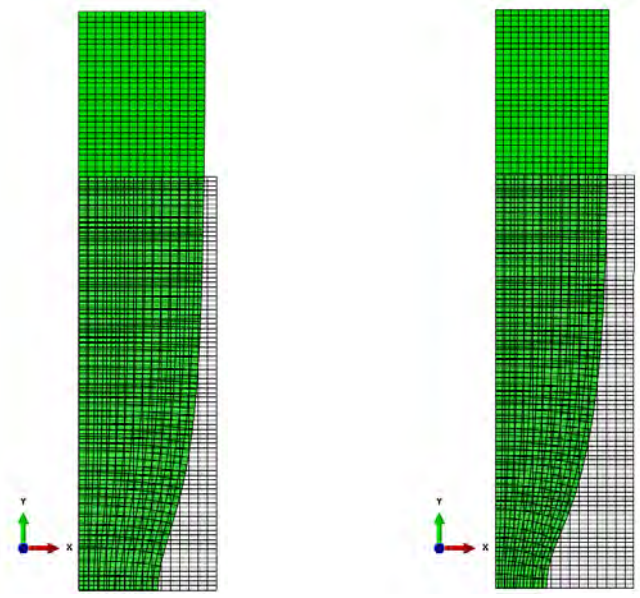

(a) (b)

Figure 5.19: Deformed and undeformed configurations for a nominal strain of 40%: a) uniaxial tension , b) plane strain tension.

the length of the specimen, and increases considerably the hardening and the range of uniform elongation of the steel.

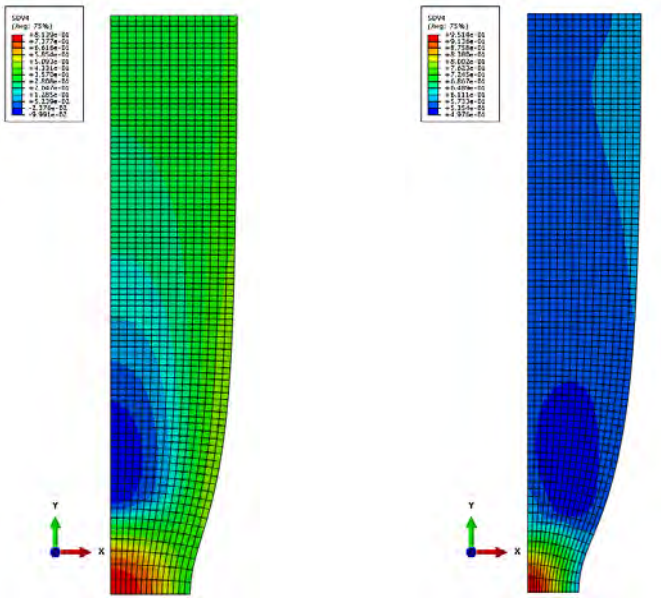

(a) (b)

Figure 5.20: Contours of triaxiality ratio X_Σ for a nominal strain of 40%: a) uniaxial tension , b) plane strain tension.

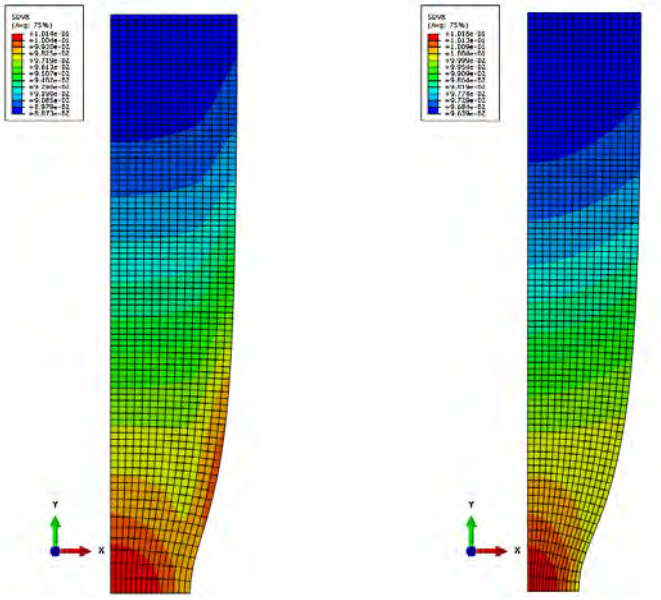

(a) (b)

Figure 5.21: Contours of volume fraction of martensite $c^{(m)}$ for a nominal strain of 40%: a) uniaxial tension , b) plane strain tension.

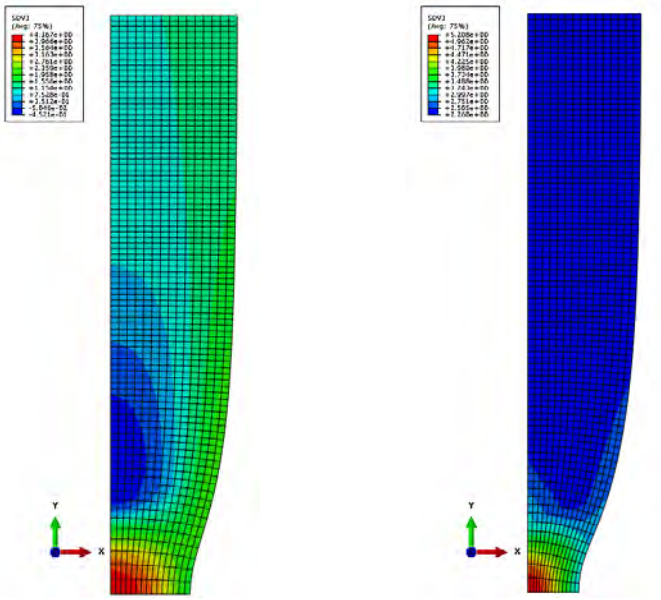

(a) (b)

Figure 5.22: Contours of hydrostatic stress $p = \sigma_{kk}/3$ for a nominal strain of 50%: a) uniaxial tension , b) plane strain tension.

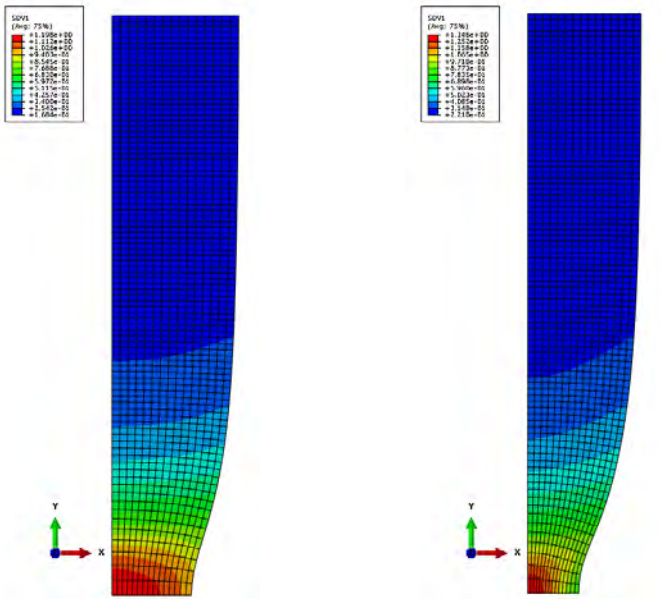

(a) (b)

Figure 5.23: Contours of equivalent plastic strain $\bar{\varepsilon} = \int \sqrt{\frac{2}{3}\,\mathbf{D}^p : \mathbf{D}^p}\,dt$ for a nominal strain of 40%: a) uniaxial tension , b) plane strain tension.

5.6 Plastic flow localization

In this section, we use the constitutive model developed for the four-phase TRIP steel to study whether a bifurcation within a localized band is possible as the material deforms homogeneously. Specifically, a problem is formulated for a rectangular block of a TRIP steel which is constrained to plane deformations and is subjected to tension in one direction. Comparisons are made with the corresponding problem in which martensitic transformation is suppressed. A detailed study of this problem for incompressible materials has been given by Rice [59]. This problem has also been examined by Hill and Hutchinson [26] and Needleman [42]. The material deforms homogeneously and at every stage of the deformation, we examine whether a bifurcation within a localized band is possible ([26],[43],[59]).

5.6.1 Problem formulation

Let $X_1 - X_2$ be the plane of deformation and X_1 the direction of stretching. Thus, the deformation gradient and the stress tensor are of the form

$$\mathbf{F} = \lambda_1 \mathbf{e}_1\mathbf{e}_1 + \lambda_2 \mathbf{e}_2\mathbf{e}_2 + \mathbf{e}_3\mathbf{e}_3 \quad \text{and} \quad \boldsymbol{\sigma} = \sigma_1 \mathbf{e}_1\mathbf{e}_1 + \sigma_3 \mathbf{e}_3\mathbf{e}_3 \tag{5.126}$$

where $(\mathbf{e}_1, \mathbf{e}_2, \mathbf{e}_3)$ are unit base vectors. Plastic flow localization in a shear band is possible when there exists a unit vector $\mathbf{n}$ on the $X_1 - X_2$ plane such (Needleman and Rice [43]):

$$\det[\mathbf{B}] = 0, \quad B_{ij} = n_k \, \mathcal{L}^{ep}_{kijl} \, n_l + A_{ij} \tag{5.127}$$

where

$$\mathbf{A} = -\frac{1}{2}\left[\boldsymbol{\sigma} - \boldsymbol{\sigma}\cdot\mathbf{nn} - (\mathbf{n}\cdot\boldsymbol{\sigma}\cdot\mathbf{n})\,\boldsymbol{\delta} + \mathbf{nn}\cdot\boldsymbol{\sigma}\right]. \tag{5.128}$$

If such an $\mathbf{n}$ exists, then the direction of the shear band is perpendicular to $\mathbf{n}$ (see Figure 5.24).

As discussed in section 5.3.2, the constitutive equations of the TRIP steel can be written in the form:

$$\overset{\nabla}{\boldsymbol{\sigma}} = \boldsymbol{\mathcal{L}}^{ep} : \mathbf{D} \tag{5.129}$$

where the fourth-order tensor of elastoplastic moduli is given by the expression

$$\boldsymbol{\mathcal{L}}^{ep} = \boldsymbol{\mathcal{L}}^{e} - 2\,G\left[\left(a_1 + \frac{A}{\Delta_v}\,b_1\right)\mathbf{N}\,\mathbf{N} + \left(a_2 + \frac{A}{\Delta_v}\,b_2\right)\mathbf{N}\,\boldsymbol{\delta}\right] - \kappa\,(b_1\,\boldsymbol{\delta}\,\mathbf{N} + b_2\,\boldsymbol{\delta}\,\boldsymbol{\delta}) \tag{5.130}$$

with

$$a_1 = \frac{2}{3\,D}\left[1 + q\frac{\kappa + X_\Sigma\,H_v}{\sigma_e}\,H\,(dX_\Sigma)\right], \qquad a_2 = -\frac{q}{D}\frac{\kappa}{\sigma_e}\left(\frac{A}{\Delta_v} + \frac{H_v}{3\,G}\right)H\,(dX_\Sigma)$$

$$b_1 = \frac{2}{3\,D}\left[m - q\,X_\Sigma\frac{H}{\sigma_e}\,H\,(dX_\Sigma)\right], \qquad b_2 = \frac{q}{D}\frac{\kappa}{\sigma_e}\left(1 + \frac{H}{3\,G}\right)H\,(dX_\Sigma)$$

$$D = 1 + \frac{H}{3\,G} + m\left(\frac{A}{\Delta_v} + \frac{H_v}{3\,G}\right) + \frac{q}{\sigma_e}\left[\kappa\left(1 + \frac{H}{3\,G}\right) + X_\Sigma\left(H_v - \frac{A}{\Delta_v}\,H\right)\right]H\,(dX_\Sigma)$$

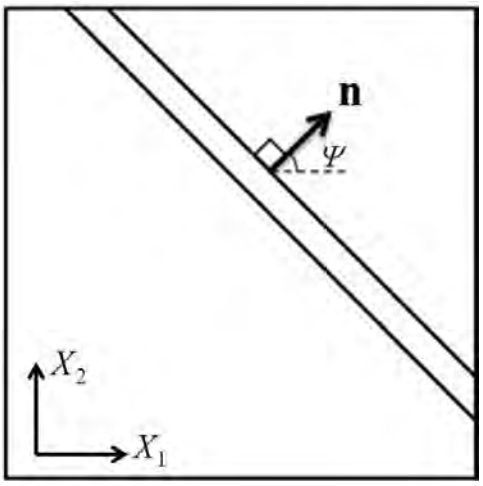

Figure 5.24: Shear band in a rectangular block subjected to tension in one direction.

and

$$m = \Delta_v \, c^{(3)} \, \alpha^{(3)} \, A_f, \qquad\qquad q = \Delta_v \, c^{(3)} \, B_f.$$

The tensor of the elastoplastic moduli has all major and minor symmetries and can be written compactly as

$$[\mathcal{L}^{ep}] = \begin{bmatrix} \mathcal{L}^{ep}_{1111} & \mathcal{L}^{ep}_{1122} & \mathcal{L}^{ep}_{1133} & 0 & 0 & 0 \\ \mathcal{L}^{ep}_{1122} & \mathcal{L}^{ep}_{2222} & \mathcal{L}^{ep}_{2233} & 0 & 0 & 0 \\ \mathcal{L}^{ep}_{1133} & \mathcal{L}^{ep}_{2233} & \mathcal{L}^{ep}_{3333} & 0 & 0 & 0 \\ 0 & 0 & 0 & \mathcal{L}^{ep}_{1212} & 0 & 0 \\ 0 & 0 & 0 & 0 & \mathcal{L}^{ep}_{1313} & 0 \\ 0 & 0 & 0 & 0 & 0 & \mathcal{L}^{ep}_{2323} \end{bmatrix}. \tag{5.131}$$

Carrying out the calculations in (5.127) we conclude that the localization condition can be written as

$$\det [B_{ij}] = 0 \tag{5.132}$$

where

$$\begin{aligned} B_{11} &= \mathcal{L}^{ep}_{1111} \, n_1^2 + \left(\mathcal{L}^{ep}_{1212} - \frac{\sigma_1}{2} \right) n_2^2, & B_{12} &= \left(\mathcal{L}^{ep}_{1122} + \mathcal{L}^{ep}_{1212} + \frac{\sigma_1}{2} \right) n_1 n_2, \\ B_{21} &= \left(\mathcal{L}^{ep}_{1122} + \mathcal{L}^{ep}_{1212} - \frac{\sigma_1}{2} \right) n_1 n_2, & B_{22} &= \mathcal{L}^{ep}_{2222} \, n_2^2 + \left(\mathcal{L}^{ep}_{1212} + \frac{\sigma_1}{2} \right) n_1^2, \\ B_{33} &= \left(\mathcal{L}^{ep}_{1313} + \frac{\sigma_1}{2} \right) n_1^2 + \mathcal{L}^{ep}_{2323} \, n_2^2 - \frac{\sigma_3}{2}, \end{aligned} \tag{5.133}$$

and $B_{13} = B_{23} = B_{31} = B_{32} = 0$. In view of the fact that the stress components σ_1 and σ_3 are of order σ_0, which is several orders of magnitude smaller than the elastoplastic moduli $\mathcal{L}_{ijkl}$, we conclude that the component B_{33} is always positive and so the localization condition (5.132) can take the form

$$B_{11} B_{22} - B_{21} B_{12} = 0 \tag{5.134}$$

The calculation of the strain at which localization of the plastic flow is probable, is carried out numerically. To elaborate, the homogeneous solution is determined numerically by increasing the axial stretch ratio λ_1 and determining the transverse stretch ratio λ_2 by iteration from the condition of zero transverse stress, $\mathbf{e}_2 \cdot \boldsymbol{\sigma} \cdot \mathbf{e}_2 = 0$. In the process of iteration, for every value of λ_1 and λ_2, the corresponding stress tensor $\boldsymbol{\sigma}$ is calculated by using the algorithm described in section 5.2.2. As soon as the homogeneous solution has been determined, we set $\mathbf{n} = \cos\Psi\,\mathbf{e}_1 + \sin\Psi\,\mathbf{e}_2$, where Ψ is the angle of inclination of the band relative to the X_1 axis, and we examine the localization condition (5.134) for values of Ψ that cover the range $0^o \leq \Psi \leq 90^o$. If a change of sign of the quantity $B_{11}B_{22} - B_{21}B_{12}$ is detected, the corresponding root that defines the localization angle Ψ is determined.

5.6.2 Results

The initial volume fractions of the four phases in the TRIP steel are assumed to be $c^{(1)} = 0.50$, $c^{(2)} = 0.38$, $c^{(a)} = 0.103$ and $c^{(m)} = 0.017$. The curves $\sigma_y^{(r)}, r = 1, 4$ that define the variation of the flow stress of the phases are those presented in section 5.4. For comparison purposes, a separate set of calculations is carried out for a non-transforming steel with the same initial values of the volume fractions of the four phases. The calculation were carried out for values of the axial strain up to $\varepsilon = \ln\lambda_1 = 2$.

Figure 5.25 shows the $\sigma - \varepsilon$ curves for both a transforming and a non-transforming material. Figure 5.25 makes it clear that the TRIP effect hardens the material. At this point, it should be noted that the parameter B_f that enters the evolution equation of f:

$$B_f = \frac{g_2}{\sqrt{2\pi}\,s_g}\,\beta_0\,(f_{sb})^r \exp\left[-\frac{1}{2}\left(\frac{g-\bar{g}}{s_g}\right)^2\right] H(\dot{X}_\Sigma), \tag{5.135}$$

as mentioned in section 5.2.1.1 takes non-zero values only when $\dot{X}_\Sigma \neq 0$. During the calculations it was observed that the stress triaxiality remained constant throughout the analysis $X_\Sigma = 1/\sqrt{3} = 0.5774$ (see Fig.5.26). Thus, we were able to set the parameter B_f equal to zero to avoid any possible artificial mistakes.

In addition, in section 5.2.2 it was mentioned that the inelastic part of the deformation rate for TRIP steels is written as the sum of the plastic part and the transformation part

$$\mathbf{D}^{in} = \underbrace{\left(\dot{\bar{\varepsilon}} + \frac{A}{\Delta_v}\,\dot{\varepsilon}_v^p\right)}_{\dot{\varepsilon}_q}\mathbf{N} + \underbrace{\frac{1}{3}\,\dot{\varepsilon}_v^p}_{\dot{\varepsilon}_p}\boldsymbol{\delta}, \tag{5.136}$$

resulting in both deviatoric and volumetric parts. In order to evaluate the contribution of the volumetric part to the inelastic deformation rate, we calculated the norm of each part and compared them. The norms E_q of the deviatoric part and E_p of the volumetric part are calculated as follows

$$\dot{E}_q^2 = (\dot{\varepsilon}_q\,\mathbf{N}) : (\dot{\varepsilon}_q\,\mathbf{N}) = \frac{3}{2}\,\dot{\varepsilon}_q^2 \quad \Rightarrow \quad \dot{E}_q = \sqrt{\frac{3}{2}}\,\dot{\varepsilon}_q$$
$$\Rightarrow \quad E_q = \sqrt{\frac{3}{2}}\int d\varepsilon_q \tag{5.137}$$

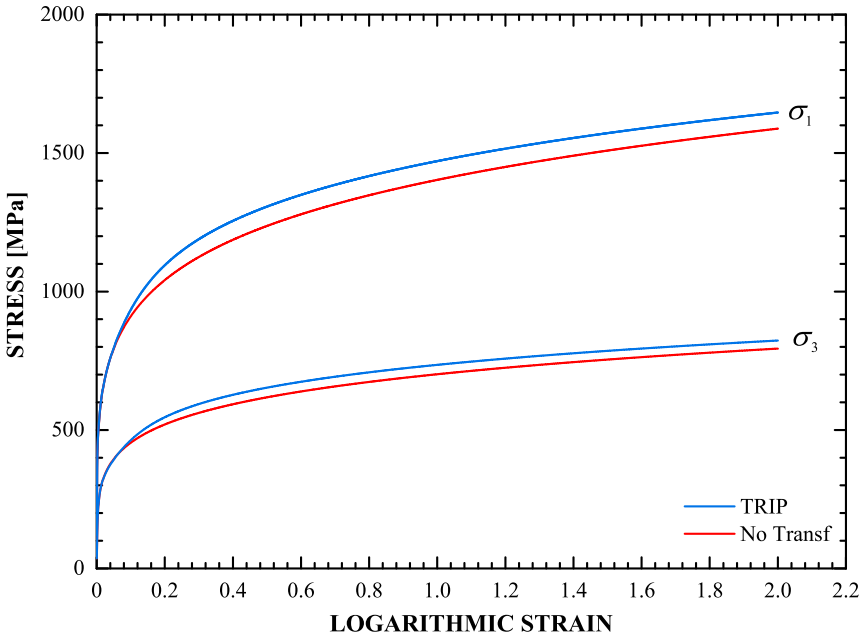

Figure 5.25: Stress-strain curves for a TRIP steel and a non-transforming steel.

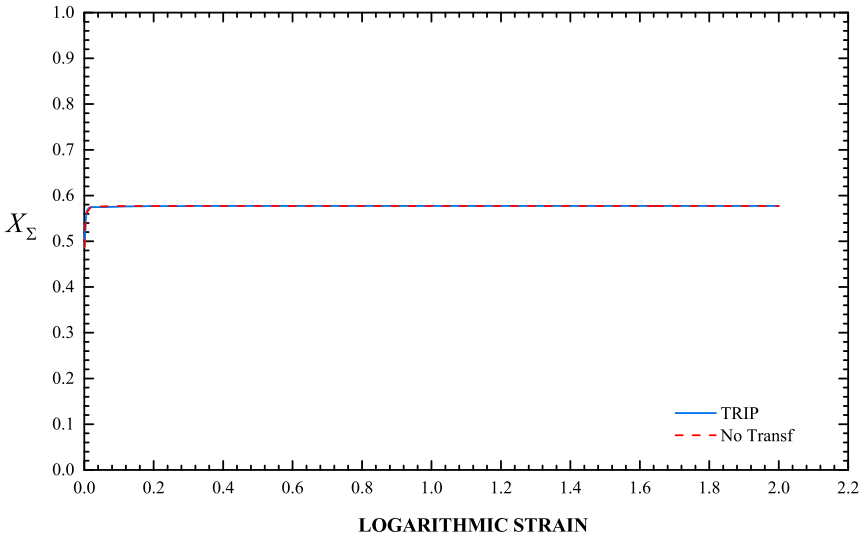

Figure 5.26: Evolution of the triaxiality ratio X_Σ for a TRIP steel and a non-transforming steel in plane-strain tension.

and

$$\dot{E}_p^2 = (\dot{\varepsilon}_p\,\boldsymbol{\delta}) : (\dot{\varepsilon}_p\,\boldsymbol{\delta}) = 3\,\dot{\varepsilon}_p^2 \quad \Rightarrow \quad \dot{E}_p = \sqrt{3}\,\dot{\varepsilon}_p$$
$$\Rightarrow \quad E_p = \sqrt{3}\int d\varepsilon_p \tag{5.138}$$

Figure 5.27 illustrates the growth of E_q and E_p as the material deforms plastically. As it can be seen the contribution of the volumetric part of the inelastic part compared to the deviatoric part is insignificant.

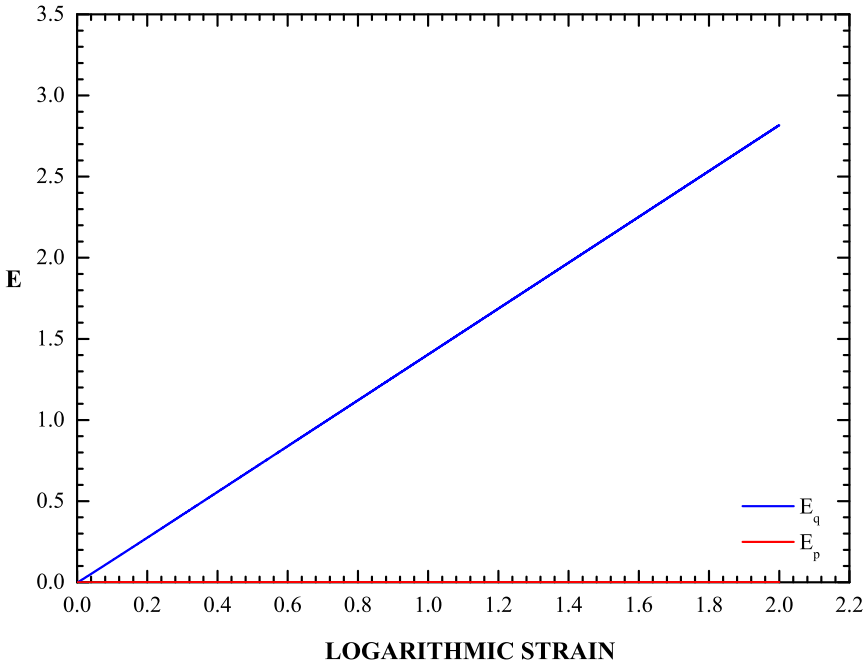

Figure 5.27: Evolution of the norm of the deviatoric part E_q and of the volumetric part E_p of the inelastic deformation for a TRIP steel in plane-strain tension.

Last but not least, during the calculations once the homogeneous solution had been determined, the localization condition $\det\mathbf{B} = 0$ was examined for the range $0^o \leq \Psi \leq 90^o$. For both the TRIP and the non transforming steel the determinant of $[B]$ decreases with ε, as it is depicted in Figure 5.28, but never equals zero in this range of strains. Therefore localization is not predicted since the localization condition is never met for values of axial strain up to $\varepsilon = \ln\lambda_1 = 2$, where the calculations are terminated.

5.7 Forming limit diagrams

In this section, the constitutive model developed for the four-phase TRIP steel is used to calculate "forming limit diagrams" for sheets made of TRIP steels. Forming limit diagrams show the maximum deformation to which a sheet metal can be subjected before the material fails. In the present thesis, we concentrate on the formation of instabilities in a narrow straight band in metal sheets deformed under plane stress conditions. The predictions of the analytical model are compared to experimental data from the same TRIP steel which was used for the calibration. For comparison purposes, a separate set of calculations is conducted for a non-transforming TRIP steel with same initial values of the volume fractions of the phases.

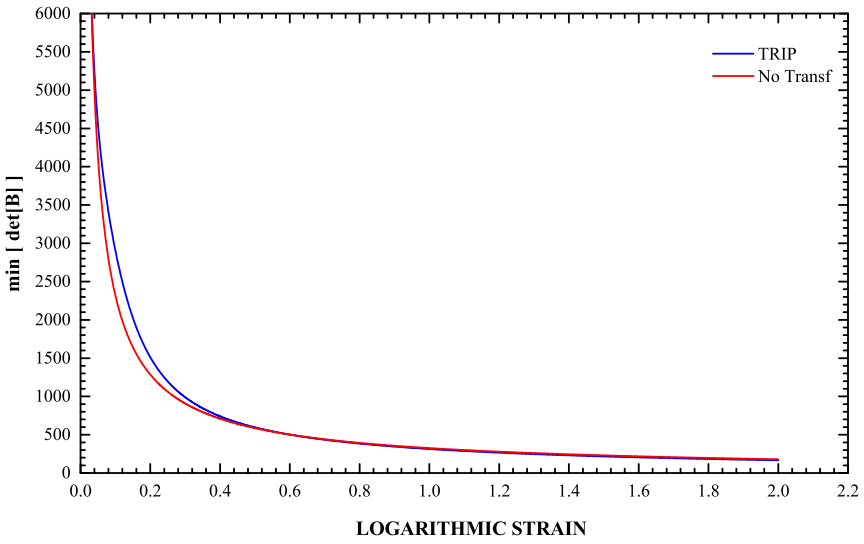

Figure 5.28: Growth of the determinant of $[B]$ for a TRIP steel and a non-transforming steel.

5.7.1 Problem formulation

We consider a sheet made of TRIP steel that is deformed uniformly on its plane in a way that the in-plane principal strain increments increase proportionally. We study the possibility of the formation of an instability in the form of a narrow straight band, as that shown in Figure 5.29.

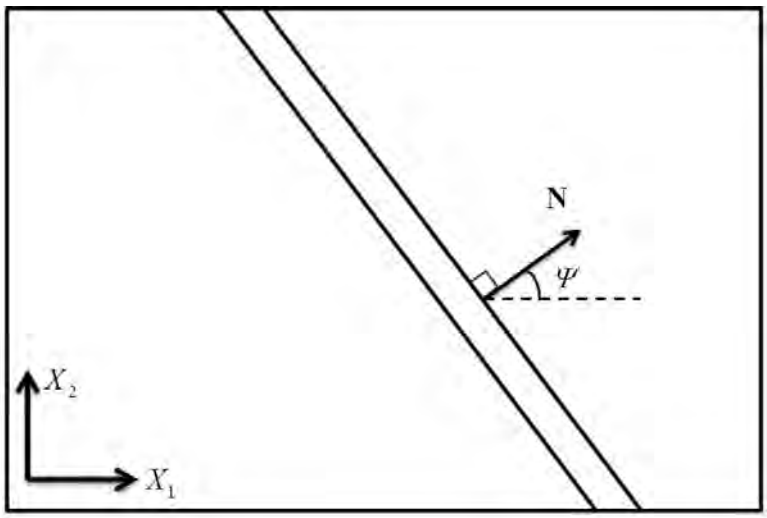

Figure 5.29: Narrow band in biaxially stretched sheet.

The constitutive equations of the TRIP steel, as it was presented in section 5.3.2, can be written as:

$$\overset{\nabla}{\boldsymbol{\sigma}} = \boldsymbol{\mathcal{L}}^{ep} : \mathbf{D} \tag{5.139}$$

where

$$\boldsymbol{\mathcal{L}}^{ep} = \boldsymbol{\mathcal{L}}^{e} - 2\,G\left[\left(a_1 + \frac{A}{\Delta_v}\,b_1\right)\mathbf{N}\,\mathbf{N} + \left(a_2 + \frac{A}{\Delta_v}\,b_2\right)\mathbf{N}\,\boldsymbol{\delta}\right] - \kappa\,(b_1\,\boldsymbol{\delta}\,\mathbf{N} + b_2\,\boldsymbol{\delta}\,\boldsymbol{\delta}) \tag{5.140}$$

with

$$a_1 = \frac{2}{3\,D}\left[1 + q\frac{\kappa + X_\Sigma\,H_v}{\sigma_e}\,H\,(dX_\Sigma)\right], \qquad a_2 = -\frac{q}{D}\frac{\kappa}{\sigma_e}\left(\frac{A}{\Delta_v} + \frac{H_v}{3\,G}\right)H\,(dX_\Sigma)$$

$$b_1 = \frac{2}{3\,D}\left[m - q\,X_\Sigma\frac{H}{\sigma_e}\,H\,(dX_\Sigma)\right], \qquad b_2 = \frac{q}{D}\frac{\kappa}{\sigma_e}\left(1 + \frac{H}{3\,G}\right)H\,(dX_\Sigma)$$

$$D = 1 + \frac{H}{3\,G} + m\left(\frac{A}{\Delta_v} + \frac{H_v}{3\,G}\right) + \frac{q}{\sigma_e}\left[\kappa\left(1 + \frac{H}{3\,G}\right) + X_\Sigma\left(H_v - \frac{A}{\Delta_v}\,H\right)\right]H\,(dX_\Sigma)$$

and

$$m = \Delta_v\,c^{(3)}\,\alpha^{(3)}\,A_f, \qquad q = \Delta_v\,c^{(3)}\,B_f$$

In our calculations we decided to work with nominal quantities, because it simplifies the formulation. First we consider the 1st Piola-Kirchhoff stress tensor $\mathbf{t} = J\,\mathbf{F}^{-1}\cdot\boldsymbol{\sigma}$ where $J = \det\mathbf{F}$. It can be proven very easily that

$$\dot{\mathbf{t}} = \mathbf{R} : \dot{\mathbf{F}}^{T} \tag{5.141}$$

where

$$R_{ijkl} = J\,F^{-1}_{im}\,F^{-1}_{kn}\,(L_{mjnl} + V_{mjnl})\,, \tag{5.142}$$

$$V_{ijkl} = \frac{1}{2}\,(\sigma_{ik}\,\delta_{jl} - \delta_{ik}\,\sigma_{jl} - \sigma_{il}\,\delta_{jk} - \delta_{il}\,\sigma_{jk}) + \sigma_{ij}\,\delta_{kl} \tag{5.143}$$

Next, we assume a state of uniform plane stress inside and outside the band and examine the possibility of the formation of a neck as shown in Figure 5.29. Let $X_1 - X_2$ be the plane of the sheet, H the initial thickness of the sheet and the superscript b denote quantities within the band whereas no superscript denotes quantities outside the band.

In view of the fact that the in-plane displacements are continuous, their spatial derivatives parallel to the band remain uniform. Therefore the only discontinuities in the displacement gradient are restricted kinematically to the following form (Hadamard [18], Hill [24], Rice [59])

$$\left[\frac{\partial u_a}{\partial X_\beta}\right] = G_a\,N_\beta \tag{5.144}$$

where $\mathbf{X}$ is the position vector of a material point in the undeformed configuration, $\mathbf{N}$ is the unit vector normal to the band in the undeformed configuration, [ ] denotes the difference of the field within the band and outside the band, and $\mathbf{G}$ is the jump in the normal derivative of $\mathbf{u}$, i.e., $[\partial\mathbf{u}/\partial N] \equiv [(\partial\mathbf{u}/\partial\mathbf{X})\cdot\mathbf{N}] = \mathbf{G}$. In the following we present a methodology for the determination of $\mathbf{G}$. We should note that Greek indices take values in the range $(1, 2)$.

Taking into account equation (5.144), we conclude that the in-plane components of the deformation gradient inside the band can be written as

$$F^{b}_{\alpha\beta} = F_{\alpha\beta} + G_a\,N_\beta \tag{5.145}$$

whereas the in-plane components of the deformation gradient outside the band are of the form

$$F_{\alpha\alpha} = \lambda_\alpha \quad \text{and} \quad F_{\alpha\beta} = 0, \quad \alpha \neq \beta \tag{5.146}$$

The deformation gradients in a matrix form are

$$[F] = \begin{bmatrix} \lambda_1 & 0 & 0 \\ 0 & \lambda_2 & 0 \\ 0 & 0 & \lambda_3 \end{bmatrix} \qquad \text{and} \qquad \left[F^b\right] = \begin{bmatrix} \lambda_1 + G_1\, N_1 & G_1\, N_2 & 0 \\ G_2\, N_1 & \lambda_2 + G_2\, N_2 & 0 \\ 0 & 0 & \lambda_3^b \end{bmatrix} \tag{5.147}$$

Next, we use the plane stress condition $\sigma_{33} = 0$ which also suggests that $t_{33} = 0$. Equation (5.141) can be expressed analytically in the following form

$$\dot{t}_{\alpha\beta} = R_{\alpha\beta kl}\dot{F}_{lk} = R_{\alpha\beta\gamma\delta}\dot{F}_{\delta\gamma} + R_{\alpha\beta 33}\dot{F}_{33} \tag{5.148}$$

So the plane stress condition $\dot{t}_{33} = 0$ can be written

$$\dot{t}_{33} = R_{33kl}\dot{F}_{lk} = R_{33\gamma\delta}\dot{F}_{\delta\gamma} + R_{3333}\dot{F}_{33} = 0 \tag{5.149}$$

which can be solved for $\dot{F}_{33}$

$$\dot{F}_{33} = -\frac{R_{33\gamma\delta}}{R_{3333}}\dot{F}_{\delta\gamma} \tag{5.150}$$

Combining equations (5.148) and (5.150) we derive

$$\dot{t}_{\alpha\beta} = R_{\alpha\beta\gamma\delta}\dot{F}_{\delta\gamma} - R_{\alpha\beta 33}\frac{R_{33\gamma\delta}}{R_{3333}}\dot{F}_{\delta\gamma} = \left(R_{\alpha\beta\gamma\delta} - R_{\alpha\beta 33}\frac{R_{33\gamma\delta}}{R_{3333}}\right)\dot{F}_{\delta\gamma} \tag{5.151}$$

Thus, we conclude that the in-plane constitutive relations needed for the analysis can be written as:

$$\dot{t}_{\alpha\beta} = C_{\alpha\beta\gamma\delta}\,\dot{F}_{\gamma\delta} \quad \text{with} \quad C_{\alpha\beta\gamma\delta} = R_{\alpha\beta\gamma\delta} - R_{\alpha\beta 33}\frac{R_{33\gamma\delta}}{R_{3333}} \tag{5.152}$$

Similarly, the in-plane constitutive relations within the band are

$$\dot{t}^b_{\alpha\beta} = C^b_{\alpha\beta\gamma\delta}\,\dot{F}^b_{\gamma\delta} = C^b_{\alpha\beta\gamma\delta}\,\left(\dot{F}_{\gamma\delta} + G_\gamma N_\delta\right) \quad \text{with} \quad C^b_{\alpha\beta\gamma\delta} = R^b_{\alpha\beta\gamma\delta} - R^b_{\alpha\beta 33}\frac{R^b_{33\gamma\delta}}{R^b_{3333}} \tag{5.153}$$

Now taking into account the equilibrium across the band we have that

$$T_\alpha \equiv H\, N_\beta\, t_{\beta\alpha} = H^b\, N_\beta\, t^b_{\beta\alpha} \equiv T^b_\alpha \tag{5.154}$$

the rate form of which is

$$\dot{T}_\alpha \equiv H\, N_\beta\, \dot{t}_{\beta\alpha} = H^b\, N_\beta\, \dot{t}^b_{\beta\alpha} \equiv \dot{T}^b_\alpha \tag{5.155}$$

Combining equations (5.152), (5.153) and (5.155) we find

$$\mathbf{A}\cdot\dot{\mathbf{G}} = \mathbf{B}\cdot\dot{\mathbf{b}} \tag{5.156}$$

where

$$A_{\alpha\beta} = N_\gamma\, C^b_{\gamma\alpha\delta\beta}\, N_\delta, \qquad B_{\alpha\beta} = N_\gamma\left(\frac{H}{H^b}\, C_{\gamma\alpha\beta\beta} - C^b_{\gamma\alpha\beta\beta}\right) \quad \text{and} \quad b_a = \lambda_\alpha \tag{5.157}$$

Lets consider a perfect sheet ($H^b = H$). In this case the right hand side of (5.156) vanishes since $\mathbf{C}^b = \mathbf{C} \Rightarrow \mathbf{B} = 0$ and the deformation remains homogenous ($\dot{\mathbf{G}} = \mathbf{0}$) until at some point the condition for local necking bifurcation is met ($\det[\mathbf{A}] = 0$).
In our calculations we follow the approach of Marciniak and Kuzyski [37], known as the M-K model, in which the sheet is assumed to contain a small initial inhomogeneity and necking results from a gradual localization of the strains at the inhomogeneity. So, in our analyses we consider a straight narrow band of reduced thickness $H^b < H$, as shown in Figure 5.29. We assume a state of uniform plane stress inside and outside the band, and the analysis consists in determining the uniform state of deformation inside the band that is consistent kinematically and statically with the prescribed uniform state outside the band (Tvergaard ([73], [74]), Needleman and Tvergaard [44]). When there is an initial thickness imperfection, the right hand side of (5.156) does not vanish and these equations can be solved for $\dot{G}_1$ and $\dot{G}_2$. The localization condition is met when the ratio of some scalar measure of the amount of incremental straining inside the band to the corresponding value outside the band becomes unbounded.
The deformation gradient outside the band $\mathbf{F}$ is prescribed in such a way that the corresponding principal logarithmic strains ε_1 and ε_2 outside the band increase proportionally, i.e.

$$dE_2/dE_1 = E_2/E_1 = \rho = \text{const.} \tag{5.158}$$

The last equation implies

$$\lambda_2 = \lambda_1^{\rho} \tag{5.159}$$

First, we determine the uniform solution outside the band by using the plane stress algorithm presented in section 5.3. Then, we use equations (5.156) to find $\Delta\mathbf{G}$ and subsequently $\mathbf{F}^b$ and finally, we determine the uniform solution inside the band using the same plane stress algorithm. The localization condition is met when $d\,|\mathbf{G}|/d\lambda_1 = \infty$ i.e. when $\det[\mathbf{A}] = 0$. At this point, we should emphasize that in the case of rate dependent plasticity this condition cannot be satisfied, so we assume that necking localization occurs when this ratio exceeds a certain high value e.g. $d\,|\mathbf{G}|/d\lambda_1 > 30$, like in the previous work of Papatriantafillou *et al.* [47] (as opposed to the rate independent plasticity used here, where the condition $d\,|\mathbf{G}|/d\lambda_1 = \infty$ is satisfied). We also note that in order to improve the accuracy of the calculations and be able to use increments of reasonable size, in (5.156) instead of the rate of equilibrium equation (5.155), we use equilibrium itself

$$\mathbf{T}_{n+1} = \mathbf{T}^b_{n+1} \tag{5.160}$$

where the subscript $n+1$ denotes values at the end of the increment. Thus, if we set $\mathbf{T}_{n+1} \simeq \mathbf{T}_n + \dot{\mathbf{T}}_n\,\Delta t$ and $\mathbf{T}^b_{n+1} \simeq \mathbf{T}^b_n + \dot{\mathbf{T}}^b_n\,\Delta t$ we derive

$$A_{\alpha\beta}|_n\;\Delta G_\beta = B_{\alpha\beta}\,b_\alpha|_n\;\Delta t + \frac{1}{H^b}\left(\mathbf{T}_n - \mathbf{T}^b_n\right) \tag{5.161}$$

which is used instead of (5.156).

5.7.2 Results

The initial volume fractions of the four phases in the TRIP steel are assumed to be $c^{(1)} = 0.50$, $c^{(2)} = 0.38$, $c^{(a)} = 0.103$ and $c^{(m)} = 0.017$. The curves $\sigma_y^{(r)}, r = 1, 4$ that define the variation of the flow stress of the phases and the material data used in the calculations are those presented in section 5.4. As mentioned earlier, calculations are also carried out for a non-transforming steel with the same initial values of the volume fractions of the four phases.
We set $\mathbf{N} = \cos\Psi\,\mathbf{e}_1 + \sin\Psi\,\mathbf{e}_2$, where Ψ is the angle of inclination of the band relative to the X_1 axis in the undeformed configuration, and for every value of $\rho = dE_2/dE_1$, we carry out calculations to determine the minimum localization strain by scanning the range $0^o \leq \Psi \leq 90^o$. We note that the critical value Ψ^{cr} for each ρ corresponds to the minimum localization strain.
Figure 5.30 illustrates forming limit curves obtained for imposed proportional straining ρ for two different values of the initial thickness imperfection, namely $H^b/H = 0.999$ and $H^b/H = 0.99$ and for the case without imperfection i.e. $H^b/H = 1$. The three solid curves correspond to the TRIP steel, whereas the dashed curves are for the non-transforming steel. As we can see, the TRIP effect increases the necking localization strains. This result was also presented by Papatriantafillou *et al.* [47], who used a rate dependent constitutive model for TRIP steels (as opposed to the rate independent model used here). In details, for no imperfection and $\rho = 0$ (plane strain), the critical strain ε_{11}^{cr} increases from 0.19228 for the non-transforming steel to 0.21203 for the TRIP steel; the corresponding values of ε_{11}^{cr} for $H^b/H = 0.999$ and $\rho = 0$ are 0.17369 for the non-transforming steel and 0.19395 for the TRIP steel and for $H^b/H = 0.99$ and $\rho = 0$ are 0.13775 for the non-transforming steel and 0.15869 for the TRIP steel.
The model predictions are also compared to available experimental data. The experimental data refer to the same TRIP steel which was used for the calibration of the model. Details on the experiments are given in Papatriantafillou [46]. The model predictions fit the experimental data reasonably well.
Figure 5.31 displays the necking development where the ratio of the maximum principal logarithmic strain inside $\left(\varepsilon_I^b\right)$ and outside (ε_1) the neck are plotted versus ε_1 for the TRIP steel for $\rho = 0$ and Figure 5.32 shows the growth of the determinant of the coefficient matrix $[A]$. As it can be observed the determinant $[\mathbf{A}]$ vanishes at the critical strain ε_{11}^{cr}.

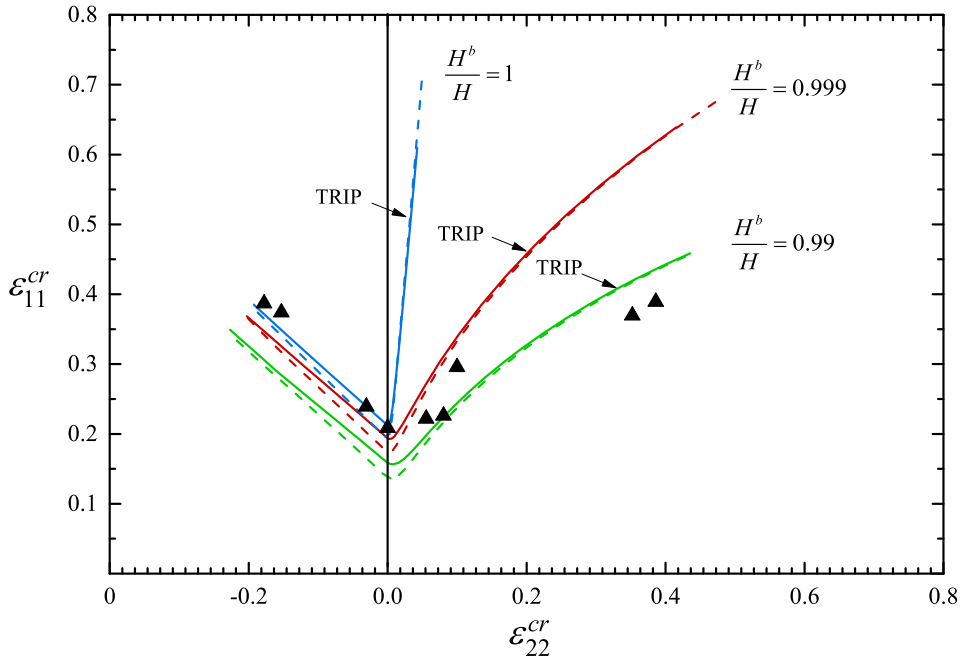

Figure 5.30: Forming limit curves for two different values of initial thickness inhomogeneities $H^b/H = 0.999$ and $H^b/H = 0.99$. The solid lines correspond to the TRIP steel, whereas the dashed lines are for a non-transforming steel. The dark triangles are experimental data.

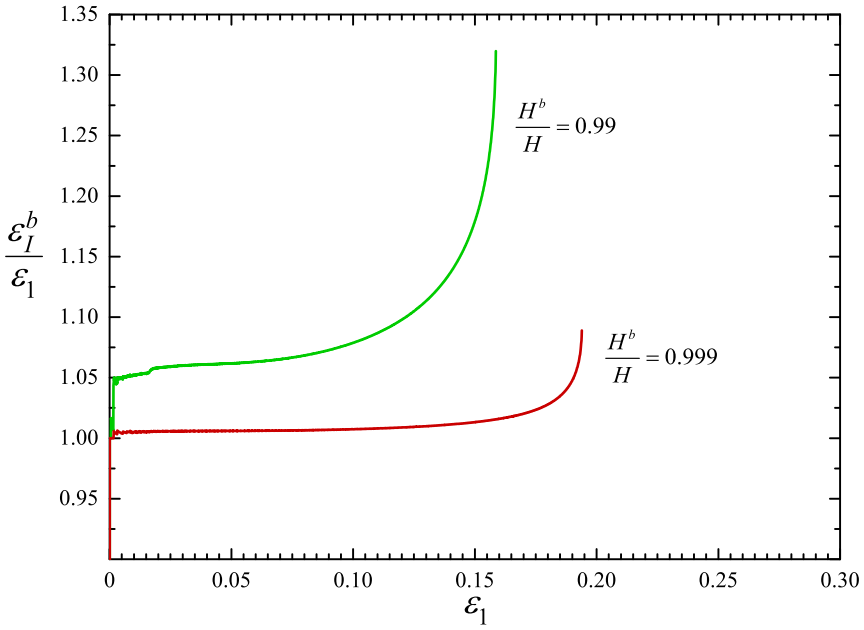

Figure 5.31: Growth of maximum principal logarithmic strain inside the band ε_I^b for the TRIP steel and $\rho = 0$.

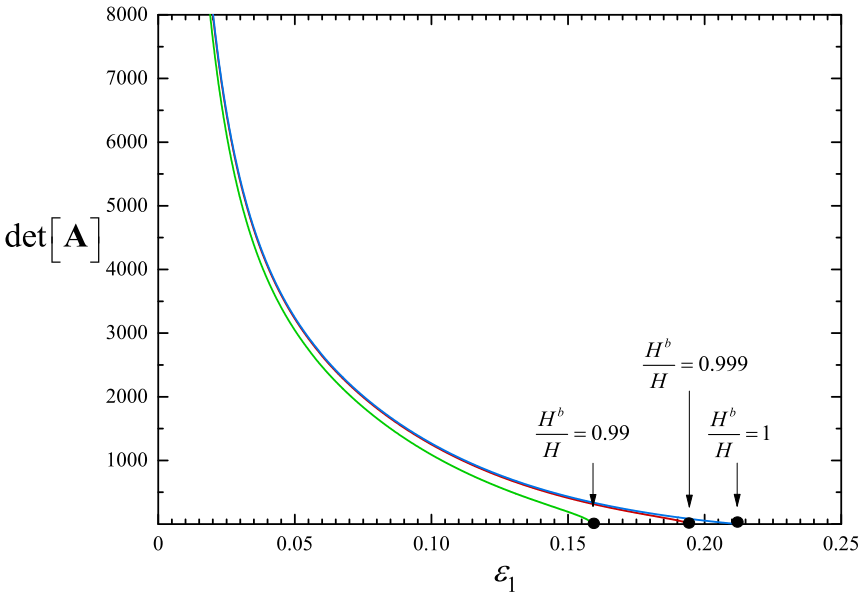

Figure 5.32: Growth of the determinant of the coefficient matrix $[A]$ for the TRIP steel and $\rho = 0$.

Chapter 6

Closure

The present Thesis presents a simple semi-analytical model for the estimation of the effective as well as the phase average response of $N-$phase incompressible isotropic elasto-plastic metallic materials. The model is based on the original variational method of Ponte Castañeda [48], which is based on a linear comparison composite technique. The resulting expression for the effective yield strength of the composite requires the solution of a constrained optimization problem for $N-1$ scalar variables and is much simpler and tractable than the original expressions given in [49]. This is achieved by use of the methodology of Kaufman *et al.* [32]. In the special case of a two-phase composite, we provide a fully explicit expression which is given via a piecewise function defined in equation (3.5). Due to its simplicity and numerical efficiency, the proposed $N-$phase model is numerically implemented in a user-material subroutine which, in turn, allows for the simulation of three dimensional geometries.
In addition, the $N-$phase analytical model is compared with full field three dimensional finite element simulations of two- and three-phase multi-particle periodic unit cells. The proposed model is found to be in good agreement with the finite element results in most of the cases considered here, even at large particle volume fractions ($c^{(2)} = 0.40$) and different hardening exponents. The agreement is good both for the effective average stress strain response, as well as for the phase average strain fields. This last observation allowed to extend the model in a heuristic manner to account for arbitrary isotropic hardening of the phases, both in a small and finite strain formalism. The present combined analytical and numerical study reveals several nontrivial features which are summarized in the following.
One of the main non-intuitive observations in the present work, which is in accord with former literature, is that in the context of a two-phase composite when the strength of the particles is almost twice that of the matrix the particles behave as being rigid for all volume fractions considered here. In other words, we obtain a rather sharp transition when the yield stress of the particle is about two times that of the matrix beyond which the strain in the particle is negligible, thus leading to an almost rigid response of the particle in the sense of straining for a large range of volume fractions. This result was shown for the effective yield stress by Suquet [68] and Idiart [29] for given particle volume fraction, whereby it is further shown here that this sharp transition is weakly sensitive to the particle volume fraction (at least for volume fractions up to 40%). This, in turn, may have significant implications in

the strengthening of the composite and possible debonding/failure of the particle/matrix interface [5], since beyond that contrast ratio the particle stops deforming. This of course leads to stress and strain concentrations in the matrix/particle interface.

A second observation, which has already been made in the context of a plastic matrix with rigid particles by Suquet [68] and Idiart [29] is that the numerical estimates exhibit a dependence on the third invariant (J_3) of the stress tensor, i.e., on the Lode parameter or Lode angle. Nonetheless, this dependence is extremely weak and thus the present model, which does not take into account this dependence, is sufficiently accurate for the estimation of the effective response as well as of the phase average strains (which depend apriori upon the normal to the yield surface). This observation of course is valid for phases described by a von Mises (J_2) yield response and does not hold in the case of plastic solids that depend directly on the third invariant J_3 via Tresca, Hoshford or Drucker-Prager plasticity (see for instance Barthélémy and Dormieux [4] and Barthélémy *et al.* [36]).

A third, and perhaps more important finding of this work at least from a more practical point of view, is related to the extension of the model to arbitrary isotropic hardening of the phases. In the present work, we carry out first the nonlinear homogenization for perfectly plastic phases and then the hardening is added heuristically at the definition of the yield stresses of each of the phases. This of course is an approximation and does not take into account explicitly the coupling between the different hardening exponents of the different phases. Nevertheless, the resulting estimates are in very good agreement with the full field finite element results (which include this coupling) suggesting that this strategy is sufficient for the materials considered in this study. This good agreement can be directly associated with the fact that the model predicts accurately enough the phase average strains. This, however, may not be true if one considers kinematic hardening of the phases but again in this case a more advanced homogenization method needs to be used such as the one proposed by Lahellec and Suquet [34].

Furthermore, in this study, we do not consider the extreme case of a three-phase composite comprising stiff particles and voids. The reason is that the presence of a soft compressible phase would introduce a dependence on an additional invariant, i.e, pressure (I_1) and the material would be plastically compressible (see for instance Garajeu and Suquet [16] and He *et al.* [21]). A vast amount of studies has been carried out in the context of voided materials and is very well known that the present method by default would lead to overly stiff estimates unless corrected (see for instance recent work of Danas and Aravas [12] and Cao *et al.* [10]).

Then, the homogenization theory was used to develop a constitutive model for TRIP steels. Specifically, we consider four-phase TRIP steels that consist of a ferritic matrix with dispersed bainite and austenite, which transforms gradually into martensite as the material deforms plastically. The total strain can be split into elastic, plastic and transformation parts. Standard isotropic linear hypoelasticity of homogeneous solids is used in order to describe the elastic behavior of the TRIP steels since the elastic properties of all phases are fundamentally the same. The homogenization techniques for non-linear composites are used

to determine the effective properties and overall behavior of TRIP steels. The transformation part is proportional to the rate of change of the volume fraction of martensite due to martensitic transformation, which is described by the modified Olson-Cohen transformation kinetics model proposed by Stringfellow *et al.* [64].
A method for the numerical integration of the resulting constitutive equations in the context of a displacement driven finite element formulation was developed and the model was implemented into the ABAQUS. We also developed a method for the numerical integration of the constitutive model under plane stress conditions.
The problems of plastic flow localization and necking in tension are analyzed in detail. The constitutive model was used also for the calculation of "forming limit diagrams" for sheets made of TRIP steels. The predictions of the analysis were compared to experimental data from the same TRIP steel which was used for the calibration. In all cases we reach the conclusion that the TRIP phenomenon not only hardens the material, but also increases considerably the range of uniform elongation.

6.1 Suggestions for future research

Several research directions may be proposed for future work. A problem of particular interest would be to develop a constitutive model for the cyclic response of composite materials. In this case, however, a more advanced homogenization method needs to be used such as the one proposed by Lahellec and Suquet [34] or the one by Agoras, Avazmohammadi and Ponte Castañeda [1].
Another interesting project would be to improve the constitutive model for TRIP steels. To elaborate, in the present Thesis we focused on strain-induced transformation of retained austenite to martensite. Nonetheless, experiments show that, in uniaxial tension, an amount of martensite appears before yielding takes place due to the stress-assisted transformation. Therefore, the kinetics of the evolution of martensite volume fraction could be described by a model which takes also into account the stress-assisted transformation in addition to the strain-induced, like the one proposed by Haidemenopoulos *et al.* [19]. At this point, we should mention that whereas all traditional mechanical constitutive equations do not have a 'length scale', this model introduces an intrinsic 'material length', which is the austenite particle size. This is of great importance, since austenite particle size refinement has a strong stabilizing influence by retarding the strain-induced transformation kinetics.
Finally, in order to further improve the simulation of the mechanical behavior of TRIP steels, we could develop an experimental method in order to measure the hardening of the constituent phases. The experimental data for the hardening curves of the constituent phases presented in Chapter 5 derived from a detailed bibliographic search. Therefore, with this method we would have more precise data.

Appendices

Appendix I

Instructions for CONMAX

We wish to find the minimum of $f(\mathbf{x})$ under the constraints $x_i \geq 0$. CONMAX defines the problem as follows:
Minimize W subjected to

$$f(\mathbf{x}^*) \leq W, \qquad \text{IPT} = 1, \qquad \text{INCTYP} = 1,$$
$$-x_i^* \leq 0, \qquad \text{IPT} = 2, \qquad \text{INCTYP} = -1$$

where if INCTYP(I)=–1 the constraint is linear and if INCTYP(I)=–2 the constraint may be nonlinear.
The smallest value W can take is the minimum value of $f(\mathbf{x})$. In the figure shown below the solution is W_{min} and corresponds to $x = x^0$.

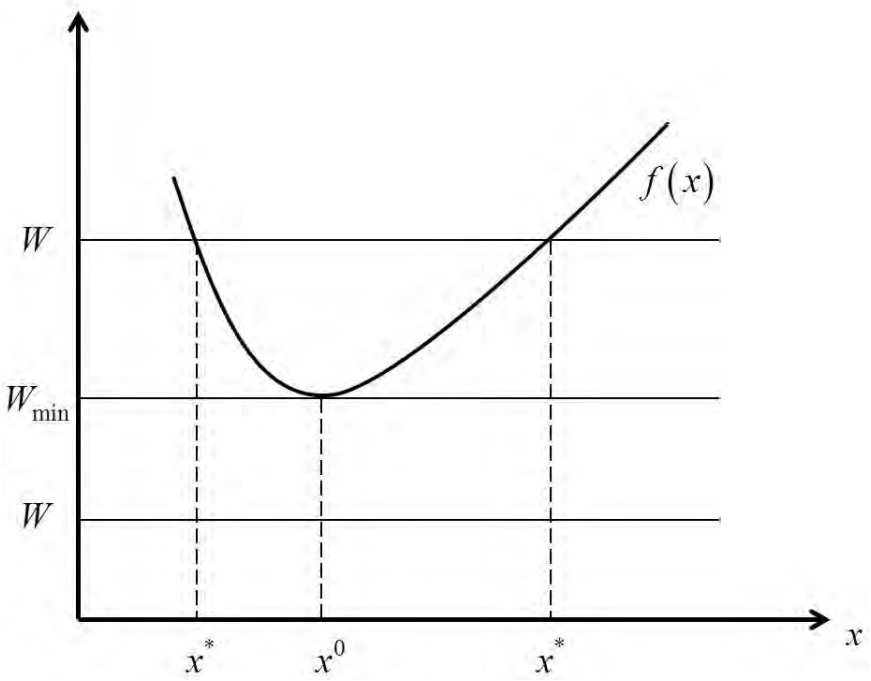

E.g., we can use the function

$$f(x_1, x_2) = (x_1 - 1)^2 + (x_2 - 2)^2 \geq 0,$$

which has a minimum at $x_1^0 = 1$, $x_2^0 = 2$ with $W_{min} = f(1,2) = 0$.

Homogenization minimization problem

Lets consider the homogenization minimization problem.
Given N, $c^{(r)}$, $\sigma_0^{(r)}$ $(r = 1, 2, ..., N)$, we need to find

$$\inf_{\substack{y^{(r)} \geq 0 \\ y^{(1)}=1}} \frac{H_\infty\left(y^{(r)}\right)}{F\left(y^{(r)}\right)} \equiv \inf_{y^{(i)} \geq 0} \left[f\left(y^{(2)}, y^{(3)}, ..., y^{(N)}\right)\right] \equiv \inf_{x^{(i)} \geq 0} \left[f\left(x^{(1)}, x^{(2)}, ..., x^{(N-1)}\right)\right]$$

where

$$f = \frac{H_\infty}{F}, \qquad \text{with} \quad x^{(i)} = y^{(1+i)} \qquad i = 1, ..., N-1$$

$$H_\infty\left(y^{(r)}\right) = \sum_{r=1}^{N} c^{(r)} \left(\sigma_0^{(r)}\right)^2 y^{(r)} = c^{(1)} \left(\sigma_0^{(1)}\right)^2 + \sum_{s=1}^{N-1} c^{(1+s)} \left(\sigma_0^{(1+s)}\right)^2 x^{(s)},$$

$$T_1 = \sum_{s=1}^{N} \frac{c^{(s)} y^{(s)}}{3\, y^{(s)} + 2}, \qquad T_2 = \sum_{s=1}^{N} \frac{c^{(s)}}{3\, y^{(s)} + 2}, \quad 3\, T_1 + 2\, T_2 = \sum_{s=1}^{N} c^{(s)} = 1,$$

$$T_2 = \sum_{s=1}^{N} \frac{c^{(s)}}{3\, y^{(s)} + 2} = \frac{c^{(1)}}{5} + \sum_{s=2}^{N} \frac{c^{(s)}}{3\, y^{(s)} + 2} = \frac{c^{(1)}}{5} + \sum_{q=1}^{N-1} \frac{c^{(1+q)}}{3\, x^{(q)} + 2}, \quad T_1 = \frac{1 - 2\, T_2}{3},$$

$$F = \frac{T_1}{T_2}.$$

For the minimization problem we need to calculate $\partial f / \partial x^{(i)}$:

$$\frac{\partial f}{\partial x^{(i)}} = \frac{1}{F} \frac{\partial H_\infty}{\partial x^{(i)}} - \frac{\partial H_\infty}{F^2} \frac{\partial F}{\partial x^{(i)}} \qquad \Rightarrow \qquad \boxed{\frac{\partial f}{\partial x^{(i)}} = \frac{1}{F} \left(\frac{\partial H_\infty}{\partial x^{(i)}} - f \frac{\partial F}{\partial x^{(i)}} \right)}$$

where

$$H_\infty\left(y^{(r)}\right) = c^{(1)} \left(\sigma_0^{(1)}\right)^2 + \sum_{s=1}^{N-1} c^{(1+s)} \left(\sigma_0^{(1+s)}\right)^2 x^{(s)} \quad \Rightarrow \quad \boxed{\frac{\partial H_\infty}{\partial x^{(i)}} = c^{(1+i)} \left(\sigma_0^{(1+i)}\right)^2} \quad i = 1, 2, ..., N-1$$

$$T_2 = \frac{c^{(1)}}{5} + \sum_{q=1}^{N-1} \frac{c^{(1+q)}}{3\, x^{(q)} + 2} \quad \Rightarrow \quad \boxed{\frac{\partial T_2}{\partial x^{(i)}} = -\frac{3\, c^{(1+i)}}{\left(3\, x^{(i)} + 2\right)^2}}$$

$$T_1 = \frac{1 - 2\, T_2}{3} \quad \Rightarrow \quad \boxed{\frac{\partial T_1}{\partial x^{(i)}} = -\frac{2}{3} \frac{\partial T_2}{\partial x^{(i)}}}$$

$$\frac{\partial F}{\partial x^{(i)}} = \frac{1}{T_2} \frac{\partial T_1}{\partial x^{(i)}} - \frac{T_1}{T_2^2} \frac{\partial T_2}{\partial x^{(i)}} \quad \Rightarrow \quad \boxed{\frac{\partial F}{\partial x^{(i)}} = \frac{1}{T_2} \left(\frac{\partial T_1}{\partial x^{(i)}} - F \frac{\partial T_2}{\partial x^{(i)}} \right)} \quad \Rightarrow$$

$$\frac{\partial F}{\partial x^{(i)}} = -\frac{2}{3\, T_2} \frac{\partial T_2}{\partial x^{(i)}} - \frac{T_1}{T_2^2} \frac{\partial T_2}{\partial x^{(i)}} = -\frac{1}{T_2} \left(\frac{2}{3} + \frac{T_1}{T_2} \right) \frac{\partial T_2}{\partial x^{(i)}} = -\frac{3\, T_1 + 2\, T_2}{3\, T_2^2} \frac{\partial T_2}{\partial x^{(i)}} =$$

$$= -\frac{1}{3\, T_2^2} \frac{\partial T_2}{\partial x^{(i)}} = -\frac{1}{3\, T_2^2} \left[-\frac{3\, c^{(1+i)}}{\left(3\, x^{(i)} + 2\right)^2} \right] = \frac{c^{(1+i)}}{\left[T_2 \left(3\, x^{(i)} + 2\right)\right]^2}, \quad i = 1, 2, ..., N-1$$

CONMAX

For $N = 4$, CONMAX defines the problem as follows:
Minimize W subjected to the constraints

$$\begin{aligned} f\left(x^{(1)}, x^{(2)}, x^{(3)}\right) &\leq W, && \text{IPT} = 1, && \text{INCTYP}(1) = 1, \\ -x^{(1)} &\leq 0, && \text{IPT} = 2, && \text{INCTYP}(2) = -1, \\ -x^{(2)} &\leq 0, && \text{IPT} = 3, && \text{INCTYP}(3) = -1, \\ -x^{(3)} &\leq 0, && \text{IPT} = 4, && \text{INCTYP}(4) = -1. \end{aligned}$$

In SUBROUTINE **KOPT** (FVALUE,SIG0,C,Y,N,NOEL,NPT)

IOPT=1 (no extra options to be used)
NPARM=3 (3 parameters $x^{(i)}$)
NUMGR=4 (1+3 constraints)
ITLIM=1000 (max number of iterations)
IFUN=1 (FUN(I) is not used)
IPTB=5, INDM=2 (see next lines)
PTTBL(IPTB, INDM)
PTTBL$(2,1) = 4$ (number of phases)
PTTBL$(2,1) = c^{(1)}$, PTTBL$(2,2) = \sigma_0^{(1)}$,
PTTBL$(3,1) = c^{(2)}$, PTTBL$(3,2) = \sigma_0^{(2)}$,
PTTBL$(4,1) = c^{(3)}$, PTTBL$(4,2) = \sigma_0^{(3)}$,
PTTBL$(5,1) = c^{(4)}$, PTTBL$(5,2) = \sigma_0^{(4)}$.
LIWRK=7*(NUMGR+NPARM)+3
LWRK=(2*NPARM+4*NUMGR+27)*NPARM+11*NUMGR+13

PARAM(1), PARAM(2), PARAM(3), PARAM(4) first guess

In SUBROUTINE **KFNSET** (NPARM,NUMGR,PTTBL,IPTB,INDM,X,IPT,
+INDFN,ICNTYP,CONFUN,NOEL,NPT)

Read data from PTTBL
IPT=constraint number (1,2,3,4)

For IPT=1
ICNTYP(IPT) = 1
CONFUN(IPT, 1) = f (define the constraint function)
if INDFN = 1 (needs the derivatives as well)
CONFUN (IPT, $1 + i$) = $\partial f / \partial x^{(i)}$, $i = 1, 2, 3$

For IPT=2, 3, 4
ICNTYP(IPT) = -1

$\text{CONFUN(IPT}, 1) = -x^{(IPT-1)}$ (define the constraint function)
if INDFN $= 1$ (needs the derivatives as well)
  $\text{CONFUN (IPT}, 1 + i) = -1, \quad i = 1, 2, 3$

Appendix II

Unit Cell Periodic Boundary Conditions

The unit cell is a cube with edge size L , as shown below. We label the faces as follows:

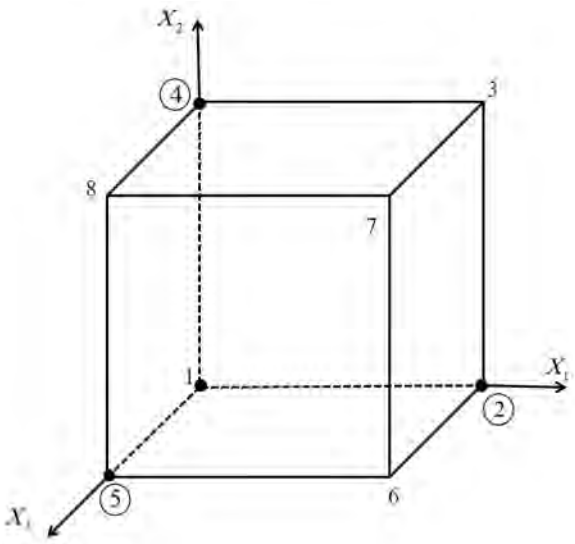

Figure II.1: Periodic unit cell.

LEFT:	$x_1 = 0,$	includes vertices	$(1, 5, 8, 4)$
RIGHT:	$x_1 = L,$	includes vertices	$(2, 6, 7, 3)$
BOT:	$x_2 = 0,$	includes vertices	$(1, 2, 6, 5)$
TOP:	$x_2 = L,$	includes vertices	$(4, 3, 7, 8)$
BACK:	$x_3 = 0,$	includes vertices	$(1, 2, 3, 4)$
FRONT:	$x_3 = L,$	includes vertices	$(5, 6, 7, 8)$

The definition of periodicity implies that the displacement field is periodic about an average (macroscopic) deformation gradient $\mathbf{F}$ so that

$$\mathbf{u}(\mathbf{X}) = (\mathbf{F} - \boldsymbol{\delta}) \cdot \mathbf{X} + \mathbf{u}^*(\mathbf{X}) \tag{II.1}$$

where $\mathbf{X}$ is the position vector of a material point in the undeformed configuration, $\boldsymbol{\delta}$ is the second-order identity tensor, and $\mathbf{u}^*(\mathbf{X})$ is a periodic field with zero mean strain on the unit cell (e.g., Suquet [1985] in "Homogenization Techniques for Composite Media", CISM). Then

$$\begin{gathered} \mathbf{u}^{*RIGHT} = \mathbf{u}^{*LEFT}, \quad \mathbf{u}^{*TOP} = \mathbf{u}^{*BOT}, \quad \mathbf{u}^{*FRONT} = \mathbf{u}^{*BACK} \\ \text{and} \\ \int\limits_{unit\ cell} (\nabla \mathbf{u}^* + \mathbf{u}^* \nabla)\, dV = \mathbf{0} \end{gathered} \tag{II.2}$$

This implies that $\mathbf{u}^*$ takes the same value at all vertices of the cube.
We fix vertex 1 in order to eliminate rigid body translations, i.e., we set

$$\mathbf{u}^{(1)} = \mathbf{u}(\mathbf{0}) = \mathbf{0} \tag{II.3}$$

In view of the periodicity of $\mathbf{u}^*$

$$u_i^{(2)} - \underbrace{u_i^{(1)}}_{0} = (F_{i1} - \delta_{i1})\, L \quad \Rightarrow \quad u_i^{(2)} = (F_{i1} - \delta_{i1})\, L = \text{known}, \qquad \text{i} = 1,2,3. \tag{II.4}$$

Similarly, we find

$$u_i^{(4)} = (F_{i2} - \delta_{i2})\, L = \text{known}, \qquad \text{i} = 1,2,3, \tag{II.5}$$

$$u_i^{(5)} = (F_{i3} - \delta_{i3})\, L = \text{known}, \qquad \text{i} = 1,2,3, \tag{II.6}$$

Next we consider nodes at the same position on opposite faces. In view of the periodicity of $\mathbf{u}^*$, we have

$$u_i^{\text{RIGHT}} - u_i^{\text{LEFT}} = (F_{i1} - \delta_{i1})\, L = u_i^{(2)} \quad \Rightarrow \quad \mathbf{u}^{\text{RIGHT}} - \mathbf{u}^{\text{LEFT}} - \mathbf{u}^{(2)} = \mathbf{0} \tag{II.7}$$

$$u_i^{\text{TOP}} - u_i^{\text{BOT}} = (F_{i2} - \delta_{i2})\, L = u_i^{(4)} \quad \Rightarrow \quad \mathbf{u}^{\text{TOP}} - \mathbf{u}^{\text{BOT}} - \mathbf{u}^{(4)} = \mathbf{0} \tag{II.8}$$

$$u_i^{\text{FRONT}} - u_i^{\text{BACK}} = (F_{i3} - \delta_{i3})\, L = u_i^{(5)} \quad \Rightarrow \quad \mathbf{u}^{\text{FRONT}} - \mathbf{u}^{\text{BACK}} - \mathbf{u}^{(5)} = \mathbf{0} \tag{II.9}$$

Equations (II.7)-(II.9) show that the periodic constraints between all corresponding ("opposite") boundary points can be written in terms of the displacements of only three vertex points, namely $\mathbf{u}^{(2)}$, $\mathbf{u}^{(4)}$, and $\mathbf{u}^{(5)}$; the displacements are defined, in turn, by equations (II.4)-(II.6) in terms of the average deformation gradient $\mathbf{F}$. In ABAQUS, for given $\mathbf{F}$, we impose boundary conditions on $\left(\mathbf{u}^{(2)}, \mathbf{u}^{(4)}, \mathbf{u}^{(5)}\right)$ according to (II.4)-(II.6), and conditions (II.7)-(II.9) are imposed by writing a "user MPC" subroutine.

Examples

i. $\mathbf{F} = \sum_{i=1}^{3} \lambda_i \, \mathbf{e}_i \mathbf{e}_i$ (principal stretching)

$$u_1^{(2)} = (\lambda_1 - 1)\, L, \qquad u_2^{(2)} = u_3^{(2)} = 0,$$
$$u_2^{(4)} = (\lambda_2 - 1)\, L, \qquad u_1^{(4)} = u_3^{(4)} = 0,$$
$$u_3^{(5)} = (\lambda_3 - 1)\, L, \qquad u_1^{(5)} = u_2^{(5)} = 0.$$

ii. $\mathbf{F} = \lambda \, \mathbf{e}_1 \mathbf{e}_1 + \lambda_t \, (\mathbf{e}_2 \, \mathbf{e}_2 + \mathbf{e}_3 \, \mathbf{e}_3)$ (uniaxial tension)

$$u_1^{(2)} = (\lambda - 1)\, L, \qquad u_2^{(2)} = u_3^{(2)} = 0,$$
$$u_2^{(4)} = (\lambda_t - 1)\, L, \qquad u_1^{(4)} = u_3^{(4)} = 0,$$
$$u_3^{(5)} = (\lambda_t - 1)\, L, \qquad u_1^{(5)} = u_2^{(5)} = 0.$$

iii. $\mathbf{F} = \boldsymbol{\delta} + \gamma \, \mathbf{e}_1 \mathbf{e}_2$ (simple shear)

$$u_2^{(2)} = \gamma \, L, \qquad u_1^{(2)} = u_3^{(2)} = 0,$$
$$\mathbf{u}^{(4)} = \mathbf{u}^{(5)} = \mathbf{0}.$$

Appendix III

Triaxiality and Lode Angle Control

Unit-cell triaxiality control (Barsoum and Faleskog, IJSS 2007)

We consider the aforementioned unit cell and define the coordinate axes of the unit cell so that they coincide with principal directions of the **average** (macroscopic) stress and the **average** (macroscopic) deformation rate, i.e., $\boldsymbol{\sigma} = \sum_{i=1}^{3} \sigma_i \, \mathbf{e}_i \mathbf{e}_i$ and $\mathbf{D} = \sum_{i=1}^{3} D_i \, \mathbf{e}_i \mathbf{e}_i$. Then the displacements of the "reference vertices" 2, 4, and 5, must be of the form

$$\mathbf{u}^{(2)}(t) = U_1(t)\,\mathbf{e}_1, \qquad \mathbf{u}^{(4)}(t) = U_2(t)\,\mathbf{e}_2, \qquad \mathbf{u}^{(5)}(t) = U_3(t)\,\mathbf{e}_3, \tag{III.1}$$

The **average** stress tensor $\boldsymbol{\sigma} = \sum_{i=1}^{3} \sigma_i \, \mathbf{e}_i \mathbf{e}_i$ and the **average** deformation rate $\mathbf{D} = \sum_{i=1}^{3} D_i \, \mathbf{e}_i \mathbf{e}_i$ can be represented as vectors in the system $\mathbf{e}_i$: $\boldsymbol{\Sigma} = \sigma_{\mathbf{i}} \, \mathbf{e}_{\mathbf{i}}$, $\dot{\boldsymbol{\Delta}} = D_i \, \mathbf{e}_i$. Let

$$\begin{aligned} \{\Sigma\} = \begin{Bmatrix} \sigma_1 \\ \sigma_2 \\ \sigma_3 \end{Bmatrix} &= c(t) \left(\frac{3\,X_\Sigma}{2} \begin{Bmatrix} 1 \\ 1 \\ 1 \end{Bmatrix} + \begin{Bmatrix} \cos\theta_D \\ -\cos\left(\theta_D + \frac{\pi}{3}\right) \\ -\cos\left(\theta_D - \frac{\pi}{3}\right) \end{Bmatrix} \right) = \\ &= c(t) \left(\frac{3\,X_\Sigma}{2} \begin{Bmatrix} 1 \\ 1 \\ 1 \end{Bmatrix} + \begin{Bmatrix} \cos\left(\theta + \frac{\pi}{6}\right) \\ \sin\theta \\ -\cos\left(\theta - \frac{\pi}{6}\right) \end{Bmatrix} \right), \quad \left(\theta_D = \theta + \frac{\pi}{6}\right) \end{aligned} \tag{III.2}$$

where $c(t)$ increases from zero, X_Σ is the stress triaxiality, θ_D the Lode angle. We also write

$$\left\{\dot{\Delta}\right\} = \begin{Bmatrix} D_1 \\ D_2 \\ D_3 \end{Bmatrix} = \begin{bmatrix} \frac{\dot{U}_1}{L_1+U_1} & & \\ & \frac{\dot{U}_2}{L_2+U_2} & \\ & & \frac{\dot{U}_3}{L_3+U_3} \end{bmatrix} = \begin{bmatrix} \frac{1}{L_1+U_1} & & \\ & \frac{1}{L_2+U_2} & \\ & & \frac{1}{L_3+U_3} \end{bmatrix} \begin{Bmatrix} \dot{U}_1 \\ \dot{U}_2 \\ \dot{U}_3 \end{Bmatrix} \equiv [Q]^{-1} \left\{\dot{U}\right\} \tag{III.3}$$

where L_i is the original length of the sides of the unit-cell and

$$[Q] = \begin{bmatrix} L_1 + U_1 & & \\ & L_2 + U_2 & \\ & & L_3 + U_3 \end{bmatrix} \tag{III.4}$$

so that

$$\left\{\dot{U}\right\} = [Q] \left\{\dot{\Delta}\right\} \tag{III.5}$$

The rate of work is

$$\dot{W} = \boldsymbol{\sigma} : \mathbf{D} = \boldsymbol{\Sigma} \cdot \dot{\boldsymbol{\Delta}} = \lfloor \boldsymbol{\Sigma} \rfloor \left\{\dot{\boldsymbol{\Delta}}\right\} \tag{III.6}$$

In ABAQUS we may let $\left\{\dot{\Delta}\right\}$ be the nodal d.o.f. of a fictitious node, prescribe the corresponding generalized nodal loads $\{\Sigma\}$, impose the relationship $\left\{\dot{U}\right\} = [Q] \left\{\dot{\Delta}\right\}$ through a user MPC, and solve the finite element problem, i.e., determine the average strains in the unit cell. The main disadvantage here is that we have load-control and this may be a problem with perfect plasticity or softening.

In order to avoid this difficulty, we introduce another coordinate system with base vectors $\mathbf{a}_i = a_k^i \, \mathbf{e}_k$, which are chosen in such a way that the generalized nodal load $\boldsymbol{\Sigma}$ of the fictitious node has only one non-zero component in the new system $\mathbf{a}_i$, i.e., we align say $\mathbf{a}_1$ with the direction of vector $\boldsymbol{\sigma}$. Let P_i be the new components. In the general case we have that

$$\boldsymbol{\Sigma} = \sigma_{\mathbf{i}} \, \mathbf{e_i} = \mathbf{P_i} \, \mathbf{a_i} \quad \Rightarrow \quad \sigma_{\mathbf{i}} = \mathbf{P_j} \, \mathbf{a_j} \cdot \mathbf{e_i} = \mathbf{P_j} \left(\mathbf{a_k^j} \, \mathbf{e_k} \right) \cdot \mathbf{e_i} = \mathbf{P_j} \, \mathbf{a_k^j} \, \delta_{\mathbf{ki}} = \mathbf{a_i^j} \, \mathbf{P_j} \quad \Rightarrow$$

$$\begin{Bmatrix} \sigma_1 \\ \sigma_2 \\ \sigma_3 \end{Bmatrix} = \begin{bmatrix} a_1^1 & a_1^2 & a_1^3 \\ a_2^1 & a_2^2 & a_2^1 \\ a_3^1 & a_3^2 & a_3^3 \end{bmatrix} \begin{Bmatrix} P_1 \\ P_2 \\ P_3 \end{Bmatrix} = \begin{bmatrix} \{\mathbf{a}_1\} & \{\mathbf{a}_2\} & \{\mathbf{a}_3\} \end{bmatrix} \begin{Bmatrix} P_1 \\ P_2 \\ P_3 \end{Bmatrix} \equiv [C] \begin{Bmatrix} P_1 \\ P_2 \\ P_3 \end{Bmatrix} \quad \Rightarrow$$

$$\{\Sigma\} = [C] \{P\}, \qquad [C] = \begin{bmatrix} \{\mathbf{a}_1\} & \{\mathbf{a}_2\} & \{\mathbf{a}_3\} \end{bmatrix},$$

where $[C] [C]^T = [\delta]$ and $\{\mathbf{a}_i\}$ are the components of $\mathbf{a}_i$ in the principal system $\mathbf{e}_i$.

Let $\left\{\dot{\delta}\right\}$ be the components w.r.t. the new system of the conjugate generalized nodal d.o.f. $\left\{\dot{\Delta}\right\}$ at the fictitious node, i.e., $\dot{\boldsymbol{\Delta}} = D_i \, \mathbf{e}_i = \dot{\delta}_i \, \mathbf{a}_i$. Then (as with stress)

$$\left\{\dot{\Delta}\right\} = [C] \left\{\dot{\delta}\right\} \tag{III.7}$$

so that

$$\dot{W} = \boldsymbol{\sigma} : \mathbf{D} = \boldsymbol{\Sigma} \cdot \dot{\boldsymbol{\Delta}} = \lfloor \sigma \rfloor \{\mathbf{D}\} = \lfloor \mathbf{P} \rfloor \left\{\dot{\delta}\right\} \tag{III.8}$$

Also, substituting (III.7) into equation (III.5), i.e., into $\left\{\dot{U}\right\} = [Q] \left\{\dot{\Delta}\right\}$, we find

$$\left\{\dot{U}\right\} = [Q] [C] \left\{\dot{\delta}\right\} \tag{III.9}$$

The choice of the orthonormal basis $\mathbf{a}_i$ is made as follows:

$$\mathbf{a}_i = \frac{\mathbf{c}_i}{|\mathbf{c}_i|} \tag{III.10}$$

with

$$\mathbf{c}_1 = \sigma_1\,\mathbf{e}_1 + \sigma_2\,\mathbf{e}_2 + \sigma_3\,\mathbf{e}_3 = \boldsymbol{\Sigma}, \tag{III.11}$$

$$\mathbf{c}_2 = \sigma_2\,\mathbf{e}_1 - \sigma_1\,\mathbf{e}_2, \tag{III.12}$$

$$\mathbf{c}_3 = \mathbf{c}_1 \times \mathbf{c}_2 = \sigma_1\,\sigma_3\,\mathbf{e}_1 + \sigma_2\,\sigma_3\,\mathbf{e}_2 - \left(\sigma_1^2 + \sigma_2^2\right)\mathbf{e}_3. \tag{III.13}$$

so that

$$\boldsymbol{\Sigma} = \sigma_{\mathbf{1}}\,\mathbf{e}_{\mathbf{1}} + \sigma_{\mathbf{2}}\,\mathbf{e}_{\mathbf{2}} + \sigma_{\mathbf{3}}\,\mathbf{e}_{\mathbf{3}} = \mathbf{P_1}\,\mathbf{a_1} \qquad \mathbf{P_1} = |\boldsymbol{\Sigma}| = \sqrt{\sigma_{\mathbf{1}}^{\mathbf{2}} + \sigma_{\mathbf{2}}^{\mathbf{2}} + \sigma_{\mathbf{3}}^{\mathbf{2}}} \qquad \dot{\mathbf{W}} = \mathbf{P_1}\,\dot{\delta}_{\mathbf{1}} \tag{III.14}$$

Note: In the special case where $\sigma_1 = \sigma_2 = 0$, (III.12) and (III.13) $\Rightarrow \mathbf{c}_2 = \mathbf{c}_3 = \mathbf{0}$. Therefore, in such a case, we set

$$\mathbf{c}_1 = \mathbf{e}_3, \qquad \mathbf{c}_2 = \mathbf{e}_1, \qquad \mathbf{c}_3 = \mathbf{e}_2 \qquad \text{so that} \qquad \boldsymbol{\Sigma} = \sigma_{\mathbf{3}}\,\mathbf{e}_{\mathbf{3}} = \sigma_{\mathbf{3}}\,\mathbf{a}_{\mathbf{1}}$$

In standard unit-cell calculations, we prescribe $\left\{\dot{U}\right\}$ in terms of the average deformation gradient $\mathbf{F}$ of the unit-cell. Instead, here we tie $\left\{\dot{U}\right\}$ to $\left\{\dot{\delta}\right\}$ according to the relationship $\left\{\dot{U}\right\} = [Q]\,[C]\left\{\dot{\delta}\right\}$ through a user MPC (see notes below) and the loads are applied through $\{P\}$ and $\left\{\dot{\delta}\right\}$ at the fictitious node. In particular, we choose the stress triaxiality X_Σ and the Lode angle θ_D, determine the principal stresses from (III.2), define $\mathbf{a}_i$ from (III.10), and then calculate $[C]$. At every increment we also calculate $[Q]$ from (III.4) and impose the relationship $\left\{\dot{U}\right\} = [Q]\,[C]\left\{\dot{\delta}\right\}$ through a user MPC. Finally, we specify $\dot{\delta}_1$ and $P_2 = P_3 = 0$, solve the finite element problem, and determine the average stresses and strains in the unit-cell.
Note: At the end of the calculation it is a good idea to check that the average values of all shear components indeed vanish, i.e., $\sigma_{12} = \sigma_{13} = \sigma_{23} = 0$ and $\varepsilon_{12} = \varepsilon_{13} = \varepsilon_{23} = 0$.

ABAQUS MPC

$$f\left(U_i, \delta_1, \delta_2, \delta_3\right) = U_i - \underbrace{\frac{U_i|_n + L_i * TMP\left(\delta_1, \delta_2, \delta_3\right)}{1 - TMP\left(\delta_1, \delta_2, \delta_3\right)}}_{AUX1} = U_i - AUX1\left(\delta_1, \delta_2, \delta_3\right) = 0 \tag{III.15}$$

where

$$TMP\left(\delta_1, \delta_2, \delta_3\right) = C_{i1}\left(\delta_1 - \delta_1|_n\right) + C_{i2}\left(\delta_2 - \delta_2|_n\right) + C_{i3}\left(\delta_3 - \delta_3|_n\right) \tag{III.16}$$

so that

$$\frac{\partial f}{\partial \delta_k} = -\frac{L_i}{1-TMP}\underbrace{\frac{\partial TMP}{\partial \delta_k}}_{C_{ik}} + \frac{U_i|_n + L_i * TMP}{(1-TMP)^2}\underbrace{\left(-\frac{\partial TMP}{\partial \delta_k}\right)}_{-C_{ik}}$$

$$= -\frac{1}{1-TMP}\left(L_i + \underbrace{\frac{U_i|_n + L_i * TMP}{1-TMP}}_{AUX1}\right) C_{ik} \tag{III.17}$$

$$= \underbrace{-\frac{L_i + AUX1}{1-TMP}}_{AUX} C_{ik} \equiv AUX * C_{ik}\ .$$

Then

$$A\,(1) = \frac{\partial f}{\partial U_i} = 1 \tag{III.18}$$

$$A\,(2) = \frac{\partial f}{\partial \delta_1} = AUX * C_{i1} \tag{III.19}$$

$$A\,(3) = \frac{\partial f}{\partial \delta_2} = AUX * C_{i2} \tag{III.20}$$

$$A\,(4) = \frac{\partial f}{\partial \delta_3} = AUX * C_{i3} \tag{III.21}$$

$$JDOFN\,(1) = i \tag{III.22}$$

$$JDOFN\,(2) = 1 \tag{III.23}$$

$$JDOFN\,(3) = 2 \tag{III.24}$$

$$JDOFN\,(4) = 3 \tag{III.25}$$

$$UE = AUX1 \tag{III.26}$$

The Lode Parameter

$$\sigma_1 = \frac{2}{3}\,\sigma_e \cos\left(\frac{\pi}{6} + \theta\right) + p = \frac{2}{3}\,\sigma_e \cos\theta_D + p \tag{III.27}$$

$$\sigma_2 = \frac{2}{3}\,\sigma_e \sin\theta + p = -\frac{2}{3}\,\sigma_e \cos\left(\theta_D + \frac{\pi}{3}\right) + p \tag{III.28}$$

$$\sigma_3 = -\frac{2}{3}\,\sigma_e \cos\left(\frac{\pi}{6} - \theta\right) + p = -\frac{2}{3}\,\sigma_e \cos\left(\theta_D - \frac{\pi}{3}\right) + p \tag{III.29}$$

where

$$\sigma_1 \geq \sigma_2 \geq \sigma_3 \qquad \text{and} \qquad \theta = \theta_D - \frac{\pi}{6}$$

Moreover

$$J_2 = \frac{1}{2}\,\mathbf{s} : \mathbf{s} = \frac{1}{3}\,\sigma_e^2, \qquad J_3 = \det\mathbf{s} = \frac{2}{27}\,\sigma_e^3 \cos 3\theta_D = -\frac{2}{27}\,\sigma_e^3 \sin 3\theta \tag{III.30}$$

so that

$$\cos 3\theta_D = -\sin 3\,\theta = \frac{27}{2}\det\frac{\mathbf{s}}{\sigma_e} = \frac{3\sqrt{3}}{2}\frac{J_3}{J_2^{3/2}}, \quad \left(-\frac{\pi}{2} \leq 3\,\theta \leq \frac{\pi}{2} \quad \text{and} \quad 0 \leq 3\,\theta_{\mathrm{D}} \leq \pi\right) \tag{III.31}$$

Also define

$$\mu = \frac{2\,\sigma_2 - \sigma_1 - \sigma_3}{\sigma_1 - \sigma_3} = \frac{3\,s_2}{s_1 - s_3} = \sqrt{3}\,\tan\left(\theta_D - \frac{\pi}{6}\right) = \sqrt{3}\,\tan\theta \tag{III.32}$$

$$L = \tan\left(\theta_D - \frac{\pi}{6}\right) = \tan\theta = \frac{\mu}{\sqrt{3}} \qquad \left(-\frac{\pi}{6} \le \theta \le \frac{\pi}{6} \quad \text{and} \quad 0 \le \theta_D \le \frac{\pi}{3}\right) \tag{III.33}$$

$$\theta = -\frac{\pi}{6} \qquad \left(\theta_D = 0, \quad \mu = -1, \quad L = -\frac{1}{\sqrt{3}}\right) \quad \sigma_1 > \sigma_2 = \sigma_3 \qquad \text{(uniaxial tension)}, \tag{III.34}$$

$$\theta = 0 \qquad \left(\theta_D = \frac{\pi}{6}, \quad \mu = 0, \quad L = 0\right) \qquad \sigma_1 > \sigma_2 = 0 > \sigma_3 = -\sigma_1 \ \text{(shear 1-3)}, \tag{III.35}$$

$$\theta = \frac{\pi}{6} \qquad \left(\theta_D = \frac{\pi}{3}, \quad \mu = 1, \quad L = \frac{1}{\sqrt{3}}\right) \qquad \sigma_1 = \sigma_2 > \sigma_3 \ \text{(uniaxial compression)}. \tag{III.36}$$

$$-\frac{\pi}{6} < \theta < \frac{\pi}{6} \left(0 < \theta_D < \frac{\pi}{3}, \quad -1 < \mu < 1, \quad -\frac{1}{\sqrt{3}} < L < \frac{1}{\sqrt{3}}\right) \quad \sigma_1 > \sigma_2 > \sigma_3. \tag{III.37}$$

Triaxiality and the Lode angle

$$X_\Sigma = \frac{p}{\sigma_e} \qquad \Rightarrow \qquad p = X_\Sigma\,\sigma_e, \tag{III.38}$$

$$\sigma_1 = \sigma_e\left[\frac{2}{3}\cos\left(\frac{\pi}{6} + \theta\right) + X_\Sigma\right] = \sigma_e\left(\frac{2}{3}\cos\theta_D + X_\Sigma\right), \tag{III.39}$$

$$\sigma_2 = \sigma_e\left(\frac{2}{3}\sin\theta + X_\Sigma\right) = \sigma_e\left[-\frac{2}{3}\cos\left(\theta_D + \frac{\pi}{3}\right) + X_\Sigma\right], \tag{III.40}$$

$$\sigma_3 = \sigma_e\left[-\frac{2}{3}\cos\left(\frac{\pi}{6} - \theta\right) + X_\Sigma\right] = \sigma_e\left[-\frac{2}{3}\cos\left(\theta_D - \frac{\pi}{3}\right) + X_\Sigma\right], \tag{III.41}$$

$$\sigma_1 \ge \sigma_2 \ge \sigma_3. \tag{III.42}$$

The case of hydrostatic tension/compression corresponds to $\boldsymbol{\sigma} = \sigma\,\boldsymbol{\delta}$, so that $\sigma_e = 0$, $p = \sigma$, $X_\Sigma = \infty$ and $\theta =$ undetermined.

Examples

$$X_\Sigma = \frac{1}{3}, \qquad \theta_D = 0^\circ \quad (\mu = -1): \quad \left\{\begin{array}{c}\sigma_1\\ \sigma_2\\ \sigma_3\end{array}\right\} = \left\{\begin{array}{c}\sigma_e\\ 0\\ 0\end{array}\right\}, \tag{III.43}$$

$$X_\Sigma = -\frac{1}{3}, \qquad \theta_D = 60^\circ \quad (\mu = 1): \quad \left\{\begin{array}{c}\sigma_1\\ \sigma_2\\ \sigma_3\end{array}\right\} = \left\{\begin{array}{c}0\\ 0\\ -\sigma_e\end{array}\right\}, \tag{III.44}$$

$$X_\Sigma = 1, \qquad \theta_D = 0^\circ \quad (\mu = -1): \quad \left\{ \begin{array}{c} \sigma_1 \\ \sigma_2 \\ \sigma_3 \end{array} \right\} = \sigma_e \left\{ \begin{array}{c} 5/3 \\ 2/3 \\ 2/3 \end{array} \right\} = \left\{ \begin{array}{c} \sigma_e \\ 0 \\ 0 \end{array} \right\} + \frac{2}{3}\sigma_e \left\{ \begin{array}{c} 1 \\ 1 \\ 1 \end{array} \right\}, \tag{III.45}$$

$$X_\Sigma = 1, \qquad \theta_D = 60^\circ \quad (\mu = 1): \quad \left\{ \begin{array}{c} \sigma_1 \\ \sigma_2 \\ \sigma_3 \end{array} \right\} = \sigma_e \left\{ \begin{array}{c} 4/3 \\ 4/3 \\ 1/3 \end{array} \right\} = \left\{ \begin{array}{c} 0 \\ 0 \\ -\sigma_e \end{array} \right\} + \frac{4}{3}\sigma_e \left\{ \begin{array}{c} 1 \\ 1 \\ 1 \end{array} \right\}, \tag{III.46}$$

$$X_\Sigma = -1, \qquad \theta_D = 0^\circ \quad (\mu = -1): \quad \left\{ \begin{array}{c} \sigma_1 \\ \sigma_2 \\ \sigma_3 \end{array} \right\} = \sigma_e \left\{ \begin{array}{c} -1/3 \\ -4/3 \\ -4/3 \end{array} \right\} = \left\{ \begin{array}{c} \sigma_e \\ 0 \\ 0 \end{array} \right\} + \frac{4}{3}\sigma_e \left\{ \begin{array}{c} -1 \\ -1 \\ -1 \end{array} \right\}, \tag{III.47}$$

$$X_\Sigma = -1, \qquad \theta_D = 60^\circ \quad (\mu = 1): \quad \left\{ \begin{array}{c} \sigma_1 \\ \sigma_2 \\ \sigma_3 \end{array} \right\} = \sigma_e \left\{ \begin{array}{c} -2/3 \\ -2/3 \\ -5/3 \end{array} \right\} = \left\{ \begin{array}{c} 0 \\ 0 \\ -\sigma_e \end{array} \right\} + \frac{2}{3}\sigma_e \left\{ \begin{array}{c} -1 \\ -1 \\ -1 \end{array} \right\}. \tag{III.48}$$

Appendix IV

Details of Calculations

Stationarity conditions in (2.40) **and the variation of** $\bar{\sigma}_0$ **with respect to** $c^{(i)}$ **and** $\sigma_0^{(i)}$

The usual stationarity conditions of (2.40) (valid for $y^{(r)} > 0$, i.e., $y^{(r)} \neq 0$) are

$$\frac{\partial}{\partial y^{(i)}}\left(\frac{\sigma_\infty^2}{F}\right) = 0 \quad \Rightarrow \quad \frac{\partial \sigma_\infty^2}{\partial y^{(i)}}\frac{1}{F} - \frac{\sigma_\infty^2}{F^2}\frac{\partial F}{\partial y^{(i)}} = 0 \quad \Rightarrow \quad \left(\frac{\partial \sigma_\infty^2}{\partial y^{(i)}} - \frac{\sigma_\infty^2}{F}\frac{\partial F}{\partial y^{(i)}}\right)\frac{1}{F} = 0 \tag{IV.1}$$

$$\frac{\partial F}{\partial y^{(i)}}\underbrace{\frac{\sigma_\infty^2}{F}}_{\bar{\sigma}_0^2} - \frac{\partial \sigma_\infty^2}{\partial y^{(i)}} = 0 \quad \text{or} \quad \frac{\partial F}{\partial y^{(i)}}\bar{\sigma}_0^2 - \frac{\partial \sigma_\infty^2}{\partial y^{(i)}} = 0 \qquad i = 2, 3, \ldots, N. \tag{IV.2}$$

We have that

$$F = \frac{T_1}{T_2}, \qquad \frac{\partial F}{\partial y^{(i)}} = \left(\frac{1}{T_1}\frac{\partial T_1}{\partial y^{(i)}} - \frac{1}{T_2}\frac{\partial T_2}{\partial y^{(i)}}\right) F, \qquad i = 1, 2, \ldots, N, \tag{IV.3}$$

$$\sigma_\infty^2 = \sum_{r=1}^{N} c^{(r)} \left(\sigma_0^{(r)}\right)^2 y^{(r)}, \qquad \frac{\partial \sigma_\infty^2}{\partial c^{(i)}} = \left(\sigma_0^{(i)}\right)^2 y^{(i)}, \qquad \frac{\partial \sigma_\infty^2}{\partial \sigma_0^{(i)}} = 2\, c^{(i)}\, \sigma_0^{(i)}\, y^{(i)}, \tag{IV.4}$$

$$\frac{\partial \sigma_\infty^2}{\partial y^{(i)}} = c^{(i)} \left(\sigma_0^{(i)}\right)^2, \qquad i = 1, 2, \ldots, N. \tag{IV.5}$$

The stationarity conditions (IV.2) can be written in the form

$$\left(\frac{\partial T_1}{\partial y^{(i)}}\frac{1}{T_2} - \frac{T_1}{T_2^2}\frac{\partial T_2}{\partial y^{(i)}}\right)\frac{\sigma_\infty^2}{T_1/T_2} - c^{(i)}\left(\sigma_0^{(i)}\right)^2 = 0 \quad \Rightarrow \tag{IV.6}$$

$$A^{(i)}\left(y^{(s)}\right) \equiv \left(\frac{1}{T_1}\frac{\partial T_1}{\partial y^{(i)}} - \frac{1}{T_2}\frac{\partial T_2}{\partial y^{(i)}}\right)\sigma_\infty^2 - c^{(i)}\left(\sigma_0^{(i)}\right)^2 = 0, \quad i = 2, 3, \ldots, N, \quad y^{(r)} \neq 0. \tag{IV.7}$$

The solution of the constrained optimization problem is found by using some standard package and equations (IV.7) are valid provided that $y^{(r)} \neq 0$ (in fact > 0). Let the optimal values be $\left(y^{(2)}, y^{(3)}, \ldots, y^{(N)}\right) = \left(\hat{y}^{(2)}, \hat{y}^{(3)}, \ldots, \hat{y}^{(N)}\right) \geq 0$, where $\hat{y}^{(r)} = \hat{y}^{(r)}\left(c^{(s)}, \sigma_0^{(s)}\right)$.

Variation of $\bar{\sigma}_0$ w.r.t. $c^{(i)}$ and $\sigma_0^{(i)}$

$$\bar{\sigma}_0^2 = \frac{\sigma_\infty^2\left(\hat{y}^{(s)}, c^{(s)}, \sigma_0^{(s)}\right)}{F\left(\hat{y}^{(s)}, c^{(s)}\right)} \qquad \Rightarrow$$

$$\begin{aligned} 2\,\bar{\sigma}_0 \frac{\partial \bar{\sigma}_0}{\partial c^{(i)}} &= \left(\frac{\partial \sigma_\infty^2}{\partial c^{(i)}} + \sum_{j=2}^{N} \frac{\partial \sigma_\infty^2}{\partial \hat{y}^{(j)}} \frac{\partial \hat{y}^{(j)}}{\partial c^{(i)}}\right) \frac{1}{F} - \underbrace{\frac{\sigma_\infty^2}{F^2}}_{\bar{\sigma}_0^2/F} \left(\frac{\partial F}{\partial c^{(i)}} + \sum_{j=2}^{N} \frac{\partial F}{\partial \hat{y}^{(j)}} \frac{\partial \hat{y}^{(j)}}{\partial c^{(i)}}\right) = \\ &= \frac{1}{F}\left[\frac{\partial \sigma_\infty^2}{\partial c^{(i)}} - \bar{\sigma}_0^2 \frac{\partial F}{\partial c^{(i)}} + \sum_{j=2}^{N} \left(\frac{\partial \sigma_\infty^2}{\partial \hat{y}^{(j)}} \frac{\partial \hat{y}^{(j)}}{\partial c^{(i)}} - bar\sigma_0^2 \frac{\partial F}{\partial \hat{y}^{(j)}} \frac{\partial \hat{y}^{(j)}}{\partial c^{(i)}}\right)\right] = \\ &= \frac{1}{F}\left[\frac{\partial \sigma_\infty^2}{\partial c^{(i)}} - \bar{\sigma}_0^2 \frac{\partial F}{\partial c^{(i)}} + \sum_{j=2}^{N} \underbrace{\left(\frac{\partial \sigma_\infty^2}{\partial \hat{y}^{(j)}} - \bar{\sigma}_0^2 \frac{\partial F}{\partial \hat{y}^{(j)}}\right)}_{0,\ \text{see(IV.2)}} \frac{\partial \hat{y}^{(j)}}{\partial c^{(i)}}\right] \quad \Rightarrow \end{aligned} \tag{IV.8}$$

$$\frac{\partial \bar{\sigma}_0}{\partial c^{(i)}} = \frac{1}{2\,\bar{\sigma}_0\,F}\left(\frac{\partial \sigma_\infty^2}{\partial c^{(i)}} - \bar{\sigma}_0^2 \frac{\partial F}{\partial c^{(i)}}\right), \qquad i = 1, 2, 3, \ldots, N, \tag{IV.9}$$

where we took into account the optimality condition (IV.2), namely $\frac{\partial \sigma_\infty^2}{\partial \hat{y}^{(j)}} - \bar{\sigma}_0^2 \frac{\partial F}{\partial \hat{y}^{(j)}} = 0$.

Note

1) If a $y^{(j)} = 0$, so that (IV.2) and (IV.7) are not valid, the quantity $\frac{\partial \sigma_\infty^2}{\partial \hat{y}^{(j)}} - \bar{\sigma}_0^2 \frac{\partial F}{\partial \hat{y}^{(j)}}$ still vanishes because $\frac{\partial \sigma_\infty^2}{\partial \hat{y}^{(j)}} = \frac{\partial F}{\partial \hat{y}^{(j)}} = 0$, i.e., equations (IV.9) are valid even for those i that correspond to $y^{(i)} = 0$.

2) All volume fractions $c^{(i)}$ are treated as independent variables. The constraint $\sum_{i=1}^{N} c^{(i)} = 1$ is taken care by the evolution equations of the volume fractions.
The quantities $\partial \sigma_\infty^2 / \partial c^{(i)}$ are defined by (IV.5). Similarly

$$\frac{\partial \bar{\sigma}_0}{\partial \sigma_0^{(i)}} = \frac{1}{2\,\bar{\sigma}_0\,F} \frac{\partial \sigma_\infty^2}{\partial \sigma_0^{(i)}} \qquad i = 1, 2, \ldots, N, \tag{IV.10}$$

where the quantities $\partial \sigma_\infty^2 / \partial \sigma_0^{(i)}$ are defined by (IV.5).

Variation of $\hat{y}^{(i)}$ with respect to $c^{(i)}$ and $\sigma_0^{(i)}$

The derivatives $\frac{\partial \hat{y}^{(i)}}{\partial \sigma_0^{(j)}}$ are needed for the calculation of $\frac{\partial \alpha^{(i)}}{\partial \sigma_0^{(j)}} = \sum_{k=1}^{N} \frac{\partial \alpha^{(i)}}{\partial y^{(k)}} \frac{\partial y^{(k)}}{\partial \sigma_0^{(j)}}$ in equation (IV.21) below. The stationarity conditions that define $\hat{y}^{(r)} = \hat{y}^{(r)}\left(c^{(s)}, \sigma_0^{(s)}\right)$ are given by equations (IV.7):

$$\begin{aligned} A^{(i)} \equiv \left[\frac{1}{T_1\left(\hat{y}^{(r)}, c^{(r)}\right)} \frac{\partial T_1}{\partial y^{(i)}}\left(\hat{y}^{(r)}, c^{(r)}\right) - \frac{1}{T_2\left(\hat{y}^{(r)}, c^{(r)}\right)} \frac{\partial T_2}{\partial y^{(i)}}\left(\hat{y}^{(r)}, c^{(r)}\right)\right] \sigma_\infty^2\left(\hat{y}^{(r)}, c^{(r)}, \sigma_0^{(r)}\right) - \\ - c^{(i)}\left(\sigma_0^{(i)}\right)^2 = 0, \qquad \underline{i = 2, 3, \ldots, N}, \qquad \underline{\hat{y}^{(i)} \neq 0}. \end{aligned} \tag{IV.11}$$

In that case

$$\frac{\partial A^{(i)}}{\partial c^{(r)}} = \left[-\frac{1}{T_1^2}\left(\frac{\partial T_1}{\partial c^{(r)}} + \sum_{j=2}^{N} \frac{\partial T_1}{\partial \hat{y}^{(j)}} \frac{\partial \hat{y}^{(j)}}{\partial c^{(r)}}\right) \frac{\partial T_1}{\partial \hat{y}^{(i)}} + \frac{1}{T_1}\left(\frac{\partial^2 T_1}{\partial \hat{y}^{(i)} \partial c^{(r)}} + \sum_{j=2}^{N} \frac{\partial^2 T_1}{\partial \hat{y}^{(i)} \partial \hat{y}^{(j)}} \frac{\partial \hat{y}^{(j)}}{\partial c^{(r)}}\right) + \right.$$
$$\left. + \frac{1}{T_2^2}\left(\frac{\partial T_2}{\partial c^{(r)}} + \sum_{j=2}^{N} \frac{\partial T_2}{\partial \hat{y}^{(j)}} \frac{\partial \hat{y}^{(j)}}{\partial c^{(r)}}\right) \frac{\partial T_2}{\partial \hat{y}^{(i)}} - \frac{1}{T_2}\left(\frac{\partial^2 T_2}{\partial \hat{y}^{(i)} \partial c^{(r)}} + \sum_{j=2}^{N} \frac{\partial^2 T_2}{\partial \hat{y}^{(j)} \partial \hat{y}^{(i)}} \frac{\partial \hat{y}^{(j)}}{\partial c^{(r)}}\right)\right] \sigma_\infty^2 +$$
$$+ \underbrace{\left(\frac{1}{T_1}\frac{\partial T_1}{\partial y^{(i)}} - \frac{1}{T_2}\frac{\partial T_2}{\partial y^{(i)}}\right)}_{c^{(i)}\left(\sigma_0^{(i)}\right)^2/\sigma_\infty^2} \left(\frac{\partial \sigma_\infty^2}{\partial c^{(r)}} + \sum_{j=2}^{N} \frac{\partial \sigma_\infty^2}{\partial \hat{y}^{(j)}} \frac{\partial \hat{y}^{(j)}}{\partial c^{(r)}}\right) - \left(\sigma_0^{(i)}\right)^2 \delta_{ir} = 0,$$
$$\underline{i = 2, 3, \ldots, N}, \quad r = 1, 2, 3, \ldots, N, \quad \underline{\hat{y}^{(i)} \neq 0}, \quad \text{(IV.12)}$$

or

$$\sum_{j=2}^{N} \left[\left(-\frac{\partial T_1}{\partial \hat{y}^{(i)}} \frac{\partial T_1}{\partial \hat{y}^{(j)}} \frac{1}{T_1^2} + \frac{\partial^2}{T_1} \partial \hat{y}^{(i)}\, \partial \hat{y}^{(j)} \frac{1}{T_1} + \frac{\partial T_2}{\partial \hat{y}^{(i)}} \frac{\partial T_2}{\partial \hat{y}^{(j)}} \frac{1}{T_2^2} - \frac{\partial^2 T_2}{\partial \hat{y}^{(i)}\, \partial \hat{y}^{(j)}} \frac{1}{T_2} \right) \sigma_\infty^2 + \right.$$
$$\left. + \frac{\partial \sigma_\infty^2}{\partial \hat{y}^{(j)}} \frac{c^{(i)} \left(\sigma_0^{(i)}\right)^2}{\sigma_\infty^2} \right] \frac{\partial \hat{y}^{(j)}}{\partial c^{(r)}} =$$
$$= \left(\frac{\partial T_1}{\partial \hat{y}^{(i)}} \frac{\partial T_1}{\partial c^{(r)}} \frac{1}{T_1^2} - \frac{\partial^2 T_1}{\partial \hat{y}^{(i)}\, \partial c^{(r)}} \frac{1}{T_1} - \frac{\partial T_2}{\partial \hat{y}^{(i)}} \frac{\partial T_2}{\partial c^{(r)}} \frac{1}{T_2^2} + \frac{\partial^2 T_2}{\partial \hat{y}^{(i)}\, \partial c^{(r)}} \frac{1}{T_2} \right) \sigma_\infty^2 -$$
$$- \frac{\partial \sigma_\infty^2}{\partial c^{(r)}} \frac{c^{(i)} \left(\sigma_0^{(i)}\right)^2}{\sigma_\infty^2} + \left(\sigma_0^{(i)}\right)^2 \delta_{ir},$$
$$\underline{i = 2, 3, \ldots, N}, \quad r = 1, 2, 3, \ldots, N, \quad \underline{\hat{y}^{(i)} \neq 0}. \quad \text{(IV.13)}$$

The above system of equations defines $\frac{\partial \hat{y}^{(j)}}{\partial c^{(r)}}$ for $j = 2, 3, \ldots, N$, $r = 1, 2, \ldots, N$ and $\hat{y}^{(i)} \neq 0$. Similarly

$$\frac{\partial A^{(i)}}{\partial \sigma_0^{(r)}} = \left[-\frac{1}{T_1^2}\left(\sum_{j=2}^{N} \frac{\partial T_1}{\partial \hat{y}^{(j)}} \frac{\partial \hat{y}^{(j)}}{\partial \sigma_0^{(r)}}\right) \frac{\partial T_1}{\partial \hat{y}^{(i)}} + \frac{1}{T_1}\left(\sum_{j=2}^{N} \frac{\partial^2 T_1}{\partial \hat{y}^{(j)} \partial \hat{y}^{(i)}} \frac{\partial \hat{y}^{(j)}}{\partial \sigma_0^{(r)}}\right) + \right.$$
$$\left. + \frac{1}{T_2^2}\left(\sum_{j=2}^{N} \frac{\partial T_2}{\partial \hat{y}^{(j)}} \frac{\partial \hat{y}^{(j)}}{\partial \sigma_0^{(r)}}\right) \frac{\partial T_2}{\partial \hat{y}^{(i)}} - \frac{1}{T_2}\left(\sum_{j=2}^{N} \frac{\partial^2 T_2}{\partial \hat{y}^{(j)} \partial \hat{y}^{(i)}} \frac{\partial \hat{y}^{(j)}}{\partial \sigma_0^{(r)}}\right)\right] \sigma_\infty^2 +$$
$$+ \underbrace{\left(\frac{1}{T_1}\frac{\partial T_1}{\partial y^{(i)}} - \frac{1}{T_2}\frac{\partial T_2}{\partial y^{(i)}}\right)}_{c^{(i)}\left(\sigma_0^{(i)}\right)^2/\sigma_\infty^2} \left(\frac{\partial \sigma_\infty^2}{\partial \sigma_0^{(r)}} + \sum_{j=2}^{N} \frac{\partial \sigma_\infty^2}{\partial \hat{y}^{(j)}} \frac{\partial \hat{y}^{(j)}}{\partial \sigma_0^{(r)}}\right) - 2\, c^{(i)}\, \sigma_0^{(i)}\, \delta_{ir} = 0,$$
$$\underline{i = 2, 3, \ldots, N}, \quad r = 1, 2, 3, \ldots, N, \quad \underline{\hat{y}^{(i)} \neq 0}. \quad \text{(IV.14)}$$

or

$$\sum_{j=2}^{N}\left[\left(-\frac{\partial T_1}{\partial\hat{y}^{(i)}}\frac{\partial T_1}{\partial\hat{y}^{(j)}}\frac{1}{T_1^2}+\frac{\partial^2 T_1}{\partial\hat{y}^{(i)}\,\partial\hat{y}^{(j)}}\frac{1}{T_1}+\frac{\partial T_2}{\partial\hat{y}^{(i)}}\frac{\partial T_2}{\partial\hat{y}^{(j)}}\frac{1}{T_2^2}-\frac{\partial^2 T_2}{\partial\hat{y}^{(i)}\,\partial\hat{y}^{(j)}}\frac{1}{T_2}\right)\sigma_\infty^2+\right.$$
$$\left.+\frac{\partial\sigma_\infty^2}{\partial y^{(j)}}\frac{c^{(i)}\left(\sigma_0^{(i)}\right)^2}{\sigma_\infty^2}\right]\frac{\partial\hat{y}^{(j)}}{\partial\sigma_0^{(r)}}=2\,c^{(i)}\,\sigma_0^{(i)}\,\delta_{ir}-\frac{\partial\sigma_\infty^2}{\partial\sigma_0^{(r)}}\frac{c^{(i)}\left(\sigma_0^{(i)}\right)^2}{\sigma_\infty^2},$$
$$\underline{i=2,3,\ldots,N},\quad r=1,2,3,\ldots,N,\quad \underline{\hat{y}^{(i)}\neq 0}. \tag{IV.15}$$

The above system of equations defines $\frac{\partial\hat{y}^{(j)}}{\partial\sigma_0^{(r)}}$ for $j=2,3,\ldots,N$,$r=1,2,\ldots,N$ and $\hat{y}^{(i)}\neq 0$. If one of the optimal values $\hat{y}^{(i)}$ vanishes, the objective function has an unconstrained minimum for negative $y^{(i)}$. In such a case, in view of the continuity of the functions involved, variation of $c^{(r)}$ and $\sigma_0^{(r)}$ changes the value of the unconstrained minimum, which still occurs at some different but still negative $y^{(i)}$. Therefore the $\hat{y}^{(i)}$ for the constrained minimization still vanishes, i.e., if $\hat{y}^{(i)}=0$, then $\frac{\partial\hat{y}^{(i)}}{\partial c^{(r)}}=0$ and $\frac{\partial\hat{y}^{(j)}}{\partial\sigma_0^{(r)}}=0$.

Variation of $\alpha^{(i)}$ with respect to $c^{(r)}$ and $\sigma_0^{(r)}$

We have that

$$\mathbf{D}^{(i)}=\alpha^{(i)}\,\mathbf{D},\qquad \alpha^{(i)}\left(c^{(s)},y^{(s)}\right)=\frac{F^{(i)}\left(y^{(i)}\right)}{\Pi\left(c^{(s)},y^{(s)}\right)}, \tag{IV.16}$$

$$F^{(i)}\left(y^{(i)}\right)=\frac{y^{(i)}}{3\,y^{(i)}+2\,y_0},\qquad \Pi\left(c^{(s)},y^{(s)}\right)=\sum_{s=1}^{N}c^{(s)}\,F\left(y^{(s)}\right). \tag{IV.17}$$

Also

$$\dot{\bar{\varepsilon}}^{(i)}=\alpha^{(i)}\left(c^{(r)},y^{(r)}\right)\,\dot{\bar{\varepsilon}}, \tag{IV.18}$$

where

$$\dot{\bar{\varepsilon}}^{(i)}=\sqrt{\frac{2}{3}\mathbf{D}^{(i)}:\mathbf{D}^{(i)}}\quad\text{(no sum on } i)\qquad\text{and}\qquad \dot{\bar{\varepsilon}}=\sqrt{\frac{2}{3}\mathbf{D}:\mathbf{D}}\,.$$

Variation of $a^{(i)}\left(c^{(r)},\sigma_0^{(r)}\right)$

$$\alpha^{(i)}\left(c^{(s)},y^{(s)}\right)=\frac{y^{(i)}}{3\,y^{(i)}+2\,y_0}\left(\sum_{s=1}^{N}\frac{c^{(s)}\,y^{(s)}}{3\,y^{(s)}+2\,y_0}\right)^{-1}=\frac{F^{(i)}\left(y^{(i)},y_0\right)}{\Pi\left(c^{(r)},y^{(r)},y_0\right)},\qquad y_0=y_0\left(c^{(r)},y^{(r)}\right), \tag{IV.19}$$

$$F^{(i)}\left(y^{(s)},y_0\right)=\frac{y^{(i)}}{3\,y^{(i)}+2\,y_0},\qquad \Pi\left(c^{(s)},y^{(s)},y_0\right)=\sum_{s=1}^{N}\frac{c^{(s)}\,y^{(s)}}{3\,y^{(s)}+2\,y_0}=\sum_{s=1}^{N}c^{(s)}\,F^{(s)}\left(y^{(s)},y_0\right). \tag{IV.20}$$

Evaluation of $\frac{\partial \alpha^{(i)}}{\partial \sigma_0^{(j)}}$

We have that

$$\frac{\partial \alpha^{(i)}}{\partial \sigma_0^{(j)}} = \sum_{k=1}^{N} \frac{\partial \alpha^{(i)}}{\partial y^{(k)}} \frac{\partial y^{(k)}}{\partial \sigma_0^{(j)}} \qquad \Rightarrow \qquad \underset{N\times N}{\left[\frac{\partial \alpha^{(i)}}{\partial \sigma_0^{(j)}}\right]} = \underset{N\times N}{\left[\frac{\partial \alpha^{(i)}}{\partial y^{(k)}}\right]} \underset{N\times N}{\left[\frac{\partial y^{(k)}}{\partial \sigma_0^{(j)}}\right]}. \tag{IV.21}$$

Therefore, we need $\frac{\partial \alpha^{(i)}}{\partial y^{(j)}}$, which is determined as follows.

$$\frac{\partial \alpha^{(i)}}{\partial y^{(j)}} = \left(\frac{\partial F^{(i)}}{\partial y^{(j)}} + \frac{\partial F^{(i)}}{\partial y_0}\frac{\partial y_0}{\partial y^{(j)}}\right)\frac{1}{\Pi} - \frac{F^{(i)}}{\Pi^2}\left(\frac{\partial \Pi}{\partial y^{(j)}} + \frac{\partial \Pi}{\partial y_0}\frac{\partial y_0}{\partial y^{(j)}}\right) \qquad \Rightarrow$$

$$\frac{\partial \alpha^{(i)}}{\partial y^{(j)}} = \frac{1}{\Pi}\left[\frac{\partial F^{(i)}}{\partial y^{(j)}} + \frac{\partial F^{(i)}}{\partial y_0}\frac{\partial y_0}{\partial y^{(j)}} - \alpha^{(i)}\left(\frac{\partial \Pi}{\partial y^{(j)}} + \frac{\partial \Pi}{\partial y_0}\frac{\partial y_0}{\partial y^{(j)}}\right)\right], \qquad i,j = 1,2,\ldots,N. \tag{IV.22}$$

We need $\frac{\partial F^{(i)}}{\partial y^{(j)}}$, $\frac{\partial F^{(i)}}{\partial y_0}$, $\frac{\partial \Pi}{\partial y^{(j)}}$, $\frac{\partial \Pi}{\partial y_0}$.

Evaluation of $\frac{\partial \alpha^{(i)}}{\partial c^{(j)}}$

$$\frac{\partial \alpha^{(i)}}{\partial c^{(j)}} = \frac{1}{\Pi}\frac{\partial F^{(i)}}{\partial y_0}\frac{\partial y_0}{\partial c^{(j)}} - fracF^{(i)}\Pi^2\left(\frac{\partial \Pi}{\partial c^{(j)}} + \frac{\partial \Pi}{\partial y_0}\frac{\partial y_0}{\partial c^{(j)}}\right) \qquad \Rightarrow$$

$$\frac{\partial \alpha^{(i)}}{\partial c^{(j)}} = \frac{1}{\Pi}\left[\frac{\partial F^{(i)}}{\partial y_0}\frac{\partial y_0}{\partial c^{(j)}} - \alpha^{(i)}\left(\frac{\partial \Pi}{\partial c^{(j)}} + \frac{\partial \Pi}{\partial y_0}\frac{\partial y_0}{\partial c^{(j)}}\right)\right], \qquad i,j = 1,2,\ldots,N. \tag{IV.23}$$

We need $\frac{\partial F^{(i)}}{\partial y_0}$, $\frac{\partial \Pi}{\partial y_0}$, $\frac{\partial \Pi}{\partial c^{(i)}}$.

We have that

$$\frac{\partial F^{(i)}}{\partial y^{(j)}} = \frac{\delta_{ij}}{3\,y^{(i)} + 2\,y_0} - \frac{y^{(i)}}{\left(3\,y^{(i)} + 2\,y_0\right)^2} 3\,\delta_{ij} = \frac{\delta_{ij}}{3\,y^{(i)} + 2\,y_0}\left(1 - \frac{3\,y^{(i)}}{3\,y^{(i)} + 2\,y_0}\right) \qquad \Rightarrow$$

$$\frac{\partial F^{(i)}}{\partial y^{(j)}} = \frac{2\,y_0\,\delta_{ij}}{\left(3\,y^{(i)} + 2\,y_0\right)^2}, \qquad \frac{\partial F^{(i)}}{\partial y_0} = -\frac{2\,y^{(i)}}{\left(3\,y^{(i)} + 2\,y_0\right)^2}. \tag{IV.24}$$

Also

$$\frac{\partial \Pi}{\partial y^{(i)}} = c^{(i)}\frac{\partial F^{(i)}}{\partial y^{(i)}}, \qquad \frac{\partial \Pi}{\partial y_0} = \sum_{i=1}^{N} c^{(i)}\frac{\partial F^{(i)}}{\partial y_0}, \qquad \frac{\partial \Pi}{\partial c^{(i)}} = F^{(i)}.$$

The value of $\frac{\partial y_0}{\partial y^{(j)}}$ depends on the model used.

i) $y_0 = y^{(1)} \qquad \Rightarrow \qquad \frac{\partial y_0}{\partial y^{(i)}} = \delta_{1i} \qquad$ and $\qquad \frac{\partial y_0}{\partial c^{(i)}} = 0,$

ii) $y_0 = \sum_{r=1}^{N} c^{(r)}\,y^{(r)} \qquad \Rightarrow \qquad \frac{\partial y_0}{\partial y^{(i)}} = c^{(i)} \qquad$ and $\qquad \frac{\partial y_0}{\partial c^{(i)}} = y^{(i)}.$

Calculation of the Jacobian of the Newton loop for equation (4.33)

Integration using a combination of the *backward* and the *forward* Euler schemes

Newton's method is used for the solution of (4.33). The Jacobian of the Newton loop is

$$\frac{\partial \Phi}{\partial \bar{\varepsilon}} = -3\,G - \sum_{k=1}^{N} \left(\frac{\partial \bar{\sigma}_0}{\partial \bar{\varepsilon}^{(k)}} \frac{\partial \bar{\varepsilon}^{(k)}}{\partial \bar{\varepsilon}} \right)_{n+1} = -3\,G - \sum_{k=1}^{N} \left(\frac{\partial \bar{\sigma}_0}{\partial \bar{\varepsilon}^{(k)}} \right)_{n+1} \alpha_n^{(i)}. \tag{IV.25}$$

Also

$$\frac{\partial \bar{\sigma}_0}{\partial \bar{\varepsilon}^{(k)}} = \frac{\partial \bar{\sigma}_0}{\partial \sigma_0^{(k)}} \frac{\partial \sigma_0^{(k)}}{\partial \bar{\varepsilon}^{(k)}} = \frac{\partial \bar{\sigma}_0}{\partial \sigma_0^{(k)}} h^{(k)},$$

so that (IV.25) $\Rightarrow$

$$\frac{\partial \Phi}{\partial \bar{\varepsilon}} = -3\,G - \sum_{k=1}^{N} \left(\frac{\partial \bar{\sigma}_0}{\partial \sigma_0^{(k)}} \right)_{n+1} h_{n+1}^{(k)}\, \alpha_n^{(i)}. \tag{IV.26}$$

A first estimate for $\bar{\sigma}_0|_{n+1}\,(\Delta\bar{\varepsilon})$ in the Newton iterations is determined as follows:

$$\begin{aligned} \bar{\sigma}_0|_{n+1}\,(\Delta\bar{\varepsilon}) = \bar{\sigma}_0\left(\bar{\varepsilon}_{n+1}^{(k)}\,(\Delta\bar{\varepsilon})\right) \simeq \bar{\sigma}_0|_n + \sum_{k=1}^{N} \left(\frac{\partial \bar{\sigma}_0}{\partial \bar{\varepsilon}^{(k)}} \frac{\partial \bar{\varepsilon}^{(k)}}{\partial \bar{\varepsilon}} \right)_n \Delta\bar{\varepsilon} = \\ = \bar{\sigma}_0|_n + \sum_{k=1}^{N} \left(\frac{\partial \bar{\sigma}_0}{\partial \sigma_0^{(k)}}\, h^{(k)}\, \alpha^{(k)} \right)_n \Delta\bar{\varepsilon} = \bar{\sigma}_0|_n + H_n\,\Delta\bar{\varepsilon}, \end{aligned} \tag{IV.27}$$

so that (4.33) becomes

$$\Phi\,(\Delta\bar{\varepsilon}) \simeq \sigma_e^e - 3\,G\,\Delta\bar{\varepsilon} - \bar{\sigma}_0|_n - H_n\,\Delta\bar{\varepsilon} = 0 \qquad \Rightarrow \qquad \Delta\bar{\varepsilon} = \frac{\sigma_e^e - \bar{\sigma}_0|_n}{3\,G + H_n}.$$

Integration using the *backward* Euler method on all variables

Solution of equations (4.37) for given Δq_i:
We write (4.37) in the form

$$P_i \equiv \Delta q_i - \Delta\bar{\varepsilon}\,\alpha^{(i)}(\mathbf{q}_n + \Delta\mathbf{q}) = 0. \tag{IV.28}$$

Newton's method is used for the solution of (IV.28). The Jacobian for Newton loop is given by the equation:

$$\frac{\partial P_i}{\partial \Delta q_j} = \delta_{ij} - \Delta\bar{\varepsilon} \left. \frac{\partial \alpha^{(i)}}{\partial \sigma_0^{(j)}} \right|_{n+1} h_{n+1}^{(j)}. \tag{IV.29}$$

Solution of yield condition (4.38) for given $\Delta\bar{\varepsilon}^p$
The yield condition is written in the form

$$\Phi\left(\Delta\bar{\varepsilon}\right) \equiv \sigma_e^e - 3\,G\,\Delta\bar{\varepsilon} - \bar{\sigma}_0|_{n+1}\left(\Delta\bar{\varepsilon}\right) = 0. \tag{IV.30}$$

and is solved by using Newton's method. The Jacobian for Newton loop is given by the equation:

$$\frac{\partial\Phi}{\partial\Delta\bar{\varepsilon}} = -3\,G - \sum_{j=1}^{N}\left(\frac{\partial\bar{\sigma}_0}{\partial\Delta\bar{\varepsilon}^{(j)}}\frac{\partial\Delta\bar{\varepsilon}^{(j)}}{\partial\Delta\bar{\varepsilon}}\right)_{n+1}, \tag{IV.31}$$

where

$$\frac{\partial\bar{\sigma}_0}{\partial\Delta\bar{\varepsilon}^{(j)}} = \frac{\partial\bar{\sigma}_0}{\partial\bar{\varepsilon}^{(j)}} = \frac{\partial\bar{\sigma}_0}{\partial\sigma_0^{(j)}}\frac{\partial\sigma_0^{(j)}}{\partial\bar{\varepsilon}^{(j)}} = \frac{\partial\bar{\sigma}_0}{\partial\sigma_0^{(j)}}h^{(j)},$$

so that (IV.31) becomes

$$\frac{\partial\Phi}{\partial\Delta\bar{\varepsilon}} = -3\,G - \sum_{j=1}^{N}\left(\frac{\partial\bar{\sigma}_0}{\partial\sigma_0^{(j)}}h^{(j)}\frac{\partial\Delta\bar{\varepsilon}^{(j)}}{\partial\Delta\bar{\varepsilon}}\right)_{n+1}.$$

The derivatives $\frac{\partial\Delta\bar{\varepsilon}^{(j)}}{\partial\Delta\bar{\varepsilon}}$ are determined from (IV.28) as follows:

$$\begin{aligned}
&\frac{\partial\Delta\bar{\varepsilon}^{(i)}}{\partial\Delta\bar{\varepsilon}} - \alpha_{n+1}^{(i)} - \Delta\bar{\varepsilon}\sum_{j=1}^{n}\left(\frac{\partial\alpha^{(i)}}{\partial\Delta\bar{\varepsilon}^{(j)}}\frac{\partial\Delta\bar{\varepsilon}^{(j)}}{\partial\Delta\bar{\varepsilon}}\right)_{n+1} = 0 \qquad \Rightarrow \\
&\frac{\partial\Delta\bar{\varepsilon}^{(i)}}{\partial\Delta\bar{\varepsilon}} - \alpha_{n+1}^{(i)} - \Delta\bar{\varepsilon}\sum_{j=1}^{n}\left(\frac{\partial\alpha^{(i)}}{\partial\sigma_0^{(j)}}h^{(j)}\frac{\partial\Delta\bar{\varepsilon}^{(j)}}{\partial\Delta\bar{\varepsilon}}\right)_{n+1} = 0 \qquad \Rightarrow \\
&\sum_{j=1}^{n}\left[\delta_{ij} - \Delta\bar{\varepsilon}\left(\frac{\partial\alpha^{(i)}}{\partial\sigma_0^{(j)}}h^{(j)}\right)_{n+1}\right]\frac{\partial\Delta\bar{\varepsilon}^{(j)}}{\partial\Delta\bar{\varepsilon}} = \alpha_{n+1}^{(i)}.
\end{aligned} \tag{IV.32}$$

The last equations provide a system of linear equations that is solved for $\frac{\partial\Delta\bar{\varepsilon}^{(i)}}{\partial\Delta\bar{\varepsilon}}$.

Calculation of the Jacobian of the Newton loop for equations (5.55) **and** (5.56)

Integration using a combination of the *backward* and the *forward* Euler schemes

Newton's method is used for the solution of equations (5.55) and (5.56). Within each iteration in the Newton loop, for given $\Delta\bar{\varepsilon}$ and $\Delta\varepsilon_v^p$, we calculate the following:

$$\begin{aligned}
c_{n+1}^{(1)} &= c_n^{(1)}\,\exp\left(-\Delta\varepsilon_v^p\right), & c_{n+1}^{(4)} &= c_n^{(4)} + \frac{\Delta\varepsilon_v^p}{\Delta_v}, \\
c_{n+1}^{(2)} &= c_n^{(2)}\,\exp\left(-\Delta\varepsilon_v^p\right), & c_{n+1}^{(3)} &= 1 - \left(c_{n+1}^{(1)} + c_{n+1}^{(2)} + c_{n+1}^{(4)}\right)
\end{aligned}$$

All the $c_{n+1}^{(i)}$ are determined completely in terms of $\Delta\varepsilon_v^p$, i.e., $c_{n+1}^{(i)} = c_{n+1}^{(i)}\left(\Delta\varepsilon_v^p\right)$.

Also

$$\sigma_e|_{n+1}(\Delta\bar{\varepsilon},\Delta\varepsilon_v^p)=\frac{\sigma_e^e-3\,G(\Delta\bar{\varepsilon}+\frac{A_0}{\Delta_v}\,\Delta\varepsilon_v^p)}{1+\frac{3\,G}{s_a^*}\frac{A_1}{\Delta_v}\,\Delta\varepsilon_v^p}$$

$$p_{n+1}(\Delta\varepsilon_v^p)=p^e-\mathrm{K}\,\Delta\varepsilon_v^p$$

$$X_\Sigma|_{n+1}(\Delta\bar{\varepsilon},\Delta\varepsilon_v^p)=\frac{p_{n+1}}{\sigma_e|_{n+1}},\qquad \Delta X_\Sigma(\Delta\bar{\varepsilon},\Delta\varepsilon_v^p)=\frac{p_{n+1}}{\sigma_e|_{n+1}}-\frac{p_n}{\sigma_e|_n}$$

$$A_f=A_f(\bar{\varepsilon}^{(3)},X_\Sigma)=\alpha\,\beta_0\,r\,(1-f_{sb})\,f_{sb}^{r-1}\,P,$$

$$B_f=B_f(\bar{\varepsilon}^{(3)},X_\Sigma,\Delta X_\Sigma)=\frac{g_2}{\sqrt{2\,\pi}\,s_g}\beta_0\,f_{sb}^r\,\exp\left[-\frac{1}{2}\left(\frac{g-\bar{g}}{s_g}\right)^2\right]H(\Delta\Sigma)$$

with

$$f_{sb}\left(\bar{\varepsilon}^{(3)}\right)=1-\exp\left(-\alpha\,\bar{\varepsilon}^{(3)}\right),$$

$$P\left(\Sigma\right)=\frac{1}{\sqrt{2\,\pi}\,s_g}\int_{-\infty}^{g(\Sigma)}\exp\left[-\frac{1}{2}\left(\frac{g'-\bar{g}}{s_g}\right)^2\right]dg',$$

$$g\left(\Sigma\right)=(g_0-g_1\,\Theta)+g_2\,\Sigma$$

The Jacobian of the Newton loop is calculated as follows:

$$J_{11}=\frac{\partial F_1}{\partial\Delta\bar{\varepsilon}}=-3\,G-\left(1+\frac{3\,G}{s_a^*}A_1\frac{\Delta\varepsilon_v^p}{\Delta_v}\right)\sum_{i=1}^{N}\frac{\partial\tilde{\sigma}_0}{\partial\bar{\varepsilon}^{(i)}}\frac{\partial\bar{\varepsilon}^{(i)}}{\partial\Delta\bar{\varepsilon}}$$

$$=-3\,G-\left(1+\frac{3\,G}{s_a^*}A_1\frac{\Delta\varepsilon_v^p}{\Delta_v}\right)\sum_{i=1}^{N}\frac{\partial\tilde{\sigma}_0}{\partial\sigma_0^{(i)}}\underbrace{\frac{\partial\sigma_0^{(i)}}{\partial\bar{\varepsilon}^{(i)}}}_{h^{(i)}}\alpha_n^{(i)}\qquad\Rightarrow$$

$$J_{11}=-3\,G-\left(1+\frac{3\,G}{s_a^*}\frac{A_1}{\Delta_v}\Delta\varepsilon_v^p\right)\sum_{i=1}^{N}\frac{\partial\tilde{\sigma}_0}{\partial\sigma_0^{(i)}}h^{(i)}\alpha_n^{(i)}$$

$$J_{12}=\frac{\partial F_1}{\partial\Delta\varepsilon_v^p}=-3\,G\left(\frac{A_0}{\Delta_v}+\frac{A_1}{\Delta_v}\frac{\tilde{\sigma}_0}{s_a^*}\right)-\left(1+\frac{3\,G}{s_a^*}\frac{A_1}{\Delta_v}\Delta\varepsilon_v^p\right)\sum_{i=1}^{N}\frac{\partial\tilde{\sigma}_0}{\partial c^{(i)}}\frac{\partial c^{(i)}}{\partial\Delta\varepsilon_v^p}$$

$$J_{21}=\frac{\partial F_2}{\partial\Delta\bar{\varepsilon}}=-\Delta_v\,c_n^{(3)}\left(A_f\frac{\partial\Delta\bar{\varepsilon}^{(3)}}{\partial\Delta\bar{\varepsilon}}+B_f\frac{\partial\Delta X_\Sigma}{\partial\Delta\bar{\varepsilon}}\right)\quad\Rightarrow\quad J_{21}=-\Delta_v\,c_n^{(3)}\left(A_f\,\alpha_n^{(3)}+B_f\frac{\partial X_\Sigma}{\partial\Delta\bar{\varepsilon}}\right)$$

$$J_{22}=\frac{\partial F_2}{\partial\Delta\varepsilon_v^p}=1-\Delta_v\,c_n^{(3)}\,B_f\frac{\partial X_\Sigma}{\partial\Delta\varepsilon_v^p}$$

Integration using the *backward* Euler method on all variables

Newton's method is used for the solution of equations (5.59) and (5.60). The Jacobian

of the Newton loop is calculated as follows:

$$J_{11} = \frac{\partial F_1}{\partial \Delta\bar{\varepsilon}} = -3\,G - \left(1 + \frac{3\,G}{s_a^*} A_1 \frac{\Delta\varepsilon_v^p}{\Delta_v}\right) \sum_{i=1}^{N} \frac{\partial \tilde{\sigma}_0}{\partial \bar{\varepsilon}^{(i)}} \frac{\partial \bar{\varepsilon}^{(i)}}{\partial \Delta\bar{\varepsilon}}$$

$$= -3\,G - \left(1 + \frac{3\,G}{s_a^*} A_1 \frac{\Delta\varepsilon_v^p}{\Delta_v}\right) \sum_{i=1}^{N} \frac{\partial \tilde{\sigma}_0}{\partial \sigma_0^{(i)}} \underbrace{\frac{\partial \sigma_0^{(i)}}{\partial \bar{\varepsilon}^{(i)}}}_{h^{(i)}} \frac{\partial \bar{\varepsilon}^{(i)}}{\partial \Delta\bar{\varepsilon}}$$

$$\Rightarrow \quad J_{11} = -3\,G - \left(1 + \frac{3\,G}{s_a^*} A_1 \frac{\Delta\varepsilon_v^p}{\Delta_v}\right) \sum_{i=1}^{N} \frac{\partial \tilde{\sigma}_0}{\partial \sigma_0^{(i)}} h^{(i)} \frac{\partial \bar{\varepsilon}^{(i)}}{\partial \Delta\bar{\varepsilon}}$$

$$J_{12} = \frac{\partial F_1}{\partial \Delta\varepsilon_v^p} = -3\,G \frac{A_0}{\Delta_v} - \frac{3\,G}{s_a^*} \frac{A_1}{\Delta_v} \tilde{\sigma}_0 - \left(1 + \frac{3\,G}{s_a^*} A_1 \frac{\Delta\varepsilon_v^p}{\Delta_v}\right) \sum_{i=1}^{N} \left(\frac{\partial \tilde{\sigma}_0}{\partial c^{(i)}} \frac{\partial c^{(i)}}{\partial \Delta\varepsilon_v^p} + \frac{\partial \tilde{\sigma}_0}{\partial \bar{\varepsilon}^{(i)}} \frac{\partial \bar{\varepsilon}^{(i)}}{\partial \Delta\varepsilon_v^p}\right)$$

$$\Rightarrow \quad J_{12} = -3\,G \left(\frac{A_0}{\Delta_v} + \frac{\tilde{\sigma}_0}{s_a^*} \frac{A_1}{\Delta_v}\right) - \left(1 + \frac{3\,G}{s_a^*} A_1 \frac{\Delta\varepsilon_v^p}{\Delta_v}\right) \sum_{i=1}^{N} \left(\frac{\partial \tilde{\sigma}_0}{\partial c^{(i)}} \frac{\partial c^{(i)}}{\partial \Delta\varepsilon_v^p} + \frac{\partial \tilde{\sigma}_0}{\partial \sigma_0^{(i)}} h^{(i)} \frac{\partial \bar{\varepsilon}^{(i)}}{\partial \Delta\varepsilon_v^p}\right)$$

$$J_{21} = \frac{\partial F_2}{\partial \Delta\bar{\varepsilon}} = -\Delta_v\, c_{n+1}^{(3)} \left(\frac{\partial A_f}{\partial \Delta\bar{\varepsilon}^{(3)}} \frac{\partial \Delta\bar{\varepsilon}^{(3)}}{\partial \Delta\bar{\varepsilon}} \Delta\bar{\varepsilon}^{(3)} + A_f \frac{\partial \Delta\bar{\varepsilon}^{(3)}}{\partial \Delta\bar{\varepsilon}} + \frac{\partial B_f}{\partial \Delta\bar{\varepsilon}^{(3)}} \frac{\partial \Delta\bar{\varepsilon}^{(3)}}{\partial \Delta\bar{\varepsilon}} \Delta X_\Sigma + B_f \frac{\partial \Delta X_\Sigma}{\partial \Delta\bar{\varepsilon}}\right)$$

$$\Rightarrow \quad J_{21} = -\Delta_v\, c_{n+1}^{(3)} \left[\left(\frac{\partial A_f}{\partial \Delta\bar{\varepsilon}^{(3)}} \Delta\bar{\varepsilon}^{(3)} + A_f + \frac{\partial B_f}{\partial \Delta\bar{\varepsilon}^{(3)}} \Delta X_\Sigma\right) \frac{\partial \Delta\bar{\varepsilon}^{(3)}}{\partial \Delta\bar{\varepsilon}} + B_f \frac{\partial X_\Sigma}{\partial \Delta\bar{\varepsilon}}\right]$$

$$J_{22} = \frac{\partial F_2}{\partial \Delta\varepsilon_v^p} = 1 - \Delta_v\, c_{n+1}^{(3)} \left[\left(\frac{\partial A_f}{\partial \Delta\bar{\varepsilon}^{(3)}} \Delta\bar{\varepsilon}^{(3)} + A_f + \frac{\partial B_f}{\partial \Delta\bar{\varepsilon}^{(3)}} \Delta X_\Sigma\right) \frac{\partial \Delta\bar{\varepsilon}^{(3)}}{\partial \Delta\varepsilon_v^p} + B_f \frac{\partial X_\Sigma}{\partial \Delta\varepsilon_v^p}\right] +$$

$$- \Delta_v \frac{\partial c_{n+1}^{(3)}}{\partial \Delta\varepsilon_v^p} \left(A_f|_{n+1}\, \Delta\bar{\varepsilon}^{(3)} + B_f|_{n+1}\, \Delta X_\Sigma\right).$$

Calculation of the Jacobian for the non-linear problem of plane stress

Newton's method is used for the solution of equations (5.107),(5.108) and (5.109). The Jacobian of the Newton loop is calculated as follows:

$$J_{11} = \frac{\partial F_1}{\partial \Delta\bar{\varepsilon}} = \frac{\partial \sigma_e|_{n+1}}{\partial \Delta\bar{\varepsilon}} - \sum_{i=1}^{N} \frac{\partial \tilde{\sigma}_0}{\partial \bar{\varepsilon}^{(i)}} \frac{\partial \bar{\varepsilon}^{(i)}}{\partial \Delta\bar{\varepsilon}} = \frac{\partial \sigma_e|_{n+1}}{\partial \Delta\bar{\varepsilon}} - \sum_{i=1}^{N} \frac{\partial \tilde{\sigma}_0}{\partial \sigma_0^{(i)}} \underbrace{\frac{\partial \sigma_0^{(i)}}{\partial \bar{\varepsilon}^{(i)}}}_{h^{(i)}} \alpha_n^{(i)} \;\Rightarrow$$

$$J_{11} = \frac{\partial \sigma_e|_{n+1}}{\partial \Delta\bar{\varepsilon}} - \sum_{i=1}^{N} \frac{\partial \tilde{\sigma}_0}{\partial \sigma_0^{(i)}} h^{(i)} \alpha_n^{(i)}$$

$$J_{12} = \frac{\partial F_1}{\partial \Delta\varepsilon_v^p} = \frac{\partial \sigma_e|_{n+1}}{\partial \Delta\varepsilon_v^p} - \sum_{i=1}^{N} \frac{\partial \tilde{\sigma}_0}{\partial c^{(i)}} \frac{\partial c^{(i)}}{\partial \Delta\varepsilon_v^p}$$

$$J_{13} = \frac{\partial F_1}{\partial \Delta E_3} = \frac{\partial \sigma_e|_{n+1}}{\partial \Delta E_3}$$

$$J_{21} = \frac{\partial F_2}{\partial \Delta\bar{\varepsilon}} = -\Delta_v\, c_n^{(3)} \left(A_f|_n\, \alpha_n^{(3)} + B_f|_n \frac{\partial X_\Sigma}{\partial \Delta\bar{\varepsilon}}\right)$$

$$J_{22} = \frac{\partial F_2}{\partial \Delta\varepsilon_v^p} = 1 - \Delta_v\, c_n^{(3)}\; B_f|_n \frac{\partial X_\Sigma}{\partial \Delta\varepsilon_v^p}$$

$$J_{23} = \frac{\partial F_2}{\partial \Delta E_3} = -\Delta_v \, c_n^{(3)} \; B_f|_n \frac{\partial \Delta X_\Sigma}{\partial \Delta E_3}$$

$$J_{31} = \frac{\partial F_3}{\partial \Delta \bar{\varepsilon}} = 3\,G \underbrace{\frac{p_{n+1}}{\sigma_e|_{n+1}}}_{X_\Sigma|_{n+1}} + \frac{\partial F_3}{\partial \sigma_e|_{n+1}} \frac{\partial \sigma_e|_{n+1}}{\partial \Delta \bar{\varepsilon}} + \frac{\partial F_3}{\partial p_{n+1}} \underbrace{\frac{\partial p_{n+1}}{\partial \Delta \bar{\varepsilon}}}_{0} \Rightarrow$$

$$J_{31} = 3\,G\,X_\Sigma|_{n+1} + \frac{\partial F_3}{\partial \sigma_e|_{n+1}} \frac{\partial \sigma_e|_{n+1}}{\partial \Delta \bar{\varepsilon}}$$

$$J_{32} = \frac{\partial F_3}{\partial \Delta \varepsilon_v^p} = 3\,G \left(\frac{A_0}{\sigma_e|_{n+1}} + \frac{A_1}{s_a^*} \right) \frac{p_{n+1}}{\Delta_v} + \frac{\partial F_3}{\partial \sigma_e|_{n+1}} \frac{\partial \sigma_e|_{n+1}}{\partial \Delta \varepsilon_v^p} + \frac{\partial F_3}{\partial p_{n+1}} \underbrace{\frac{\partial p_{n+1}}{\partial \Delta \varepsilon_v^p}}_{-\kappa}$$

$$J_{33} = \frac{\partial F_3}{\partial \Delta E_3} = \frac{4}{3} G + \frac{\partial F_3}{\partial \sigma_e|_{n+1}} \frac{\partial \sigma_e|_{n+1}}{\partial \Delta E_3} + \kappa \frac{\partial F_3}{\partial p_{n+1}}$$

The derivatives needed for the calculation of the jacobian are:

$$\frac{\partial c_{n+1}^{(1)}}{\partial \Delta \varepsilon_v^p} = -c_n^{(1)} \, \exp\left(-\Delta \varepsilon_v^p\right) \quad \Rightarrow \quad \frac{\partial c_{n+1}^{(1)}}{\partial \Delta \varepsilon_v^p} = -c_{n+1}^{(1)}, \quad \frac{\partial c_{n+1}^{(2)}}{\partial \Delta \varepsilon_v^p} = -c_{n+1}^{(2)}, \quad \frac{\partial c_{n+1}^{(4)}}{\partial \Delta \varepsilon_v^p} = \frac{1}{\Delta_v} \tag{IV.33}$$

$$c_{n+1}^{(1)} + c_{n+1}^{(2)} + c_{n+1}^{(3)} + c_{n+1}^{(4)} = 1 \quad \Rightarrow \quad \frac{\partial c_{n+1}^{(3)}}{\partial \Delta \varepsilon_v^p} = -\left(\frac{\partial c_{n+1}^{(1)}}{\partial \Delta \varepsilon_v^p} + \frac{\partial c_{n+1}^{(2)}}{\partial \Delta \varepsilon_v^p} + \frac{\partial c_{n+1}^{(4)}}{\partial \Delta \varepsilon_v^p} \right) \Rightarrow$$

$$\Rightarrow \quad \frac{\partial c_{n+1}^{(3)}}{\partial \Delta \varepsilon_v^p} = c_{n+1}^{(1)} + c_{n+1}^{(2)} - \frac{1}{\Delta_v} \tag{IV.34}$$

$$\frac{\partial \Delta \bar{\varepsilon}^{(i)}}{\partial \Delta \bar{\varepsilon}} = \alpha_n^{(i)} \tag{IV.35}$$

$$\frac{\partial \Delta X_\Sigma}{\partial \Delta \bar{\varepsilon}} = -\frac{p_{n+1}}{\left(\sigma_e|_{n+1}\right)^2} \frac{\partial \sigma_e|_{n+1}}{\partial \Delta \bar{\varepsilon}} \quad \Rightarrow \quad \frac{\partial \Delta X_\Sigma}{\partial \Delta \bar{\varepsilon}} = -\frac{X_\Sigma|_{n+1}}{\sigma_e|_{n+1}} \frac{\partial \sigma_e|_{n+1}}{\partial \Delta \bar{\varepsilon}} \tag{IV.36}$$

$$\frac{\partial \Delta X_\Sigma}{\partial \Delta \varepsilon_v^p} = \frac{1}{\sigma_e|_{n+1}} \underbrace{\frac{\partial p_{n+1}}{\partial \Delta \varepsilon_v^p}}_{-\kappa} - \frac{p_{n+1}}{\left(\sigma_e|_{n+1}\right)^2} \frac{\partial \sigma_e|_{n+1}}{\partial \Delta \varepsilon_v^p} \quad \Rightarrow \quad \frac{\partial \Delta X_\Sigma}{\partial \Delta \varepsilon_v^p} = -\frac{1}{\sigma_e|_{n+1}} \left(\kappa + X_\Sigma|_{n+1} \frac{\partial \sigma_e|_{n+1}}{\partial \Delta \varepsilon_v^p} \right) \tag{IV.37}$$

$$\frac{\partial \Delta X_\Sigma}{\partial \Delta E_3} = \frac{1}{\sigma_e|_{n+1}} \underbrace{\frac{\partial p_{n+1}}{\partial \Delta E_3}}_{\kappa} - \frac{p_{n+1}}{\left(\sigma_e|_{n+1}\right)^2} \frac{\partial \sigma_e|_{n+1}}{\partial \Delta E_3} \quad \Rightarrow \quad \frac{\partial \Delta X_\Sigma}{\partial \Delta E_3} = \frac{1}{\sigma_e|_{n+1}} \left(\kappa - X_\Sigma|_{n+1} \frac{\partial \sigma_e|_{n+1}}{\partial \Delta E_3} \right) \tag{IV.38}$$

$$\frac{\partial p_{n+1}}{\partial \Delta \varepsilon_v^p} = -\kappa, \qquad \frac{\partial p_{n+1}}{\partial \Delta E_3} = \kappa \tag{IV.39}$$

$$\frac{\partial \sigma_e|_{n+1}}{\partial \Delta \bar{\varepsilon}} = \frac{-3\,G}{1+\frac{3\,G}{s_a^*}\frac{A_1}{\Delta_v}\Delta\varepsilon_v^p} \tag{IV.40}$$

$$\begin{aligned}\frac{\partial \sigma_e|_{n+1}}{\partial \Delta \varepsilon_v^p} &= \frac{-3\,G\frac{A_0}{\Delta_v}}{1+\frac{3\,G}{s_a^*}\frac{A_1}{\Delta_v}\Delta\varepsilon_v^p} - \frac{G\left[F\left(\Delta E_3\right)-3\left(\Delta\bar{\varepsilon}+\frac{A_0}{\Delta_v}\Delta\varepsilon_v^p\right)\right]}{\left(1+\frac{3\,G}{s_a^*}\frac{A_1}{\Delta_v}\Delta\varepsilon_v^p\right)^2}\frac{3\,G}{s_a^*}\frac{A_1}{\Delta_v} \\ &= \frac{-3\,G\frac{A_0}{\Delta_v}}{1+\frac{3\,G}{s_a^*}\frac{A_1}{\Delta_v}\Delta\varepsilon_v^p} - \frac{\sigma_e|_{n+1}}{1+\frac{3\,G}{s_a^*}\frac{A_1}{\Delta_v}\Delta\varepsilon_v^p}\frac{3\,G}{s_a^*}\frac{A_1}{\Delta_v} \quad \Rightarrow \\ \Rightarrow \frac{\partial \sigma_e|_{n+1}}{\partial \Delta \varepsilon_v^p} &= -\frac{3\,G}{\Delta_v+\frac{3\,G}{s_a^*}A_1\,\Delta\varepsilon_v^p}\left(A_0+\frac{\sigma_e|_{n+1}}{s_a^*}A_1\right)\end{aligned} \tag{IV.41}$$

$$\frac{\partial \sigma_e|_{n+1}}{\partial \Delta E_3} = \frac{G}{1+\frac{3\,G}{s_a^*}\frac{A_1}{\Delta_v}\Delta\varepsilon_v^p}\frac{dF}{d\Delta E_3} \tag{IV.42}$$

$$\frac{dF}{d\Delta E_3} = \frac{1}{2}\frac{6\frac{\bar{s}_{33}^e}{G}+8\,\Delta E_3}{\sqrt{\left(\frac{\bar{\sigma}_e^e}{G}\right)^2+6\frac{\bar{s}_{33}^e}{G}\Delta E_3+4\,\Delta E_3^2}} \quad \Rightarrow \quad \frac{dF}{d\Delta E_3} = \frac{1}{F}\left(3\frac{\bar{s}_{33}^e}{G}+4\,\Delta E_3\right) \tag{IV.43}$$

$$\frac{\partial F_3}{\partial \sigma_e|_{n+1}} = -\frac{3\,G}{\left(\sigma_e|_{n+1}\right)^2}\left(\Delta\bar{\varepsilon}+\frac{A_0}{\Delta_v}\Delta\varepsilon_v^p\right)p_{n+1} \quad \Rightarrow \quad \frac{\partial F_3}{\partial \sigma_e|_{n+1}} = -\frac{3\,G}{\sigma_e|_{n+1}}\left(\Delta\bar{\varepsilon}+\frac{A_0}{\Delta_v}\Delta\varepsilon_v^p\right)X_\Sigma|_{n+1} \tag{IV.44}$$

$$\frac{\partial F_3}{\partial p_{n+1}} = 1+3\,G\left[\frac{\Delta\bar{\varepsilon}}{\sigma_e|_{n+1}}+\left(\frac{A_0}{\sigma_e|_{n+1}}+\frac{A_1}{s_a^*}\right)\frac{\Delta\varepsilon_v^p}{\Delta_v}\right] \tag{IV.45}$$

Bibliography

[1] M. Agoras, R. Avazmohammadi and P. Ponte Castañeda, 'Incremental variational procedure for elasto-viscoplastic composites and application to polymer- and metal-matrix composites reinforced by spheroidal elastic particles', *Int. J. Solids Struct.* **97–98** (2016), 668–686.

[2] N. Aravas and P. Ponte Castañeda, 'Numerical methods for porous metals with deformation-induced anisotropy', *Comp. Methods Appl. Mech. Eng.* **193** (2004), 3767–3805.

[3] I. Barsoum and J. Faleskog, 'Rupture mechanisms in combined tension and shear — Micromechanics', *Int. J. Solids Struct.* **44** (2007), 5481–5498.

[4] J.F. Barthélémy, L. Dormieux, 'A micromechanical approach to the strength criterion of drucker-prager materials reinforced by rigid inclusions', *Int. J. Numer. Anal. Methods Geomech.* **28** (2004), 565–582.

[5] F. Bignonnet, L. Dormieux , E. Lemarchand, 'Strength of a matrix with elliptic criterion reinforced by rigid inclusions with imperfect interfaces', *European Journal of Mechanics A/Solids* **52** (2015), 95–106.

[6] R. Blondé, E. Jimenez-Melero, L. Zhao. N. Schell, E. Bruck, S. van der Zwaag, N.H. van Dijk, 'The mechanical stability of retained austenite in low-alloyed TRIP steel under shear loading', *Mater. Sci. Eng. A* **594** (2014), 125-134.

[7] D. Bonnenfant, F. Mazerolle and P. Suquet, 'Compaction of powders containing hard inclusions: experiments and micromechanical modeling', *Mechanics of Materials* **29** (1998), 93–109.

[8] L. Brassart, L. Stainier, I. Doghri, L. Delannay, 'A variational formulation for the incremental homogenization of elasto-plastic composites', *J. Mech. Phys. Solids*, **59** (2011), 2455–2475.

[9] P. W. Bridgman, 'Studies in large plastic flow and fracture with special emphasis on the effects of hydrostatic pressure', *McGraw-Hill Book Co.* (1952).

[10] T.-S. Cao, M. Maziere, K. Danas, J. Besson, 'A model for ductile damage prediction at low stress triaxialities incorporating void shape change and void rotation', *Int. J. Solids Struct.* **63** (2015), 240-263.

[11] K. Danas, private communication, (2013).

[12] K. Danas and N. Aravas, 'Numerical modeling of elasto-plastic porous materials with void shape effects at finite deformations', *Composites: Part B* **43** (2012), 2544–2559.

[13] G. deBotton and P. Ponte Castañeda, 'Elastoplastic constitutive relations for fiber-reinforced solids', *Int. J. Solids Struct.* **30** (1993), 1865–1890.

[14] J.D. Eshelby, 'The determination of the elastic field of an ellipsoidal inclusion and related problems', *Proc. R. Soc. Lond. A* **241** (1957), 376–396.

[15] F. Fritzen, S. Forest, T. Böhlke, D. Kondo, T. Kanit, 'Computational homogenization of elasto-plastic porous metals', *Int.J. Plast.* **29** (2012), 102–119.

[16] M. Gărăjeu and P. Suquet, 'Effective properties of porous ideally plastic or viscoplastic materials containing rigid particles', *J. Mech. Phys. Solids* **45** (1997), 873–902.

[17] A. Giompliakis, 'Three dimensional unit cell modeling of multiphase steels', MSc thesis. University of Thessaly. Greece (2013).

[18] J. Hadamard, 'Leçons sur la propagation des ondes et les équations de l' hydrodynamique', Libraire Scientifique A, Hermann, Paris (1903).

[19] G.N. Haidemenopoulos, N. Aravas and I. Bellas, 'Kinetics of strain-induced transformation of dispersed austenite in low-alloy TRIP steels', *Mater. Sci. Eng. A* **615** (2014), 416-423.

[20] Z. Hashin and S. Shtrikman, 'A variational approach to the theory of the effective magnetic permeability of multiphase materials', *Int.J. Appl. Phys.* **33** (1962), 3125-3131.

[21] Z. He, L. Dormieux, D. Kondo, 'Strength properties of a DruckerPrager porous medium reinforced by rigid particles', *Int. J. Plasticity* **51** (2013), 218–240.

[22] A.V. Hershey, 'The elasticity of an isotropic aggregate of anisotropic cubic crystals', *Int.J. Appl. Mech.* **21** (1954), 236-240.

[23] H.D. Hibbitt, 'ABAQUS/EPGEN — A general purpose finite element code with emphasis in nonlinear applications', *Nucl. Engng. Des.* **77** (1977), 271–297.

[24] R. Hill, 'Discontinuity relations in mechanics of solids', *Progress in Solid Mechanics*, Vol. II, Chapt. 6 (eds. I. N. Sneddon and R. Hill), 247–276, North Holland Publ. Co., Amsterdam (1961).

[25] R. Hill, 'A self-consistent mechanics of composite materials', *J. Mech. Phys. Solids* **13** (1965), 213–222.

[26] R. Hill and J.W. Hutchinson, 'Bifurcation phenomena in the plane tension test', *J. Mech. Phys. Solids* **23** (1975), 239-264.

[27] J. W. Hutchinson, 'Bounds and Self-Consistent Estimates for Creep of Polycrystalline Materials', *Proc. R. Soc***A348** (1976), 101.

[28] J. W. Hutchinson, K. W. Neal and A. Needleman, 'Sheet necking – I. Validity of plane stress assumptions of the long-wavelength approximation', *Mechanics of Sheet Metal Forming* (eds. D. P. Koistinen and N-M. Wang), 111–126, Plenum Press, New York-London (1978).

[29] M. Idiart, 'Modeling the macroscopic behavior of two-phase nonlinear composites by infinite rank laminates', *J. Mech. Phys. Solids* **56** (2008), 2599–2617.

[30] M.I. Idiart, H. Moulinec, P. Ponte Castañeda and P. Suquet, 'Macroscopic behavior and field fluctuations in viscoplastic composites: Second-order estimates versus full-field-simulations', *J. Mech. Phys. Solids* **54** (2006), 1029–1063.

[31] M. Kailasam and P. Ponte Castañeda, 'A general constitutive theory for linear and nonlinear particulate media with microstructure evolution', *J. Mech. Phys. Solids* **46** (1998), 427–465.

[32] E.H. Kaufman, Jr., D.J. Leeming and G.D. Taylor, 'An ODE-based approach to nonlinearly constrained minimax problems', *Numerical Algorithms* **9** (1995), 25–37 (CONMAX software available at http://www.netlib.org/cgi-bin/search.pl).

[33] E. Kröner, 'Berechnung der elastichen konstanten des vielkristalls aus den konstanden des einkristalls', *Z. Phys.* **151** (1958), 504-518.

[34] N. Lahellec, P. Suquet, 'On the effective behavior of nonlinear inelastic composites: I. Incremental variational principles', *J. Mech. Phys. Solids***55** (2007a), 1932–1963.

[35] O. Lopez-Pamies, T. Goudarzi, K. Danas, 'The nonlinear elastic response of suspensions of rigid inclusions in rubber. II. A simple explicit approximation for finite-concentration suspensions', *J. Mech. Phys. Solids* **61** (2013), 19–37.

[36] S. Maghous, L. Dormieux, J.F. Barthélémy, 'Micromechanical approach to the strength properties of frictional geomaterials', *Eur. J. Mech. A/Solids* **28** (2009), 179–188.

[37] Z. Marciniak and K. Kuczynski, 'Limit strains in the process of stretch forming sheet metal', *Int. J. Mech. Sciences* **9** (1967), 609–620.

[38] A. Mbiakop, A. Constantinescu and K. Danas, 'On void shape effects of periodic elastoplastic materials subjected to cyclic loading', *Eur. J. Mech. A/Solids* **49** (2015), 481–499.

[39] A. Mbiakop, A. Constantinescu and K. Danas, 'An analytical model for porous single crystals with ellipsoidal voids', *J. Mech. Phys. Solids* **84**, (2015), 436–467.

[40] J.C. Michel, P. Suquet, 'The constitutive law of nonlinear viscous and porous materials', *J. Mech. Phys. Solids* **40**, (1992), 783–812.

[41] J.C. Michel, H. Moulinec and P. Suquet, 'Effective properties of composite materials with periodic microstructure: a computational approach', *Comp. Methods Appl. Mech. Eng.* **172** (1999), 109–143.

[42] A. Needleman, 'Non-normality and bifurcation in plane strain tension and compression', *J. Mech. Phys. Solids* **27** (1979), 231-254.

[43] A. Needleman and J.R. Rice, 'Limits to ductility set by plastic flow localization', in: D.P. Koistinen, N.-M. Wang (Eds.), Mechanics of Sheet Metal Forming, Plenum Press, New York, London, (1978) 237-267.

[44] A. Needleman and V. Tvergaard, 'Limits to formability in rate-sensitive metal sheets', *Mechanical Behavior of Materials – IV* (eds. J. Carlsson and N. G. Ohlson), 51–65, Pergamon Press, Oxford and New York, London (1984).

[45] G. B. Olson and M. Cohen, 'Kinetics of strain-induced martensitic nucleation', *Metall. Trans.* **6A** (1975), 791–795.

[46] I. Papatriantafillou, 'TRIP steels: Constitutive modeling and computational issues', PhD thesis, University of Thessaly (2005).

[47] I. Papatriantafillou, M. Agoras, N. Aravas and G. Haidemenopoulos, 'Constitutive modeling and finite element methods for TRIP steels', *Comp. Methods Appl. Mech. Eng.* **195** (2006), 5094–5114.

[48] P. Ponte Castañeda, 'The effective mechanical properties of nonlinear isotropic composites', *J. Mech. Phys. Solids* **39** (1991), 45–71.

[49] P. Ponte Castañeda, 'New variational principles in plasticity and their application to composite materials', *J. Mech. Phys. Solids* **40** (1992), 1757–1788.

[50] P. Ponte Castañeda, 'Exact second-order estimates for the effective mechanical properties of nonlinear composite materials', *J. Mech. Phys. Solids* **44** (1996) 827–862.

[51] P. Ponte Castañeda, 'Nonlinear composite materials: Effective constitutive behavior and microstructure evolution', in *Continuum Micromechanics*, CISM Courses and Lectures No. 377 (ed. P. Suquet), Springer-Verlag (1997), 131–195.

[52] P. Ponte Castañeda, 'Nonlinear composites', *Advances in Applied Mechanics* **34** (1998), 171–302.

[53] P. Ponte Castañeda, 'Second-order homogenization estimates for nonlinear composites incorporating field fluctuations: I–theory', *J. Mech. Phys. Solids* **50** (2002) 737–757.

[54] P. Ponte Castañeda, 'Heterogeneous Materials', *Lecture Notes*, École Polytechnique, Department of Mechanics, ISBN 2-7302-1267-1 (2005).

[55] P. Ponte Castañeda and G. deBotton, 'On the homogenized yield strength of two-phase composites', *Proc. R. Soc. Lond.* A **438** (1992), 419–431.

[56] P. Ponte Castañeda and M. Zaidman, 'Constitutive models for porous materials with evolving microstructure', *J. Mech. Phys. Solids* **42** (1994), 1459–1497.

[57] P. Ponte Castañeda and P. Suquet, 'On the effective mechanical behavior of weakly inhomogeneous nonlinear materials', *Eur. J. Mech. A/Solids* **14** (1995), 205–236.

[58] P. Ponte Castañeda and P. Suquet, 'Nonlinear Composites and Microstructure evolution', in H. Aref and J. Phillips (eds.) Mechanics for a new Millenium, Kluwer Acad. Pub.,(2001), 253–273, .

[59] J. R. Rice, 'The localization of plastic deformation', *Proceedings of the 14th International Congress on Theoretical and Applied Mechanics* (ed. W. T. Koiter), 207–220, North-Holland Publishing Corporation, (1977).

[60] M.D. Rintoul and S. Torquato, 'Reconstruction of the structure of dispersions', *J. Collois Inter. Sci.* **186** (1997), 467–476.

[61] L. Samek, E. De Moor, J. Penning, and B.C. De Cooman, 'Influence of alloying elements on the kinetics of strain-induced martensitic nucleation in low-alloy, multiphase high-strength steels', *Metall. Mater. Trans. A*, **37A** (2006), 109-124.

[62] J. Schöberl, 'NETGEN An advancing front 2D/3D-mesh generator based on abstract rules', *Computing and Visualization in Science*, **1**, (1997), 41–52.

[63] J. Segurado and J. Llorca, 'A numerical approximation to the elastic properties of sphere-reinforced composites', *J. Mech. Phys. Solids* **50** (2002), 2107–2121.

[64] R. G. Stringfellow, D. M. Parks and G. B. Olson, 'A constitutive model for transformation plasticity accompanying strain-induced martensitic transfrmation in metastable austenitic steels', *Acta metall. mater.* **40** (1992), 1703–1716.

[65] P. Suquet, 'Elements of homogenization for inelastic solids', in *Homogenization Techniques for Composite Media*, (eds. E. Sanchez-Palencias and A. Zaoui), Springer-Verlag (1987), 194–278.

[66] P. Suquet, 'Overall potentials and extremal surfaces of power law or ideally plastic composites', *Eur. J. Mech. A/Solids* **41** (1993), 981–1002.

[67] P. Suquet, 'Overall properties of nonlinear composites: a modified secant moduli theory and its link with Ponte Castañeda's nonlinear variational procedure', *CR Acad Sci Paris II* **320** (1995), 563–71.

[68] P. Suquet, 'Effective properties of nonlinear composites', in *Continuum Micromechanics*, CISM Courses and Lectures No. 377 (ed. P. Suquet), Springer-Verlag (1997) 197–264.

[69] P. Suquet and P. Ponte Castañeda, 'Small-contrast perturbation expansions for the effective properties of nonlinear composites', *C. R. Acad. Sci. Paris (Série II)* **317** (1993), 1515–1522.

[70] D.R.S. Talbot and J.R. Willis, 'Variational Principles for Inhomogeneous Non-linear Media', *IMA Journal of Applied Mathematics* **35** (1985), 39–54.

[71] D.R.S. Talbot and J.R. Willis, 'Some simple explicit bounds for the overall behavior of nonlinear composites', *Int. J. Solids Struct.* **29** (1992), 1981–1987.

[72] Technical Steel Research: 'Modeling of mechanical properties and local deformation of high-strength multi-phase steels', Final Report, European Commission, Contract No. 7210-Pr/044, (2002).

[73] V. Tvergaard, 'Effect of kinematic hardening on localized necking in biaxially stretched sheets', *Int. J. Mech. Sci.* **20** (1978), 651–658.

[74] V. Tvergaard, 'Bifurcation and imperfection sensitivity at necking instabilities', *Zeits. ang. Math. Mech.* **60** (1980), T26–T34.

[75] J.R. Willis, 'Bounds and self-consistent estimates for the overall properties of anisotropic composites', *J. Mech. Phys. Solids***25** (1977), 185–202.

[76] J.R. Willis, 'Elasticity theory of composites', in *Mechanics of Solids*, The Rodney Hill 60th Anniversary Volume (eds. H.G. Hopkins and M.J. Sewell), Pergamon Press (1982), 653–686.

[77] J.R. Willis, 'The Overall Elastic Response of Composite Materials', *J. Appl. Mech.* **50(4b)** (1983), 1202–1209.

[78] H.K. Yeddu, A. Borgenstam, J. Agren, 'Stress-assisted martensitic transformations in steels: A 3-D phase-field study', *Acta Materialia* **61** (2013) 2595-2606.